INVESTIGATION OF THE ^{30}Si(p,γ)^{31}P REACTION

John Robert Dermigny

A dissertation submitted to the faculty at the University of North Carolina at Chapel Hill in partial fulfillment of the requirements for the degree of Doctor of Philosophy in the Department of Physics.

Chapel Hill
2018

Approved by:

Christian Iliadis

Arthur E. Champagne

Richard Longland

Fabian Heitsch

Nick Law

ABSTRACT

John Robert Dermigny: Investigation of the ^{30}Si(p,γ)^{31}P Reaction
(Under the direction of Christian Iliadis)

Abundance anomalies in globular clusters provide strong evidence for multiple stellar populations within each cluster. These populations are usually interpreted as distinct generations, with the currently observed second-generation stars having formed in part from the ejecta of massive, first generation "polluter" stars, giving rise to the anomalous abundance patterns. The precise nature of the polluters and their enrichment mechanism are still unclear. Even so, the chemical abundances measured in second-generation stars within the cluster NGC 2419 have provided insight into this puzzling process.

We performed a sensitivity study using Monte Carlo reaction rate network calculations based on a simple enrichment model for NGC 2419. This work suggested four thermonuclear reactions that have a significant impact on the elemental abundances in this cluster. A firm understanding of the astrophysical source of the pollution material is precluded by their large reaction rate uncertainties.

In the present study, one of these reactions, ^{30}Si(p,γ)^{31}P, has been investigated at the Laboratory for Experimental Nuclear Astrophysics (LENA). The resonance strengths of the $E_r^{lab} = 433.5 \pm 0.3$ keV and $E_r^{lab} = 499.5 \pm 0.2$ keV resonances have been measured. For the former, which was previously unobserved, we obtain $\omega\gamma = 88 \pm 19$ μeV. For the latter, we obtain $\omega\gamma = 188 \pm 14$ meV. This is consistent with the most recent measurement while improving upon the uncertainty. Based on these results, the thermonuclear reaction rate has been re-evaluated. The impact of the new measurements is to lower the reaction rate by a factor of 10 at temperatures important to the study of NGC 2419. The rate uncertainty at these temperatures has been reduced by a factor of 30.

For Alex.

"*So long, and thanks for all the fish.*"

— Douglas Adams, The Hitchhiker's Guide to the Galaxy

ACKNOWLEDGEMENTS

First, I would like to thank my wife, Alexandra, who has been an incredible source of inspiration for me these past couple months. She is the most hardworking and tenacious person I know, and I aspire to be more like her. She has borne the brunt of the tremendous commitment this document represents, taking on the full suite of responsibilities at home while I was writing in various cafes and libraries. It could not have been done without her steadfast support.

I am incredibly thankful for my parents, Jack and Susanne. They grew up with considerably less than I did, and made me and my siblings' education a top-priority while accomplishing a great deal themselves. They encouraged hard work and curiosity and made sure that I had every opportunity to explore, experiment, and wonder. This dissertation is a testament to the sacrifices they made for their children.

My advisor, Christian Iliadis, has been an superb mentor. He is peerless in his dedication to his students and their professional development. I have benefited enormously from his careful eye for scientific writing and presentation, and am very grateful for all the time he spent working with me on my research papers and talks. I will fondly remember our espresso fueled discussions, trying to wrangle truth from some subtle piece of statistical sorcery.

I consider myself very lucky to have worked with Art Champagne. This thesis project most certainly would have been delayed if not for his support. When faced with the choice to either order my targets from a collaborator or refurbish and install the SNICS source, Art fully supported the latter. This was in spite of the potential risks involved with having a graduate student dismantling the work-horse ion source of TUNL. Getting the SNICS working would end up being one my prouder moments as a student.

I am also very fortunate that my career at TUNL overlapped with Richard Longland's faculty career at NCSU. Richard's software contributions to the LENA group made me strive early on to be a better scientific programmer, and this would later become a strength of mine. Richard would later have the bad luck of having an office next to mine, and I had the fortune of running

experiments, analysis techniques, and other ideas by him. His careful approach to experimental physics and statistics has certainly left an indelible mark on me.

Finally, I would to thank the LENA group at large for making these past few years so much fun. I have had the opportunity to work with some tremendous physicists in an environment that engenders creativity, risk-taking, and collaboration. This has allowed me to identify my personal strengths and weaknesses as a scientist, professional, and lab citizen in ways that other groups or laboratories would be hard-pressed to match.

TABLE OF CONTENTS

LIST OF TABLES

LIST OF FIGURES

CHAPTER 1: INTRODUCTION

Section 1.1: Globular Clusters

Globular clusters are extremely dense aggregates of gravitationally bound stars. In the Milky Way galaxy alone, there are about 150 that have been identified, comprising anywhere from tens of thousands to millions of stars. They reside far out in the galactic halo and are distributed spherically around the galactic core. Notable examples of these spectacular structures are M22 in the constellation *Sagittarius* and ω Centauri in the constellation *Centaurus*.

For many reasons, globular clusters are ideal laboratories for testing the theories of stellar structure and evolution. They are also among the oldest known structures in the Universe, so they sample the earliest phases of galaxy formation and provide a lower limit to the age of the Universe [Kruijssen, 2014, Forbes *et al.*, 2018]. Since they are made up of many stars, located at virtually the same distance from us, and possibly of similar age and chemical composition, they are the best known examples of simple stellar populations. The usefulness of a simple stellar population to astronomy can be illustrated using a color-magnitude diagram. Figure 1.1 shows the observed color-magnitude diagram of the globular cluster M3. For each star in the diagram, its position is given by its color (B-V) on the x-axis, and the observed apparent magnitude (V) on the y-axis. Since each star is thought to have the same initial chemical composition, its location is determined by their evolutionary rate, which is itself determined by its stellar mass. The stars all appear to lie on a single *isochrone*. The sequence of events along the isochrone make up the evolutionary history of the stars within M3.

Stellar evolution is broadly driven by (i) the mass of the star, (ii) the fuel source of nuclear burning (e.g., H, He, C), and (iii) the sites of this burning, i.e., whether it occurs in the core, a surrounding shell, or both. The various stages of evolution are indicated in Figure 1.1. Stars begin on the main sequence (MS) after the gravitational contraction of a (pre-main sequence) proto-star increases its central temperature beyond several million kelvin, where the fusion of hydrogen to

helium starts to occur. Eventually, the energy released from nuclear reactions is able to support the star against gravitational contraction, and the star reaches hydrostatic and thermal equilibrium. Stars spend $\approx 90\%$ of their life at this stage, gradually converting the hydrogen in their core to helium via the pp-chain as their main source of energy. This continues until core hydrogen has been exhausted, at which point the star evolves off the main sequence. This is known as the turn-off (TO) point. A relationship between the luminosity of the turn-off point and the age of the stars can be derived, making the turn-off point a unique and powerful tool for determining the age of a cluster. If an absolute age can be determined, then it can provide a stringent lower-limit to the age of the Universe [Di Cecco *et al.*, 2010]. Additionally, relative ages can be obtained reliably by measuring the position of the turn-off relative to another feature of the color-magnitude diagram. Relative ages are useful for distinguishing between competing formation histories for the Milky Way [Rosenberg *et al.*, 1999, De Angeli *et al.*, 2005].

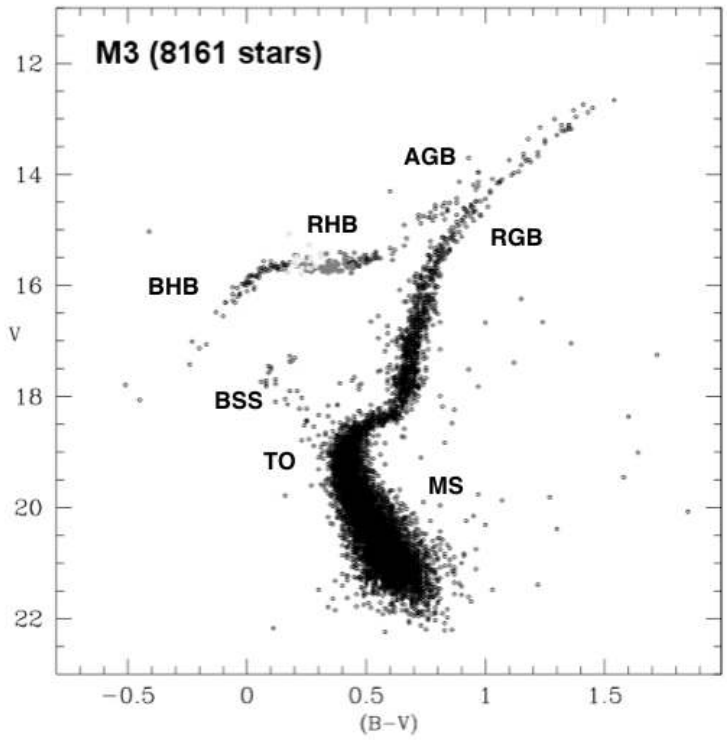

Figure 1.1: The stars of the globular cluster M3 are shown in this color-magnitude diagram. The x-axis is the B-V color index. Along the y-axis, the absolute magnitude is shown. The main-sequence (MS), turn-off point (TO), red giant branch (RGB), asymptotic giant branch (AGB), red horizontal branch (RHB), and blue horizontal branch (BHB) are indicated. The blue stragglers (BSS) are also shown. Figure is from Fusi-Pecci and Clementini [2001].

After the turn-off, the star begins burning hydrogen in a thick shell near the helium core where there is still hydrogen left. The core, no longer able to balance gravitational contraction, begins to contract, which causes further heating. At this point the outer envelope of the star begins to expand, growing more luminous as it ascends the red giant branch (RGB). At the tip of the RGB, the stellar temperature in the helium core has advanced to 100 MK. In an event called the "helium flash", helium burning via the triple-α process begins in the core, and the star quickly restructures and begins quiescent helium burning on either the red (RHB) or blue (BHB) horizontal branch. Eventually, when helium becomes depleted in the core, it will again undergo contraction while burning starts in the surrounding shell. The star, now characterized by a carbon-oxygen core surrounded first by a helium burning shell and then by a hydrogen burning shell, evolves upwards on the color-magnitude diagram and merges into the RBG during the asymptotic giant branch (AGB) phase. Stellar evolution in the AGB phase is highly dependent on the mass of the star. For a low-mass star, such as the Sun (1 $M_{\odot}$), the helium and hydrogen shells will continue to burn until a significant portion of its mass is lost to the interstellar medium via stellar winds. Eventually, the star will retire as a dim carbon-oxygen white dwarf with nearly half of its initial mass, cooling slowly by radiating away its thermal energy.

The evolutionary sequence presented above is only a cursory overview. In general, each stage is influenced by the mass, chemical composition, and metallicity of the star. There are many open questions regarding how these traits influence stellar evolution that globular clusters continue to shed light on. For example, the color distribution of cluster stars along the horizontal branch (HB) is referred to as the 'HB morphology' of the cluster, where the number of stars on the red (RHB) and blue (BHB) sides describes the overall HB morphology. Early on, this was thought to be dependent only on the metallicity of the stars. However, several exceptions to this rule have been found. This inconsistency is known as the *second parameter problem*. Age, helium content, and metal abundance ratios are the additional parameters most often invoked to explain the observed morphologies [Gratton *et al.*, 2010]. Another question pertains to the nature of the *blue stragglers* (BSS). These are stars that lie off the main sequence, above the turn-off point. The reason for their enhanced temperature and luminosity is not yet understood, but the prevailing theory is that the stragglers have acquired new mass, either though mass transfer or merger with a main sequence star [Parada *et al.*, 2016]. Their origin could provide new perspectives on the dynamics within the

cluster and its effect on stellar evolution.

Section 1.2: Abundance Anomalies

The single stellar population is clearly a very useful concept. However, in the last few decades compelling evidence has come to light that suggests globular cluster formation is far more complicated. Although a color-magnitude diagram may appear to contain a single isochrone, a closer inspection will reveal several distinct isochrones, suggesting that multiple populations of stars are present within the cluster that each have their own unique chemical inventories. A famous example is shown in Figure 1.2, where high resolution photometry of the globular cluster NGC 2808, measured by Piotto *et al.* [2007], reveals that the main sequence actually comprises three distinct isochrones. Analysis of these isochrones suggests that they correspond to stellar populations with increasing levels of helium (from left to right). Since it is difficult to imagine a scenario where three populations formed at the same time, from the same proto-cluster material, yet have drastically dissimilar chemical abundances, a common interpretation is that the different populations are in fact different *generations* of stars, which formed from progressively enhanced intra-cluster material. The precise sequence of events that could have led to the formation of such populations is yet unknown.

The growing evidence for multiple populations is not limited to the color-magnitude diagram. The red giant stars of many globular clusters have been studied using high resolution spectroscopy to discover star-to-star abundance variations in the light elements (e.g., C, N, O, Na, Al, Mg, Si F). One important example is the Na-O anticorrelation, characterized by the presence of both Na-poor/O-rich and Na-rich/O-poor stars. The sodium enhancement is puzzling, since the observed low-mass red giants do not reach the temperatures necessary to produce this signature themselves. Instead, it must have been imprinted onto the gas from which these stars formed. It has been shown that the Na-rich stars correspond to helium enhanced stars, reinforcing the position that they belong to a different population altogether [Gratton *et al.*, 2010]. The Na-O anticorrelation has been observed in every cluster for which it has been looked for [Carretta *et al.*, 2010], suggesting that the presence of multiple stellar generations is a ubiquitous feature of globular clusters.

Departure from the simple stellar population paradigm has broader implications for globular

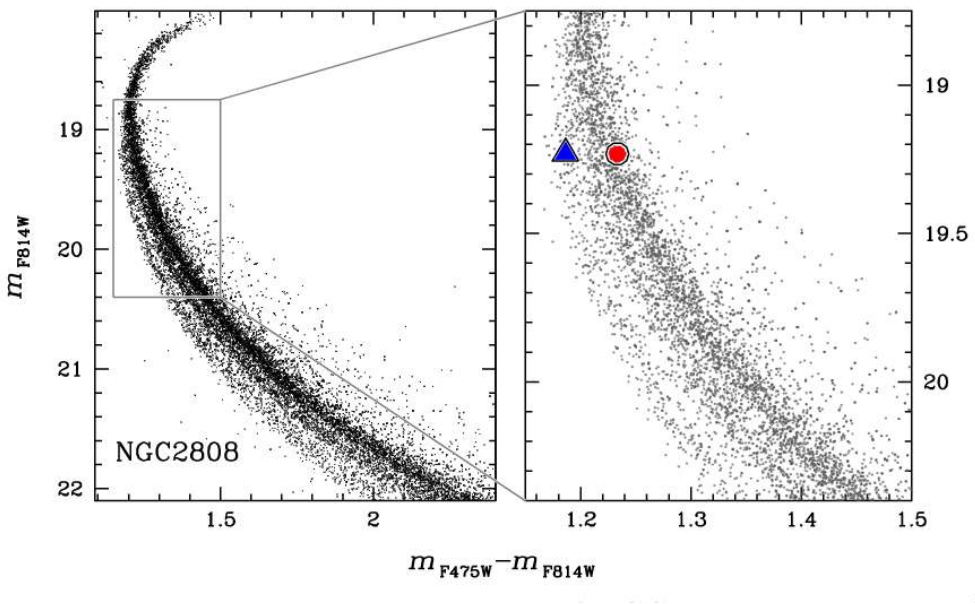

Figure 1.2: Triple main-sequence of the cluster NGC 2808. Figure is from Bragaglia *et al.* [2010], based on the photometry measure by Piotto *et al.* [2007]. The blue triangle and red circle refer to measurements by Bragaglia *et al.* [2010] and are not pertinent to the present discussion.

clusters than just an additional spread of stellar formation times or chemical inhomogeneities. For example, Carretta *et al.* [2010] found that the HB morphology of a cluster is strongly correlated with the distribution of Na-O abundances, suggesting that multiple populations, or perhaps the mechanism responsible, may play a role in the second parameter problem. Similar findings have been reported by Marino *et al.* [2013] and Milone [2014]. Further, since globular clusters are one of our main probes of early galactic evolution, the dynamical history and chemical enrichment of these populations are important problems. This has therefore been the focus of an intense campaign of theoretical investigations [Prantzos *et al.*, 2007a, D'Ercole *et al.*, 2010, Bekki, 2011].

Several schemas have been put forth to explain the presence of the observed populations and their so-called abundance anomalies. Contemporary models now include several episodes of star formation that give rise to a primordial generation, a first generation, and a second generation of stars. The primordial generation refers to the zero-metal population III stars that formed after the big bang. These are responsible for initially seeding the proto-cluster gas with metals through ejecta and stellar winds of massive stars. Eventually, the first-generation stars form from this material. The massive stars among these evolve quickly and reach more advanced stages of stellar evolution, where higher temperatures enable further nuclear processing. It is at this stage that the abundance

enhancements observed today are thought to be synthesized. These *polluter* stars then eject some of their material back into the intra-cluster gas. The second generation then forms, inheriting the nucleosynthetic signatures of both the primordial and first-generation stars. Within a cluster, both the first and second generations are observed today, giving rise to the distinct isochrones and the abundance variations.

The above picture is supported by nucleosynthesis simulations. In Prantzos *et al.* [2007b], nuclear reaction network calculations were performed which explored the chemical enrichment of the first-generation polluter stars. Their focus was NGC 6752, a globular cluster with measured C-N, O-Na, and Mg-Al abundance correlations. They adopted realistic initial abundances for the "pristine" proto-cluster gas, and then simulated hydrogen burning at various temperatures. Under this simple model, the nuclearly processed material represented the polluter material before ejection back into the cluster. By mixing this with the pristine gas, they found that the observed anticorrelations could be reproduced in the second-generation stars under certain conditions. First, the polluter material must be processed at a narrow temperature range around $T = 75$ MK. This is necessary to produce the extreme abundance variations observed, e.g., those found in the sodium-enriched and oxygen-depleted stars. Second, the abundance (anti)correlations could be reproduced only by mixing the polluted and pristine material in different proportions, with the most extreme abundances requiring a mixture of $\approx 30\%$ pristine material. These results placed strong constraints on the identity of the polluter stars and also the mixing mechanism responsible for the observed abundance anomalies. Based on these results, they suggested that processing of the polluter material could be taking place in AGB stars and/or massive main sequence stars ($M \approx 40 M_{\odot}$). Further study by D'Ercole *et al.* [2010] and Bekki [2011], which focused on the AGB pollution scenario, also found that AGB stars are good first-generation polluter candidates. Other candidates include rapidly rotating massive stars [Decressin *et al.*, 2007], massive stars in interacting binary systems [de Mink *et al.*, 2009], stellar collisions [Sills and Glebbeek, 2010], supermassive stars [Denissenkov and Hartwick, 2014], super-AGB stars [Ventura *et al.*, 2012], and novae [Maccarone and Zurek, 2012].

Several questions remain regarding the origin of these abundance correlations and their role in the evolution of globular clusters. While there are several viable polluter candidates, they all fail to reproduce the observed He abundances, an issue known as the *mass budget problem* [Bastian

et al., 2015]. To make strides in this area, the dynamics of star formation for the first and second-generation stars requires further research. Nucleosynthesis calculations provide a strong foundation for exploring the different pollution scenarios that give rise to the light-element abundance variations observed in globular clusters.

Section 1.3: NGC 2419

Recent photometric measurements of the globular cluster NGC 2419 have added a new dimension to the mystery of abundance anomalies. This cluster is located in the outer halo, further away than the Small and Large Magellanic clouds, at a galactocentric distance of 87.5 kpc. This great distance has earned it the moniker, *the intergalactic wanderer*, since it was once erroneously thought not to be in orbit around the Milky Way. It is 12.3 ± 1.3 Gy old [Forbes and Bridges, 2010], and has an orbital period of about 3 Gy [Di Criscienzo *et al.*, 2011]. These features alone make it an interesting cluster. However, NGC 2419 is better known for its unique chemical inventory. Measured abundances from several of its red giant member stars are shown in Figure 1.3. These data were taken by Mucciarelli *et al.* [2012] (red points) and Cohen and Kirby [2012] (blue points). The most striking feature of NGC 2419 is the clearcut anticorrelation in the magnesium and potassium abundances, shown in the upper-left panel. Two distinct populations are observed. One has potassium and magnesium abundances consistent with those of low-mass population II stars ([K/Fe][1] ≈ 0.5, [Mg/Fe] ≈ 0.5). The other is highly enhanced in potassium ([K/Fe] ≈ 1.5) and depleted in magnesium ([Mg/Fe]≈ -0.5). This was the first discovery of a Mg-K anticorrelation. It has been observed since then, although to a lesser extent, in NGC 2808 [Mucciarelli *et al.*, 2015].

There are strong indications that the Mg-K anticorrelation is related to the presence of multiple generations within NGC 2419. In Di Criscienzo *et al.* [2011], the potassium enhanced population ($\approx$ 30% of its member stars) was found to have a higher helium content ($Y \approx 0.42$) than the 'normal' stars ($Y \approx 0.24$), suggesting that they formed from a different, more helium enhanced gas mixture. This scenario is consistent with the self-pollution evolutionary model described before. Further, alternative channels of potassium synthesis, such as type II supernovae, are not a viable

[1] According to common convention, abundances are given as $[A/B] = \log_{10}(N_A/N_B)_\star - \log_{10}(N_A/N_B)_\odot$, where N_i are number abundances of elements A and B observed in a star ($\star$) or the sun ($\odot$); while the quantity $[A/B]$ is unitless, differences between the two values are expressed in units of dex ("decimal exponent").

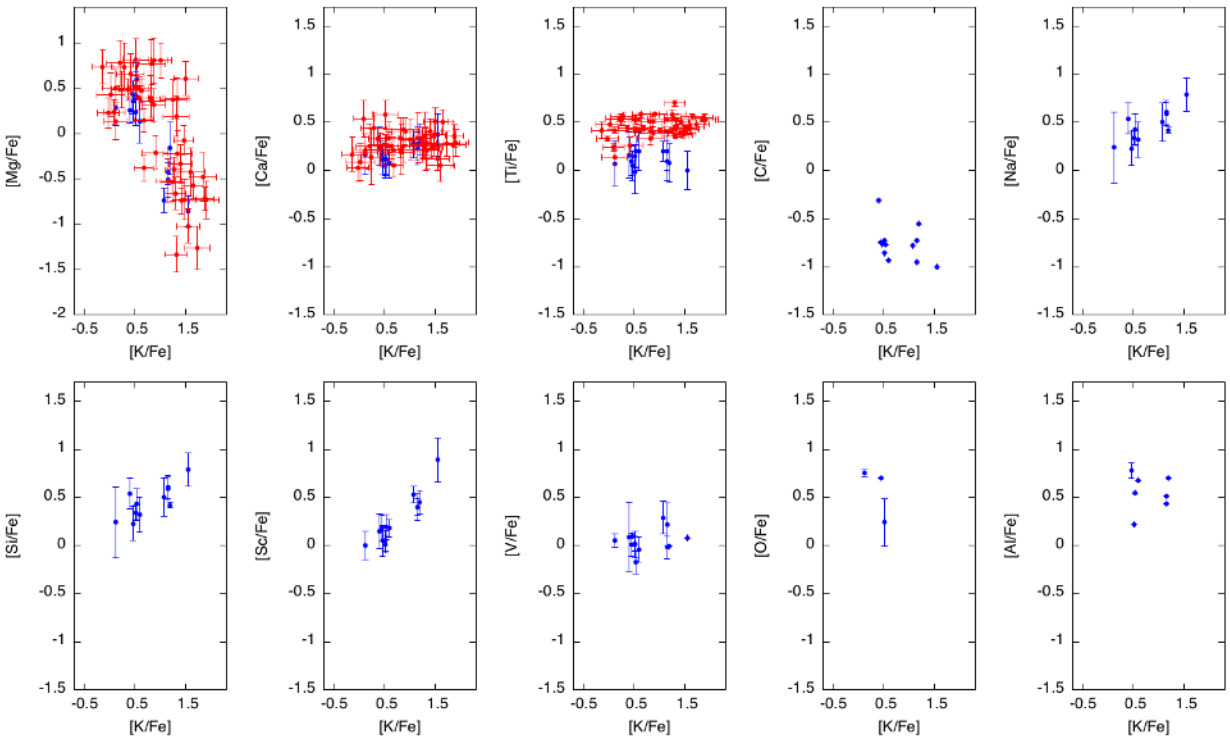

Figure 1.3: Elemental abundances, with respect to Fe, versus K abundance for red giants in NGC 2419. Data were taken by Mucciarelli *et al.* [2012] (red points) and Cohen and Kirby [2012] (blue points).

explanation since there is no star-to-star variation in iron. On the contrary, the observed stars have an average metallicity of [Fe/H] $= -2.09 \pm 0.02$, with no intrinsic spread present [Mucciarelli *et al.*, 2012, Cohen and Kirby, 2012]. Variation in the α-process elements, e.g., Si, Ca, Ti, would also be expected. However, their abundances are found to be mostly constant with respect to [K/Fe], with only a slight correlation in [Si/Fe] present.

The Mg-K anticorrelation raises many new questions. What are the internal cluster dynamics necessary to create such a signature and why do they appear unique to NGC 2419? What (if any) connection is there to early galaxy formation? How is it related to the more commonly observed light-element abundance variations, e.g., the Na-O anticorrelation? What kind of first-generation polluter stars gave rise to the anticorrelation and what was their initial composition? The solutions to these problems are critical to furthering the new globular cluster evolutionary framework.

By improving our understanding of the nucleosynthesis within NGC 2419, this dissertation aims to create a firmer footing from which these questions can be answered. In the next chapter, we explore simulations of the self-enrichment scenario in NGC 2419 and identify though a series of

sensitivity studies those reactions that are the most important to understanding the abundance profile of this strange cluster. One of these reactions, ^{30}Si(p,γ)^{31}P, becomes the focus of the dissertation, since it is found to be an influential reaction in our proposed model and remains poorly understood. The rest of this work represents the substantial effort of improving its thermonuclear reaction rate through a series of resonance measurements. In Chapter 3, nuclear astrophysics theory is introduced, with the intention of connecting the ideas of resonant and non-resonant proton capture to the thermonuclear reaction rate. Then, in Chapter 4, the proton accelerators and γ-ray detection system at the Laboratory for Experimental Nuclear Astrophysics, where these experiments took place, are described. The spectroscopic analysis method adopted in this work is then detailed in Chapter 5. In Chapter 6, we discuss the fabrication and analysis of the nuclear targets used in the resonance experiments. In Chapter 7, the resonant experiments are described, and the application of the spectroscopic analysis method is detailed. This leads to the calculation of the ^{30}Si(p,γ)^{31}P reaction rate in Chapter 8, based on the new measurements as well as a thorough literature evaluation. Finally, in Chapter 9, a summary is given.

CHAPTER 2: NUCLEOSYNTHESIS SIMULATIONS

In this chapter we review nucleosynthesis simulations of the self-enrichment scenario in NGC 2419. As a part of this dissertation, a sensitivity study was performed that explored the nuclear reaction rate network and the individual roles of certain reactions. This work was published in Dermigny and Iliadis [2017] and served as a springboard for the experimental work presented in subsequent chapters. It is reproduced here in a condensed form, and the interested reader is directed to the journal article for more detail.

Section 2.1: Previous Work

Several studies have been dedicated to understanding the unique abundances of the globular cluster NGC 2419. The first was by Ventura *et al.* [2012]. In that work, they explored a scenario where the second-generation stars formed from the processed ejecta of AGB and super-AGB stars. Using stellar evolution models, they evolved material of the same metallicity as the cluster through the AGB phase over a range of stellar masses. The final chemical abundances of these first-generation AGB stars were then compared to the observed potassium and magnesium abundances. They found that the AGB models could explain the Mg-K anticorrelation, though only if model parameters, in particular, the mass loss rate [Bloecker, 1995], were fine tuned. It was also necessary to increase the thermonuclear rate by a factor of 100 for the ^{38}Ar(p,γ)^{39}K reaction, an important link in the Ar-K nucleosynthesis chain. Ultimately, they were able show that AGB and super-AGB stars could be viable polluters, though their dependence on the poorly understood mass loss parameter and the reaction rate adjustment did not allow for a firmer conclusion.

Later, Iliadis *et al.* [2016] approached this problem more generally. Their methodology was based on the earlier work by Prantzos *et al.* [2007b] studying the origin of the Na-O anticorrelation. For the chemical abundances of the pristine intra-cluster gas, they adopted the results of a one-zone chemical evolution model for the Milky Way halo. This model is an updated version of Goswami and Prantzos [2000], which reproduces, with minor adjustments, the reported abundances of field

stars of the same average metallicity as NGC 2419 (for details, the interested reader is directed to the Appendix of Iliadis *et al.* [2016]). Pristine gas was then processed using a Monte Carlo nuclear reaction network simulation to create the polluter material. The network followed the evolution of 213 nuclides, ranging from p, n, ^{4}He, to ^{55}Cr. The thermonuclear reaction rate linking these nuclides (2373 total) were adopted from STARLIB [Sallaska *et al.*, 2013]. This nuclear burning was performed at the stellar temperature, T, and density, ρ, and was halted after a variable amount of hydrogen, $\Delta X^H = X_i^H - X_f^H$, was consumed. These three parameters (T, ρ, ΔX^H) were each sampled randomly for each network simulation, effectively exploring the astrophysical parameter space irrespective of stellar evolution models. Additionally, each reaction rate involved in the reaction network was sampled within its rate uncertainty for each simulation using the procedure in Iliadis *et al.* [2015]. After processing the pristine gas into the polluter material at these environmental conditions, the polluter material was then diluted back with the pristine gas over a range of different mixtures, imitating the unknown ejection process of the polluter stars. If, for any of these mixtures, the abundance profile matched *all* the abundances of Mg, Si, K, Ca, Ti, and V observed in the potassium-enhanced stars, then the astrophysical conditions were considered a plausible site of polluter nucleosynthesis.

The results of their analysis are shown in Figure 2.1. Each blue point represents the temperature and density of one of these plausible polluter sites. There is a narrow band of solutions, ranging from $\approx$ 200 MK at $\approx 10^{-1}$ g cm^{-3} to $\approx$ 130 MK at $\approx 10^{5}$ g cm^{-3}. The temperature and density tracks of several polluter candidates are also shown. Their overlap illustrates whether a particular candidate, as predicted by their model, is capable of producing the Mg-K anticorrelation. By this measure, classical novae ("CN") involving either carbon-oxygen or oxygen-neon white dwarfs certainly make compelling polluter candidates. Super-AGB stars, though not overlapping with the solution-space, are close enough to remain a possibility.

Iliadis *et al.* [2016] also found that reaction rate uncertainties play an important role in the width of the temperature-density solution space, suggesting that our predictions of the astrophysical conditions responsible could be improved though nuclear reaction measurements. If certain critical reactions could be identified and measured, then perhaps the temperature range in Figure 2.1 would narrow as a result of the improved rates, indicating that the polluter burning occurs in even fewer environments. Conversely, the range could widen, in which case several different polluter scenarios

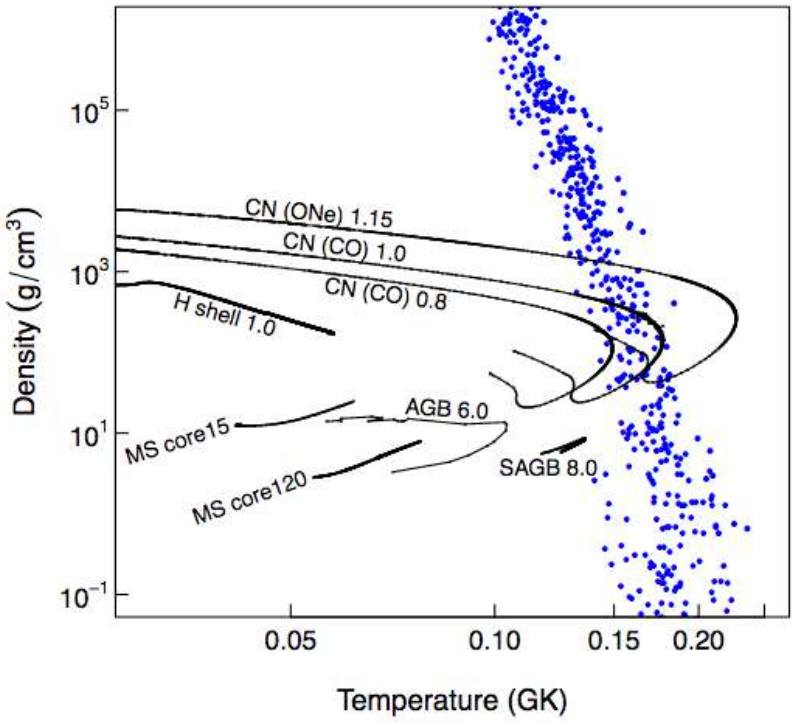

Figure 2.1: Stellar density vs. temperature for sets of (T, ρ, X_H^f) values that reproduce the measured elemental abundances in NGC 2419. These results were obtained by sampling of T, ρ, and X_H^f, as well as all the nuclear rates used in the reaction network. The temperature and density tracks are shown for several hydrogen-burning polluter candidates: massive main sequence stars ("MS"), hydrogen shell burning, carbon-oxygen and oxygen-neon classical novae ("CN"), AGB, and super-AGB models. Figure from Iliadis *et al.* [2016].

could be equally plausible. This was the impetus for a sensitivity study that we performed in Dermigny and Iliadis [2017] as a part of this dissertation, where the goal was simple: to identify those critical reactions.

Section 2.2: Sensitivity Study

The role of each reaction in creating the abundance signatures was explored in two ways. First, the procedure outlined in Iliadis *et al.* [2016] was repeated once for each reaction in the network, totaling 2373 unique Monte Carlo network calculations. In each of these, only a single reaction was allowed to vary within its statistical uncertainty, producing a temperature-density solution space unique to the reaction rate in question. All other rates remained *fixed* at their recommended value. The width of the temperature distribution was then measured for each of these simulations

and ranked. Those reactions which produced the largest temperature range were considered the most important, since they had the greatest impact on the range of astrophysical sites. Using this procedure, we identified (in decreasing order of importance) the ^{30}Si(p,γ)^{31}P, ^{37}Ar(p,γ)^{38}K, and ^{38}Ar(p,γ)^{39}K reactions as being the most influential. Their relevance to the Mg-K anticorrelation will be discussed shortly.

Next, we explored what effect systematic variations in the reaction rates had on the temperature-density space. We repeated the procedure from Iliadis *et al.* [2016], with each run focused on one rate in the Ne-Na, Mg-Al, Al-Si and Ar-K reaction chains. This time, the reaction of interest was multiplied by a systematic variation factor, α. This factor changed the magnitude of the reaction rate by 1/10, 1/5, 5, or 10. The results of this exercise are shown in Figure 2.2, where the rows correspond (from top to bottom) to the ^{30}Si(p,γ)^{31}P, ^{37}Ar(p,γ)^{38}K, ^{38}Ar(p,γ)^{39}K, and ^{39}K(p,γ)^{40}Ca reactions. For all of the other reactions considered, the effect of the variation was found to be much less impactful. The variation factor α is displayed in the top right-hand corner of each plot. The case with no artificial systematic effect, i.e., $\alpha = 1$, is shown in the foreground (red dots) for comparison. The effect on the broadening of the temperature and density conditions (black dots) reveals their sensitivity to the magnitude of each reaction rate.

The role that each of these reactions play can be surmized based on this work. For example, when the ^{30}Si(p,γ)^{31}P reaction is increased by a factor of 5, the width of the temperature-density distribution (black dots) grows narrower, with the high-temperature edge receding at any given density. The simulated abundances at these conditions (e.g., T = 170 MK, ρ = 100 g/cm^3, $X_f^H = 0.50$) are found to be depleted in silicon when compared with the $\alpha = 1$ case, with a net reduction of $\approx$ 1.3 dex. This indicates that the narrowing is caused by the onset of silicon depletion via ^{30}Si(p,γ)^{31}P.

Adjustments to the ^{37}Ar(p,γ)^{38}K, ^{38}Ar(p,γ)^{39}K, and ^{39}K(p,γ)^{40}Ca reactions reveal a similar effect on the potassium abundance. Note that as both the ^{37}Ar(p,γ)^{38}K and ^{38}Ar(p,γ)^{39}K reaction rates are increased, the temperature-density scatter increases, with newly viable conditions appearing on the low-temperature side. For the ^{38}Ar(p,γ)^{39}K reaction, the difference between the leftmost and rightmost plot is particularly stark. Under the same test conditions as before, the elemental potassium abundance increases by $\approx$ 1.0 dex when this reaction is varied from $\alpha = 1/10$ to $\alpha = 10$ times its recommended value. The succeeding reaction, ^{39}K(p,γ)^{40}Ca, has the opposite

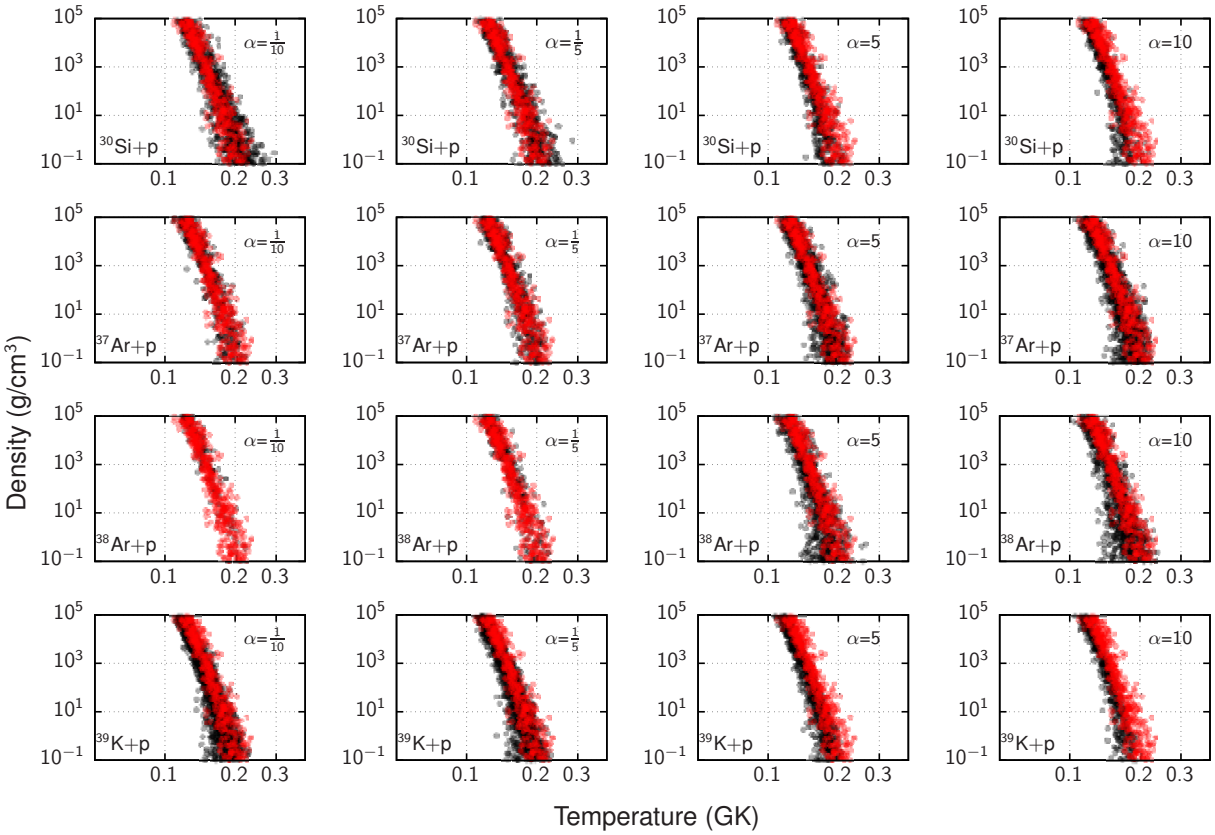

Figure 2.2: Sensitivity of the temperature-density conditions to the influence of the unknown systematic effects in the reaction ^{30}Si(p,γ)^{31}P (first row), ^{37}Ar(p,γ)^{38}K (second row), and ^{38}Ar(p,γ)^{39}K (third row), and ^{39}K(p,γ)^{40}Ca (fourth row). The variation factors (α = 1/10, 1/5, 5, 10) applied to each reaction rate are shown increasing from left to right. The temperature and density combinations that provide an acceptable match between simulated and observed abundances are shown as black dots. The case with no artificial systematic effect (α = 1) is shown as red dots, for comparison. Figure is from Dermigny and Iliadis [2017].

effect of depleting potassium by $\approx$ 0.8 dex. This is made apparent by comparing the α = 1/10 and 10 cases, where it can be seen that the high temperature conditions no longer satisfy the abundance constraints when the rate is increased.

In that work, we identified the ^{30}Si(p,γ)^{31}P, ^{37}Ar(p,γ)^{38}K, ^{38}Ar(p,γ)^{39}K, and ^{39}K(p,γ)^{40}Ca reactions as being critical to the Mg-K anticorrelation. We concluded by recommending a series of nuclear experiments, designed to improve their reaction rates in the temperature range 100 to 300 MK. In this dissertation, the ^{30}Si(p,γ)^{31}P reaction is measured via nuclear resonance experiments. This is the inaugural work in the experimental campaign to better understand the bizarre chemical inventory of NGC 2419.

Section 2.3: ^{30}Si(p,γ)^{31}P

That the ^{30}Si(p,γ)^{31}P reaction rate is important is not intuitively obvious, since it does not directly create or destroy either magnesium or potassium. Instead, it is significant because it consumes ^{30}Si, which makes up a large percentage of the elemental silicon at these high temperatures. The silicon abundances measured by Cohen and Kirby [2012] place a strong additional constraint on the nucleosynthesis calculations in Iliadis *et al.* [2016] and Dermigny and Iliadis [2017], since any polluter sites that produce the Mg-K anticorrelation *must* also reproduce the Si-K correlation.

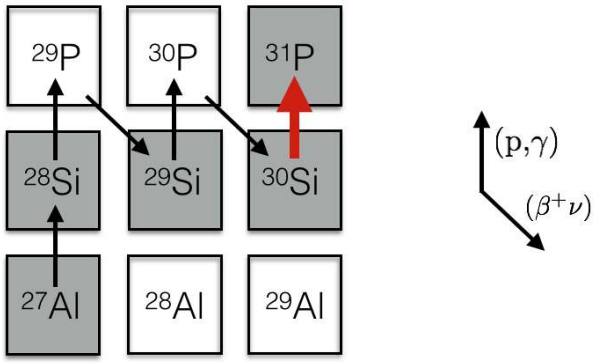

Figure 2.3: The nuclear reaction network for the Al-P nuclides. Reactions are shown as solid arrows, as indicated by the key on the right. The red arrow denotes the ^{30}Si(p,γ)^{31}P reaction. Gray isotopes denote stable nuclides.

Silicon synthesis and destruction varies precipitously in the 100 - 200 MK temperature range, making the silicon abundance constraint a very sensitive test for the nucleosynthesis calculations. At the lower end ($<$ 140 MK), silicon is primarily made up of the isotope ^{28}Si. In this regime, destruction via proton capture is sufficiently slow, allowing the elemental abundance of silicon to increase steadily by way of the ^{27}Al(p,γ)^{28}Si reaction. This relationship is shown in Figure 2.3, which illustrates the reaction network in the Al-P mass region. The different nuclear reactions are indicated by solid arrows. At higher temperatures, ^{28}Si is more efficiently converted to ^{30}Si via the sequence ^{28}Si(p,γ)^{29}P($\beta^+\nu$)^{29}Si(p,γ)^{30}P($\beta^+\nu$)^{30}Si. At temperatures above about 160 MK, the accumulated ^{30}Si is rapidly consumed via the ^{30}Si(p,γ)^{31}P reaction, reducing the silicon abundance to sub-solar values. This final reaction is shown as a red arrow in Figure 2.3.

The ^{30}Si(p,γ)^{31}P reaction rate at these temperatures was found to be strongly dependent on a proton capture resonance at $E_r^{lab} = 435 \pm 4$ keV. Nothing is known about this resonance, save for

the predicted energy, which was estimated using indirect reaction data from Vernotte *et al.* [1990]. Therefore, as a means to understanding the origin of the abundance anomalies in NGC 2419, the goal of this dissertation is to measure this resonance and to reevaluate the ^{30}Si(p,γ)^{31}P reaction rate. A nearby resonance at $E_r^{lab} = 498.3 \pm 1.0$ keV [Kuperus *et al.*, 1959] is also studied, since it is important in this temperature regime and has been measured only a few times, with little consistency in the measured quantities. In the next chapter, a brief introduction to nuclear astrophysics theory is presented. The connection between resonances and the thermonuclear reaction rate will be explained.

CHAPTER 3: NUCLEAR ASTROPHYSICS THEORY

The following is a brief introduction to the nuclear physics of thermonuclear reaction rates. The discussion is kept within the purview of this dissertation and is meant to serve as reference for later chapters. The treatment mirrors that of *Nuclear Physics of Stars* [Iliadis, 2015], and the reader is directed to that work for a thorough exposition.

Section 3.1: Thermonuclear Reaction Rates

Thermonuclear reaction rates quantify the nuclear reaction probabilities in a dense, high-temperature plasma. They are therefore paramount to our understanding of nucleosynthesis in astrophysical environments. The derivation for a thermonuclear rate begins with the nuclear cross section. This quantity, σ, is the probability that a nuclear interaction occurs between the target nuclide and an incident particle. It is defined in the context of a laboratory experiment:

$$\sigma \equiv \frac{\textit{interactions per unit time}}{\textit{incident particles per unit time} \times \textit{target nuclei per unit area}}. \tag{3.1}$$

The cross section is reported in units of barns (1 b = 10^{-24} cm^2). It has a complicated velocity (or energy) dependence that is determined by the penetrability of the Coulomb barrier, resonant and non-resonant phenomena, and in some cases, interference effects. If possible, it must be measured experimentally for all reactions.

In a stellar plasma, the target and incident nuclei have a temperature dependent velocity distribution, $P(v)$. The reaction rate per particle pair is therefore given by a convolution of the velocity dependent cross section and the distribution of relative velocities:

$$\langle \sigma v \rangle = \int_0^\infty v P(v) \sigma(v) dv \ . \tag{3.2}$$

The velocity distribution of interacting nuclei in a stellar plasma at thermal equilibrium can be

described by the Maxwell-Boltzmann distribution:

$$P(v)dv = P(E)dE = \frac{2}{\sqrt{\pi}} \frac{1}{(kT)^{3/2}} \sqrt{E} e^{E/kT} dE \ , \tag{3.3}$$

where k is the Boltzmann constant, and T is the temperature. For the reaction rate per particle pair, in units of cm^3 mol^{-1} s^{-1}, we obtain:

$$N_A \langle \sigma v \rangle = N_A \left(\frac{8}{\pi m_{01}} \right)^{1/2} \frac{1}{(kT)^{3/2}} \int_0^\infty E\sigma(E) e^{-E/kT} dE \ , \tag{3.4}$$

where E is the center-of-mass energy, m_{01} is the reduced mass of the interacting particles, and N_A is Avogadro's number. For tabulations of reaction rates in the literature, $N_A \langle \sigma v \rangle$ is the quantity reported over a range of stellar temperatures.

The cross section, σ, contains all the nuclear physics information relevant to this calculation. In the case of the ^{30}Si(p,γ)^{31}P reaction, the largest contribution to σ arises from narrow resonances, while a smaller portion is due to a non-resonant component. The thermonuclear rate can be written as a sum of each of these:

$$N_A \langle \sigma v \rangle_{\text{total}} = N_A \langle \sigma v \rangle_{\text{narrow resonances}} + N_A \langle \sigma v \rangle_{\text{non-resonant}} \ . \tag{3.5}$$

For the calculation of each component, a unique form of Equation 3.4 is invoked. Understanding the requirements of either formulation is critical to this dissertation, as they inform us of how thermonuclear reaction rates may be improved.

Section 3.2: Non-Resonant Reaction Rates

Non-resonant capture of the incident particle by the target nucleus is dictated by the transmission probability through the Coulomb barrier. The measured cross section for the ^{16}O(p,γ)^{17}F reaction in the top panel of Figure 3.1 illustrates this effect for center-of-mass energies from 0.2 MeV to 2.5 MeV. At low energies, the cross section drops dramatically because of the decreasing transmission probability.

Since the non-resonant cross section spans several orders of magnitude, it is far easier to compare

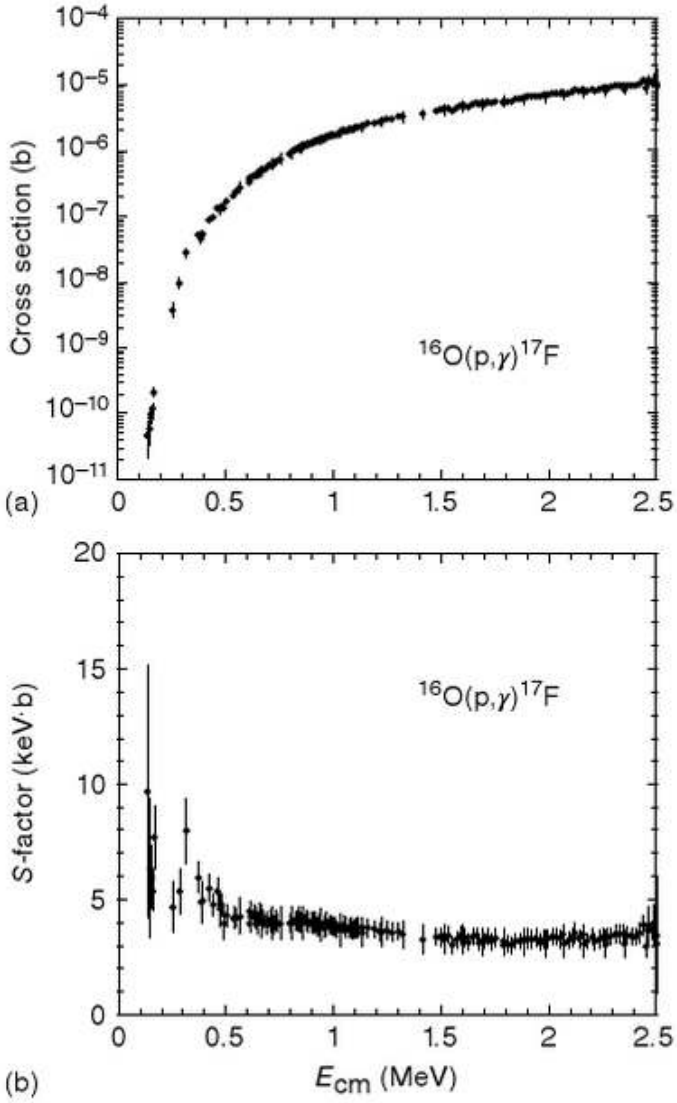

Figure 3.1: (Top) Experimental cross section of the ^{16}O(p,γ)^{17}F reaction. Data is from Angulo *et al.* [1999]. (Bottom) The corresponding S-factor. Note that the cross section varies by several orders of magnitude below 1 MeV. The S-factor, on the other hand, is relatively smooth on a linear scale. Figure from Iliadis [2015].

measurements or calculations using the astrophysical S-factor, defined by:

$$\sigma(E) = \frac{1}{E} e^{-2\pi\eta} S(E) \,, \tag{3.6}$$

where $e^{-2\pi\eta}$ is the Gamow factor (defined shortly). This removes both the $1/E$ dependence of the cross section and the s-wave Coulomb barrier transmission probability. The S-factor for the ^{16}O(p,γ)^{17}F reaction is shown in the bottom panel of Figure 3.1, where it can be seen that it varies

far less with energy than the cross section.

The non-resonant thermonuclear reaction rate is therefore:

$$N_A\langle\sigma v\rangle_{\text{non-resonant}} = N_A\left(\frac{8}{\pi m_{01}}\right)^{1/2}\frac{1}{(kT)^{3/2}}\int_0^\infty e^{-2\pi\eta}S(E)e^{-E/kT}dE\ . \tag{3.7}$$

The Gamow factor is given numerically by:

$$2\pi\eta = 0.9895 Z_0 Z_1\sqrt{\frac{M_0M_1}{M_0+M_1}\frac{1}{E}}\ , \tag{3.8}$$

where the relative nuclear masses M_i and the energy E are in units of u and MeV, respectively. The calculation of the non-resonant reaction rate is made easier by expanding the S-factor into a Taylor series around $E = 0$:

$$S(E) \approx S(0) + S'(0)E + \frac{1}{2}S''(0)E^2\ . \tag{3.9}$$

Substitution of this into Equation 3.7 then yields the following analytical expression:

$$N_A\langle\sigma v\rangle_{\text{non-resonant}} = \frac{1}{3}\left(\frac{4}{3}\right)^{3/2}\frac{\hbar}{\pi}\frac{N_A}{m_{01}Z_0Z_1e^2}S_{\text{eff}}\tau^2e^{-\tau}\ . \tag{3.10}$$

The temperature dependence is contained in the new parameter, τ:

$$\tau = 4.2487\left(Z_0^2Z_1^2\frac{M_0M_1}{M_0+M_1}\frac{1}{T_9}\right)^{1/3} \tag{3.11}$$

where T_9 is given in GK. The effective S-factor, S_{eff} is given by:

$$S_{\text{eff}}(E_0) = S(0)\left[1+\frac{5}{12\tau}+\frac{S'(0)}{S(0)}\left(E_0+\frac{35}{36}kT\right)+\frac{1}{2}\frac{S''(0)}{S(0)}\left(E_0^2+\frac{89}{36}E_0kT\right)\right]\ . \tag{3.12}$$

Section 3.3: Resonant Reaction Rates

At certain discrete interaction energies, the intensity of the incident particle wave-function in the nuclear interior is at a maximum. At these *resonance energies*, the probability for capture into an unbound state of the compound nucleus is much greater than through the non-resonant process.

Resonances are predicted to occur when the sum of the (center-of-mass) energy of the system plus the proton separation energy, matches that of an excited state in the compound nucleus:

$$E_r + Q = E_x \ . \tag{3.13}$$

As we will see in Chapter 6, this relationship can be used to identify resonances based on a knowledge of the level structure in the compound nucleus. This is helpful especially in the case of weak resonances, which might otherwise go undetected.

Although resonances account for a relatively small portion of the total cross section, they are usually the dominant contributors to thermonuclear reaction rates, owing to the dramatic increase in the cross section near E_r. The resonance cross section is parameterized by the total width, Γ, and the partial widths, Γ_a and Γ_b, for the incoming and outgoing channels, respectively. The total width is simply the sum of the partial widths. For a (p,γ) reaction with only two open channels, these are the proton width, Γ_p, and the γ-ray width, Γ_γ.

In this dissertation, we are primarily concerned with isolated (non-overlapping) narrow resonances. The condition that a resonance is narrow is fulfilled if the energy-dependent partial widths are relatively constant over the total resonance width. The Breit-Wigner formula describes the cross section due to a narrow resonance at E_r:

$$\sigma_{\text{narrow res}}(E) = \frac{\lambda^2}{4\pi}\frac{(2J+1)}{(2j_0+1)(2J_1+1)}\frac{\Gamma_a\Gamma_b}{(E_r-E)^2+\Gamma^2/4} \tag{3.14}$$

where λ is the deBroglie wavelength, J is the spin of the resonance state, and j_0 and j_1 are the spins of the incident particle and target nuclei. Equation 3.4 can be written:

$$N_A\langle\sigma v\rangle_{\text{narrow res}} = N_A\frac{\sqrt{2\pi}\hbar^2}{(m_{01}kT)^{3/2}}e^{-E_r/kT}\omega\frac{\Gamma_a\Gamma_b}{\Gamma}\int_0^\infty \frac{\Gamma/2}{(E_r-E)^2+\Gamma^2/4}dE \ , \tag{3.15}$$

where the definition $\omega \equiv (2J+1)/(2j_0+1)(2j_1+1)$ was used. The integral may be solved analytically. We define the *resonance strength*, $\omega\gamma = \omega\Gamma_a\Gamma_b/\Gamma$, and the thermonuclear reaction rate becomes:

$$N_A\langle\sigma v\rangle_{\text{narrow res}} = N_A\left(\frac{2\pi}{m_{01}kT}\right)^{3/2}\hbar^2 e^{-E_r/kT}\omega\gamma \ , \tag{3.16}$$

The reaction rate due to a narrow resonances depends only on the resonance energy, E_r, and the resonance strength, $\omega\gamma$, and not on the individual partial widths or total width. This greatly simplifies the experiments necessary to improve the reaction rate. Finally, the reaction rate due to multiple resonances is an incoherent sum of their individual contributions:

$$N_A\langle\sigma v\rangle_{\text{narrow res}} = \frac{1.5399\times10^{11}}{\left(\frac{M_0M_1}{M_0+M_1}T_9\right)^{3/2}}\sum_i(\omega\gamma)_i e^{-11.605E_i/T_9}\ , \tag{3.17}$$

where i labels the different resonances, $(\omega\gamma)_i$ and E_i are in units of MeV, and M_i are the relative atomic masses in u.

Section 3.4: Gamow Peak

At a given temperature, there is a range of interaction energies that occur within a stellar plasma as a consequence of the Maxwell-Boltzmann energy distribution (Equation 3.3). For non-resonant capture, this limits nuclear reactions to an effective energy range called the *Gamow peak*. This is apparent when we consider the integrand in Equation 3.7, where the S-factor is convolved with the function $e^{-2\pi\eta}e^{-E/kT}$. The factor $e^{-E/kT}$, originating from the Maxwell-Boltzmann distribution, approaches zero at larger energies, while the Gamow factor, $e^{-2\pi\eta}$, approaches zero at small energies. Their product is plotted in Figure 3.2 for three different astrophysical temperatures. The solid lines represent the relative probability for a non-resonant nuclear reaction at the center-of-mass energy, $E_{c.m.}$. The Gamow peak is an important concept in nuclear astrophysics since it conveys which regions of the cross section are important to thermonuclear reaction rates at a given temperature. For example, Figure 3.2 illustrates that the non-resonant cross section at $E_{c.m.} = 0.8$ MeV has a negligible effect on the reaction rate at stellar temperatures of $T = 100$ MK.

This concept can also be used to consider which narrow resonances may be important at a given temperature, though not without a caveat. Since the Gamow factor does not appear in Equation 3.16, it is in general not applicable. However, for (p,γ) resonances where $\Gamma_p \ll \Gamma_\gamma$, which is usually the case for resonances below $E_{c.m.} \approx 0.5$ MeV, the energy dependence of the proton partial width behaves like $e^{-2\pi\eta}$ [Newton *et al.*, 2007]. The upshot is that the Gamow peak can be useful at these energies, though it should be regarded as a crude estimate.

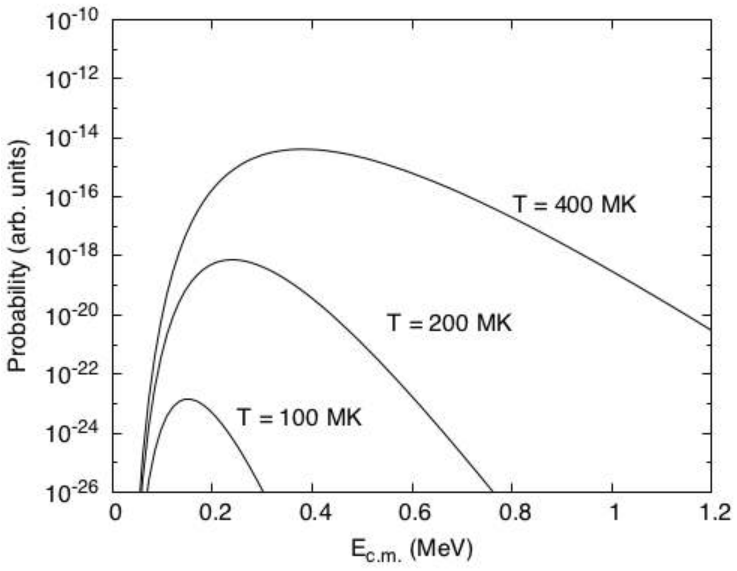

Figure 3.2: Effective center-of-mass energy range of non-resonant nuclear reactions, based on the Gamow peak, as predicted by the function $e^{-2\pi\eta}e^{-E/kT}$. The solid lines represent, roughly, the relative probability of a nuclear reaction at the stated temperature. Note that for the calculation of this function, the reaction ^{30}Si(p,γ)^{31}P was assumed.

In this dissertation, any reference to the Gamow peak implicitly assumes the Gaussian approximation. The centroid of the peak is given by:

$$E_0 = 0.1220 \left(Z_0^2 Z_1^2 \frac{M_0 M_1}{M_0 + M_1} T_9^2 \right)^{1/3} \text{ (MeV)} , \tag{3.18}$$

and the $1/e$ width, Δ, is given by:

$$\Delta = 0.2368 \left(Z_0^2 Z_1^2 \frac{M_0 M_1}{M_0 + M_1} T_9^5 \right)^{1/6} \text{ (MeV)} . \tag{3.19}$$

Non-resonant thermonuclear reactions occur mainly in the energy range from $E_0 - \Delta/2$ to $E_0 + \Delta/2$. According to the points made above, this range can also be useful in a limited capacity for narrow resonances.

CHAPTER 4: ACCELERATORS AND DETECTOR SYSTEM

For the nuclear resonance measurements proposed in the previous chapter, an accelerator laboratory is needed to provide an intense ion beam to initiate proton capture on ^{30}Si nuclei. The beam must be well defined, having a narrow energy distribution, and impinge upon the nuclear target in the presence of a γ-ray detector in order to observe and count the decay products of the reaction. The Laboratory for Experimental Nuclear Astrophysics (LENA) in Durham, North Carolina, is a unique facility designed specifically to excel at these types of measurements.

LENA is located on the campus of Duke University in Durham, NC, and is part of the Triangle Universities Nuclear Laboratory (TUNL). It is dedicated primarily to the study of nuclear cross sections at energies corresponding to the those relevant to nucleosynthesis in astrophysical processes. These take place in stellar environments at energies far too low for most accelerator facilities to probe effectively. The difficulties lie in the reduced transmission probability due to the Coulomb barrier, which suppresses the reaction signal below the limits of most detector systems. To counteract this effect, LENA employs two high-current proton accelerators in conjunction with a low-background $\gamma\gamma$-coincidence spectrometer. These two features work in tandem, boosting the total number of reactions taking place while reducing the presence of environmental background to enhance signal detection. A schematic of the LENA facility is shown in Figure 4.1. The accelerators, the 1 MV JN Van de Graaff (LENA I) and the 240 kV ECR ion source (LENA II) share an analyzing dipole magnet, which transports proton beam to the target station. Each segment of the beam-line has electromagnetic steerers and quadrupoles for directing and focusing the beam. Not shown in the diagram is the detector system, which is placed in close proximity to the target station in order to maximize the detection efficiency. The JN was used exclusively for this experiment, since the reference resonance, $E_r^{lab} = 619.6 \pm 1.2$ keV [Kuperus *et al.*, 1959], and those being measured, the previously unobserved $E_r^{lab} = 435 \pm 4$ keV [Vernotte *et al.*, 1990] resonance and $\mathrm{E_p}^{lab} = 498.3 \pm 1.0$ keV [Kuperus *et al.*, 1959] resonance, lie within its energy range. Information regarding the ECR ion source can be found in Cesaratto *et al.* [2010] and Cooper *et al.* [2018]. The

JN accelerator, the target station, and the detector system will now each be described.

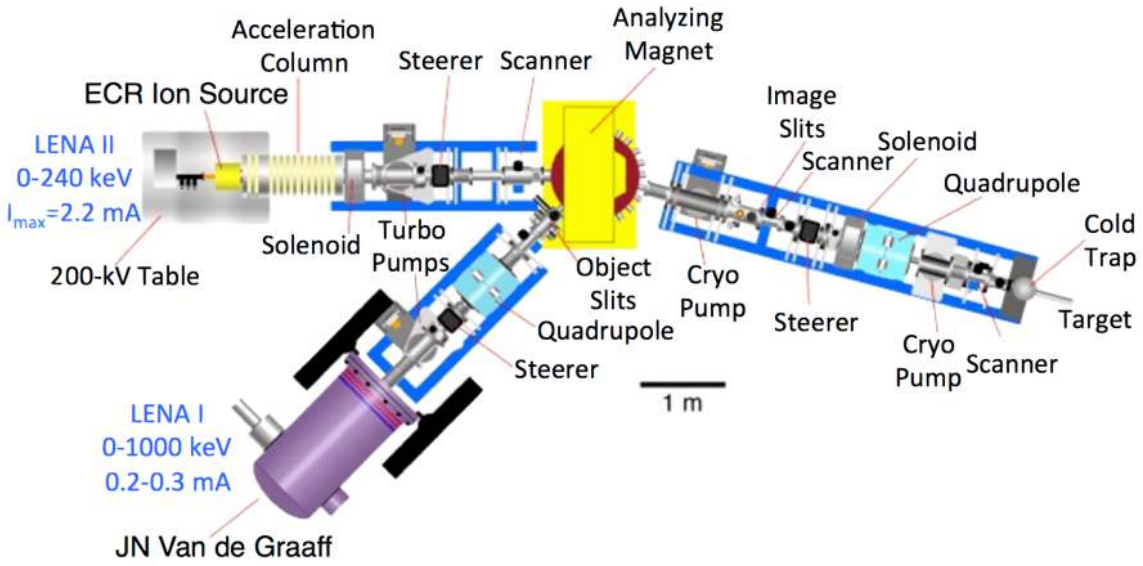

Figure 4.1: A top-level view of LENA. The two proton accelerators, the 1 MV JN Van de Graaff (LENA I) and the 240 kV ECR ion source (LENA II), transport beam to a shared dipole magnet, which momentum analyses and bends it towards the target station. On each segment of the beamline there are electromagnetic steerers and quadrupoles for beam shaping. Image courtesy of Art Champagne.

Section 4.1: LENA I, the JN Van de Graff

LENA I is an upgraded High Voltage Engineering Corporation 1 MV model JN Van de Graaff accelerator. It can produce up to ≈ 150 μA of H^+ at energies between $\approx 0.15 - 1$ MeV. There have been many modifications to this accelerator over the years to improve beam stability and current output. These include an upgraded terminal RF power supply, new slit-feedback circuitry, and

a new acceleration column and charging belt. Recently, the Terminal Potential Stabilizer (TPS) system has been upgraded to a model TPS-6 from *National Electrostatics Corp.*, which considerably improved the stability and precision of the beam-energy over previous studies using this facility. As a point of comparison, the *full width at half maximum* of the beam-energy profile observed during this dissertation was only 0.8 keV, several times smaller than the 2-3 keV spread observed in Buckner [2014].

Prior to the resonance measurements, the JN was physically realigned with the dipole magnet as part of a campaign to improve beam transport, thereby invalidating the magnet calibration used in previous experiments. An accurate magnet calibration is necessary to measure resonance energies and make certain that the proton beam is probing the target layer at the right depth. The bending magnetic field associated with the energy of the beam, E, produced by the JN is given by Iliadis [2015]:

$$B = \frac{k}{q}\sqrt{2mc^2E + E^2} \tag{4.1}$$

where mc^2 and q are the rest mass and charge state of the ion, respectively. The constant, k, is dependent on the trajectory of the beam through the magnet and must be determined by calibration. To calibrate the dipole magnet, the magnetic field strength corresponding to the energies of three well-known resonances in the ^{27}Al(p,γ)^{28}Si reaction was measured using yield curve analysis (see Section 6.2). Several measurements were also made using the ^{12}C(p,γ)^{13}N reaction, which produces a γ-ray with an energy that is determined by the energy of the proton beam. Table 4.1 lists the measured resonances and direct capture energies used in the calibration and their associated magnetic field measurements. These values are plotted in the top panel of Figure 4.2. The solid-line represents the fit of the data using Equation 4.1. In the lower-panel, the residual for each point, the experimentally observed energy minus the best fit result, is shown. In general there is good agreement between data sets, though the ^{12}C capture data have a larger scatter, particularly at higher energies. While this data set is by no means expansive, it nevertheless provides a sufficient calibration for the experiments in this dissertation.

Reaction	E_p^{lab} (keV)	B-Field (Tesla)
^{27}Al(p,γ)^{28}Si	405.5 ± 0.3	0.25857
	446.7 ± 0.5	0.27125
	611.46 ± 0.04	0.31753
^{12}C(p,γ)^{13}N	375.0 ± 0.5	0.24858
	400.1 ± 0.8	0.25674
	437.4 ± 0.8	0.26837
	493.4 ± 0.4	0.28564
	661.0 ± 0.4	0.32988

Table 4.1: Dipole magnet calibration data obtained from the ^{27}Al(p,γ)^{28}Si and ^{12}C(p,γ)^{13}N reactions. Resonance energies and their uncertainties for the ^{27}Al(p,γ) resonances are adopted from Endt [1990]. For the ^{12}C(p,γ) data, energies and their uncertainties were determined by a fit to spectroscopic data.

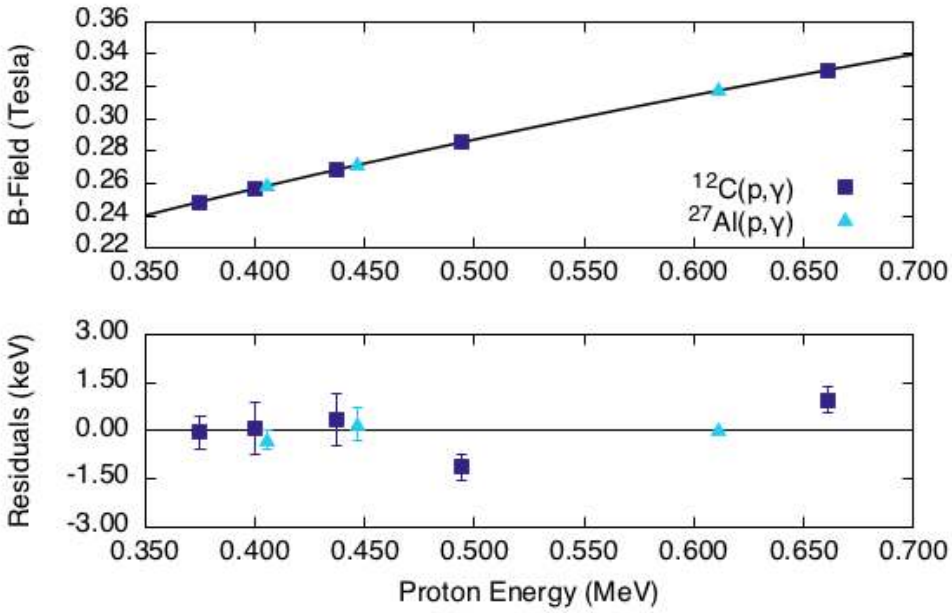

Figure 4.2: A fit of the dipole magnet calibration data. (Top Panel) The magnetic field strength required to transport the proton beam for each datum listed in Table 4.1 is plotted. (Bottom Panel) The deviation of each point from the best fit line is shown.

Section 4.2: The Target Station

After the proton beam is momentum analyzed by the dipole magnet, it is transported to the end of the beam-line, where the target is mounted on the water-cooled end-cap of the target station. The target station, depicted in Figure 4.3, acts as a Faraday cup, allowing the incident charge to be measured and integrated over the course of the experiment. It was designed primarily

with two goals in mind: the realization of a high vacuum, contaminant free environment, and the minimization of error in the incident charge measurement. Towards the fulfillment of the first goal, running along the length of the target station is a copper tube cold trap, cooled to liquid nitrogen temperature to minimize the migration of gaseous contaminants onto the surface of the target. The cold trap also contains a copper collimator with a diameter of 9.5 mm, which serves to limit the target area exposed to the beam. This also prevents charge accumulation on unimplanted or inert regions of the target. Below the cold-trap is a turbo-molecular pump, backed by an oil-free scroll pump. The combined effect of these two elements is a vacuum pressure of $1 - 2 \times 10^{-7}$ Torr during operation. The primary source of error in charge integration is the emission of secondary electrons on the surface of the target, which are knocked out by the incident proton beam and contribute to the current measured on target. To halt these electrons, a suppressing electric field is created by biasing an electrically isolated copper ring at the end of the cold-trap to -300 V. Finally, as a further measure to improve charge collection, the water used to cool the target is deionized.

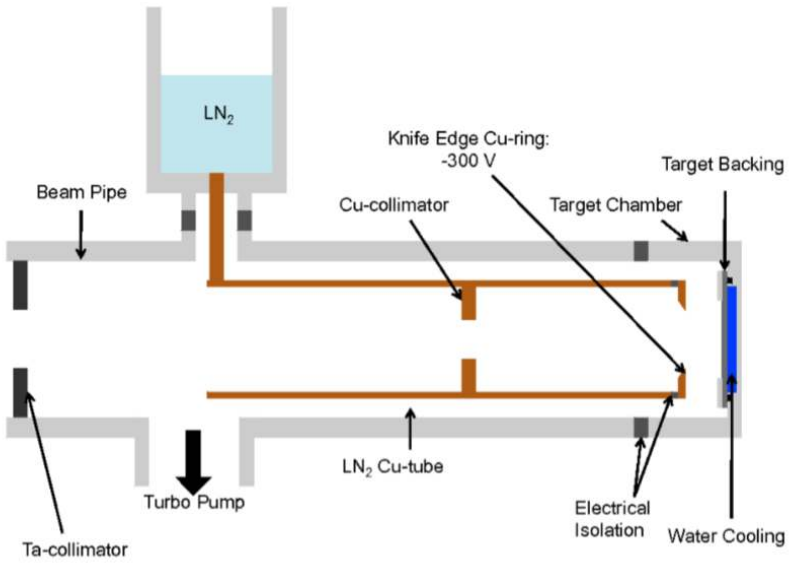

Figure 4.3: A schematic of the LENA target station (not to scale). A liquid nitrogen cooled copper tube, the cold-trap, runs through the length of target beam-pipe. The cold trap also determines the beam-profile via the 9.5 mm diameter collimator. At the end, an electrically isolated copper ring is biased to -300 V to suppress secondary electrons. The target backing is directly water cooled by deionized water. Figure is from Cesaratto [2011].

Section 4.3: The $\gamma\gamma$-Coincidence Spectrometer

Broadly speaking, the premise of a resonance yield measurement is to count the number of reactions that have taken place per incident particle. In the previous section, we saw how the incident protons can be counted using a specially designed Faraday cup. To count the nuclear reactions taking place, we rely on the nuclear deexcitations of the daughter nuclei produced in the reaction. In the case of ^{30}Si(p,γ)^{31}P, the excited ^{31}P nucleus decays quickly ($\tau \approx$ fs), emitting one or more γ-rays until it is in the ground-state. In the presence of a radiation detector, these γ-rays can be counted to estimate the number of reactions taking place. However, other sources of radiation such as environmental background or beam-induced contaminant reactions often drown out the desired signal, requiring higher rates of data collection to achieve acceptable statistics. The $\gamma\gamma$-coincidence spectrometer employed at LENA was designed specifically to address this issue [Longland *et al.*, 2006].

The system comprises a 135% high-purity germanium (HPGe) detector, oriented at 0° with respect to the beam axis, surrounded by a 16-segment NaI(Tl) annulus. These are enclosed in a lead shield, which is in turn surrounded by five sides of plastic scintillator paddles. A rendering of the detector system, shown in Figure 4.4, illustrates its geometry with respect to the target chamber, which is in contact with the HPGe crystal for maximum detection efficiency. Each segment of the NaI(Tl) annulus is optically isolated, allowing them to function independently. This setup is designed to exploit γ-ray cascade detection by using the peripheral energy deposition in the NaI(Tl) segments to classify HPGe events. An illustration of this is shown in Figure 4.5. Consider the reaction, X(p,γ)Y, which gives rise to an immediate two-step γ-ray cascade, depositing γ_{12} (6 MeV) and γ_{10} (3 MeV) in the HPGe and NaI(Tl) annulus respectively. The events are then plotted in the two-dimensional energy spectrum. By demanding that each HPGe event be accompanied by a NaI(Tl) event, with the further stipulation that the summed deposition energy, $E^{HPGe}+E^{NaI}$, falls between 5 and 10 MeV, an HPGe coincidence spectrum can be recorded, which preferentially admits γ-rays from the X(p,γ)Y cascade. Environmental background and beam-induced contaminant reactions often produce only a single γ-ray. Since these cannot satisfy the coincidence gate, they are actively suppressed by this technique. The efficacy of this depends largely on the details of the decay and the gating scheme. Additional discriminating power is afforded by

the use of the scintillator paddles, which are used in anti-coincidence mode to actively veto muon-induced events. The use of this spectrometer for $\gamma\gamma$-coincidence spectroscopy has been reported previously in Buckner *et al.* [2015, 2012], Cesaratto *et al.* [2013]. A more detailed description of $\gamma\gamma$ techniques employed at LENA is given in Longland *et al.* [2006].

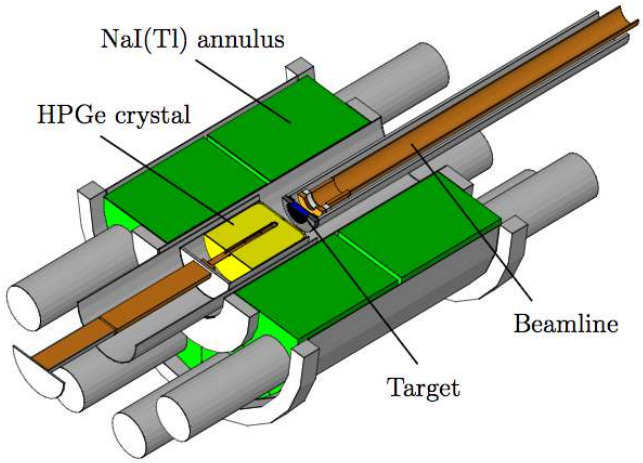

Figure 4.4: The LENA $\gamma\gamma$-coincidence spectrometer. A 135% HPGe detector (yellow) is surrounded by a 16-segment Na(Tl) annulus (green). The HPGe is put directly in contact with the target chamber for maximum efficiency. Not shown is the lead shield and plastic scintillator paddles. Figure from Dermigny *et al.* [2016]

4.3.1: Detection Efficiencies

The response of the HPGe detector to incident radiation is dependent on the geometry of the crystal (e.g., length, diameter) and also the geometry of the detector-target set-up. In a typical counting experiment, these figures are not known precisely. Instead, the peak efficiency of the detector, η_p, given by [Knoll, 2002]:

$$\eta^p = \frac{\text{net intensity of full-energy peak}}{\text{number of } \gamma\text{-rays emitted by source}} , \tag{4.2}$$

is measured over a wide energy range using calibrated radioactive sources in the same configuration as the experiment. Once this relationship is understood over the energy range in question, the intensity of a full-energy peak can be used to calculate the total number of γ-rays emitted. This procedure works well for experiments operating in single detection or "singles" mode, however

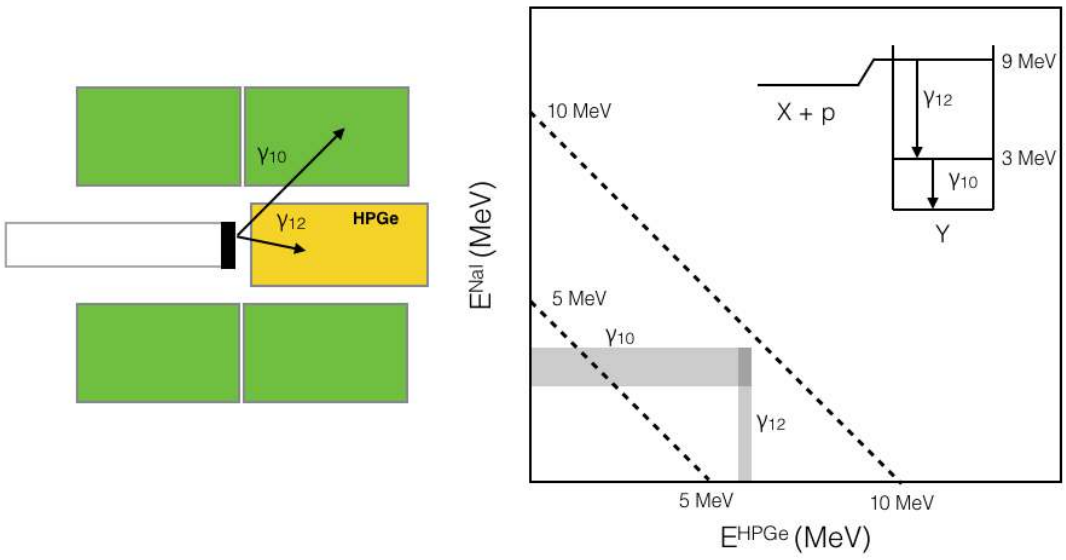

Figure 4.5: An illustration of the $\gamma\gamma$-coincidence spectrometer gating scheme. The example reaction, X(p,γ)Y, initiates the two step γ-ray cascade, depositing γ_{12} and γ_{10} in the HPGe (yellow) and NaI(Tl) annulus (green) respectively. By keeping only the events that fall between the dotted lines on the 2-d spectrum, the background can be reduced by several orders of magnitude.

its usefulness is limited when we consider its application to $\gamma\gamma$-spectrometry. In a coincidence spectrum, the net intensity of a full-energy peak is dependent not only on the detection efficiency of that specific γ-ray, but on the detection efficiency of all other γ-rays in that cascade with regard to the entire NaI(Tl) annulus. At LENA, this problem is circumvented using a high-fidelity simulation of the $\gamma\gamma$-coincidence spectrometer.

Written using the detector simulation toolkit, Geant4 [Agostinelli *et al.*, 2003], the program `LENAGe` uses precise measurements of the detector system geometry, as well as the details of the decay scheme, to generate the two-dimensional E^{HPGe} versus E^{NaI} spectrum seen in Figure 4.5. By applying the exact same gating scheme to both the experimental and simulated data, the simulated coincidence spectrum can then be used to estimate the total number of γ-rays emitted during the experiment. These simulations play a large role in this dissertation and are at the core of the analysis described later. In Chapter 3, the methodology for analyzing spectra will be detailed at length. The goal of this section is to demonstrate the level of agreement between the observed

detector efficiencies and those simulated using `LENAGe`, which will serve as a proof-of-concept for the discussion later.

Research featuring the `LENAGe` program has been reported previously in Longland *et al.* [2006], Howard *et al.* [2013] and Dermigny *et al.* [2016]. The simulated HPGe detector geometry is based on measurements made by Carson *et al.* [2010]. In that work, computed tomography was used to determine the internal dimensions of the detector, such as the crystal length and diameter. For the NaI(Tl) annulus, the dimensions are based on information provided by the manufacturer. Several tests of the accuracy of the simulations have also been made. In Howard *et al.* [2013], a spectrum was taken from a calibrated ^{22}Na source and compared to a simulated singles spectrum, normalized to the equivalent number of decays. The simulated and measured intensities of the full-energy 1275-keV peak were in agreement, to within 2% error, suggesting that the simulated HPGe detector response is accurate. The simulated NaI(Tl) response was then studied by applying a coincidence gate with the condition that the NaI(Tl) fully detects two 511-keV γ-rays emitted during the decay. The simulated and measured coincidence intensity of the 1275-keV peak were again in agreement to within 3% error.

To compare the simulated and observed detector response for the present experiment, an absolute efficiency calibration was performed using the *sum-peak* method [Kim *et al.*, 2003]. This procedure takes advantage of the two-step γ-ray cascade following $^{60}\mathrm{Co}(\beta^-\bar{\nu_e})^{60}\mathrm{Ni}$ decay to provide peak efficiencies that are independent of the source activity. Consider the predominant decay channel (99.98%) of deexciting ^{60}Ni nucleus, which can be represented by the following notation, $2 \rightarrow 1 \rightarrow 0$, where $2 \rightarrow 1$ is the primary γ-ray ($\mathrm{E}_{21} = 1173.228(3)$ keV) and $1 \rightarrow 0$ is the secondary ($\mathrm{E}_{10} = 1332.501(5)$ keV). In close geometries, these two coincident γ-rays can sum together in the detector to form a sum-peak at $\mathrm{E}_{20} = 2505.7$ keV. The sum-peak method then yields the peak efficiencies for the primary and secondary γ-rays:

$$\eta^p_{21} = \frac{1}{W(\theta)}\sqrt{\frac{N_{21}N^2_{20}}{N_{10}N_{20}N_t + N_{21}N^2_{10}}} \tag{4.3}$$

$$\eta^p_{10} = \frac{1}{W(\theta)}\sqrt{\frac{N_{10}N^2_{20}}{N_{21}N_{20}N_t + N_{10}N^2_{21}}}, \tag{4.4}$$

where N_{21}, N_{10}, and N_{20} are the primary, secondary, and sum-peak intensities, N_t is the background-

corrected total intensity, and $W(\theta)$ is the angular correlation of the two emitted photons. $W(\theta)$ is determined by the angular momenta of the decaying states and also the geometry of the detector. It is given by the expression [Iliadis, 2015]:

$$W(\theta) = 1 + \frac{5}{49} Q_2^{10} Q_2^{21} P_2(\cos\theta) + \frac{4}{411} Q_4^{10} Q_4^{21} P_4(\cos\theta), \tag{4.5}$$

where P_2 and P_4 are the 2nd and 4th order Legendre polynomials, and the Q_k^{ij} are the solid angle attentuation factors for each γ-ray, γ_{ij}. These were calculated for γ_{21} and γ_{10} using `LenaGe` by simulating the isotropic emission of γ-rays in the same geometry. For each of the N detected (simulated) γ-rays in their respective full-energy peaks, the attenuation factors were given by:

$$Q_k^{ij} = \frac{1}{N} \sum_{l=0}^{N} P_k \cos\theta_l, \tag{4.6}$$

where the θ is the emission angle with respect to the beam-axis for each photon that contributes to the full-energy photopeak.

This procedure was carried out using a ^{60}Co source (sealed in a mylar puck), which was fixed to the inside of the target station end-cap at atmospheric pressure. The $\gamma\gamma$-coincidence spectrometer was then placed in the run geometry while a singles spectrum was collected over several hours. The net intensities of the three full-energy peaks were recorded and Equations 4.3 and 4.4 were used to calculate the peak efficiencies for γ_{21} and γ_{10}, assuming emission from a "puck" source. The obtained values were:

$$\eta_{21}^{p}(1173.2 \text{ keV}) = 0.0379 \pm 0.0009$$
$$\eta_{10}^{p}(1332.5 \text{ keV}) = 0.0352 \pm 0.0008,$$

where the uncertainties are determined by counting statistics. These values are indicated by black triangles in Figure 4.6, where the full-energy peak efficiency is plotted as a function of γ-ray energy. The dotted line represents the peak efficiency predicted by the `LENAGe` program for the same "puck" geometry. The discrepancy between the sum-peak calibration and their predicted values is within 1% error. This level of agreement was obtained in the present work by iteratively fine-

tuning the HPGe crystal geometry within the uncertainties published by Carson *et al.* [2010]. For tables detailing the adopted crystal geometry values and the simulated efficiencies and attenuation coefficients, see Appendix B.1.

Using the same crystal geometry, the peak efficiencies were then calculated for a "beam-spot" configuration, which assumes that the γ-rays are emitted from a 9.5 mm diameter circular area on the face of the tantalum target, the same area of the target exposed to proton beam. In Figure 4.6, these are represented by the solid black line. To verify the shape of the efficiency curve, several well-known reactions were studied. Pulse-height spectra were recorded for the ^{56}Co$(e^-,\nu)^{56}$Fe decay reaction using a puck source, and also the $E_r^{lab} = 278.0 \pm 0.3$ keV resonance in ^{14}N(p,γ)^{15}O [Daigle *et al.*, 2016] and the $E_r^{lab} = 405.5 \pm 0.3$ keV resonance in the ^{27}Al(p,γ)^{28}Si reaction [Meyer *et al.*, 1975] using proton beam from the JN. Peak efficiencies for the observed full-energy photopeaks were then calculated using the coincidence summing correction procedure outlined in Semkow *et al.* [1990]. A description of the code used to implement this method is given in Appendix C. It is similar to the sum-peak method, but is applicable to more generalized decays, those with multiple levels, feeding fractions, and branching ratios. The trade-off is that precise peak efficiencies cannot be calculated without a precisely known source activity, which is difficult to obtain for both puck sources and beam-induced resonance reactions. The peak efficiencies from these reactions therefore cannot be considered to be absolute calibrations. Instead, they are scaled to agree with the beam-spot efficiency curve predicted by `LENAGe`. Their agreement with the trend of the peak efficiency curve in Figure 4.6, in addition to those efficiencies derived using the sum-peak method, serve to corroborate the accuracy of the simulations. For the data analysis in this dissertation, a conservative systematic error of $\pm$4% is assumed for the full-energy peak efficiencies for data taken in singles mode. This interval is shown as a gray band around the beam-spot efficiency function.

Demonstrating the veracity of the NaI(Tl) annulus portion of the simulation is a bit more complicated. Since the NaI(Tl) hits are only used to classify HPGe events in the context of $\gamma\gamma$-coincidences, what is important is not the individual crystal efficiencies, but rather, how well the annulus performs as a whole in coincidence mode. The expectation for an ideal simulation is that given identical decays and gating schemes, the simulated $\gamma\gamma$-spectrometer would predict the same net-intensity of γ-rays in coincidence mode as is observed in the laboratory. To test this, we define

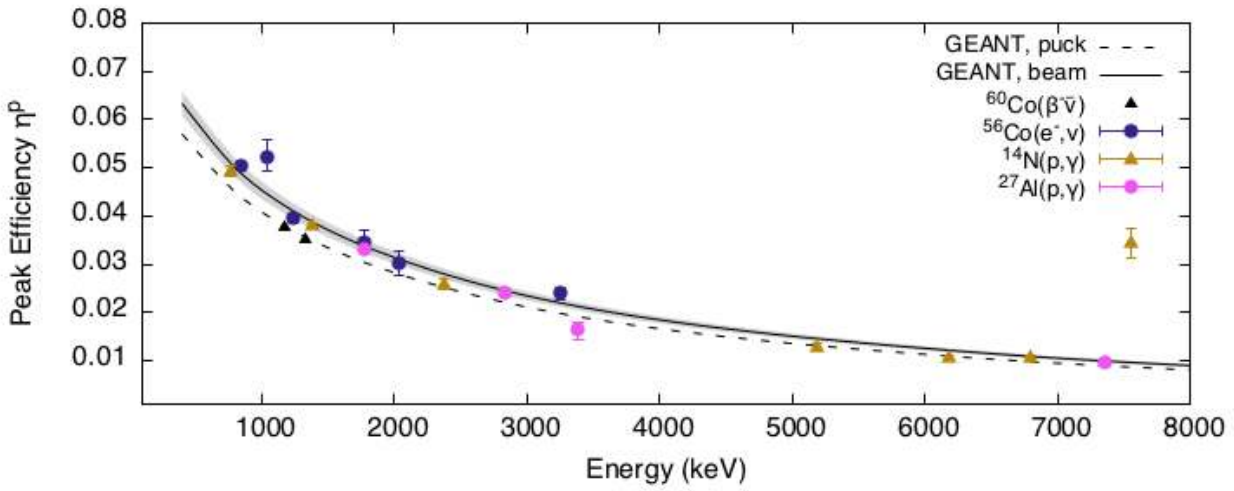

Figure 4.6: A comparison of the simulated versus measured full-energy peak efficiencies for the source "puck" geometry (dashed line) and the beam-spot geometry (solid line). The efficiency of a γ-ray emitted in the beam-spot geometry is 11% greater than that of the puck geometry. The ^{60}Co efficiencies are absolute measurements determined using the sum-peak method. They are shown as solid black triangles. The ^{56}Co, ^{14}N(p,γ)^{15}O, and ^{27}Al(p,γ)^{28}Si efficiency data are normalized to the simulated beam-spot efficiencies.

the coincidence response metric, C^p, as:

$$C^p = \frac{(N^{\rm coin}_{\rm Geant}/N^{\rm sing}_{\rm Geant})}{(N^{\rm coin}_{\rm Obs}\ /\ N^{\rm sing}_{\rm Obs})} \tag{4.7}$$

where the N are the singles and coincidence net-intensities of a full-energy peak, obtained through experiment ("Obs") and simulation ("Geant"). If the simulated $\gamma\gamma$-spectrometer behaves identically to the real system, then C^p would be unity. Using the same resonance reaction and β-decay data as in the HPGe efficiency measurements, C^p was measured for the same set of γ-ray transitions. A spectrum from the ^{22}Na($\beta^+\nu$)^{22}Ne reaction was also included. For the coincidence spectra, several different gating schemes were used. For the ^{56}Co, ^{60}Co, and ^{22}Na β-decay data, the gate was set so that all coincidences, regardless of the deposited energies, were accepted. For the ^{14}N(p,γ)^{15}O resonance reaction, with a deexcitation energy of 7.556 MeV [Daigle *et al.*, 2016], the gate was set so that $3.0 < \mathrm{E}^{\rm HPGe} + \mathrm{E}^{\rm NaI} < 10.0$ MeV. Finally, for the ^{27}Al(p,γ)^{28}Si resonance reaction, with a deexcitation energy of 11.976 MeV [Meyer *et al.*, 1975], the gate was set to $3.0 < \mathrm{E}^{\rm HPGe} + \mathrm{E}^{\rm NaI} < 14.0$ MeV. The measured C^p values are shown in Figure 4.7, where the uncertainties on each measurement are from counting statistics only. With the exception of the two

lowest-energy points, the general trend suggests that the detector system is well modeled. Disregarding these two outliers, the average coincidence response, C^p, over the energy range from 1 MeV to 8 MeV, is 1.012 ± 0.003. Since this is in such close agreement with the ideal case, no additional systematic error is assumed for the analysis of coincidence spectra in this dissertation. Instead, for both the singles and coincidence mode spectra, the adopted systematic error is determined solely by that of the HPGe crystal efficiencies, i.e., a conservative $\pm 4\%$ error. This interval is shown as a gray band, centered at unity.

For the measurements in this dissertation, an intense proton beam and state-of-the-art detector system is necessary in order to obtain sufficient count rates. In this chapter, the instruments used at LENA and their role in this project were described. In particular, we looked at the $\gamma\gamma$-coincidence spectrometer employed at LENA and the `Geant4` simulation used to predict its response to γ-rays. Measurements of the peak efficiency function in singles mode corroborate the accuracy of the simulations with regard to the HPGe crystal. To validate coincidence mode simulations, we defined and studied a response metric based on the observed and simulated γ-ray cascades and found that the predicted coincidence spectra were in close agreement with observations. In the next chapter, the use of these simulations to analyze pulse height spectra is described in detail.

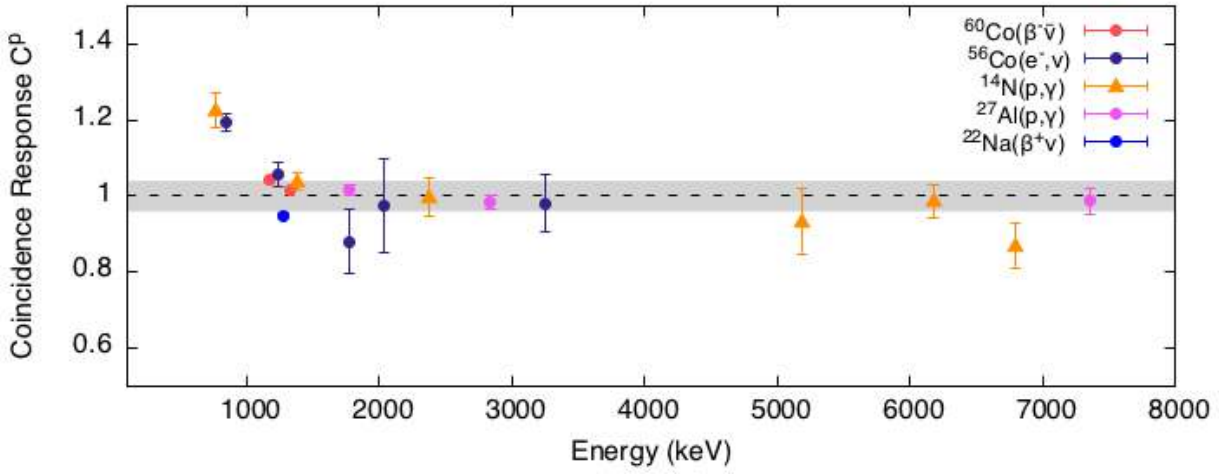

Figure 4.7: The $\gamma\gamma$-coincidence response function, as defined in Equation 4.7. On the y-axis, the ratio of the simulated coincidence full-energy peak net intensities over their observed values are shown for several γ-rays from several radioactive sources and different (p,γ) reactions. The coincidence intensities were first normalized to the simulated and observed "singles" mode full-energy peak intensities.

CHAPTER 5: FITTING METHOD

This chapter concerns the fitting method used in the analysis of measured pulse height spectra in Chapter 7. The method, known informally as "fraction-fitting", was published in Dermigny *et al.* [2016] and is part of this thesis. Sections 5.1 - 5.3 are key excerpts from that article. Minor adjustments have been made so that it fits more naturally into the broader story of this dissertation. In Section 5.4, the value of different goodness-of-fit tests are discussed. This material is presented for the first time.

Section 5.1: Introduction

Of main interest in the study of nuclear capture reactions are (i) the fractions of primary γ-ray decays from the compound state to lower-lying levels, i.e., the primary γ-ray branching ratios, and (ii) the total number of nuclear reactions that took place. Traditionally, the net intensities of all full-energy primary transition peaks are measured and are carefully corrected for the detection efficiency to determine the reaction yield. While this is an attractive option for simple spectra, γ-ray cascades are often sufficiently complex that this "peak-by-peak" analysis is challenging. Coincidence summing effects, coupled with angular correlations, complicate the analysis by requiring cumbersome corrections to each measured peak.

The situation is even more complicated for $\gamma\gamma$-coincidence spectroscopy. As was seen in the previous chapter, a coincidence spectrometer operates by requiring multiple hits across two or more detectors. By applying timing or energy conditions (or *cuts*), unwanted signals, such as environmental backgrounds, can be minimized; this affords an increase in detection sensitivity. Each coincidence event satisfies timing and energy gates; the measured peak intensity not only depends on the detection efficiencies, but also on the detailed decay of the entire $\gamma\gamma$-cascade initiated by a primary transition. This effect, compounded by the challenges described above, makes the analysis of coincidence spectra difficult.

In light of the above challenges, we present a new method of spectral analysis that has two

innovations. First, we model our data using a binned likelihood function. This allows us to fit the entire spectrum — every full-energy peak, as well as their Compton distributions and escape peaks — using Monte Carlo simulated spectra, or *templates*. Second, we determine the fraction of the experimental spectrum belonging to each template using a Bayesian statistical approach. This allows for the extraction of the primary γ-ray branching ratios and the total number of reactions, not *only* from individual full-energy peaks, but from the entire pulse height spectrum. Explicit corrections for coincidence summing and angular correlations are no longer necessary, as these effects are implicitly included in the Monte Carlo simulations used to generate the templates. This method applies to both singles and coincidence spectra, removing many difficulties faced in a traditional "peak-by-peak" analysis.

Section 5.2: Analysis Method

A measured pulse height spectrum consists of contributions arising from different sources: room background, beam-induced background, and the reaction of interest, itself consisting of primary γ-ray transitions and their corresponding secondary decays. Each of these contributions requires a template, containing the entire pulse height information (e.g., full-energy peaks, Compton continua, and escape peaks). We discuss strategies for generating the templates in Sec. 5.3. In the following, we define a formalism where, for each template, j, we predict the fraction of nuclear reaction events, F_j, present in the experimental spectrum that results from source j.

To model our data, we adopt the *extended* binned likelihood function [Barlow, 1990]. This likelihood function, that is, the probability of obtaining the data, $\boldsymbol{D}$, given the m template fractions, $\boldsymbol{F}$, is given by Barlow and Beeston [1993]:

$$P(\boldsymbol{D}|\boldsymbol{F}) = \left[\sum_{i=1}^{n} D_i \ln f_i - f_i\right] + \left[\sum_{i=1}^{n}\sum_{j=1}^{m} a_{ji} \ln A_{ji} - A_{ji}\right], \tag{5.1}$$

where, for each of the n bins, i, f_i is the total number of events contributed by all the templates, and A_{ji} and a_{ji} are the predicted mean and observed number of events in template j, respectively. The A_{ji} account for the statistical fluctuations in the a_{ji}, as they are sampled from finite Monte

Carlo calculations. The f_i for each bin are given by:

$$f_i = \sum_{j=1}^{m} \frac{A^{data}}{A_j^{sim}} F_j A_{ji} \ , \tag{5.2}$$

where A^{data} and A_j^{sim} are the total areas (within the fit limits) of the measured spectrum and of template j, respectively. In a previous study [Buckner *et al.*, 2015], the estimates for the fractions, F_j, were obtained through maximization of the likelihood using the MINUIT library [James and Roos, 1975]. In the present work, however, we have decided to follow an entirely different approach. Instead, we apply Bayes' theorem [Bayes, 1763] to build a full probability model for our data and parameters. This allows some practical advantages over a maximum-likelihood estimate. Most importantly, using a Bayesian data analysis we can derive probability density functions for the parameters, i.e., the fraction values. These probability distributions can then be used to calculate uncertainties and place meaningful upper-limits on weak transitions. A brief review of Bayesian statistical inference is given in Appendix C to motivate its use in the present analysis.

In a Bayesian framework, we make inferences using the multivariate joint posterior distribution, $P(\boldsymbol{F}|\boldsymbol{D})$, as defined by Bayes' theorem:

$$P(\boldsymbol{F}|\boldsymbol{D}) = \frac{P(\boldsymbol{D}|\boldsymbol{F})P(\boldsymbol{F})}{\int_{\boldsymbol{F}} P(\boldsymbol{D}|\boldsymbol{F})P(\boldsymbol{F})} \ , \tag{5.3}$$

where $P(\boldsymbol{F})$ is the joint prior probability function for the model parameters and $P(\boldsymbol{D}|\boldsymbol{F})$ is the likelihood function, as defined by Eq. 5.1. In constructing the joint prior distribution, we assume that each fraction value has a prior distribution which is independent from the rest. Further, for each parameter, we adopt a scale-invariant, non-informative Jeffreys prior [Jeffreys, 1946]. This choice was motivated by the requirement that the prior convey equal probability per decade, meaning that each fraction value is as likely to be in range (0.001,0.01) as in (0.1,1.0). Thus, the joint prior distribution is given by

$$P(\boldsymbol{F}) = \prod_{j=0}^{m} \left[\frac{1}{F_j} \right] \ . \tag{5.4}$$

The joint posterior distribution is then calculated using the *evidence* procedure [MacKay, 1999], where the A_{ji} are replaced by their maximum-likelihood estimates using the method of Barlow and Beeston [1993]. This adjustment eliminates the A_{ji} as nuisance parameters, thereby making the

analysis more tractable.

The marginal posterior distribution for each fraction value is then computed using a Markov chain Monte Carlo routine to sample the joint posterior distribution. This routine uses the *Metropolis-Hastings* algorithm, with a multivariate Gaussian as the proposal distribution. The number of samples required for the Markov chain is determined by the complexity of the fit. In general, higher numbers of samples are needed for each additional template involved. For the fraction-fitting performed in Chapter 7, the parameters of the sampling routine will be specified. From the resulting marginal posterior distributions, estimates on the fraction values, F_j, are obtained using the median of the probability distribution. The boundaries of the 68% highest density interval are calculated and reported as the corresponding uncertainty. For distributions with a significant probability density at zero, we instead report an upper-limit using the 95% credible interval.

The fractions, F_j, may then be used to calculate the number of compound nucleus decays of component j, N_j, that gave rise to the measured spectrum [Buckner *et al.*, 2015]

$$N_j = \frac{A^{data}}{A_j^{sim}} F_j N_j^{sim}, \tag{5.5}$$

where N_j^{sim} is the number of simulated compound nucleus decays used to generate template j. For our purposes, each reaction template for the reaction of interest represents a primary γ-ray transition from a resonant state including all associated secondary decays; the N_j values are then the number of primary decays of component j that contributed to the experimental spectrum. This approach allows a calculation of the total number of reactions by summing over all primary γ-ray decay branches:

$$N_R = \sum_j N_j. \tag{5.6}$$

The branching ratios for each primary transition follow from the partial and total number of reactions:

$$B_j = \frac{N_j}{N_R}. \tag{5.7}$$

The γ-ray branching ratios and total number of reactions are therefore obtained without explicitly correcting each individual full-energy peak for detector efficiencies, angular correlation effects, or

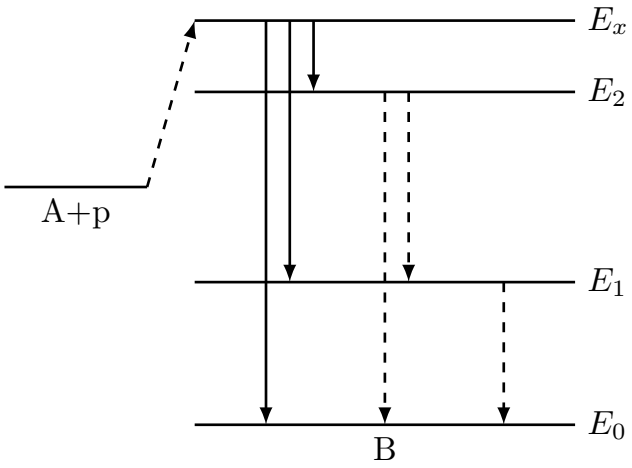

Figure 5.1: A generic proton capture with decay scheme. For illustrative purposes we show the compound state, E_x, which can decay to the ground state, E_0, or to the first two excited states (E_1, E_2). These decays are called *primary* transitions (solid arrows). Each of these, except for the ground state transition, $E_x \rightarrow E_0$, gives rise to *secondary* transitions, e.g., $E_2 \rightarrow E_0$, $E_2 \rightarrow E_1 \rightarrow E_0$ (dashed lines). For this example, three separate templates would be created, each corresponding to a possible primary transmission, that would be fitted to the experimental spectrum.

coincidence summing, as is required in traditional γ-ray spectroscopy. This is made possible by incorporating these experimental artifacts implicitly into the simulated template spectra. In the next section, we will discuss these points in detail.

Section 5.3: Geant4 Simulations

5.3.1: General Strategy

The form of the likelihood function (Equation 5.1) is predicated on the presumption that the experimental spectrum can be described by a set of templates. Therefore, it is important to identify the source of every peak, e.g., primary or secondary transition, environmental background, or beam-induced background. Based on the results of this analysis, templates must be generated for each source. We will discuss the procedure for environmental and beam-induced background templates in Sec. 5.3.3. For the reaction of interest, it is important that (i) every observed primary γ-ray transition is described by a template, and (ii) each template represents the detector response to the initial (primary) decay *and* all associated secondary decays. An example decay scheme is shown in Fig. 5.1. The target nucleus, A, captures a proton. The resulting compound nucleus, B, deexcites from the resonant level E_x to a lower lying level: E_2, E_1, or the ground state, E_0. Each of these

deexcitations represents a *primary* transition and thus requires a simulated template. The $E_x \rightarrow E_2$ and $E_x \rightarrow E_1$ transitions are accompanied by *secondary* γ-ray decays, (shown as dashed lines). These transitions must also be included in the primary transition templates. A code was written which uses the `Geant4.9.6` [Agostinelli *et al.*, 2003] framework to simulate the compound nucleus deexcitation γ-cascade during a nuclear reaction.

The simulated γ-ray cascades are used to populate template histograms. The cascade begins at the energy of the compound nucleus in the resonant state, E_x. The compound level decays to the secondary state (e.g., E_2), emitting a unique γ-ray of energy E_x-E_2. The subsequent secondary decays are then simulated by randomly sampling over the known secondary γ-ray decay branchings. The simulation continues until the γ-cascade terminates at the ground state, E_0. All simulated γ-rays for the reaction of interest originate from the ion beamspot on the target and are tracked as they interact with the spectrometer and the environment (e.g., the beamline, target holder, target backing, shielding, cooling water, etc.) via photoelectric absorption, Compton scattering and pair production. The veracity of the simulated detector response was the focus of Section 4.3.1, where it was estimated that both the singles and coincidence mode full-energy peaks were well within a 4% systematic error. Energy deposition in the active detector volume is recorded for each event and written to an output file. The output, accumulated over many simulated decays, is then used to construct a template histogram with the same energy and timing gates applied to the measured pulse height spectrum.

5.3.2: Corrections to Simulated Templates

A number of corrections must be performed before simulated templates can be used to analyze a measured pulse-height spectrum. For instance, simulating a γ-ray cascade requires input of all excitation energies and secondary branching ratios. While this is sufficient in reproducing the approximate *location* of many full-energy peaks at their observed energies, the γ-ray energies of primary decays may need to be adjusted in the simulations by several keV to account for Doppler and recoil shifts.

It is also important that the simulation reproduces the measured peak *widths*. This is achieved in two steps. First, we convolve each raw simulated spectrum with a Gaussian of width $\sigma(E)$,

where $\sigma(E)$ is the energy-dependent detector resolution function, characterized by the measured full width at half maximum (FWHM) of room background or secondary-transition full-energy peaks. The width, σ, of each peak is then determined using the relationship FWHM $= 2\sqrt{2\ln 2}\sigma$. Second, we may need to consider an additional broadening or shaping necessary for primary transition peaks. For example, γ-ray transitions from a short-lived resonant state are frequently Doppler broadened. Furthermore, experience has shown that intense primary transition full-energy peaks have shapes that depart from that of a Gaussian. The most notable difference is in the low-energy region of the peak, where an extra "tail" appears due to incomplete charge collection in the HPGe crystal [Knoll, 2010]. To account for these effects, the pulse height spectrum primary transition peaks are fit using a function based on the γ-ray peak characterization from MacMullin [2015]. This parameterizes the low-energy tail component, as well as the extra broadening due to the Doppler effect. The parameters for each primary transition peak are then used to build matching probability distributions, which are sampled for those peaks when populating their templates from the raw simulated spectrum. This procedure supersedes the initial broadening mentioned above.

Depending on the experimental alignment and the angular momentum coupling involved in the reaction of interest, the γ-ray emission following a nuclear reaction may be anisotropic. For these transitions, the angular distribution for the emitted radiation is described by [Iliadis, 2015]:

$$W_{ij}(\theta) = 1 + a_2 P_2(\cos\theta) + a_4 P_4(\cos\theta) \tag{5.8}$$

where a_2 and a_4 are angular correlation coefficients that depend on the angular momentum coupling involved in the reaction, θ is the polar coordinate with the z-axis oriented toward the direction of the incident beam, and P_2 and P_4 represent the second and fourth order Legendre polynomials. For a known angular correlation, the coefficients can be directly adopted in Eq. 5.8. If the angular correlation has not been measured yet, the coefficients can frequently be calculated (see Appendix D in Iliadis [2015]). When simulating the decay of the compound nucleus, γ-rays are emitted according to an angular probability distribution, where the probability for emittance into the solid angle $\mathrm{d}\Omega$ is weighted such that $p(\Omega)\mathrm{d}\Omega = W(\theta)d\Omega$. This correction is frequently only necessary for primary transition γ-rays, as the effect is usually much smaller for secondary transitions.

5.3.3: Background Contaminants

Radiation from radionuclides present in the environment, as well as from beam-induced reactions, contribute unwanted background to experimental spectra. Environmental radionuclides, such as ^{40}K and ^{208}Tl, can be accounted for by measuring the room background in the run geometry for an extended period of time. Since the environmental background may vary with meteorological conditions, two background spectra should be recorded, one before and one after the reaction measurement. The combined pulse height spectrum can then used as a measured background template. Beam-induced reactions result from contaminants (e.g., ^{19}F, ^{11}B and ^{12}C) in the target or backing. Their γ-ray contributions can be simulated in the same manner as the reaction of interest, or measured directly by an off-resonance run or by using a blank backing without target material.

Section 5.4: Goodness of Fit Testing

In this section, we discuss goodness of fit testing. Historically, fraction-fitting has produced results that appear to describe the analyzed spectra precisely, but somehow fail to satisfy the standard suite of goodness-of-fit tests. This can complicate the communication of results, since according to long trusted metrics they appear to be uncredible. We will explore why this is happening through a series of simple tests and then propose a method that allows for a more reliable fit metric.

The issue is that the likelihood function provided by Barlow and Beeston (Equation 5.1) assumes that the experimental data and the Monte Carlo generated templates are sampled from a probability distribution that strictly obeys Poisson statistics for the counts in each bin. While this is the obvious choice for modeling nuclear counting processes, the assumption places strong constraints on the data that make the analysis of high count-rate data difficult. The problem is that the Poisson distribution (and the respective likelihood equation) is relatively inflexible with regard to variance. When the data (or the templates) are overdispersed — having a higher statistical fluctuation than is predicted by theory — the fitting routine is over penalized for deviating from the mean, resulting in untenable goodness-of-fit measures and underestimated parameter errors.

The data collected in this thesis are particularly sensitive to this issue, since there are several high-count photo-peaks corresponding to intense transitions in the deexciting ^{31}P nucleus. While modeling these peaks in Geant4 appears to be effective "by-eye", slight discrepancies in the simu-

lated and measured peak-width and tail characteristics lead to bin to bin differences on the order of 1-3 %. This becomes the dominant source of error in bins with contents above 1000. The effect of overdispersion on the final fit can best be understood by looking at a toy model.

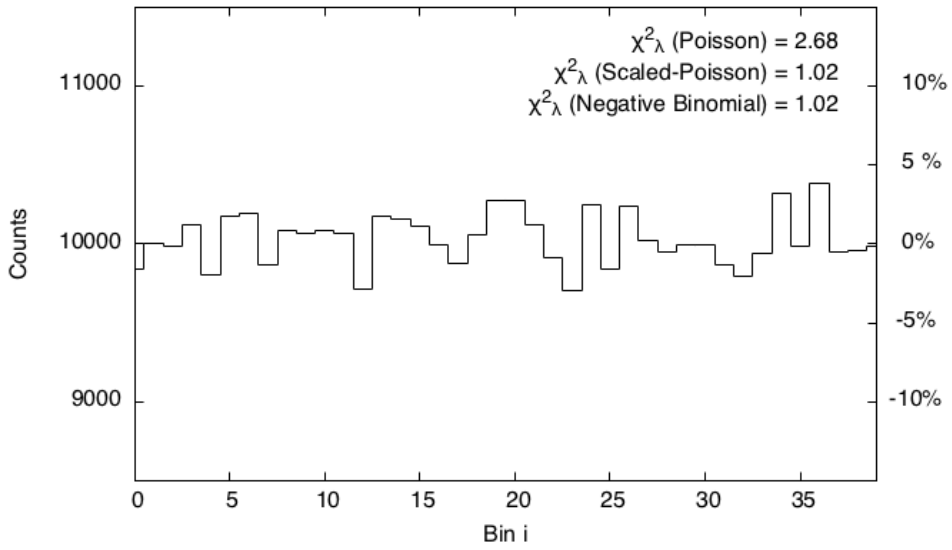

Figure 5.2: A simulated overdispersed data set. The bin contents were determined by sampling a normal distribution with mean $\lambda = 10,000$ and variance $[V] = 3\lambda$. In the upper-right hand corner, likelihood ratios for various models are shown.

Consider the histogram shown in Figure 5.2. The contents of each of the 40 bins were determined by sampling a normal distribution with mean $\lambda = 10,000$ and variance $[V] = 3\lambda$. This amounts to a standard deviation that is a factor $\sqrt{3}$ larger than what is anticipated by an ordinary nuclear decay counting experiment. The log-likelihood of the data set x_i, assuming Poisson statistics, is given by:

$$\ln L(\lambda|\hat{x}) = \sum_{i=0}^{N} x_i \ln \lambda - \lambda \tag{5.9}$$

The mean of the underlying probability distribution can easily be estimated from the data using the maximum-likelihood method. However, trouble arises when considering an appropriate goodness-of-fit test. The most popular among experimental physicists, owing to its close ties to the classical χ^2, is the likelihood ratio, as defined by

$$\chi^2_\lambda = -2 \ln L(\hat{\lambda}|\hat{x}) + 2 \ln L(\hat{x}|\hat{x}), \tag{5.10}$$

where $\hat{\lambda}$ represents the point estimate for the mean. Like the classical χ^2 test, the likelihood ratio can be used to determine how well the data is described by the fit. The calculated reduced likelihood ratio for the data in Figure 5.2, based on the Poisson likelihood, is $\chi^2_\lambda/\nu = 2.68$, where ν is the number of degrees of freedom. This remarkably high value implies that out of 20 million new data sets, only one would be expected to deviate from the model as much as the observed data. Clearly, overdispersion in the data set must be addressed before results can be reported confidently.

The best way to correct for this effect is to build a probability model that explicitly anticipates that the data have a higher variance. An excellent choice is the negative binomial distribution. Its canonical usage is in modeling the number of successes in a sequence of independent and identically distributed Bernoulli trials before a specified number of failures occurs. However, it has a more useful interpretation. It can also be used as an alternative to the Poisson distribution for data whose sample variance exceeds the sample mean [de Souza *et al.*, 2015]. The distribution takes the form:

$$f(x|\mu,k) = \frac{\Gamma(x+k)}{x!\Gamma(k)}\left(\frac{k}{\mu+k}\right)^k\left(\frac{\mu}{\mu+k}\right)^x, \tag{5.11}$$

where the mean of the distribution is given by μ and the overdispersion is quantified by the factor k. The variance is given by $[V] = \mu + \mu^2/k$, and thus it can be seen that as k goes to infinity, this parameterization of the negative binomial approaches the Poisson distribution. Estimates for k and μ can be obtained using the maximum-likelihood method, and the goodness-of-fit can be assessed using the likelihood ratio test. The variance of the data set, based on the point estimates for k and μ, is found to be 2.6μ, in close agreement with the true value, 3μ. The calculated reduced likelihood ratio, using the negative binomial distribution, is $\chi^2_\lambda/\nu = 1.02$. In an ensemble of identically collected data sets, only 43% would deviate further from the model, suggesting that the negative binomial offers a much better description of the data than the Poisson likelihood.

While these results are encouraging, analyzing nuclear data using the negative binomial likelihood may not be the most practical choice. Foremost, this is *terra incognita* within the nuclear physics community. An in-depth study of the application of the negative binomial to the problem of fitting histograms with Monte Carlo samples is necessary, and that is at present beyond the scope of this dissertation. However, a simpler alternative to fitting the data, while still using the tried and true Barlow and Beeston likelihood (Equation 5.1), does exist. By scaling the data by a

constant factor, the flexibility of the negative binomial likelihood can be emulated. Consider the following "Scaled Poisson" likelihood function:

$$\ln L\big(\lambda|\hat{x},\alpha\big) = \sum_{i=0}^{N} \frac{x_i}{\alpha} \ln\lambda - \lambda \tag{5.12}$$

where α is the scaling factor. By choosing α carefully, the data are treated as if they have a variance a factor of α larger than that given by their mean. The reduced likelihood ratio for the data shown in Figure 5.2, calculated assuming $\alpha = 2.6$, is $\chi^2_\lambda/\nu = 1.02$, the same value given by the negative binomial case, and most importantly, an indication of an acceptable fit. This means that by performing this simple scaling procedure, we are now able to analyze over-dispersed data in a meaningful way.

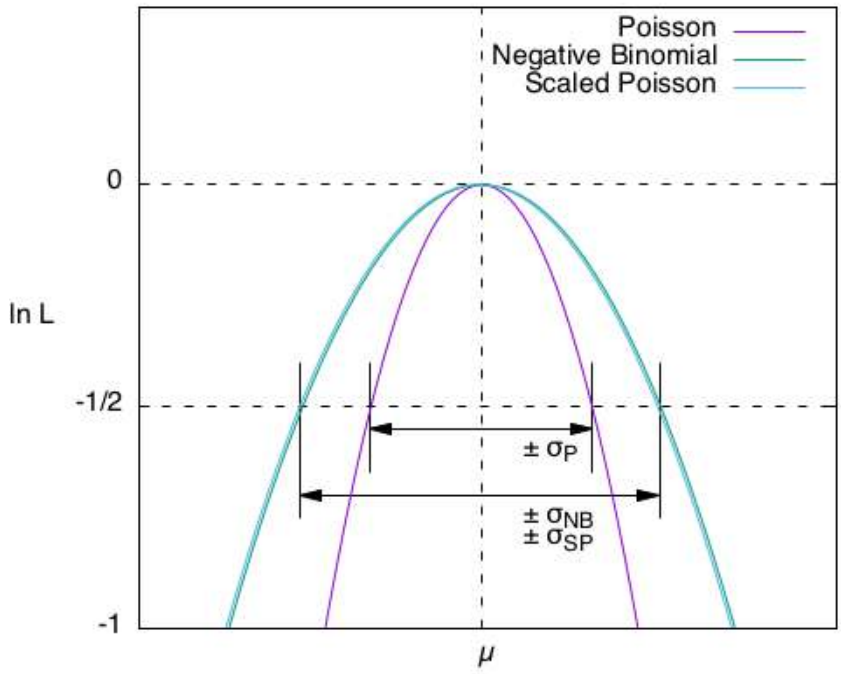

Figure 5.3: The Log-Likelihood plotted as a function of the mean rate parameter μ for the three probability models: the Poisson, the Negative Binomial, and the scaled Poisson. Note that the latter two overlap completely. The vertical dotted-line represents the point estimate for μ. Where the models cross the dotted line at $\ln \mathrm{L} = -1/2$ deliniates the confidence interval for μ.

The choice between likelihood functions not only affects goodness-of-fit tests, but also the parameter uncertainties. Since the purpose of the present analysis is to report reasonable errors on branching ratios and decay rates, it is important to understand how these might be influenced.

Using the maximum-likelihood method, parameter errors are estimated by finding the values of each parameter where the log-likelihood is 0.5 below the maximum [James, 2006]. This is illustrated in Figure 5.3, where the log-likelihood function is plotted for the three different probability models considered here as a function of the mean rate parameter, μ. The confidence interval, $\pm\sigma$, derived from each model is labeled. The key point is that the standard Poisson model leads to a considerably smaller confidence interval for μ than either the negative binomial or the scaled-Poisson models. Since the standard Poisson is a poor fit to begin with (based on the reduced log-likelihood ratio), it seems likely that the error is being underestimated for overdispersed data. On the other hand, the likelihood functions that anticipate overdispersion, the negative binomial and the scaled-Poisson, predict more conservative and likely more credible errors.

In this section, we found that overdispersed data can be dealt with in creative ways. By scaling the data judiciously, higher variance can be tolerated, leading to more conservative errors on the model parameters. With regard to fraction-fitting, since we are ultimately interested in the template fractions, F_j, which sum to unity, rescaling the data in this way does not affect the outcome of the analysis, since they are (by definition) insensitive to the total intensity. For the data taken during this dissertation, this rescaling procedure is performed on each spectrum, singles and coincidence, so that the reduced log-likelihood ratio is ≈ 1. This is done with the intention of keeping the fraction errors as conservative as possible. Still, since we are in effect tuning the log-likelihood ratio, it would appear that the standard goodness-of-fit test is no longer valid. To mitigate these concerns, a different goodness-of-fit test, the "run test", is used instead. In the next section, the run test is described.

5.4.1: Run Test

The likelihood ratio test is based on the *magnitude* of the discrepancy between the measured data and the fit. The run test provides additional information by deriving a statistic based on the *direction* of the discrepancy. This point is illustrated in Figure 5.4, where a sinusoidal variation has been superimposed onto otherwise linear data. The uncertainties associated with each datum are calculated assuming Poisson statistics. A 1st order polynomial fit to this data, based on the log-likelihood minimization, can be obtained without difficulty. The reduced log-likelihood ratio

is $\chi^2_\lambda/\nu = 0.86$, suggesting that the data is described well by this simple model. However, it is apparent that the data has some component that is both not attributable to the proposed model and which cannot be due to statistical uncertainties. The log-likelihood ratio fails to identify this issue.

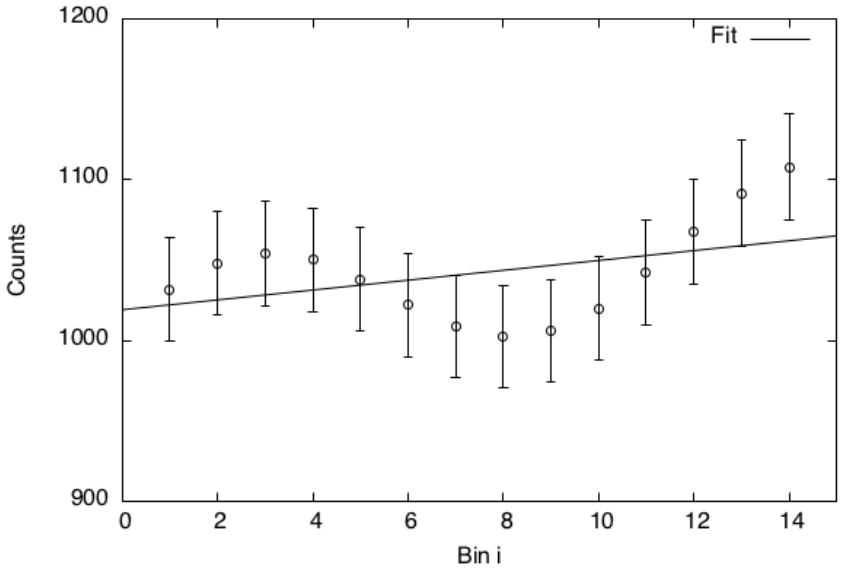

Figure 5.4: Example data that is poorly described by a simple linear fit. The log-likelihood ratio test fails to identify a problem, even though there is a clear sinusoidal effect.

The run test, however, offers compelling evidence that this model is incomplete. A run is defined as a single contiguous region where the data are either over-predicted (the model suggests a smaller number of counts) or under-predicted (the model suggests a higher number). For the sequence of data in Figure 5.4, this can be visualized as follows:

$$+\,+\,+\,+\,+\,-\,-\,-\,-\,-\,-\,-\,+\,+\,+ \ ,$$

where a plus (minus) sign corresponds to a datum that is above (below) what is predicted by the model. In this case, there are three runs: the first five points are under-predicted, followed by six that are over-predicted, then three that are under-predicted again. If the model were correct, then whether a datum is under- or over-predicted can be considered a Bernoulli trial, with equal

probabilities for each outcome. The expected number of runs is then given by [Barlow, 1989]:

$$\langle r \rangle = 1 + \frac{2N_+N_-}{N} \ , \tag{5.13}$$

with a variance given by:

$$V[r] = \frac{2N_+N_-(2N_+N_- - N)}{N^2(N-1)} \ , \tag{5.14}$$

where N_+ is the number of data that are above (+) , N_- is the number of data that are below (−), and N is their sum. The predicted number of runs for the data in Figure 5.4, based on the correct model, is then $r_{\text{pred.}} = 7.8 \pm 1.8$. The observed number of runs, $r_{\text{obs.}} = 3$, is 2.7 standard deviations below the mean. This discrepancy is significant at the 1% level (one-tailed test). Thus, despite the verdict rendered by the log-likelihood ratio test, the run test strongly advocates instead for rejecting the 1st order polynomial fit to the data.

In the context of fraction-fitting, the run test is performed by comparing the measured pulse height (data) spectrum with the reconstructed (model) spectrum, where the content of each bin i is given by the total template intensity, f_i (Equation 5.2). To communicate the results, we adopt the *significance level* formalism [James, 2006]. This is within the purview of classical hypothesis testing. In this case, the null hypothesis, H_0, claims that the observed number of runs is consistent with a sequence of Bernoulli trials. In other words, it suggests that the underlying probability distribution for the data is given by the fraction-fit results. The alternative hypothesis, H_1, claims that the sequence of over- and under-predicted data is non-random, or equivalently, that the underlying model is in some way incomplete. For our test statistic, we use the z-value, the number of standard deviations that the observed number of runs, r, is from the expected value, $\langle r \rangle$. A z-value of -2.33 corresponds to the 1% significance level, assuming a single-tailed test. If the z-value for a run test is less than this threshold, the null hypothesis, H_0, is in conflict with observations.

In Chapter 7, the run test is used to assess the credibility of each fit, instead of the more common log-likelihood ratio. This is far from the perfect solution. Ideally, both tests could be used since they complement each other nicely. However, experience has repeatedly shown that the log-likelihood ratio test is not a reliable goodness of fit test for the fraction-fitting results. This is especially true in light of the arguments presented in the last section. Nevertheless, the run test

alone offers good grounds to reject a fit.

Section 5.5: Summary

In this chapter, a methodology for the analysis of pulse height spectra was detailed. Examples of previous analyses can be found in Buckner *et al.* [2015], Dermigny *et al.* [2016] and Daigle *et al.* [2016]. In Chapter 7, fraction-fitting using Bayesian estimation is used to study the resonance spectra of the E_r^{lab} = 435 keV, 498 keV, and 620 keV resonances in the ^{30}Si(p,γ)^{31}P reaction. First, the fabrication and analysis of the targets used for these measurements is discussed.

CHAPTER 6: TARGETS

Nuclear reaction measurements require targets with a high concentration of the nuclide of interest that are stable under ion bombardment. These two conditions are met easily for most compounds, however, there are many other qualities that will dictate the lifetime and usefulness of the target. For example, the presence of elements with large proton capture cross-sections (e.g., ^{11}B, ^{12}C, ^{19}F) introduces troublesome beam-induced background into the pulse height spectrum. These contaminant full-energy peaks and their associated Compton continua may hinder the identification of the useful peaks or raise the detector dead-time to unacceptable levels, making "clean" targets highly desirable. Other considerations include the uniformity of the target layer, its reactivity to air or water, and the sputtering properties of the material. All of these must be examined carefully when designing a target for nuclear experimentation. For the ^{30}Si(p,γ)^{31}P experiment, the chemical properties of the target material demanded a unique solution.

Section 6.1: Silicon Targets

Silicon targets in the literature have taken many forms. Direct reaction experiments, such as those considered here, typically use evaporated targets, where layers of SiO_2 or Si are deposited onto thick target backings [Paine and Sargood, 1979, Moss, 1969]. The advantages of these targets are their uniformity and relative ease of fabrication, however, they are ill-suited for an experiment at LENA. In the case of evaporated Si targets, repeated exposure of the target layer to atmosphere over the course of an experiment poses the risk of substantial target degradation through oxidation. This can be mitigated by measuring frequent target yield curves, however, this procedure is labor intensive. SiO_2 is a much more stable target material but contains ^{16}O, a significant source of beam-induced background. To avoid these issues, implanted ^{30}Si targets were chosen for the ^{30}Si(p,γ)^{31}P experiments. Previous experiments involving these targets [Downen Private Comm.] have demonstrated that they are long-lived, withstanding over 20 C of proton bombardment, with a uniform target layer. Below, the process for fabricating these targets is detailed.

6.1.1: Tantalum Backings

Tantalum was chosen for the target backing material since it is stable, resistant to corrosion, and does not interact with the proton beam at any of the experimental energies considered here. It also has a high melting point (3017°C) and relatively high resistivity (131 nΩ·m at 20°C), allowing for resistive heating, an important step in making sure the targets are as devoid of contaminants as possible. A sheet of Ta metal (0.50 mm thick, 99.5% metals basis) was purchased from *Alfa Aesar* and cut into several 1.5×1.5 inch backings by the UNC machine shop. Before implantation, each backing was cleaned to the extent possible at LENA.

First, the backings were acid etched in a bath to remove contaminants that might have been introduced during the machining process. The primary concern was that cutting oil, used either by the machine shop or the manufacturer, was present in small amounts on the surface. The acid solution was prepared according to the recipe in Vermilyea [1953]; it is a mixture of 95% sulfuric acid, 70% nitric acid, and 48% hydrofluoric acid, in the proportion 75:30:30 (by volume). After etching, the thickness of the target backings range from 0.30-0.40 mm, a reduction of 60-80%.

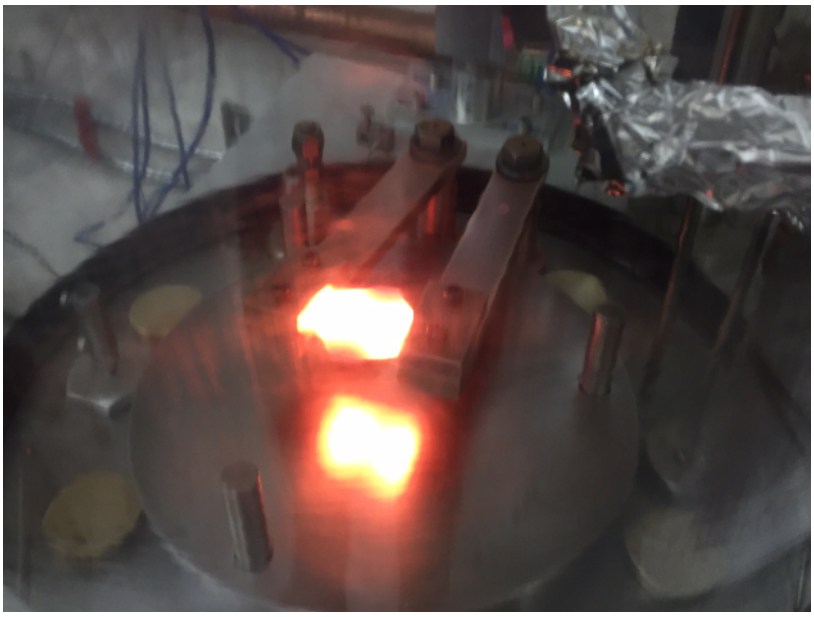

Figure 6.1: The setup for target backing preparation in the UNC evaporator. The tantalum backing is held in place by two water-cooled copper electrodes and then heated resistively in vacuo.

Next, target backings were resistively heated in vacuo to outgas contaminants from the bulk of the material. This is particularly effective at removing fluorine, a prolific byproduct of the

extraction process for tantalum refinement. This was done using the UNC evaporator, described previously in Cesaratto [2011]. The setup for a single backing is shown in Figure 6.1. The backing was held in place by two water-cooled copper electrodes, while the chamber pressure was kept below 1×10^{-6} torr. The current passing through the backing was increased until it glowed dark red; this occurred at 200-300 amps AC. The outgassing was monitored using the vacuum gauge, which reported a factor of 10 increase in pressure that returned to the baseline after 15 minutes. Once outgassing had concluded, the current was shut off and the backing was allowed to cool. The chamber was then backfilled with nitrogen gas and the target backing was moved to a vacuum box for safe keeping. Although the levels of fluorine and carbon contamination were not measured before these two cleaning procedures, the analysis in Longland *et al.* [2009] suggests that both were reduced by factors of 10-100.

6.1.2: SNICS Source

Experiments at LENA that have used implanted targets [Longland *et al.*, 2010a, Kelly *et al.*, 2017] relied on a modified Eaton ion implanter, located at the University of North Carolina at Chapel Hill, to produce the high-current beams needed for sufficient implantation. For silicon beams, the standard practice in the semiconductor industry calls for silicon tetrafluoride (SiF_4) as a dopant gas [Yedave *et al.*, 2014]. Despite its ubiquity in industry, an alternative was needed for this experiment for a few reasons. Foremost, a significant challenge associated with the use of SiF_4 is its volatility: it compromises the source lifetime by creating an acidic environment through the dissociation of SiF_4 into Si, F, and various SiF_x species. Since this is shared resource, accelerated degradation of the ion source or vacuum system is undesirable. Additionally, a fluorine contamination in the system could have been detrimental to present and future experiments.

A *Source of Negative Ions by Cesium Sputtering*, or a SNICS source, was chosen instead to generate the ^{30}Si beam. These sources produce beam from the sputtering of solid material by cesium ions, circumventing the use of any caustic gas. A schematic of the source chamber is shown in Figure 6.2. The sputter target and surface ionizer are in a common chamber containing cesium vapor. At the surface of the heated ionizer coil, Cs^+ ions are created which then accelerate towards the negatively biased target cathode. This beam of Cs^+ in turn sputters the target material and

generates a beam of negatively charged target ions, with a current that depends on the electronegativity of the material. In the case of silicon, with an electron affinity of 1.4 eV, beam currents of 200 μA have been reported [Middleton, 1984].

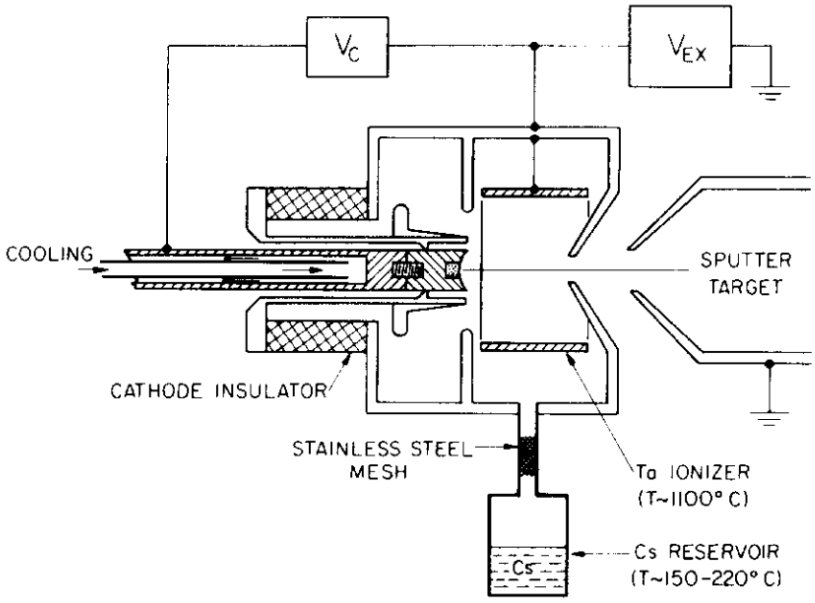

Figure 6.2: A schematic of a SNICS source. The source body is negatively biased (relative to ground) at V_S. The target cathode is negatively biased (relative to V_S) while the extraction plate is positively biased (relative to V_S) at V_{Ex}. Below the source, the cesium reservoir is heated to 200 °C.

Since there was no dedicated SNICS target implantation beamline at TUNL, a focus of this dissertation was the design and installation of a suitable system. To leverage the existing beam-optics components and LABView control system, a General Ionex Model 860 source was refurbished and installed in place of the DENIS II duoplasmatron, which is used to make unpolarized H^- and D^- beams for injection into the TUNL FN Tandem accelerator. Many of the high-voltage power supplies used to operate the DENIS II source (e.g., table and focus) found analogous use for the SNICS source. To bias the target cathode (−5 kV) and extraction electrode (+10 kV), as well as provide power to the ionizer coil (200 W), separate supplies were installed on an insulated platform within the source cage, as shown in Figure 6.3. Owing to the geometry of the enclosure, the table voltage was limited to −50 kV, placing the maximum beam energy at 55 keV (table plus cathode bias).

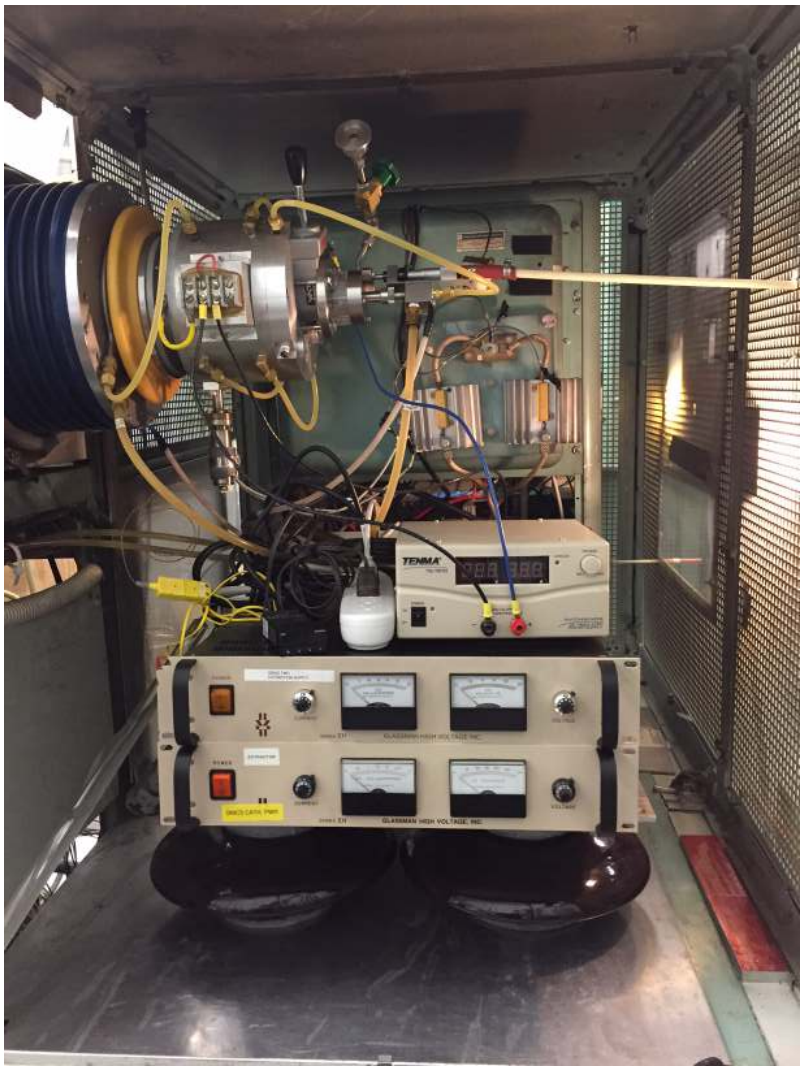

Figure 6.3: The SNICS source, installed in place of the DENIS II duoplasmatron. The ceramic feet provide the insulation necessary for the high-voltage power supplies.

In typical operation, the H^- or D^- beam is transported down a 4 meter beamline and momentum analyzed by the "NIS" dipole magnet, where it is redirected for injection into the FN Tandem accelerator. For target implantation, a dedicated beamline was built using a spare exit port on the NIS magnet. The deflection required for this beamline is 45°. A diagram of the new target implantation line is shown in Figure 6.4. Immediately upon egress from the magnet, the beam is subjected to a pair of vertical magnetic steerers. These are also present on the Tandem injection line and are required to correct for a slight slope ($< 2°$) of the magnet. A set of adjustable horizontal and vertical slits follows. Current from each slit is fed into a difference amplifier which is read out in the control room, allowing the operator to monitor and adjust the beam position. Between the

slits and the target there is also a vertical-horizontal magnetic beam steerer and an einzel lens. The steerer is meant to provide greater tuning capacity and also the option for a rastering system. The einzel lens is capable of being biased to 15 kV and provides a convergent quality to the beam, which is otherwise unfocused. All of the optical elements are tuned using the LABView system in the control room.

The target station comprises a copper collimator and a 10 inch copper shroud. The shroud is electrically and thermally isolated, allowing it to operate as both a cold trap and secondary-electron suppressor. A target backing is mounted on a water-cooled beamstop at the end of the line. Current on both the target backing and collimator can be monitored, allowing the operator to control the accumulated dose of the ion implantation. This beamline also has a vacuum circuit which includes a turbomolecular pump, a roughing pump, and two vacuum gauges. During operation, the baseline pressure near the target station was 8×10^{-7} torr.

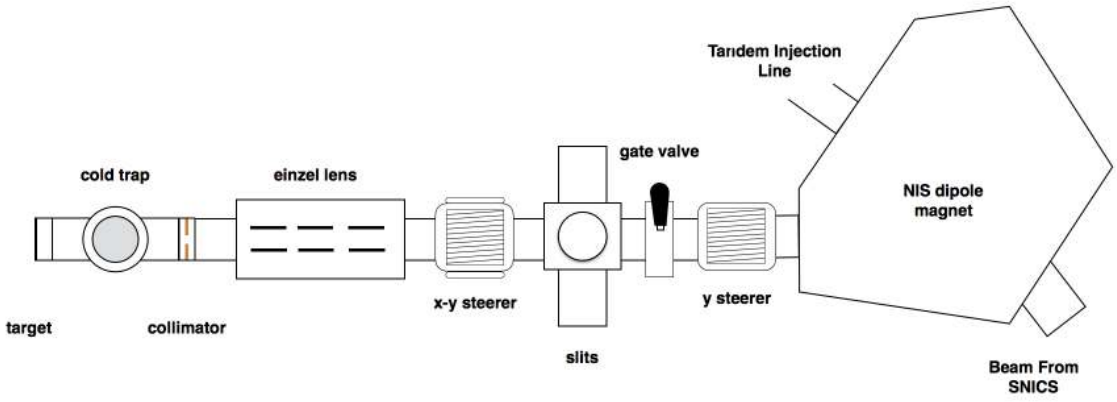

Figure 6.4: A bird's eye view of the target implantation line built to compliment the SNICS source. Upon egress from the NIS dipole magnet, the beam is subjected to a horizontal steerer and a set of two beam-attenuating slit pairs. Next, a horizontal-vertical steerer provides more positional control. Before the target, there is a copper collimator and an einzel lens for enhanced beam focusing.

6.1.3: Implantation

Due to the high-demand for the DENIS source, installation, testing, and target fabrication using the SNICS source took place over several noncontiguous run weeks during Fall 2016 and Spring 2017. Preliminary tests focused on the extraction of a silicon beam using unenriched material.

Following the suggestions in Middleton [1984], 5 mg of silicon powder was crushed and pressed into the target cathode. This was found to be a superb way of preparing cathodes, since silicon powder compacts readily into a form that is highly resistant to mechanical stress. During source operation, these cathodes produced a prolific ^{nat}Si beam, measuring at 100 μA (unanalyzed) immediately downsteam on the first beam-stop. This output lasted for several hours before dropping, indicating depletion of the cathode material. These tests also showed that transport of the beam from source to target was severely limited by the lack of a proper focusing element before the magnet. Of the 100 μA measured at the source, only 1/20th of that was deliverable to target. This discovery prompted the addition of the einzel lens in the target beam-line (see Figure 6.4) and also provided estimates for how much enriched material was necessary for a ^{30}Si target.

Silicon powder enriched in ^{30}Si was purchased from *Isoflex USA* to produce targets for the resonance measurements. The isotopic purity of the 30 mg batch was reported to be greater than 99.64%. Targets were produced from this material during two run periods via implantation of 55 keV $^{30}Si^{-}$ ions into tantalum backings, cleaned using the methods described in Section 6.1.1. The average beam on target during these implantation sessions was 10 μA, indicating a slight improvement with the addition of the einzel lens. Each target required two cathodes of material, totaling about 12 mg of ^{30}Si metal each. The total exposure time for each target was 6 hours and 10 hours, corresponding to a total implanted dose of 60 μA·hrs and 100 μA·hrs, respectively. Although these figures fall short of the 400 μA· hr recommendation in Iliadis [2015], they were both found to be excellent targets. Since the second target had a higher dose of implanted ions, it was used exclusively for the resonance measurements.

6.1.4: Target Cleaning

Over the course of this dissertation, the target was exposed to several Coulomb of incident proton beam. Although the conditions of the vacuum environment are optimized each time a target is run on, there was a gradual build-up of carbon on the face of the target. The source of this carbon is not yet known, though it is thought to be the result of outgassing by vacuum o-rings along the length of the beam-line. Before the experiment had concluded, the layer of carbon was so thick that beam currents exceeding 20 μA were not possible due to the overwhelming intensity

of the $^{12}C(p,\gamma)^{13}N$ direct-capture photopeak and its associated Compton continuum. This was a considerable handicap, since it meant that in addition to the beam-induced background, greater levels of environmental background would have to be tolerated to reach the desired signal statistics.

To combat this problem, the target was cleaned using the Emitech K-1050X Plasma Asher at the Duke University Shared Materials Instrumental Facility. A marketing photograph of this device is shown in Figure 6.5. After loading the target, the chamber was evacuated to 0.1 - 0.2 Torr, and O_2 was introduced. RF power (100 W) was then applied around the chamber, exciting the gas and dissociating the O_2 into chemically active atoms. The plasma then reacted with and removed the surface carbon layer. The combustion products (CO_2 and CO) were continuously pumped out of the chamber. Over the course of just two minutes, the carbon layer was visibly removed. Subsequent tests of the target showed that 97% of the carbon and 94% of the fluorine present had been removed without affecting the dose of ^{30}Si atoms. After treatment, the ^{12}C direct-capture process was no longer an impediment. Thus, this method of cleaning was very effective at increasing the longevity of target.

Figure 6.5: The Emitech K-1050X Plasma Asher. In the right photograph, the door to the plasma chamber is ajar. The target was placed on the platform during cleaning.

Section 6.2: Target Yield Curves

In this dissertation, we make extensive use of target yield curves or *excitation functions* to study the properties of the ^{30}Si target. They provide crucial information such as the stoichiometry and depth of the implanted region, and also can be used to determine whether the target is changing over the course of the experiment. Yield curves are measured by counting the total number of char-

acteristic γ-rays observed while the target is bombarded by an particle beam at or near resonance energies. According to Iliadis [2015], the yield, $Y(E_0)$, is given by:

$$Y(E_0) = \frac{1}{\epsilon_r} \int_{E_0-\Delta E}^{E_0} dE' \int_{E_i=0}^{\infty} dE_i \int_{E=0}^{E_i} \sigma(E) g(E_0 - E_i) f(E_i - E, E') dE, \tag{6.1}$$

where E_0 is the energy of the incident beam as it strikes the face of the target and ϵ_r is the stopping power of the material. The function $\sigma(E)$ is the reaction cross section, g represents the energy-independent beam width, and f represents depth-dependent beam straggling. The details of the convolution procedure can be found in Iliadis [2015]. A program to calculate $Y(E_0)$ was used to analyze the measured curves and derive Bayesian posterior probability distributions for the maximum yield, the beam-width, the effect of beam straggling, and the thickness of the implanted region. This is a modified version of the `YCurve.R` program, which has been used successfully in several theses [Cesaratto, 2011, Buckner, 2014, Kelly, 2016]. For details regarding the choice of priors, Markov Chain Monte Carlo implementation, and example traces, see Appendix A.1.

To study the ^{30}Si target, protons provided by the JN Van de Graaff accelerator were used to measure the yield at the standard resonance, $E_r^{lab} = 619.6 \pm 1.2$ keV [Kuperus *et al.*, 1959], in the ^{30}Si(p,γ)^{31}P reaction. The net intensity of the ground state transition γ-ray, R$\rightarrow$ 0, was measured using the HPGe detector in singles mode. This was done at regular intervals to assess the stability of the target. In Figure 6.6, multiple yield curves are shown, with two curves taken before the resonance experiments in the top panel, and two curves taken immediately after their conclusion in the bottom panel. For the analysis of resonance data in Chapter 7, an important consideration is whether or not this target degraded over the course of the experiment. These two data sets illustrate the extent of that possible degradation. The "initial" and "final" data sets were each fit by assuming their constituent yield curves each had a small systematic offset from the true yield. This systematic offset could be the result of a small discrepancy in the detector positioning during run time or a result of an error in charge integration, for example. The assumed uncertainties for each data point are Gaussian, with the magnitude determined by the counting statistics of the R$\rightarrow$0 photopeak.

Posterior distributions for both data sets were used to derive the 68% highest probability intervals for the maximum yield, the dose of ^{30}Si atoms in the center of the target layer. Changes

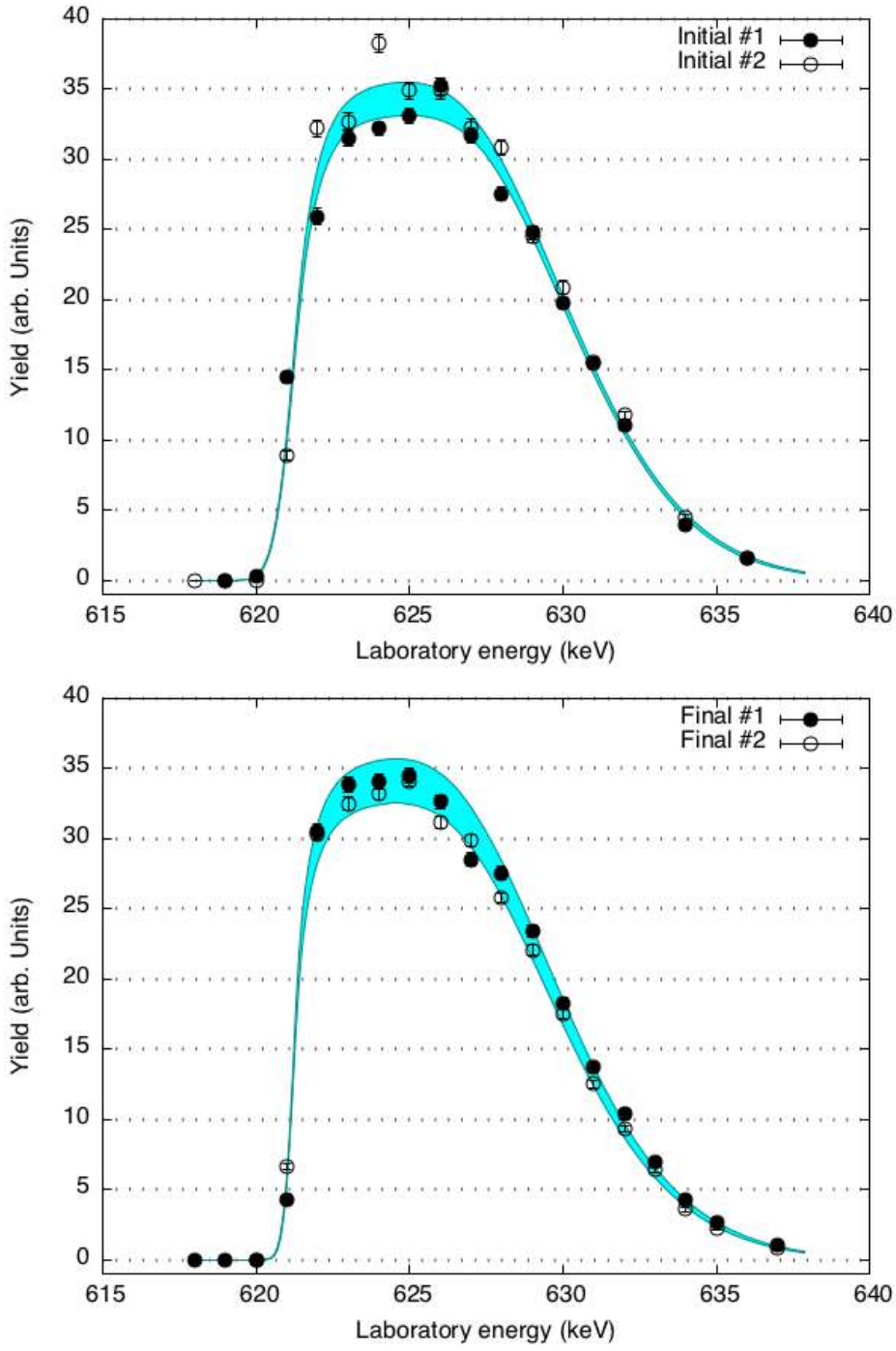

Figure 6.6: (Top) Yield curves taken before the resonance experiments. The target had also just been freshly cleaned, as explained in Section 6.1.4. (Bottom) The yield curves taken after the target had been exposed to ≈ 5 Coulombs. The energy of the proton beam is shown on the x-axis, while the yield (the number of R$\rightarrow$0 transitions observed per incident micro-ampere) is on the y-axis. The cyan curves represents the 95% highest probability interval for the yield given the data.

to the stoichiometry due to diffusion, sputtering, or implantation of contaminant particles (e.g., ^{12}C) would reduce this value. The maximum yield for each data set, in units of counts/μC, was determined to be

$$Y_{max}^{\text{init.}} = 34.82^{+0.83}_{-0.76}, \qquad \text{and} \qquad Y_{max}^{\text{final}} = 34.11^{+0.81}_{-0.78}.$$

The agreement between these two intervals suggests that the target was unaffected by the proton bombardment incurred over the course of the experiment. Therefore, for the analysis of the resonance data in Chapter 5, no correction is necessary to account for target degradation. As for the stoichiometry of the target layer, this calculation is rather expansive, so it has been relegated to Appendix B.2. The stoichiometry was found to be $Ta_5Si_{7.5\pm1.2}$, suggesting that silicon atoms outnumber tantalum in the bulk of the target layer.

Besides the maximum yield, the other features of the yield curves offer meaningful insight. For example, the beam-width, representing the spread in energy of the incident beam, can serve as an indication of beam quality. The target thickness (in keV) indicates the loss of energy incurred by the proton as it traverses the target layer and can be used in conjunction with stopping power data to calculate the target thickness at other energies. Further, the total area under the curve, which is proportional to the absolute number of ^{30}Si atoms in the target, enters into calculations for resonance strengths (See Equation B.2). All of the parameters measured from the final yield curve set are shown in Table 6.1. The measured beam-width reflects the improved beam-control of the new terminal potential stabilizer system and also recent efforts to align the JN with the LENA dipole magnet. As a point of comparison, the JN beam-width observed in Buckner [2014] was 2-3 keV.

Yield Parameter	16%	50%	84%	Units
Beam-width FWHM	0.70	0.71	0.72	keV
Target Thickness	8.66	8.70	8.74	keV
Straggling Constant	2.52	2.57	2.63	keV$^{1/2}$
Maximum Yield	33.33	34.11	34.92	counts μC^{-1}
Area	290.0	296.9	303.7	counts keV μC^{-1}

Table 6.1: Results of the Bayesian analysis for the final set of yield curves. The 16$^{\text{th}}$, 50$^{\text{th}}$ and 84$^{\text{th}}$ percentiles of the posterior distributions are shown for each parameter.

There is a subtle point regarding the straggling energy loss in the target that is worth discussing.

An important assumption in the calculation of the parameters in Table 6.1 is that the target layer is well-defined, with a sharp cutoff at the interface of the implantation layer and the backing material. The shape of the yield function tail should then be predominantly determined by the effect of energy loss straggling. This is probably not the case with this target. Because it was implanted, there is simply no reason to assume that the ^{30}Si distribution is perfectly uniform. Instead, the tail is much more likely an indication that the dose falls off continuously as a function of depth. While this observation does not affect the measured maximum yield or area, it is worthwhile to check that the yield in the center of the target (based on the measured target thickness) is consistent with the maximum, since this assumption is important for the measurement of resonance strengths at lower energies. The posterior distribution of the yield at $E_p = E_r + \frac{1}{2}\Delta E$, where ΔE is the thickness of the target, is $34.21^{+0.83}_{-0.38}$ and $34.09^{+0.57}_{-0.92}$ counts$\cdot\mu$C^{-1} for the initial and final sets, respectively. Since these are consistent with their observed maximum yields, it is safe to assume that the resonance strength experiments performed at the center of the target also satisfy this criteria.

In this chapter, the procedure for making and cleaning ^{30}Si targets was outlined. An analysis of the yield excitation functions shows that the target used is reliable; it has a high-dose of implanted ^{30}Si and was unaffected by the proton bombardment incurred over the course of the resonance measurements. Issues regarding the departure from an ideal target were addressed, and it was found that there is no cause for concern. In the next chapter, the use of this target to derive new resonance strengths is detailed.

CHAPTER 7: ^{30}Si(p,γ)^{31}P PROTON CAPTURE

The first investigation into the excited states of ^{31}P was performed by Endt and Paris [1957]. In that work, lead-phosphate targets were bombarded by protons with energies of 6.5 and 7.0 MeV. Inelastically scattered protons via ^{31}P(p,p$'$)^{31}P were then observed through a high-resolution magnetic analyzer. The measured spectrum revealed for the first time the level structure of the ^{31}P nucleus. Soon thereafter, the first direct measurements of the ^{30}Si(p,γ)^{31}P reaction were made by Broude *et al.* [1958a]. Using a proton beam impinging upon a ^{30}Si target, the excitation function was recorded over an energy range from 450 keV to 1100 keV, revealing ten (p,γ) resonances. Two of the resonances studied in this dissertation, $E_r^{lab} = 498.3 \pm 1.0$ keV [Kuperus *et al.*, 1959] and $E_r^{lab} = 619.6 \pm 1.2$ keV [Kuperus *et al.*, 1959], were first observed in this work. Using the excited state energies measured by Endt and Paris [1957], they were also able to lay the ground-work for the deexcitation branching ratios.

In the decades since then, the body of work surrounding the ^{31}P level structure and the ^{30}Si(p,γ)^{31}P reaction has grown significantly. The reaction Q-value, based on the most recent atomic mass evaluation, is now known precisely: $Q = 7296.55 \pm 0.02$ keV [Wang *et al.*, 2017]. With the advent of both the tandem Van de Graaff accelerator and the split-pole magnetic spectrograph, deuteron angular distributions from the ^{30}Si(^{3}He,d)^{31}P reaction have allowed for measurements of spectroscopic factors and proton partial widths while also providing evidence necessary for level spin assignments [Vernotte *et al.*, 1990, McCulloch *et al.*, 1984, Moss, 1969]. Several expansive (p,γ) experiments [de Neijs *et al.*, 1975, Willmes and Harris, 1967, Wolff *et al.*, 1968] have measured the intensity of deexcitation γ-rays to determine branching ratios as well as the level parity and spins through γ and $\gamma\gamma$ angular correlations. The energy level diagram for the ^{31}P nucleus, based on the most recent nuclear data evaluation [Ouellet and Singh, 2013], is shown in Figure 7.1, with several levels omitted for clarity. With regard to resonance strengths, these past (p,γ) experiments have focused primarily on resonances in the range $E_r^{lab} = 0.6 - 3.0$ MeV. Consequently, there are no measurements of the $E_r^{lab} = 435 \pm 4$ keV resonance. Evidence of its existence is limited to the iden-

tification of the compound state, $E_x = 7718 \pm 4$ keV, in Vernotte *et al.* [1990]. The strength of the $E_r^{lab} = 498.3$ keV resonance has been measured directly twice, but the details of the measurements either remain unpublished [Hoogenboom, 1958] or are reported unsatisfactorily [Riihonen *et al.*, 1979]. These are shown in Figure 7.1, denoted by their center-of-mass energies. The connection between the proton energy and the compound excited state energy, E_x, is also illustrated.

In this chapter, I present two new resonance strength measurements made at the Laboratory for Experimental Nuclear Astrophysics (LENA). The details of the experimental procedure, as well as the analysis of the data, are described in full. Section 7.1 concerns the yield of the $E_r^{lab} = 619.6$ keV resonance, which serves as the reference for the $E_r^{lab} = 498.3$ keV and $E_r^{lab} = 435$ keV resonance measurements, covered in Sections 7.2 and 7.3, respectively.

Section 7.1: 620 keV Resonance

The $E_r^{lab} = 620$ keV resonance in the ^{30}Si(p,γ)^{31}P reaction has been studied extensively. The history is summarized in Table 7.1, which shows the measured $\omega\gamma$ values throughout the years. For experiments that measured related quantities, e.g., the partial widths Γ_γ and Γ_p, the resonance strength has been calculated. The first investigation of this resonance is attributed to Smith and Endt [1958]. In that work, the Doppler-shifted deexcitation γ-ray of the 7896-keV level was resonantly reabsorbed by phosphorous powder. Transmission through the absorber was measured at different angles θ, relative to the incident proton beam. The absorption curve was then used to determine the total resonance width, Γ, and the ground state decay width, Γ_γ. This experiment was then repeated independently by Hough *et al.* [1968], whose results were in reasonable agreement.

Later, Lyons *et al.* [1969] measured the absolute strength, $(2J+1)\Gamma_\gamma\Gamma_p/\Gamma$, using a thick-target yield on an enriched silicon target. The resonance strength determined from their data was markedly higher than the resonance absorption values. Seeking to resolve this discrepancy, a thick target resonance measurement was performed again by Riihonen *et al.* [1979]. Their work did little to help the issue, however, having measured a resonance strength that was higher still. That same year, Paine and Sargood [1979] measured this resonance as part of a campaign to improve resonance strengths in the Z range $11 - 20$. Their work produced three independent measurements of the $E_p^{lab} = 620$ keV resonance strength. The first was determined through a thick target

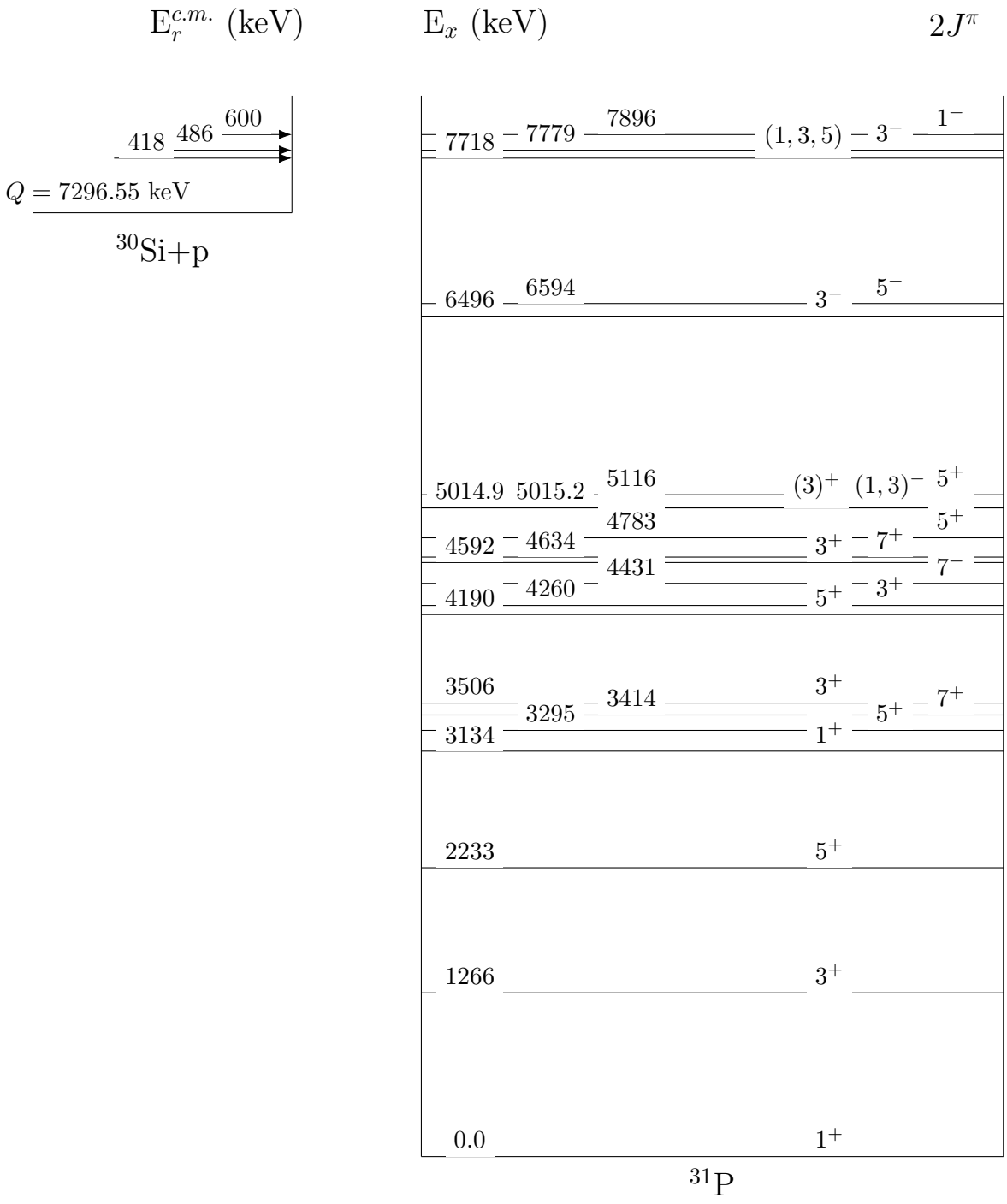

Figure 7.1: Energy level diagram for ^{31}P with the ^{30}Si+p resonances under investigation. Several levels have been omitted for clarity. Level energies and $2J^\pi$ values are based on those suggested in Ouellet and Singh [2013]. Note the presence of the doublet at $E_x = 5015$ keV.

yield experiment performed relative to the E_p = 632 keV resonance in $^{27}Al(p,\gamma)^{28}Si$. Absolute measurements were then performed using two methods: (1) a standard thick target yield and (2), Rutherford back-scattering of protons using a transmission target. These two measurements were in excellent agreement with one another, their relative measurement, and the results of Lyons *et al.* [1969]. Thus, in spite of the apparent advantages of resonant absorption measurements, which do not depend on target composition, beam current integration, or absolute detection efficiency, these results called into question the consistency of the method. For the present work, the resonance strength recommended by Paine and Sargood [1979], $\omega\gamma_{620} = 1.95 \pm 0.10$ eV, is adopted for all calculations. This is a weighted average of their results and that of Lyons *et al.* [1969]. The value reported by Riihonen *et al.* [1979], which is in conflict with these, is not included.

Ref.	$\omega\gamma$ (eV) [a]
Smith and Endt [1958]	1.55 ± 0.13 [b]
Hough *et al.* [1968]	1.7 ± 0.4 [b]
Lyons *et al.* [1969]	1.97 ± 0.20
Riihonen *et al.* [1979]	2.5 ± 0.2
Paine and Sargood [1979]	2.0 ± 0.2 [c]
	1.92 ± 0.17
	1.97 ± 0.16 [d]
Present (adopted)	1.95 ± 0.10

Table 7.1: The literature values for the E_p = 620 keV resonance strength, $\omega\gamma$. The value adopted in the present work is a weighted average of the results of Paine and Sargood [1979] and Lyons *et al.* [1969].

[a] All measurements are absolute except where noted
[b] Based on resonant absorption
[c] Relative measurement using the E_p = 632 keV resonance in $^{27}Al(p,\gamma)^{28}Si$
[d] Based on Rutherford back-scattering of protons

The E_p = 620 keV resonance is an excellent choice for a standard resonance for a few reasons. As demonstrated above, there are several high-quality measurements of the resonance strength, $\omega\gamma$, that support a precise average value, with an uncertainty of only 5%. It is a strong resonance, which means that the yield can be measured with less incident charge. This allows for quick data collection with minimal damage to the target. Further, the decay of the compound state, E_x = 7896 keV, has been studied several times. The primary γ-ray branching ratios are therefore well-known.

Lastly, the spin-parity of the state has been determined using proton-transfer reactions [Vernotte *et al.*, 1990] and $\gamma\gamma$ angular correlations studies [Broude *et al.*, 1958b], with overwhelming support for the designation of $\frac{1}{2}^-$. Since the spin-parity of the ground-state ^{30}Si nucleus is 0^+, this means that an unpolarized proton beam will populate the $m = 2$ substates of the compound state with an equal probability. The deexcitation γ-rays are therefore emitted isotropically [Iliadis, 2015]. For detector systems that cover only a portion of the full solid angle, such as the system employed at LENA, this property greatly simplifies the analysis of pulse height spectra since no correction is necessary to account for anisotropic radiation patterns.

The general strategy behind a relative measurement is to observe the maximum yield, Y_{max}, in the bulk of the target layer at the standard resonance energy. Since the resonance strength, $\omega\gamma$, is well-known, the measured yield can then be used to determine properties of the target, such as stoichiometry or dose. For resonances under investigation, a measurement of the maximum yield, coupled with the deduced properties of the target, can be used to calculate the resonance strengths. In this case, the $E_p = 620$ keV was studied in order to then measure the $E_p^{lab} = 498$ keV and $E_p^{lab} = 435$ keV resonances. In the next section, the measurement and analysis of the 620-keV resonance data are presented.

7.1.1: Measurement

The maximum yield of the $E_p^{lab} = 620$ keV resonance in ^{30}Si(p,γ)^{31}P was measured following the two initial yield curves discussed in Section 6.2. Proton beam from the JN Van de Graaff accelerator was made incident on the ^{30}Si implanted target with the $\gamma\gamma$-coincidence spectrometer in the run geometry. The energy of the proton beam was $E_p = 625$ keV, corresponding to the maximum of the yield curve. To minimize the influence of any inhomogeneities in the implanted dose over the target surface, the beam was rastered over the exposed target surface using a horizontal-vertical magnetic steering system. The detector dead time was monitored throughout the experiment by feeding a pulser signal into the HPGe preamp. The number of pulses was recorded using a scalar counting module, and this was compared to the artificial pulser peak in the pulse-height spectrum to obtain the dead-time of the detector system. To avoid pulse pileup effects, the dead-time was kept below 5%. The total amount of charge incident on the target was 3781 μC, accumulated over

the course of 4805 seconds, yielding a small proton beam current of 0.79 μA. Based on the yield curve analysis in Section 6.2, it can safely be assumed that the reaction yield did not change over the course of this experiment.

Data from the HPGe, NaI(Tl) annulus, and the plastic scintillator paddles were sorted using the data acquisition software, `JAM` [Swartz *et al.*, 2001]. The pulse-height spectra for the singles and coincidence mode data are shown in Figure 7.2. Only events that were anti-coincident with a hit in the muon-veto paddles were included. For the coincidence data, the gating condition, 3.0 MeV $<$ E^{HPGe}+E^{NaI} $<$ 9.0 MeV was chosen in order to encompass the compound state excitation energy, E_x = 7896 $\pm$ 1 keV [Ouellet and Singh, 2013], while also suppressing environmental background. The full-energy peaks corresponding to the primary transitions away from the compound state (here denoted "R"), are labeled along with their escape peaks, where applicable. All of the primary and secondary transitions previously observed in [de Neijs *et al.*, 1975] were identified in the measured pulse-height spectrum. No new transitions were observed. The background-subtracted intensities of the primary transitions are shown in Table 7.2, along with their observed full-energy peak energy. Note that coincidence summing effects are present and not corrected for in this tabulation. Environmental background is a minor presence. Full-energy peaks from the decay of ^{238}U, ^{232}Th, and ^{40}K are observed in the singles spectrum but are absent in coincidence since they do not satisfy the gating condition.

Transition	$2J_f^\pi$	E_γ (MeV)	Intensity (counts) singles	coincidence
R $\rightarrow$ 0	1^+	7904.9(12)	126600(400)	—
R $\rightarrow$ 1266	3^+	6639.3(10)	2100(200)	1300(130)
R $\rightarrow$ 3134	1^+	4770.0(7)	1300(100)	860(100)
R $\rightarrow$ 3506	3^+	4393.5(6)	970(100)	690(80)
R $\rightarrow$ 5014.9	$(3)^+$	2884.6(4)	7400(130)	5200(100)

Table 7.2: The observed E_r^{lab} = 620 keV resonance primary transitions and their full-energy peak energies and net intensities in the singles and coincidence spectra. The total incident charge was 3781 μC, collected at E_p^{lab} = 625 keV. The spin-parities of the final states are also shown. All transitions were also reported in de Neijs *et al.* [1975].

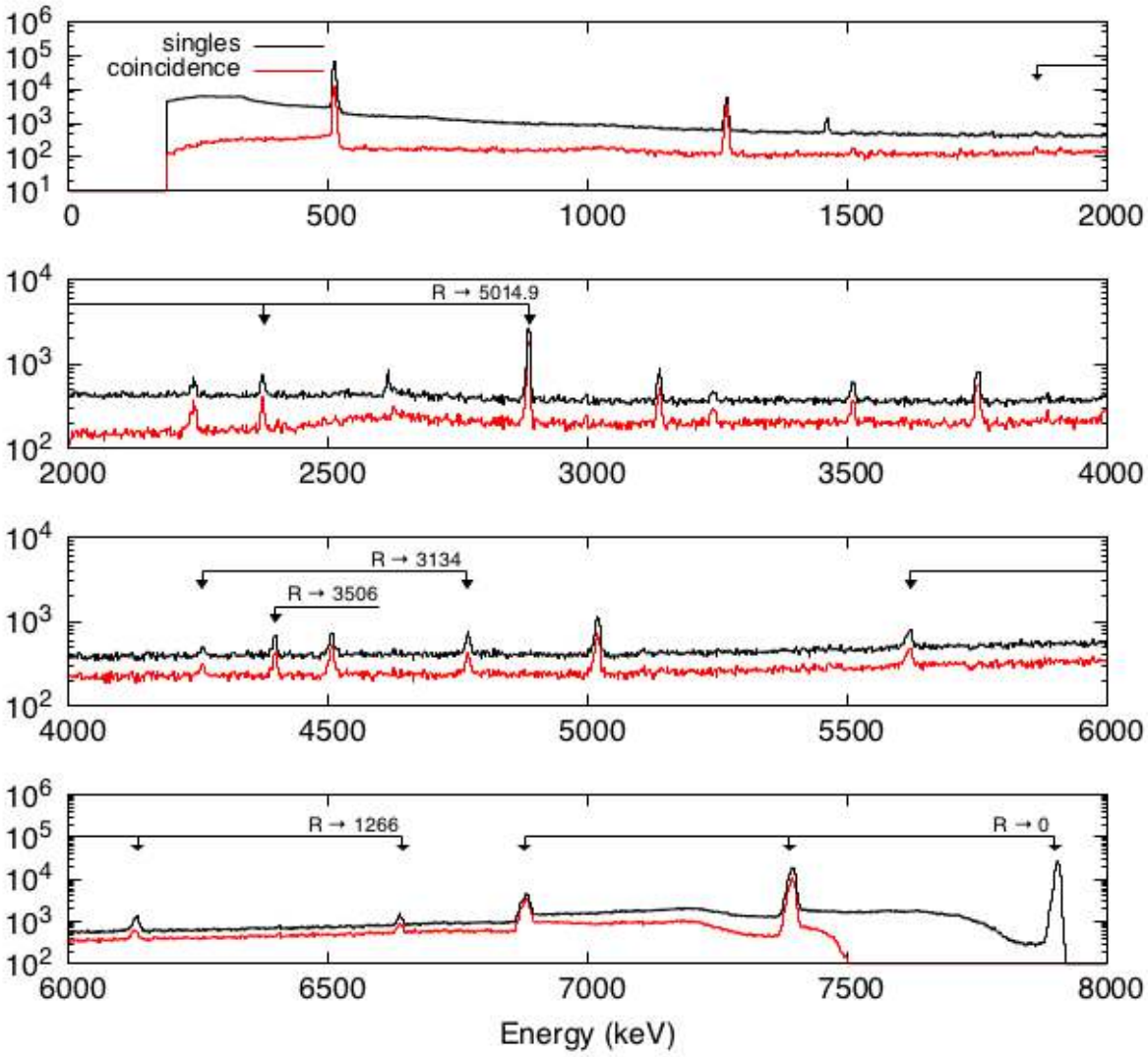

Figure 7.2: Pulse-height spectrum taken at the $E_r^{lab} = 620$ keV resonance using the $\gamma\gamma$-coincidence spectrometer. Full-energy peaks corresponding to primary transitions from the 7896-keV compound state, here denoted "R", are shown along with their escape peaks where applicable. Both the singles (black line) and coincidence (red line) spectra are shown.

7.1.2: Analysis

The singles and coincidence mode spectra were analyzed using the methodology outlined in Chapter 5. For each primary transition listed in Table 7.2, a Monte Carlo template was simulated using the program `LENAGe`. The secondary branching ratios for the decay of bound states in ^{31}P were adopted from the recommended values in Ouellet and Singh [2013], which are based on measurements by de Neijs *et al.* [1975]. A table of adopted secondary branching ratios is provided in Appendix B.3. Although environmental background is present in the singles mode spectrum, all of the primary transitions are at energies higher than the characteristic ^{208}Tl peak (2614 keV), so their impact on the fit is negligible. Therefore, no background templates were necessary. The fit was limited to regions surrounding the primary transition full-energy peaks. The only exception was in the coincidence analysis, where the single-escape peak for the R $\rightarrow$ 0 transition is used since no full-energy peak is present.

The fractional contribution of each primary decay to the measured spectra was determined using an implementation of Metropolis-Hastings Markov chain Monte Carlo, which was provided by the `pymc` software library [Patil *et al.*, 2010]. The joint posterior probability distribution (Equation 5.3) included each of the templates mentioned above. The routine was run for 80,000 iterations, with the first 20,000 discarded as "burn-in", since the sampler had not yet converged. The accumulated samples for each template fraction, or the *chains*, were then thinned, saving only every 5th sample. The marginalized posterior densities for each fractional contribution were then built from their respective chain. These are shown in a scatter-plot matrix in Appendix A.4. The success of the fit is illustrated in Figures 7.3 and 7.4 for the singles and coincidence cases, respectively. The fit regions for each primary transition are indicated by the vertical dashed lines in each panel. The 95% credibility region is shown (cyan) for each primary transition full-energy peak. This band represents the statistical fluctuations of the simulated template-sum spectrum as the joint posterior probability distribution was sampled. In general, it is in good agreement with the observed data (black), with the higher-statistics primaries, i.e., R $\rightarrow$ 0 and R $\rightarrow$ 5014.9, tracking the band more closely. Both analyses also pass the run test described in Section 5.4.1, with Z-values of -1.43 and -0.37. These values suggest that the sequence of over- and under-predicted bins, as given by the best fit, is described well by random chance, indicating that the simulation of the templates was

done adequately.

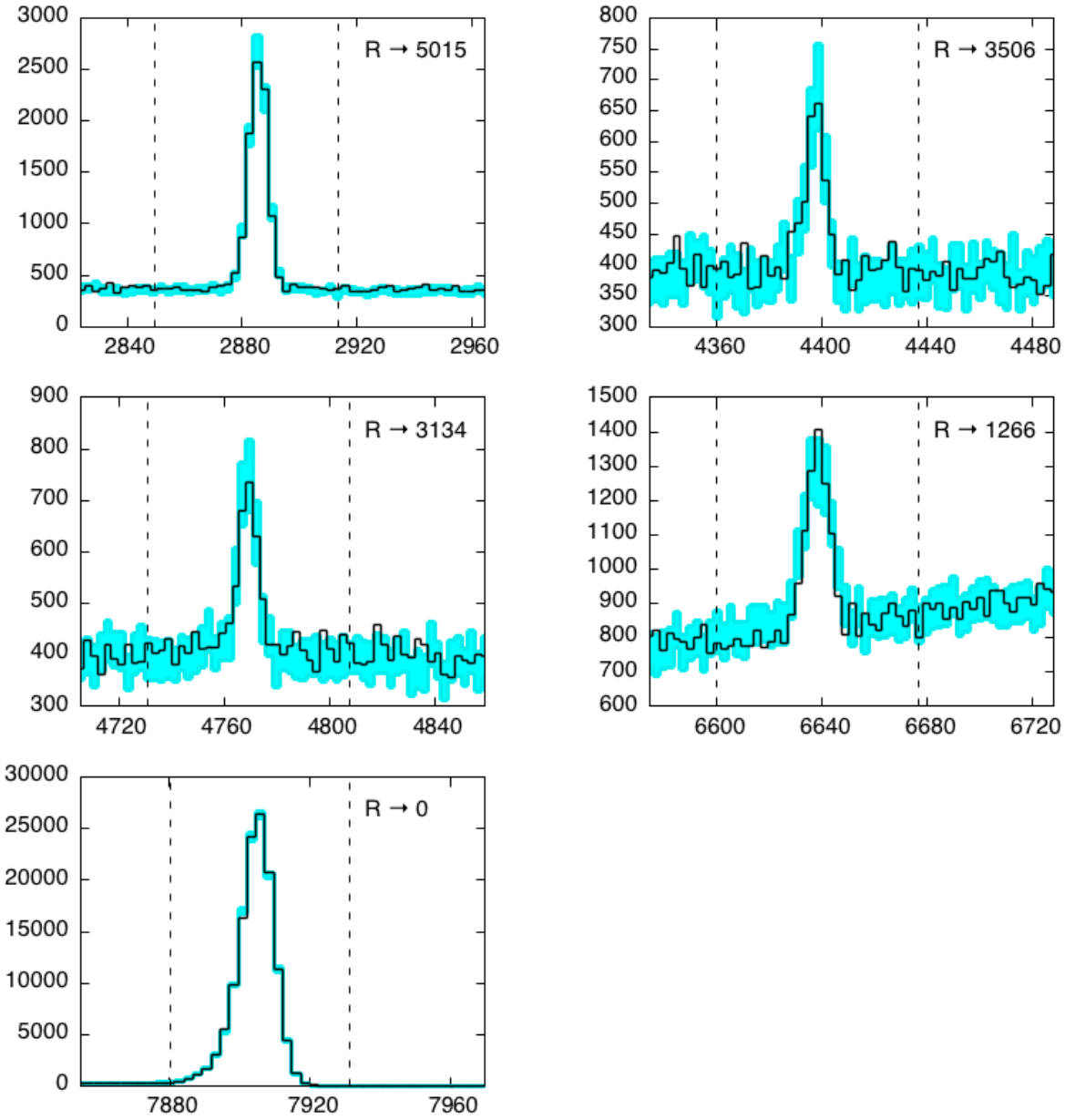

Figure 7.3: Plots of the simulated posterior histograms for the $E_r^{lab} = 620$ keV resonance singles analysis for each of the primary transition photopeaks. The cyan histogram corresponds to the 95% credibility region, while the black line represents the pulse-height spectrum of the observed data. The vertical dashed lines denote the fit region used for each peak.

Based on the derived fraction values, Equation 5.5 was used to calculate the partial number of reactions: the number of decays belonging to a particular primary transition decay chain. These are shown in Table 7.3 for the singles and coincidence mode. The calculated branching ratios are

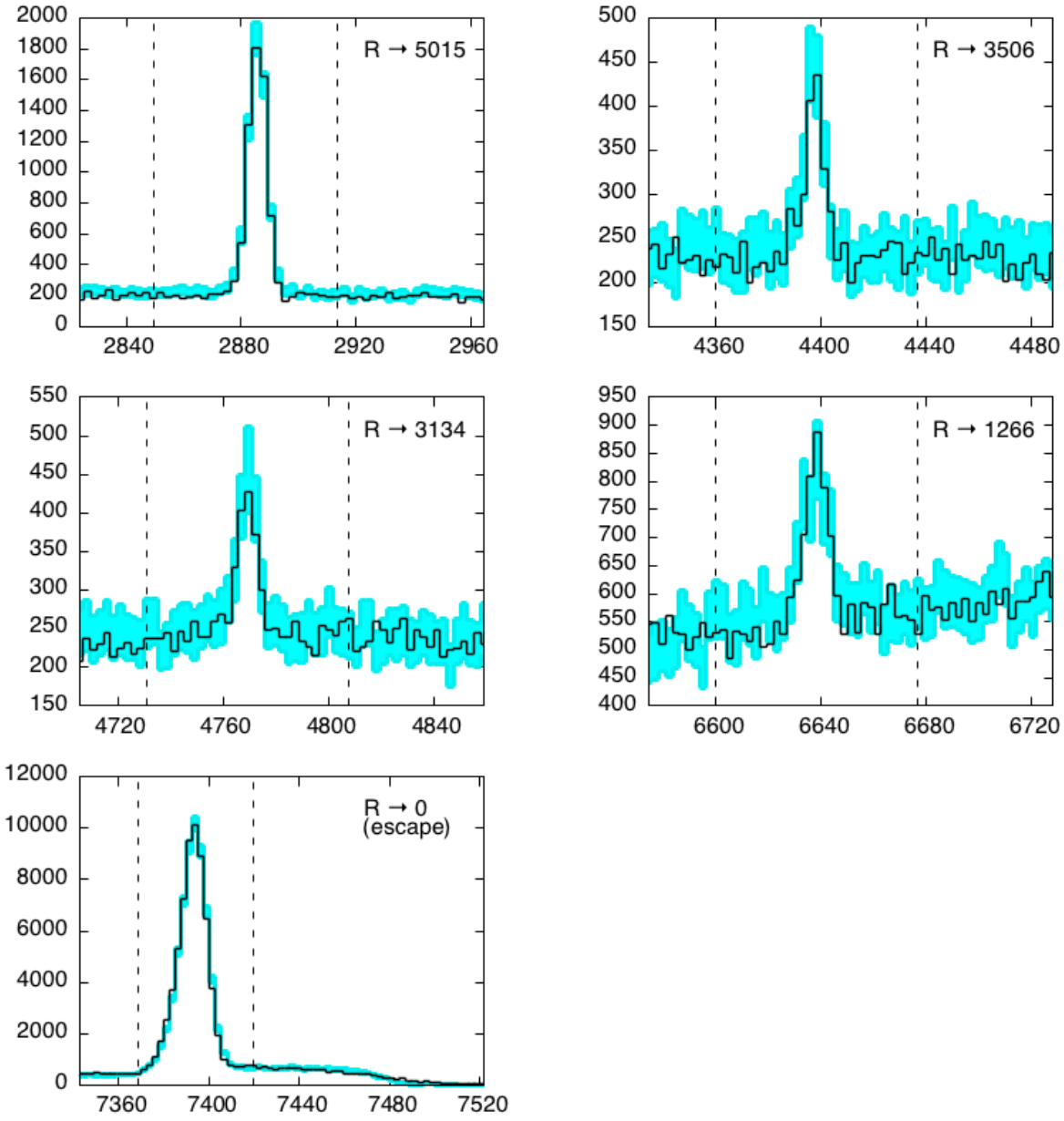

Figure 7.4: Plots of the simulated posterior histograms for the $E_r^{lab} = 620$ keV resonance coincidence analysis for each of the primary transition photopeaks. For the ground state transition, R $\rightarrow$ 0, the single-escape peak is shown instead. The cyan histogram corresponds to the 95% credibility region, while the black line represents the pulse-height spectrum of the observed data. The vertical dashed lines denote the fit region used for each peak.

also shown along with their values measured in de Neijs *et al.* [1975] for comparison. Regarding the partial reaction intensities, the singles and coincidence values are in agreement with only one exception. The number of ground-state transitions, i.e., R $\rightarrow$ 0, predicted by either mode are in conflict with one another, with the coincidence result being 2.6% lower. This is not so troubling, since these are within the 4% systematic error attributed to the detector simulations in Section 4.3.1. It would nevertheless be interesting to understand the origin of the discrepancy, which remains unclear. For the calculation of the total number of reactions, which is the most necessary component of this analysis, the average of the singles and coincidence result is adopted. The branching ratios for the primary transitions, calculated for both the singles and coincidence mode, are in excellent agreement with each other and also broadly agree with the results of de Neijs *et al.* [1975]. Unfortunately, since no errors were published for the de Neijs *et al.* [1975] results, it is difficult to quantify the level of agreement.

	Partial Reactions		Branching Ratios (%)		
Transition	singles	coincidence	singles	coincidence	de Neijs *et al.* [1975]
R $\rightarrow$ 0	$14.25(7) \times 10^6$	$13.88(9) \times 10^6$	94.4(2)	94.5(2)	95
R $\rightarrow$ 1266	$2.7(2) \times 10^5$	$2.7(3) \times 10^5$	1.79(13)	1.85(18)	1.4
R $\rightarrow$ 3134	$9.9(8) \times 10^4$	$7.8(10) \times 10^4$	0.65(6)	0.53(7)	0.6
R $\rightarrow$ 3506	$8.0(8) \times 10^4$	$6.9(9) \times 10^4$	0.53(5)	0.47(6)	0.5
R $\rightarrow$ 5015	$3.96(9) \times 10^4$	$3.86(10) \times 10^4$	2.63(6)	2.63(7)	2.5
N_{Total}[a]	$15.10(7) \times 10^6$	$14.69(10) \times 10^6$			

[a] For future calculations, we use the weighted average of these two results: $N_{Total^{avg}} = 14.93(10) \times 10^6$. Note that the larger uncertainty has been adopted.

Table 7.3: The calculated partial reaction values and branching ratios for the singles and coincidence analysis of the $E_r^{lab} = 620$ keV data. The total number of reactions, N_{Total}, is also shown. Branching ratios from de Neijs *et al.* [1975] are included for comparison.

7.1.3: Resonance Energy

The energies of the primary transition full-energy peaks afford the opportunity to measure the resonance energy. According to Iliadis [2015], the γ-ray energy associated with the deexcitation following a resonance reaction is given by:

$$E_\gamma = \frac{Q(m_a c^2 + m_A c^2 + m_B c^2)/2 + m_A c^2 E_a}{m_a c^2 + m_A^2 c^2 + E_a - \cos\theta \sqrt{E_a(2 m_a c^2 + E_a)}} \quad , \tag{7.1}$$

where the subscripts, a, A, and B, refer to the proton, and the ^{30}Si and ^{31}P nuclei, respectively, and E_a is the lab-frame energy of the incoming proton. This expression takes into account the Doppler shift of the observed γ-ray as well as the energy loss due to the recoiling ^{31}P atom. Here, Q refers to the energy liberated from the decay of the compound state, ^{30}Si + p, to the bound-states involved in the decay. For example, for the decay to the $E_x = 1266.33$ keV level, the parameter Q is given by the Q-value of the ^{30}Si(p,γ)^{31}P reaction, 7296.55 ± 0.02 keV [Ouellet and Singh, 2013], minus the state energy, E_x.

For the primary transitions listed in Table 7.2, Equation 7.1 was used to calculate the lab-frame proton energy. For the $\cos\theta$ term, which incorporates the geometry of the detector system, the 1st-order peak attenuation coefficient, $Q_1^p \equiv \cos\theta_{mean}$, was interpolated from Table B.1. The average laboratory frame proton energy was found to be $E_r^{lab} = 620.2 \pm 0.3$ keV. This value is in agreement with and improves upon the measurement of Kuperus *et al.* [1959], $E_r^{lab} = 619.6 \pm 1.2$ keV.

Section 7.2: 498 keV Resonance

The resonance at $E_p^{lab} = 498.3 \pm 1.0$ keV [Kuperus *et al.*, 1959] has appeared in several studies, though measurements of the resonance strength are quite limited. The first reported direct measurement appears in Endt and Van der Leun [1967] and is attributed to Hoogenboom [1958], an unpublished dissertation experiment performed at Utrecht University. The only other (p,γ) measurement was by Riihonen *et al.* [1979]. Unfortunately, very few details of their work at $E_r = 498$ keV are given in the text, with the only reference being the reported strength value appearing in a table. Based on the abstract, it can be surmised that this was an absolute measurement. Perhaps owing to their lack of detail, little regard for their reported $\omega\gamma$ value can be found outside of the paper. In the most recent evaluation by Ouellet and Singh [2013], it is not taken into consideration, and the much older value reported by Hoogenboom [1958] is suggested instead for the $E_r = 498$ keV resonance strength. Those values reported by Hoogenboom [1958] and Riihonen *et al.* [1979] are shown in Table 7.4. Note that they are in conflict, differing by nearly a factor of two. A new measurement of this resonance strength could improve the situation considerably.

The spin-parity of the $E_x = 7779.3 \pm 1.0$ keV compound state has been determined through the angular correlation work of Broude *et al.* [1958b]. In that study, the anisotropy of the ground-state

Ref.	$\omega\gamma$ (eV)
Hoogenboom [1958]	0.086 ± 0.008
Riihonen *et al.* [1979]	0.165 ± 0.025

Table 7.4: The literature values for the $E_r^{lab} = 498$ keV resonance strength.

transition γ-ray was measured and found to be consistent with $J^\pi = \frac{3}{2}^-$. This has been upheld by further angular correlation measurements [Riihonen *et al.*, 1979] and also proton-transfer reaction studies [Vernotte *et al.*, 1990]. This has important consequences for the analysis of measured pulse height spectra, which will be explained shortly.

7.2.1: Measurement

The $E_r^{lab} = 498$ keV yield was measured using the same experimental setup described in Section 7.1.1. Since the resonance is relatively strong ($\omega\gamma \approx$ eV), an excitation function was measured over the implanted target layer. The energy of the incident proton beam was increased from 498 to 516 keV in 1-keV increments. A pulse height spectrum was recorded at each step using the $\gamma\gamma$-coincidence spectrometer. At $E_r^{lab} = 503$ keV, corresponding to the maximum yield, a longer, higher-statistics run was taken so that the deexcitation branching ratios could be measured precisely. The total incident charge for the high-statistics run was 40027 μC, accumulated over 3168 seconds, yielding an average proton beam current of 12.6 μA. At the other energies, an average of 1900 μC was accumulated. An off-resonance run (0.5 C) was also taken at $E_p^{lab} = 495$ keV to aid in the identification of contaminant peaks. The yield curve is shown in Figure 7.5, where the net intensity of the primary transition, R $\rightarrow$ 1266, per incident μC is plotted as a function of the proton energy. In Table 7.5, the results of a Bayesian yield curve analysis are given. The deduced full-width at half-maximum of the beam-width is consistent with the results obtained via yield curve analysis in Section 6.2, as is the straggling constant. As predicted, the target layer appears thicker (in keV) due to the effects of the increased stopping power at lower proton energies. The observed total area under the yield curve will be of importance in Section 7.2.4.

The singles and coincidence mode pulse-height spectra collected at the maximum yield are shown in Figure 7.6. The gating and timing conditions used in the previous section were applied to this

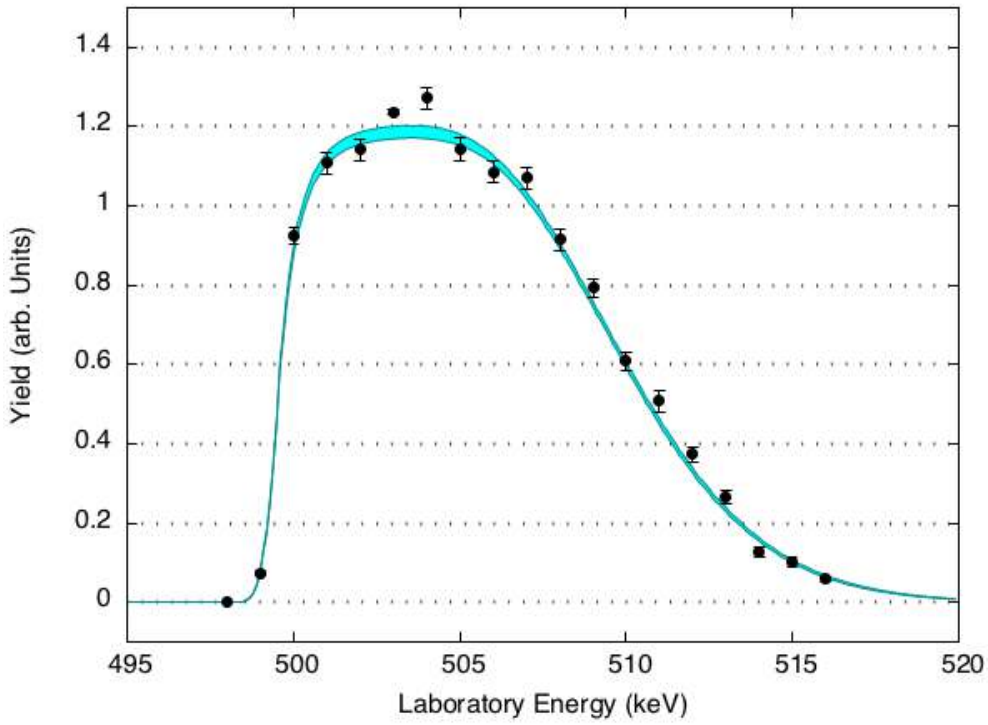

Figure 7.5: An excitation function over the $E_r^{lab} = 498$ keV resonance in the ^{30}Si(p,γ)^{31}P reaction. The net intensity of the R $\rightarrow$ 1266 transition γ-ray per incident μC of proton beam is shown. The cyan curve represents the 68% credibility interval, as determined by a Bayesian analysis.

data as well. In addition to those reported in de Neijs *et al.* [1975], several new primary transitions were observed in the present experiment. These transitions proceed from the compound state at $E_x = 7779$ keV to the bound states at $E_x = 5116$, 6496, and 6594 keV. Since their full-energy peaks are found in a region of the pulse-height spectrum shared by environmental and beam-induced background, it is altogether reasonable that they escaped detection in de Neijs *et al.* [1975].

The intensities of the measured primary transitions for the singles and coincidence spectra are

Yield Parameter	16%	50%	84%	Units
Beam-width FWHM	0.937	0.954	0.982	keV
Thickness	10.16	10.24	10.32	keV
Straggling Constant	2.51	2.62	2.74	keV$^{1/2}$
Maximum Yield	1.20	1.24	1.28	counts μC^{-1}
Area	12.33	12.72	13.11	counts keV μC^{-1}

Table 7.5: Results of the Bayesian analysis for the $E_r^{lab} = 498$ keV excitation function. The 16$^{\text{th}}$, 50$^{\text{th}}$ and 84$^{\text{th}}$ percentiles of the posterior distributions are shown for each parameter.

shown in Table 7.6.

Transition	$2J_f^\pi$	Intensity (counts)		
		E_γ (MeV)	singles	coincidence
R → 0	1^+	7786.8(12)	48400(200)	—
R → 1266	3^+	6520.2(10)	45600(300)	27600(200)
R → 2233	5^+	5552.8(8)	7290(150)	5270(160)
R → 3134	1^+	4652.6(7)	13800(200)	8750(160)
R → 3295	5^+	4492.0(7)	1100(100)	900(80)
R → 4260	3^+	3521.8(6)	1750(100)	1300(80)
R → 4783	5^+	2998.5(5)	6000(100)	4400(100)
R → 5014.9	$(3)^+$	2767.7(5)	6530(120)	5000(100)
R → 5116[a]	5^+	2665.4(5)	900(100)	800(100)
R → 6496[a]	3^-	1284.9(5)	2480(120)	1560(90)
R → 6594[a]	5^-	1186.5(5)	1350(120)	860(90)

[a] First observation.

Table 7.6: The observed $E_r^{lab} = 498$ keV resonance primary transitions and their full-energy peak energies and net intensities in the singles and coincidence spectra. The total incident charge was 40027 μC, collected at $E_p^{lab} = 503$ keV. The spin-parity of the final states are also shown. All transitions were also reported in de Neijs *et al.* [1975], unless noted.

7.2.2: Analysis

The determination of branching ratios based on the pulse-height spectra is complicated by the spin-parity of the 498-keV resonance. Because of the widely accepted value of $\frac{3}{2}^-$, there is a strong alignment of the deexciting ^{31}P nucleus following the (p,γ) reaction, which produces anisotropic radiation patterns. Since the HPGe crystal subtends only a fraction of the solid angle, the net intensity of each primary transition full-energy peak must be corrected based on the spins of the initial and final levels involved in the decay as well as the angular momentum of the emitted photon.

A treatment of angular correlations and their relevance to nuclear astrophysics experiments can be found in Iliadis [2015]. In general, for the decay of a compound state following proton capture, the angular distribution of a deexcitation γ-ray is given by:

$$W(\theta) = 1 + a_2 P_2(\cos\theta) + a_4 P_4(\cos\theta) + ... \tag{7.2}$$

where θ is the emission angle relative to the beam direction, and the P_n are the nth-order Legendre polynomials. The coefficients, a_n, are determined either from theoretical calculations or measure-

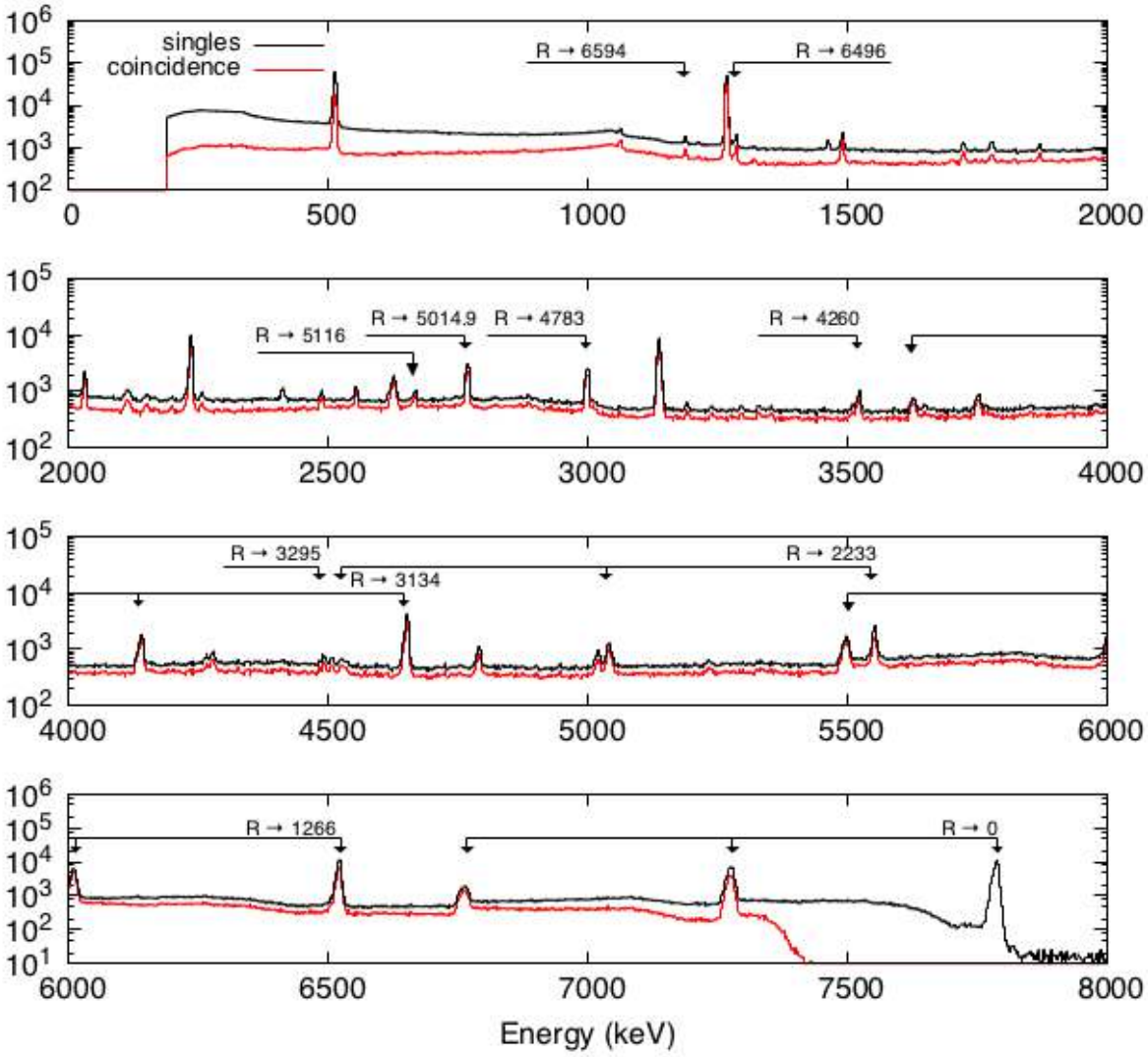

Figure 7.6: Pulse-height spectrum taken at the $E_r^{lab} = 498$ keV resonance using the $\gamma\gamma$-coincidence spectrometer. Full-energy peaks corresponding to primary transitions from the 7779-keV compound state, here denoted "R", are shown along with their escape peaks where applicable. Both the singles (black line) and coincidence (red line) spectra are shown.

ment in a laboratory. When a resonance is populated through a unique orbital angular momentum value, i.e., s-wave or p-wave, and can decay through only one possible photon multipolarity value, L, then $W(\theta)$ can be computed exactly. Otherwise, mixing in both channels must be accounted for to accurately describe the emission patterns. In the case of the 498-keV resonance, conservation of angular momentum and parity demands that the compound state can only be populated by p-wave (ℓ_p=1) protons. Regarding the possible values of the γ-ray multipolarity, for the decay from a spin-$\frac{3}{2}$ state to a spin-$\frac{1}{2}$, $\frac{3}{2}$ or $\frac{5}{2}$ state, several L values are allowed. In each case, the two lowest (and most important) L values are $L = 1$ and 2. The γ-ray multipolarity mixing ratio, δ_γ, defined by the relation $\delta_\gamma^2 = \Gamma_{\gamma 2}/\Gamma_{\gamma 1}$, would ordinarily need to be measured for each transition from the 7779-keV compound state to fully describe $W(\theta)$. These values, especially for low-energy resonances, are scarcely known. Fortunately, the situation is made much better by considering that all but two of the observed transitions from the compound state proceeds to a bound state with parity $\pi = +1$. Conservation of parity implies then that the $L = 1$ radiation is of electric-dipole character (E1) while the $L = 2$ component is of magnetic-quadrupole character (M2). Mixtures of E1/M2 are frequently unimportant, since E1 radiation dominates [Iliadis, 2015]. Therefore, for the present analysis, $\delta_\gamma^2 = 0$ for these primary transitions, allowing for an exact calculation of their angular correlation distribution, $W(\theta)$. The other two decays, R$\rightarrow$ 6496 and R$\rightarrow$ 6594, proceed through M1/E2 radiation. Since their mixing ratio is unknown, we are forced to assume $\delta_\gamma^2 = 0$ for these transitions. These are very weak transitions, though, so their overall effect on the analysis promises to be minimal.

For the analysis of the pulse-height spectra in Figure 7.6, the templates were simulated by sampling the photon emission angles for each primary transition from their respective $W(\theta)$ function. The calculated a_2 coefficients are shown in Table 7.7 below. The available experimental data is also shown for comparison. Although Riihonen *et al.* [1979] and Rinsvelt and Endt [1966] only studied the angular correlation for the R $\rightarrow$ 3134 transition (final $2J^\pi = 1^+$), their work suggests that the electric-dipole approximation is sound, since the multipolarity mixing ratio, δ_γ, must be close to zero to account for the observed anisotropy. Higher order contributions, i.e., a_4, are zero for this particular resonance reaction. This has been confirmed experimentally by Riihonen *et al.* [1979] ($a_4 = 0.00 \pm 0.02$) and Rinsvelt and Endt [1966] ($a_4 = -0.01 \pm 0.01$). Secondary transitions from the $2J^\pi = 3^+, 5^+$ bound states in ^{31}P will, in general, also be emitted in an anisotropic distribution

that depends on the manner in which they were populated. However, the fit is limited only to regions surrounding the primary transition full-energy peaks and certain background peaks, so the secondary transition intensities only influence the coincidence spectrum through their interaction with the NaI(Tl) annulus. Since the annulus covers nearly a solid angle of 4π, and thus effectively integrates over the largest part of the angular correlation function, the overall effect of the anisotropy is reduced significantly. Therefore, we assumed in the simulations that photons from the decay of all bound states are emitted isotropically.

final $2J^\pi$	a_2	Riihonen *et al.* [1979]	Rinsvelt and Endt [1966]
1^+	-0.5	-0.49 ± 0.03	-0.39 ± 0.01
3^+	0.4		
5^+	-0.1		
3^-	0.4		
5^-	-0.1		

Table 7.7: Calculated and measured angular correlation coefficients for the decay from the $E_r^{lab} = 498$ keV resonance ($E_x = 7779$ keV) to several $\pi = +1$ bound states. No contribution from the M2 or E2 channel is assumed. Measurements of the R$\rightarrow$ 3134 transition angular correlation a_2 coefficient are included for comparison.

Templates were also used for the environmental and beam-induced background, since several primary transition full-energy peaks lie in their Compton continuum. For the environmental background (e.g., ^{40}K, ^{208}Tl), the template was simply a background run, taken with the detector system in the run geometry with no beam on target. A full-energy peak belonging to the ^{12}C(p,γ)^{13}N reaction was observed at $E_\gamma = 2400$ keV. A template was generated for this peak using the `LENAGe` program, which assumed isotropic emission of a mono-energetic γ-ray.

The joint posterior distributions for the singles and coincidence data sets were sampled using the same number of iterations, burn-in, and thinning parameters as in the previous section. As before, the fit was limited to regions surrounding the primary transition full-energy peaks. Also included in the singles mode analysis were the ^{40}K peak at 1461 keV and the ^{12}C(p,γ)^{13}N peak mentioned above. The fitted spectra are shown in Figures 7.7 and 7.8 for singles mode, and Figures 7.9 and 7.10 for coincidence mode. Each of the primary transition full-energy peaks identified in Table 7.6 are compared with the 95% credibility region (cyan), with their fit regions indicated by the vertical dashed lines. In general, the credibility region is in good agreement with the observed spectra, with

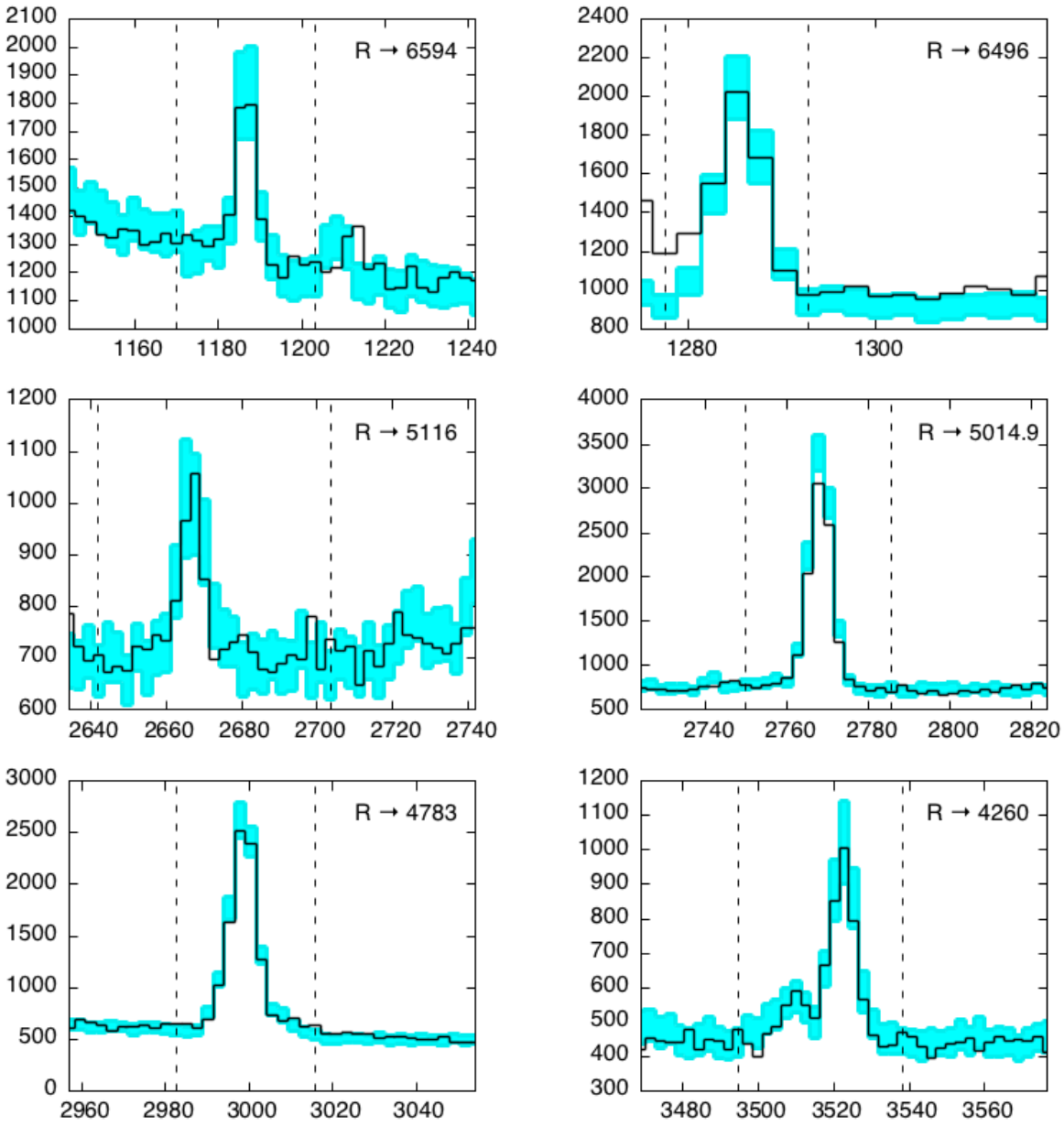

Figure 7.7: Plots of the simulated posterior histograms for the $E_r^{lab} = 498$ keV resonance singles analysis for each of the primary transition photopeaks. The cyan histogram corresponds to the 95% credibility region, while the black line represents the pulse-height spectrum of the observed data. The vertical dashed lines denote the fit region used for each peak.

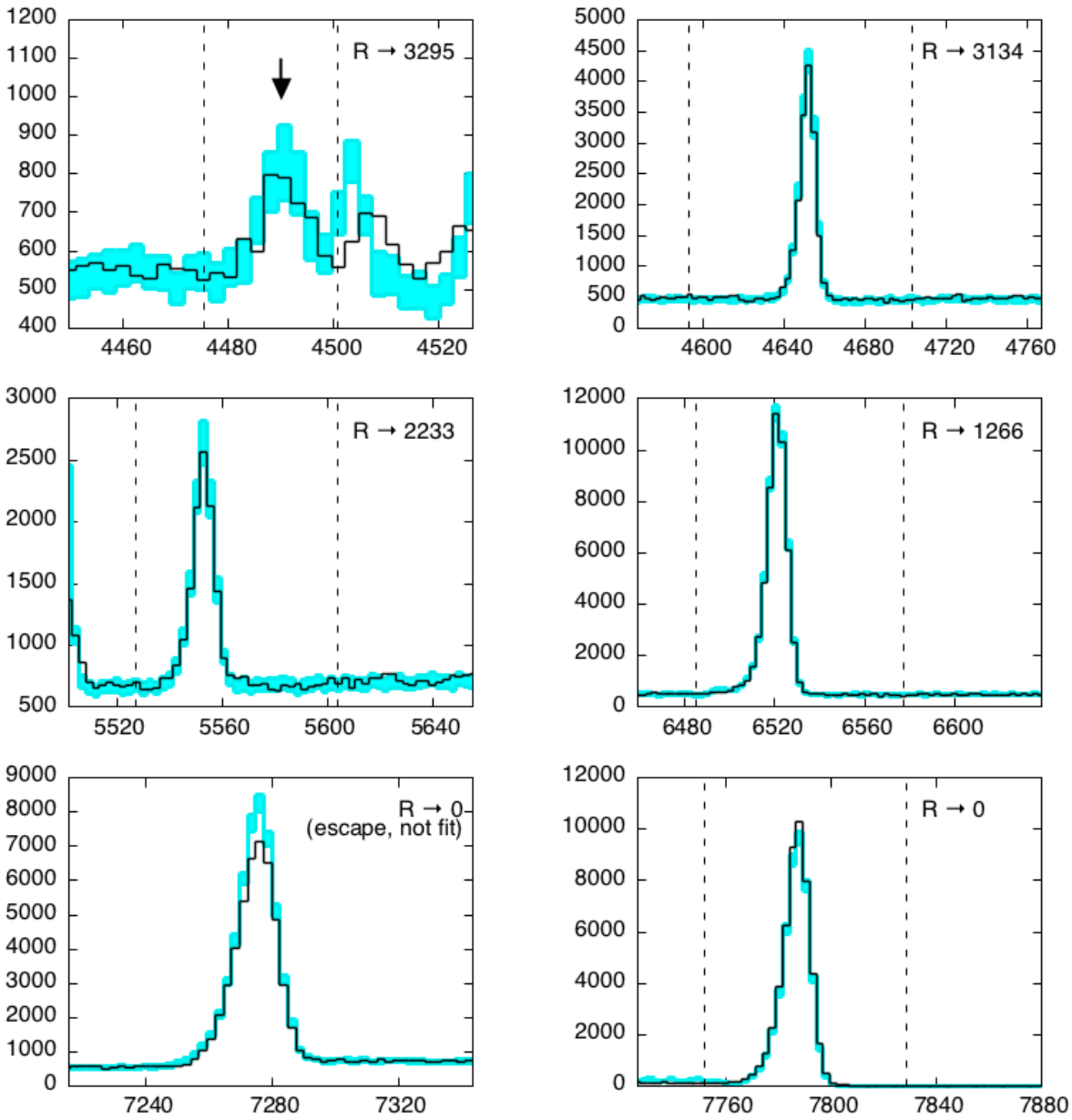

Figure 7.8: Plots of the simulated posterior histograms for the $E_r^{lab} = 498$ keV resonance singles analysis (continued) for each of the primary transition photopeaks. The cyan histogram corresponds to the 95% credibility region, while the black line represents the pulse-height spectrum of the observed data. The vertical dashed lines denote the fit region used for each peak. The arrow in the upper left panel indicates the full-energy peak corresponding to the R→3295 transition. The escape peak for the R→ 0 transition, although not included in the fit, is shown in the lower left panel.

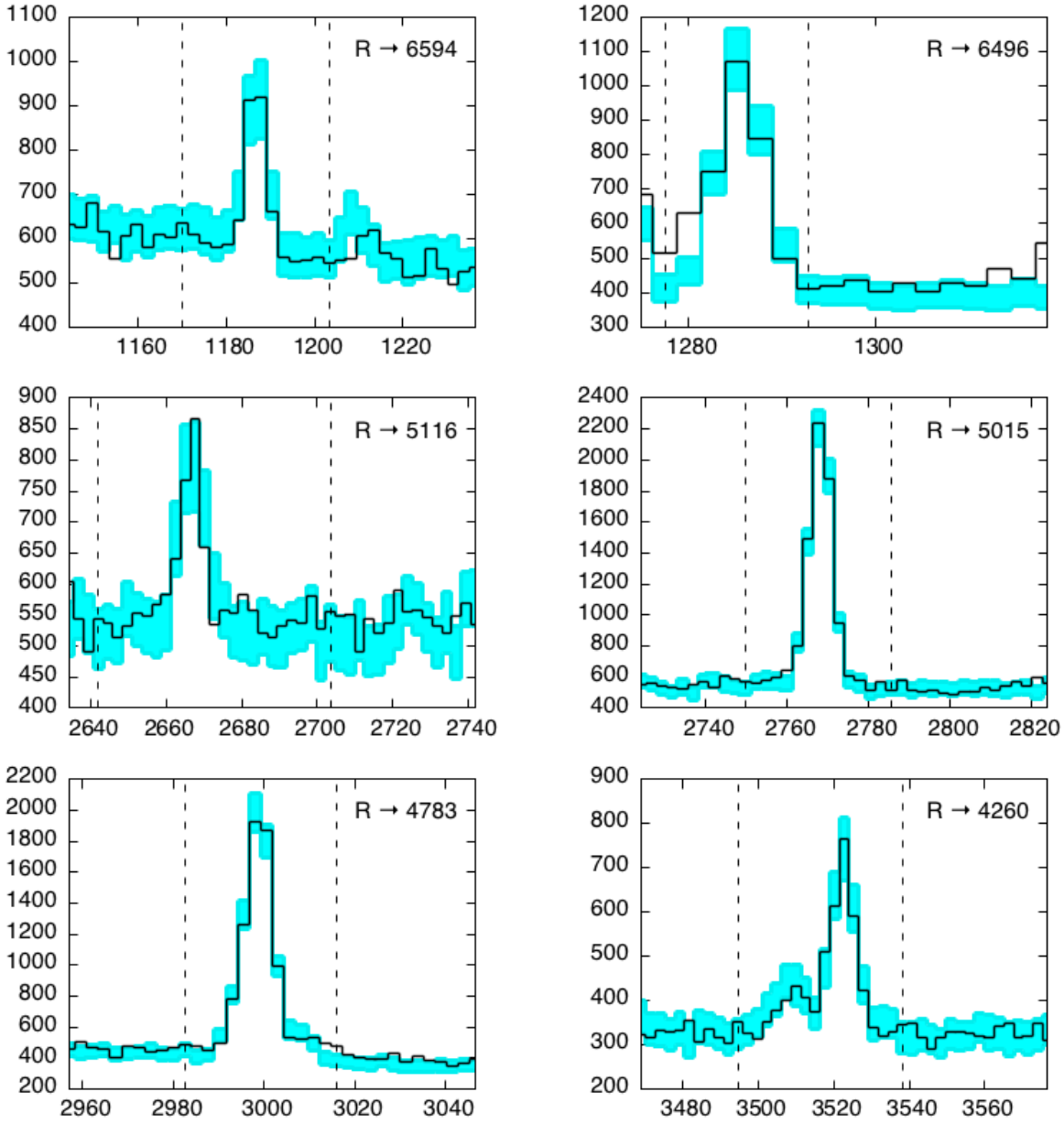

Figure 7.9: Plots of the simulated posterior histograms for the $E_r^{lab} = 498$ keV resonance coincidence analysis for each of the primary transition photopeaks. The cyan histogram corresponds to the 95% credibility region, while the black line represents the pulse-height spectrum of the observed data. The vertical dashed lines denote the fit region used for each peak.

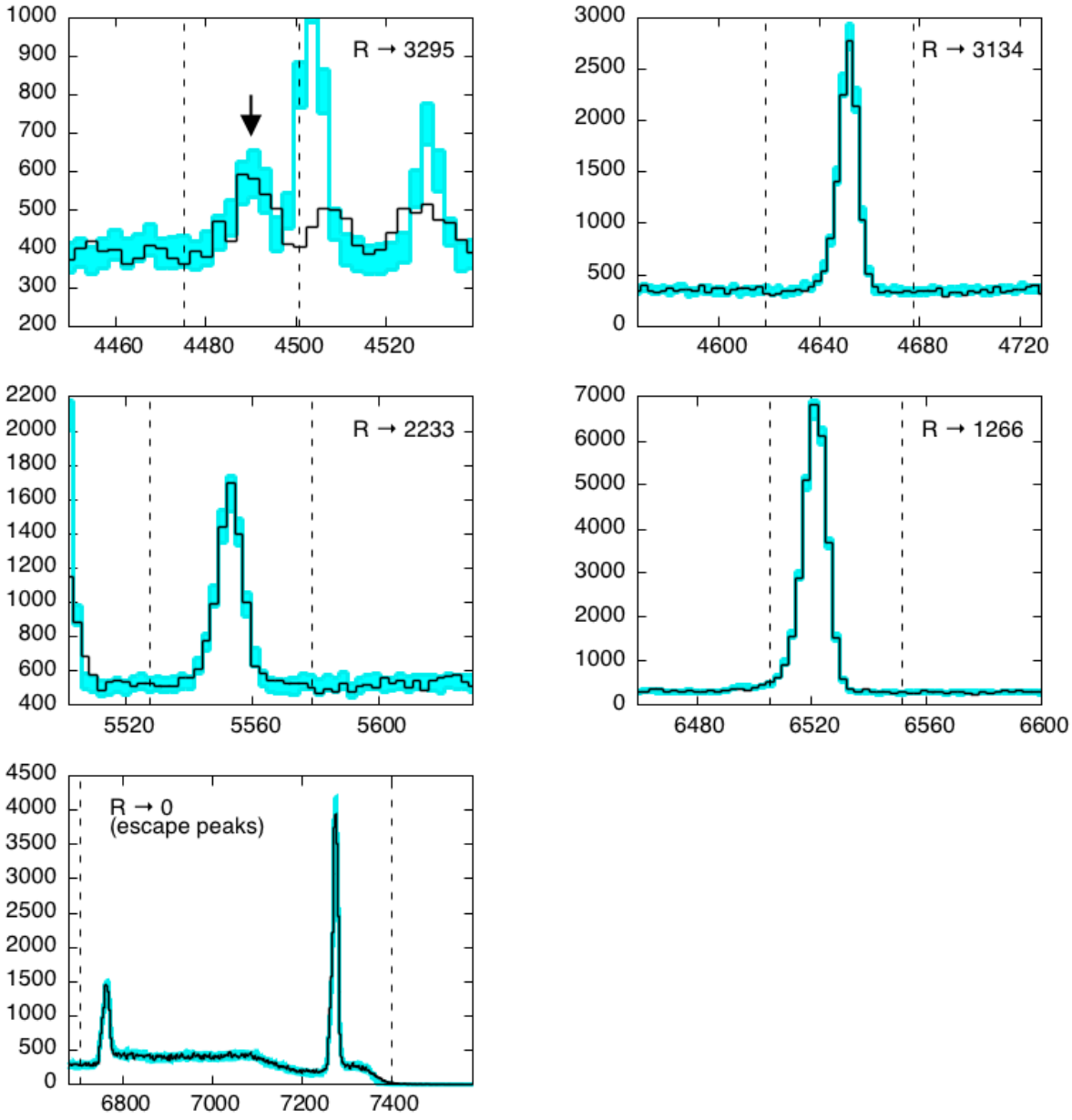

Figure 7.10: Plots of the simulated posterior histograms for the $E_r^{lab} = 498$ keV resonance coincidence analysis (continued) for each of the primary transition photopeaks. The cyan histogram corresponds to the 95% credibility region, while the black line represents the pulse-height spectrum of the observed data. The vertical dashed lines denote the fit region used for each peak. The arrow in the upper left panel indicates the full-energy peak corresponding to the R→3295 transition.

both analyses passing the run test with Z-values of -2.0 and -2.1, for the singles and coincidence case, respectively. However, a few minor issues are worth addressing. For the fit of the R$\rightarrow$ 3295 full-energy peak, there is a predicted excess in counts to the right of the primary (denoted with an arrow). This is the single escape peak for the 5014.9 $\rightarrow$ 0 secondary transition. The over-prediction may be evidence that the branching ratios for the decay of this bound state are erroneous, which is altogether reasonable since it is a member of a poorly resolved doublet, or it could indicate that the angular correlation for the 5014.9 $\rightarrow$ 0 decay is far from isotropic. Regardless, this peak is outside of the fitting region, so it does not affect the branching ratio or yield calculations. Finally, the single-escape peak for the R$\rightarrow$ 0 transition is shown in Figure 7.8 for the singles analysis. Although these bins were omitted from the fit, the peak intensity is over-predicted substantially, suggesting that it ultimately may be a poor indicator of the R $\rightarrow$ 0 transition for the coincidence analysis. This point will be addressed shortly.

The partial reaction numbers for each transition and their branching ratios are shown below in Table 7.8. For comparison, the branching ratios measured in de Neijs *et al.* [1975] are included. With the exception of the R$\rightarrow$ 0 and R$\rightarrow$ 5014.9 transitions, there is good agreement between the singles and coincidence partial reaction numbers. Regarding the R$\rightarrow$ 0 (ground-state) transition, there is a discrepancy between the singles and coincidence results, amounting to an 8% difference. A similar effect was also observed in the analysis of the 620-keV spectra, but to a much lesser extent (2.6%). As noted above, there appear to be inconsistencies for this peak between the simulated and observed data in the singles spectrum fit comparison, suggesting that the discrepancy is not inherent to coincidence gating or errors in the simulated NaI(Tl) detector response. Instead, it seems that the simulated spectra over-predict the intensity of the escape peak. While this is still explicable through systematic error, that the ground-state transitions appear especially prone to this deserves further research.

For the R$\rightarrow$5014.9 transition, the coincidence result for the partial reaction number is 40% higher than that of the singles analysis. The most likely cause of this discrepancy is a under-prediction of the coincidence efficiency, which could be due to incorrect branching ratios for the 5014.9-keV bound state. Since this scenario helped to explain the 5014.9 $\rightarrow$ 0 mismatch mentioned before, a better understanding of the decay of the 5014.9-keV bound state would be helpful. Finally, the total number of reactions, N_{total}, calculated from the two analyses are not in agreement, with a

percent error of 2.7%. The discrepancy appears to be predominately due to the problems associated with the coincidence R $\rightarrow$ 0 value.

The branching ratios for both the singles and coincidence case are consistent with those of de Neijs *et al.* [1975], though again the lack of uncertainties on their results preclude a more qualitative assessment. This is unfortunate, as a proper measurement of the R$\rightarrow$0 transition branching ratio might provide some insight into the nature of the observed discrepancy. In the following resonance strength analysis, the average of the singles and coincidence results will be used.

	Partial Reactions		Branching Ratios (%)		
Transition	singles	coincidence	singles	coincidence	de Neijs *et al.* [1975]
R $\rightarrow$ 0	$7.59(9) \times 10^6$	$7.00(4) \times 10^6$	50.2(4)	47.5(2)	52
R $\rightarrow$ 1266	$4.06(5) \times 10^6$	$4.17(4) \times 10^6$	26.8(3)	28.3(2)	27
R $\rightarrow$ 2233	$7.3(3) \times 10^5$	$6.9(2) \times 10^5$	4.8(2)	4.7(2)	5.0
R $\rightarrow$ 3134	$1.57(3) \times 10^6$	$1.56(3) \times 10^6$	10.4(2)	10.6(2)	11
R $\rightarrow$ 3295	$1.19(15) \times 10^5$	$9.3(10) \times 10^4$	0.8(1)	0.6(1)	0.6
R $\rightarrow$ 4260	$9.2(7) \times 10^4$	$9.5(5) \times 10^4$	0.6(1)	0.6(1)	0.5
R $\rightarrow$ 4783	$4.1(15) \times 10^5$	$4.0(10) \times 10^5$	2.7(1)	2.7(1)	2.3
R $\rightarrow$ 5014.9	$3.6(1) \times 10^5$	$5.0(1) \times 10^5$	2.4(1)	3.4(1)	1.6
R $\rightarrow$ 5116	$7.0(10) \times 10^4$	$7.6(7) \times 10^4$	0.5(1)	0.5(1)	—
R $\rightarrow$ 6496	$7.3(5) \times 10^4$	$7.9(4) \times 10^4$	0.5(1)	0.5(1)	—
R $\rightarrow$ 6594	$6.2(7) \times 10^4$	$5.3(5) \times 10^4$	0.4(1)	0.4(1)	—
N_{Total}[a]	$1.51(1) \times 10^7$	$1.47(6) \times 10^7$			

[a] For future calculations, we use the weighted average of these two results: $N_{Total^{avg}} = 1.50(6) \times 10^7$. Note that the larger uncertainty has been adopted.

Table 7.8: The calculated partial reaction values and branching ratios for the singles and coincidence analysis of the $E_r^{lab} = 498$ keV data. The total number of reactions, N_{Total}, is also shown. Branching ratios from de Neijs *et al.* [1975] are included for comparison.

7.2.3: Resonance Energy

The energies of the observed primary transition full-energy peaks were used to derive the laboratory frame resonance energy using the same procedure described in Section 7.1.1. Based on the measured energies listed in Table 7.6, the laboratory frame resonance energy is found to be $E_r^{lab} = 499.5 \pm 0.2$ keV. This is an improvement upon the previous measurement by Kuperus *et al.* [1959], $E_p^{lab} = 498.3 \pm 1.0$ keV.

7.2.4: Resonance Strength

Armed now with the yield excitation functions of the 498-keV and 620-keV resonances, as well as the branching ratios and total reaction intensities from the analysis, we are in a position to calculate the resonance strength, $\omega\gamma$, of the 498-keV resonance relative to the 620-keV resonance. We begin by stating Equation 4.129 from Iliadis [2015]:

$$\frac{\omega\gamma_{498}}{\omega\gamma_{620}} = \frac{\lambda_{620}^2}{\lambda_{498}^2}\frac{(B\eta W)_{620}}{(B\eta W)_{498}}\frac{A_{Y,498}}{A_{Y,620}}, \tag{7.3}$$

where $A_{Y,i}$ is the integrated yield for each resonance and the λ_i^2 are the deBroglie wavelengths for the incident proton. This expression relates the two resonance strengths, independent of the stoichiometry or effective stopping power. The quantity $(B\eta W)_i$ is the factor converting the detected full-energy peak intensity to the total number of reactions, where B is the branching ratio for that transition, η is the detection efficiency, and W accounts for angular correlations, if present. The fraction-fitting formalism provides a nice measurement of this quantity. The ratio $(I_{R\rightarrow E_x}/N_{\text{total}})$, where $I_{R\rightarrow E_x}$ is the full-energy peak intensity observed in the higher statistics run, and N_{total} is the calculated total reaction intensity, contains all of this information. Further, any coincidence-summing effects present in the observed peaks (either summing-in or summing-out) are explicity corrected for in this ratio. Using Tables 7.6 and 7.8, the corrective factor $(B\eta W)$ for the 498-keV yield can be calculated:

$$(B\eta W)_{498} = \frac{\mathrm{I_{R\rightarrow 1266}}}{\mathrm{N_{total,498}}} = \frac{45600 \pm 300}{(1.50 \pm 0.06)\times 10^7} = 0.0030 \pm 0.0001 \quad . \tag{7.4}$$

Drawing from Tables 7.2 and 7.3 for the 620-keV term:

$$(B\eta W)_{620} = \frac{\mathrm{I_{R\rightarrow 0}}}{\mathrm{N_{total,620}}} = \frac{126600 \pm 400}{(14.93 \pm 0.10)\times 10^6} = 0.00858 \pm 0.00006 \quad . \tag{7.5}$$

Using the yield curve areas from Tables 6.1 and 7.5, and assuming 499.5 ± 0.2 keV and 620.2 ± 0.3 keV for the laboratory frame resonance energies:

$$\omega\gamma_{498} = 0.188 \pm 0.014 \quad \text{eV} \ , \tag{7.6}$$

where the adopted-value of the standard resonance, $\omega\gamma_{620} = 1.95 \pm 0.10$ eV, has been used. This new resonance strength value is compared to previous measurements and calculations in Figure 7.11. It is in conflict with the original measurement by Hoogenboom [1958], while being consistent with the Riihonen *et al.* [1979] value. Both of these are absolute measurements performed using the ^{30}Si(p,γ)^{31}P reaction. The Iliadis *et al.* [2010a] value is based on the recommended resonance strength by Endt [1990], which is a weighted average of the previous measurements. It was used to evaluate the ^{30}Si(p,γ)^{31}P thermonuclear reaction rate for the STARLIB library [Sallaska *et al.*, 2013]. It is included in Figure 7.11 to illustrate the effect that the new measurement will have on the nuclear physics input for the reaction rate. Based on the nearly factor of two increase over this value, the contribution of the 498 keV resonance to the rate is expected to double. In Chapter 8, the ^{30}Si(p,γ)^{31}P reaction rate is re-evaluated and the full impact of the new measurement will be explored.

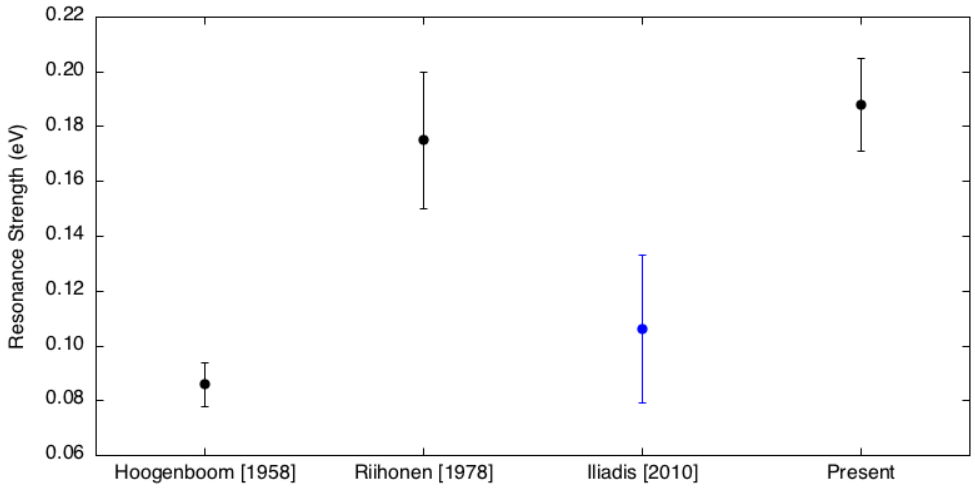

Figure 7.11: A comparison of the present value for the 498-keV resonance strength, $\omega\gamma$, with previous measurements (black) and a previously suggested value (blue). Note that Hoogenboom [1958] and Riihonen *et al.* [1979] are absolute measurements. The Iliadis *et al.* [2010a] value, which was used as nuclear physics input for the STARLIB reaction rate library, is based on a recommendation in Endt [1990].

Section 7.3: 435-keV Resonance

The last resonance presents the most difficult analysis. Unlike the 620-keV and 498-keV resonances, which had a well known spin-parity as well as deexcitation branching ratios, little is known

about the resonance at $E_p^{lab} = 435 \pm 4$ keV [Vernotte *et al.*, 1990]. All observations of this state have so far been limited to indirect-reaction studies. The first evidence of its existence is credited to Betigeri *et al.* [1966]. In that work, the scattered deuterons from the ^{30}Si(^{3}He,d)^{31}P stripping reaction were observed through a split-pole magnetic spectrograph. Based on their measured energy spectrum, they reported a bound-state at $E_x = 7720 \pm 15$ keV in the ^{31}P nucleus. Although they declined to make a spin-parity designation, they note that the deuteron angular distribution implies $\ell_p = 2$ proton transfer, which is consistent with $J^\pi = (\frac{3}{2}, \frac{5}{2})^+$.

Later, using the ^{29}Si(^{3}He,p)^{31}P reaction, Moss [1969] observed a bound-state at $E_x = 7718 \pm 9$ keV. Further work using ^{29}Si(^{3}He,p)^{31}P by Al-Jadir *et al.* [1980] provided a few more clues as to the spin of the state, which they reported at $E_x = 7713$ keV. Based on the angular distribution of protons through a split-pole spectrometer, Al-Jadir *et al.* [1980] used the Distorted Wave Born Approximation (DWBA) to characterize the deuterium spin transfer for this excited state. Their analysis suggested that spin $\ell_d = 0 + 2$ transfer was the most likely but that $\ell_d = 1 + 3$ could not be excluded. They argued further that pure $\ell_d = 0$ is not likely, excluding $J^\pi = \frac{1}{2}^-$ from consideration. Based on the suggestion of $\ell_d = 0 + 2$ or $\ell_d = 1 + 3$ transfer, they recommended $J^\pi = \frac{1}{2}^+, \frac{3}{2}^\pm$ and $\frac{5}{2}^-$ as plausible spin-parity values. Most recently, this state was observed by Vernotte *et al.* [1990] using the ^{30}Si(^{3}He,d)^{31}P reaction. They reported the most precise excitation energy so far, $E_x = 7718 \pm 4$ keV. Unfortunately, no spin-parity arguments can be made given their data.

If the spin-parity suggestions from the above experiments are each taken to be credible, then the only value consistent with all observations is $J^\pi = \frac{3}{2}^+$. Unfortunately, as was seen in the analysis of the 498-keV resonance, the angular correlations for the deexcitation γ-rays, which affect the full-energy photopeak intensities, are determined solely by this value. If in fact the spin-parity is assigned in error, then the measured resonance strength, $\omega\gamma$, will be in error accordingly. For the present analysis, a resonance strength is calculated which takes into account the uncertainty in the spin-parity for this state.

7.3.1: Measurement

Unlike the previous resonance experiments, a yield excitation curve over the 435-keV resonance is not the most effective way to carry out a relative measurement. The problems lies in the amount of beam-time required to measure the yield at each of the twenty-five or so proton energies, which could span weeks given modest beam-currents. Further, the amount of charge necessary could degrade the target, resulting in a changing stoichiometry over the course of the experiment. As a last point, the carbon buildup incurred in the LENA target chamber (See Section 6.1.4) would require frequent target cleaning and downtime. Instead, the reliability of the yield curves taken at the 498-keV and 620-keV resonances supports the use of thick-target maximum yield measurement. The general idea is to obtain the yield at a single proton energy which corresponds to the maximum yield. The thickness of the target at $E_p^{lab} = 435$ keV can then be estimated using stopping power data from Ziegler *et al.* [2010], circumventing the need for a full yield curve.

The maximum yield measurement for the 435-keV resonance took place over two days. Preceding the run, the ^{30}Si target was cleaned using the method described in Section 6.1.4. Thanks to the low-levels of ^{12}C(p,γ)^{13}N direct-capture background, in combination with a high current output from the JN Van de Graaff accelerator, the experiment was completed in about one-fifth the time expected. While the $\gamma\gamma$-spectrometer was in the run geometry, 1.997 Coulomb of $E_r^{lab} = 437$ keV protons were made incident on the target face. Immediately afterwards, off-resonance data was taken with a $E_p^{lab} = 428$ keV beam to aid in the identification of beam-induced background. The average beam current on target for the maximum yield measurement was 76 μA. Detector dead-time was monitored and found to be only 1.4% over the course of the experiment.

Below, the first ever direct measurement of the 435-keV resonance spectroscopic signature is shown in Figure 7.12. The singles (black line) and coincidence mode (red line) spectra are annotated. The coincidence mode gating condition are, as before, 3.0 MeV $< E^{HPGe}+E^{NaI} <$ 9.0 MeV. Three primary transition full-energy photo peaks were observed, corresponding to the deexcitation of the 7718 ± 4 keV compound state to the 3295, 4431, and 5014.9 keV bound states. Their measured photopeak energies and intensities are shown in Table 7.9.

The identity of the deexcitation to a doublet member (i.e., R$\rightarrow$ 5014.9 versus R$\rightarrow$ 5015.2 keV) was inferred based on the secondaries, 5014.9 $\rightarrow$ 0 and 5014.9 $\rightarrow$ 1266. The relative intensity

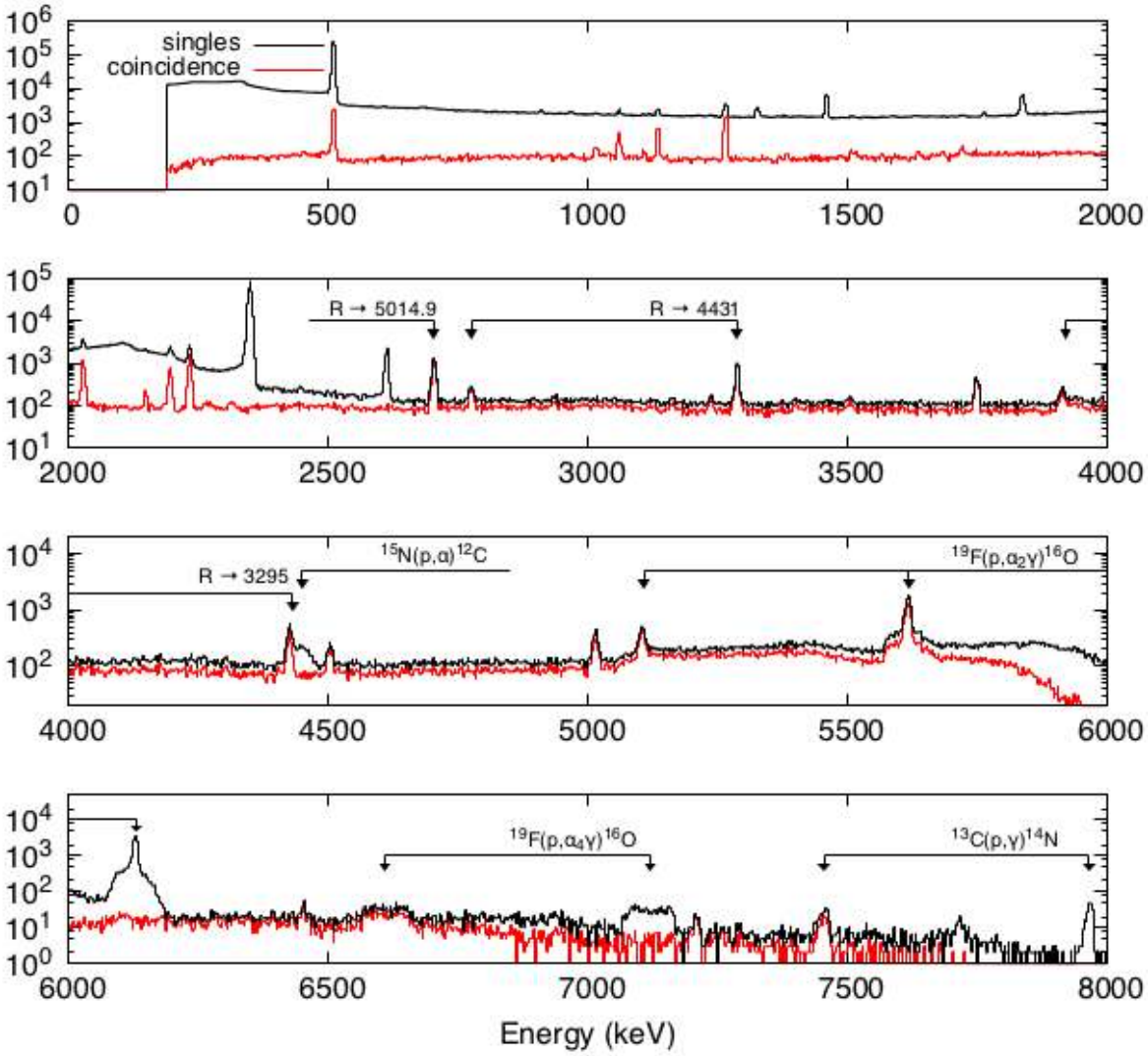

Figure 7.12: Pulse-height spectrum taken at the $E_r^{lab} = 435$ keV resonance using the $\gamma\gamma$-coincidence spectrometer. Full-energy photopeaks corresponding to primary transitions from the 7718 ± 4-keV compound state, here denoted "R", are shown along with their escape peaks where applicable. Photopeaks due to beam-induced contaminant reactions are also indicated. Both the singles (black line) and coincidence (red line) spectra are shown.

Transition	$2J_f^\pi$	E_γ (keV)	Intensity (counts) singles	coincidence
R $\rightarrow$ 3295	5^+	4425.2(7)	3590(80)[a]	2680(70)
R $\rightarrow$ 4431	7^-	3288.1(5)	2930(80)	2620(70)
R $\rightarrow$ 5014.9	$(3)^+$	2704.1(4)	1250(80)	1090(60)

[a] Intensity is based on simple background subtraction, which is heavily influenced by the contaminant ^{15}N(p,$\alpha\gamma$)^{12}C peak.

Table 7.9: Observed primary transitions and their photopeak energies and net intensities in the singles and coincidence spectra. The spin-parities of the final states are also shown.

of these two full-energy photopeaks is consistent with the branching ratios for the decay of the 5014.8-keV state published by de Neijs *et al.* [1975]. Several beam-induced reactions photopeaks are identified in Figure 7.12. In addition to the common ^{19}F(p,$\alpha_2\gamma$)^{16}O reaction photopeak at 6130 keV, a photopeak from the ^{19}F(p,$\alpha_4\gamma$)^{17}O reaction, which instead populates the short-lived ($T_{1/2}$ = 8.3 fs) ^{16}O bound state at E_x = 7116 keV, is present [Tilley *et al.*, 1998]. Owing to the prompt decay of this state and the recoil of the α-particle, the full-energy and single-escape peaks are over 40 keV wide. Additionally, peaks from the ^{15}N(p,$\alpha\gamma$)^{12}C and ^{13}C(p,γ)^{14}N reactions are present. The ^{15}N(p,$\alpha\gamma$)^{12}C peak originates from the deexcitation of the E_x = 4438 keV bound state of ^{12}C [Ajzenberg-Selove, 1990]. The broadening of this peak, which is due to the α-particle recoil energy, obscures the R$\rightarrow$ 3295 full-energy photopeak. Fortunately, since this reaction does not satisfy the coincidence gating conditions, the photopeak is absent from the coincidence spectrum. The ^{13}C(p,γ)^{14}N direct capture reaction gives rise to a single narrow photopeak at 7966 keV.

7.3.2: Resonance Energy

The most pressing question regarding the collected data is whether or not it is representative of the maximum yield. Recall that the uncertainty on the resonance energy is rather large: $\Delta E_r^{lab} = \pm 4$ keV [Vernotte *et al.*, 1990]. A measurement at E_p^{lab} = 437 keV could easily be below the resonance or somewhere on the front-edge of the yield curve, invalidating a key assumption of the analysis. Fortunately, a measurement of the resonance energy, based on the procedure in Section 7.1.3, supports the present experiment. Using the measured energies of the primary transition full-energy photopeaks in Table 7.9, the lab-frame resonance energy is found to be $E_r^{lab} = 433.5 \pm 0.3$

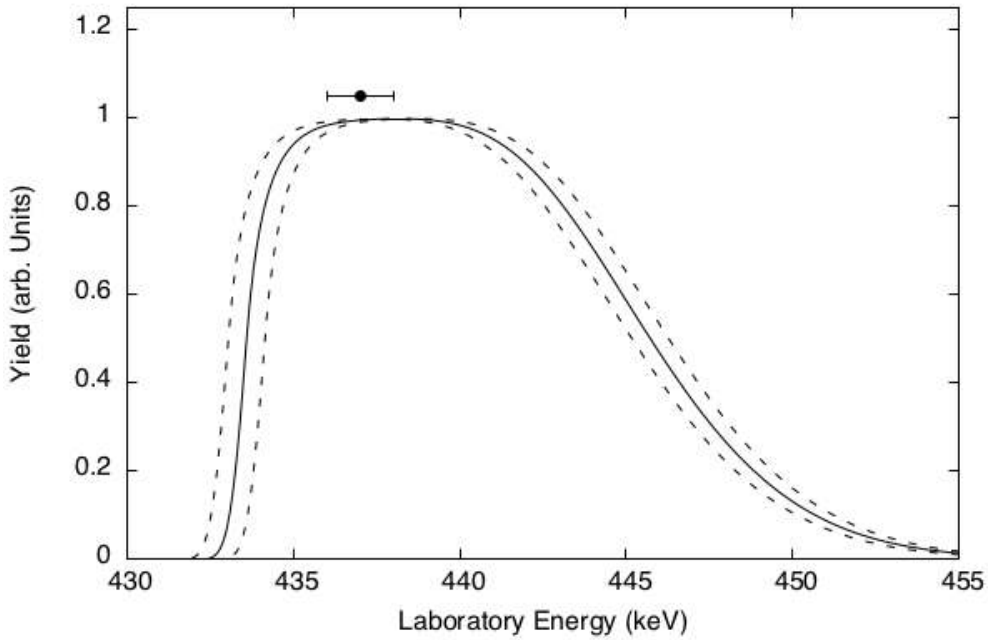

Figure 7.13: Simulated yield curves are plotted for the 435-keV resonance based on the analysis of the primary transition full-energy photopeaks. The solid line represents the mean resonance energy, $E_r^{lab} = 433.5$-keV. The dashed lines represent the 95% credibility interval, [433.0, 434.1] keV. The data point illustrates the energy of the incident beam energy, with ± 1 keV error assumed for the dipole magnet energy calibration.

keV. A set of calculated yield curves based on this interval is shown in Figure 7.13. The solid line represents the yield based on the mean E_r^{lab} calculated. The dashed lines denote the 95% credibility interval, [433.0, 434.1]. The other yield parameters (e.g., straggle constant, and beam-width) are taken from the results of the 498-keV yield fit, and the target-thickness was estimated using the stopping power data in Table B.2. The data point represents the energy of the incident proton beam. The errors bars, ± 1 keV, are a conservative estimate of the error in the dipole magnet energy calibration. This figure illustrates that the accumulated spectrum can safely be assumed to be representative of the yield curve maximum. Even in the worse case scenario, with the resonance at its upper-limit and a -1 keV offset in the energy calibration, the loss of yield is negligible. For the sake of consistency, this resonance will continue to be referred to as the "435-keV" resonance.

7.3.3: Analysis

Analysis of the 435-keV data is complicated by the ambiguous spin-parity assignment of the resonance state. We anticipate some level of anistropy in the emitted radiation pattern, which

will be dependent not only on the spin-parity, but also the γ-ray mixing ratios for each decay. Unfortunately, since this is the first direct measurement of this resonance, no mixing ratios are available. Since the angular correlations are dependent on unknown discrete (spin-parity) and unknown continuous (mixing ratio) parameters, the spectrum fit is done assuming isotropic decay for all transitions. Corrective measures to account for anisotropy are taken afterwards.

Templates were generated for each of the observed primary transitions in Table 7.9 and also two of the beam-induced contaminant reactions noted above. In this analysis, they play a greater part since they lie close to the important ^{30}Si(p,γ)^{31}P photopeaks. By excluding them, their Compton continua would not be accounted for within the fit regions, which could potentially skew the results. The inclusion of a ^{15}N(p,$\alpha\gamma$)^{12}C template is especially important since its photopeak overlaps with that of the R$\rightarrow$ 3295 transition. The ^{19}F(p,$\alpha_2\gamma$)^{16}O reaction is the dominant contributer of background counts to the data and so was also included. The higher energy peaks due to the ^{13}C(p,γ)^{14}N and ^{19}F(p,$\alpha_4\gamma$)^{16}O reactions were found to contribute negligibly to the primary transition fit regions and were excluded accordingly.

The joint posterior probability distribution for the singles and coincidence analyses were sampled using Metropolis Hastings MCMC. The same number of iterations, burn-in period, and thinning parameter were adopted from the 498-keV and 620-keV analyses. A comparison of the fit to the observed data are shown in Figures 7.14 and 7.15 for the singles and coincidence cases, respectively, where the 95% credibility interval (cyan) is compared with the observed spectra (black line). Owing to the resonance's few deexcitation channels, these fit regions are relatively clean of secondaries and other features. The clear advantage of using the $\gamma\gamma$-coincidence spectroscopy is on display: the option to filter out these unwanted peaks via coincidence gating, as observed in the R$\rightarrow$ 3295 coincidence case, where the broad ^{15}N(p,α)^{12}C photopeak has been removed entirely.

The partial number of reactions, calculated using the fit results, are shown in Table 7.10, as are the branching ratios. Note that all values presented are based on isotropic emission. The agreement between the singles and coincidence results for the R $\rightarrow$ 4431 and R $\rightarrow$ 5014.9 partial reaction intensities is exceptional. There is a small discrepancy (16%) in the R $\rightarrow$ 3295 results. This is likely due to the modeling of the contaminant ^{15}N(p,α)^{12}C photopeak in the singles case. Although the R$\rightarrow$ 3295 comparison in Figure 7.14 appears to be fit well, there is some ambiguity as to where the low-energy tail of ^{15}N(p,α)^{12}C photopeak begins. How far this tail extends into the R

$\rightarrow$ 3295 full-energy photopeak influences their calculated intensities. Since this is not a concern for the coincidence case, the results of the coincidence analysis will be used exclusively in subsequent calculations. The run-test Z-scores for both analyses, -1.3 and -0.7, for singles and coincidence, respectively, argue strongly that the two fits describe the observed spectra well.

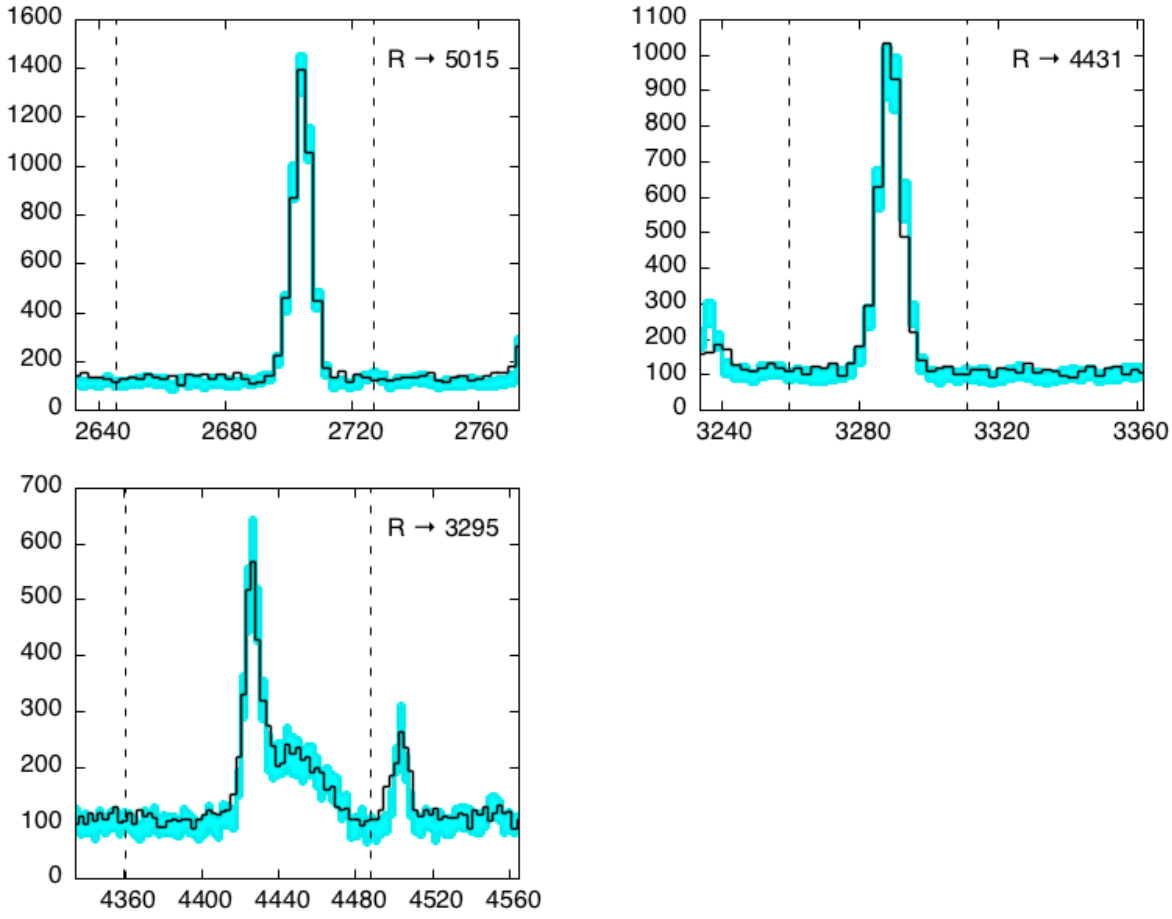

Figure 7.14: Plots of the posterior histograms for the $E_r^{lab} = 435$ keV resonance singles analysis for each of the primary transition photopeaks. The cyan histogram corresponds to the 95% credibility region, while the black line represents the pulse-height spectrum of the observed data. The vertical dashed lines denote the fit region used for each peak.

7.3.4: Angular Correlation Correction

Based on the transfer reactions studies of Betigeri *et al.* [1966] and Al-Jadir *et al.* [1980], there is evidence that the spin-parity of the 435-keV resonance is either $\frac{1}{2}^+$, $\frac{3}{2}^\pm$, or $\frac{5}{2}^\pm$. These two experiments were performed using two different reactions: proton transfer via ^{30}Si(^{3}He,d)^{31}P and deuteron transfer via ^{29}Si(^{3}He,p)^{31}P. The only value consistent with both analyses is $\frac{3}{2}^+$. While it

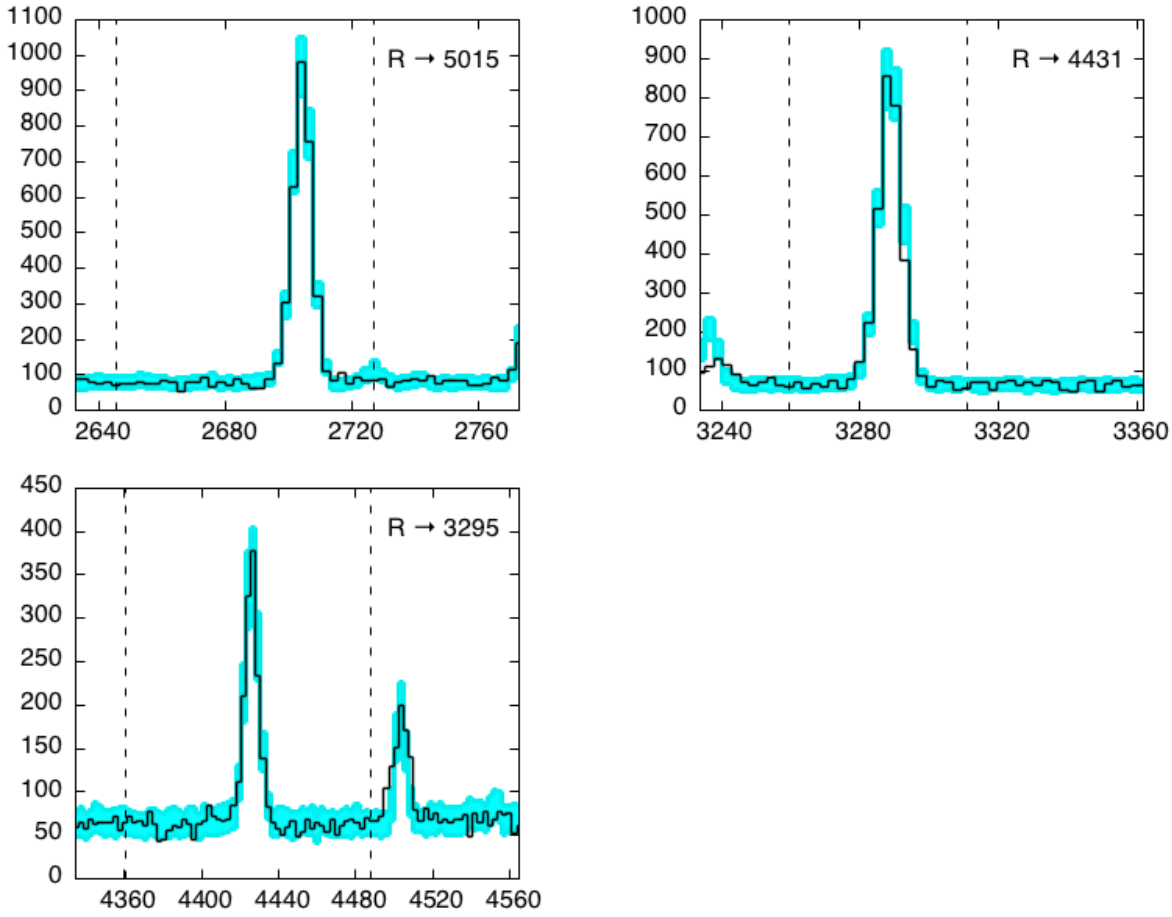

Figure 7.15: Plots of the posterior histograms for the $E_r^{lab} = 435$ keV resonance coincidence analysis for each of the primary transition photopeaks. The cyan histogram corresponds to the 95% credibility region, while the black line represents the pulse-height spectrum of the observed data. The vertical dashed lines denote the fit region used for each peak.

Transition	Partial Reactions		Branching Ratios (%)	
	singles	coincidence	singles	coincidence
R $\rightarrow$ 3295	$1.27(7) \times 10^5$	$1.09(6) \times 10^5$	23.6(10)	20.7(10)
R $\rightarrow$ 4431	$2.07(6) \times 10^5$	$2.19(7) \times 10^5$	38.5(10)	41.5(10)
R $\rightarrow$ 5014.9	$2.04(5) \times 10^5$	$2.00(6) \times 10^5$	37.9(9)	37.8(10)
N_{Total}	$5.4(1) \times 10^5$	$5.3(1) \times 10^5$		

Table 7.10: The calculated partial reaction values and branching ratios for the singles and coincidence analysis of the $E_r^{lab} = 435$ keV data. The total number of reactions, N_{Total}, is also shown.

is an attractive option to adopt this as the spin-parity for this state, the lack of commitment on the part of Betigeri *et al.* [1966] to formally assign a spin-parity suggests that their data were not conclusive. For the present analysis then, all of these spin-parity values are considered. Despite the elevated status of $J^\pi = \frac{3}{2}^+$, each value is weighted equally.

We begin by considering the general form of the experimental angular correlation factor appropriate for a resonance populated by a single proton spin (e.g., s-wave), which can decay through multiple γ-ray channels to a bound state, E_x [Iliadis, 2015]:

$$W^{exp}_{R\rightarrow E_x} = 1 + \frac{(\beta_0 + 2\beta_1\delta + \beta_2\delta^2)}{(1+\delta^2)} Q_2^p \,, \tag{7.7}$$

where the parameters β are calculated based on the spins of the interacting particles and photons. The γ-ray mixing ratio, δ, which has both magnitude and phase, describes the mixing of competing γ-ray decay channels, i.e., M1/E2. The 2nd-order peak attenuation coefficient, Q_2^p, which is determined by the geometry of the experiment, determines the effect that the anisotropy has on the intensity of the relevant full-energy peak in the pulse height spectrum. For $Q_2^p = 0$, for example, which would be expected for a 4π detector, there would be no correction necessary.

The strategy for correcting the results of the 435-keV resonance fit is to first calculate the W^{exp} factor for each primary transition for all of the plausible spin-parity values. For a specific value of J^π, the corrected total number of reactions, $N^{corr.}_{\text{total}}$, can then be calculated from the individual partial reaction numbers, $N^{R\rightarrow E_x}_{\text{partial}}$, and their W^{exp} factor. This calculation is given by:

$$N^{corr.}_{\text{total}} = \xi N^{meas.}_{\text{total}} = \frac{N^{R\rightarrow 3296}_{\text{partial}}}{W^{R\rightarrow 3296}_{exp}} + \frac{N^{R\rightarrow 4431}_{\text{partial}}}{W^{R\rightarrow 4431}_{exp}} + \frac{N^{R\rightarrow 5014.9}_{\text{partial}}}{W^{R\rightarrow 5014.9}_{exp}} \quad . \tag{7.8}$$

Since the angular correlation factors are dependent on the unknown γ-ray mixing ratios, δ, this calculation is carried out many times, each time sampling a new phase and magnitude for the mixing ratio. The correction factor, ξ, given by the ratio $N^{corr.}_{\text{total}}/N^{meas.}_{\text{total}}$, is calculated for each iteration. By observing the distribution of ξ values, over all possible spin-parities, meaningful corrections can be made to the fit results of Section 7.3.3.

The adopted spin-parity values and their associated transitions are shown in Table 7.11. Also shown are the assumed γ-ray multipolarities for each of these transitions. Only E1, M1/E2, and E2 are considered, since all others are highly unlikely. Spin-parity values were excluded on the basis of whether they required an unlikely transition to explain any of the three observed decays (See Table 7.9). For example, since $J^\pi = \frac{1}{2}^+$ would decay via electric-octopole (E3) emission to the $E_x = 4431$ keV state ($J^\pi_f = \frac{7}{2}^-$), we excluded this spin-parity outright as a plausible assignment for the $E^{lab}_r = 435$ keV resonance and omitted it from this sampling procedure.

For pure E1 and E2 decays, a mixing ratio of $\delta = 0$ is adopted at each iteration. For M1/E2 decays, δ is sampled from a uniform random distribution between 0 and 1. The sign for each δ value is also determined randomly. For each of the four spin-parity values considered, 100,000 corrected total reaction intensities were calculated using Equation 7.8. In Figure 7.16, the distributions for each case are shown, where the x-axis illustrates the magnitude of the correction factors. The $2J^\pi = 3^-$ case, which decays via three pure transitions, has a single value, meaning that if this were the spin-parity of the resonance state, a corrective factor of $\xi = 0.91$ would be all that is necessary to correct for angular correlations. The $2J^\pi = 5^+$, 5^-, and 7^+ cases are more difficult. Owing to the unknown mixing in these hypothetical decays, their correction factors, ξ, effectively range from 0.8 to 1.5.

In the bottom-most histogram, the corrected factors from all four spin-parities are shown. Since they are all given equal weight, this histogram represents the probability distribution of the correction factors relevant to this analysis. Unfortunately, the shape of this distribution is not amenable to a Gaussian description. The inclusion of the $2J^\pi = 3^-$ case forces the median and mode below unity, which, given the likelihood of any other spin cases, is not a corrective factor reflective of all possibilities. Despite the problems with this distribution, an informative corrective factor and its uncertainty is calculated based on the 16th and 84th percentiles and their midpoint. These are illustrated as dashed-lines on the "Total" histogram. The adopted correction factor is

	β_0	β_1	β_2	Multipolarity
$J^\pi = \frac{3}{2}^-$				
R $\rightarrow$ 3295	-0.1000	-0.5916	-0.3571	E1
R $\rightarrow$ 4431	0.1429	-0.4629	-0.5000	E2
R $\rightarrow$ 5014.9	0.4000	0.7746	0.000	E1
$J^\pi = \frac{5}{2}^-$				
R $\rightarrow$ 3295	-0.4571	0.5421	-0.2041	E1
R $\rightarrow$ 4431	-0.1429	-0.7423	-0.3469	M1/E2
R $\rightarrow$ 5014.9	-0.4000	1.0141	0.2041	E1
$J^\pi = \frac{5}{2}^+$				
R $\rightarrow$ 3295	-0.4571	0.5421	-0.2041	M1/E2
R $\rightarrow$ 4431	-0.1429	-0.7423	-0.3469	E1
R $\rightarrow$ 5014.9	-0.4000	1.0141	0.2041	M1/E2
$J^\pi = \frac{7}{2}^+$				
R $\rightarrow$ 3295	-0.3571	1.0310	0.0850	M1/E2
R $\rightarrow$ 4431	0.4762	0.4124	-0.2721	E1
R $\rightarrow$ 5014.9	0.5102	0.5511	0.5952	E2

Table 7.11: The adopted angular correlation coefficients used in Equation 7.7 to determine an appropriate correction factor. The γ-ray multipolarites, given the spin-parity, are also shown.

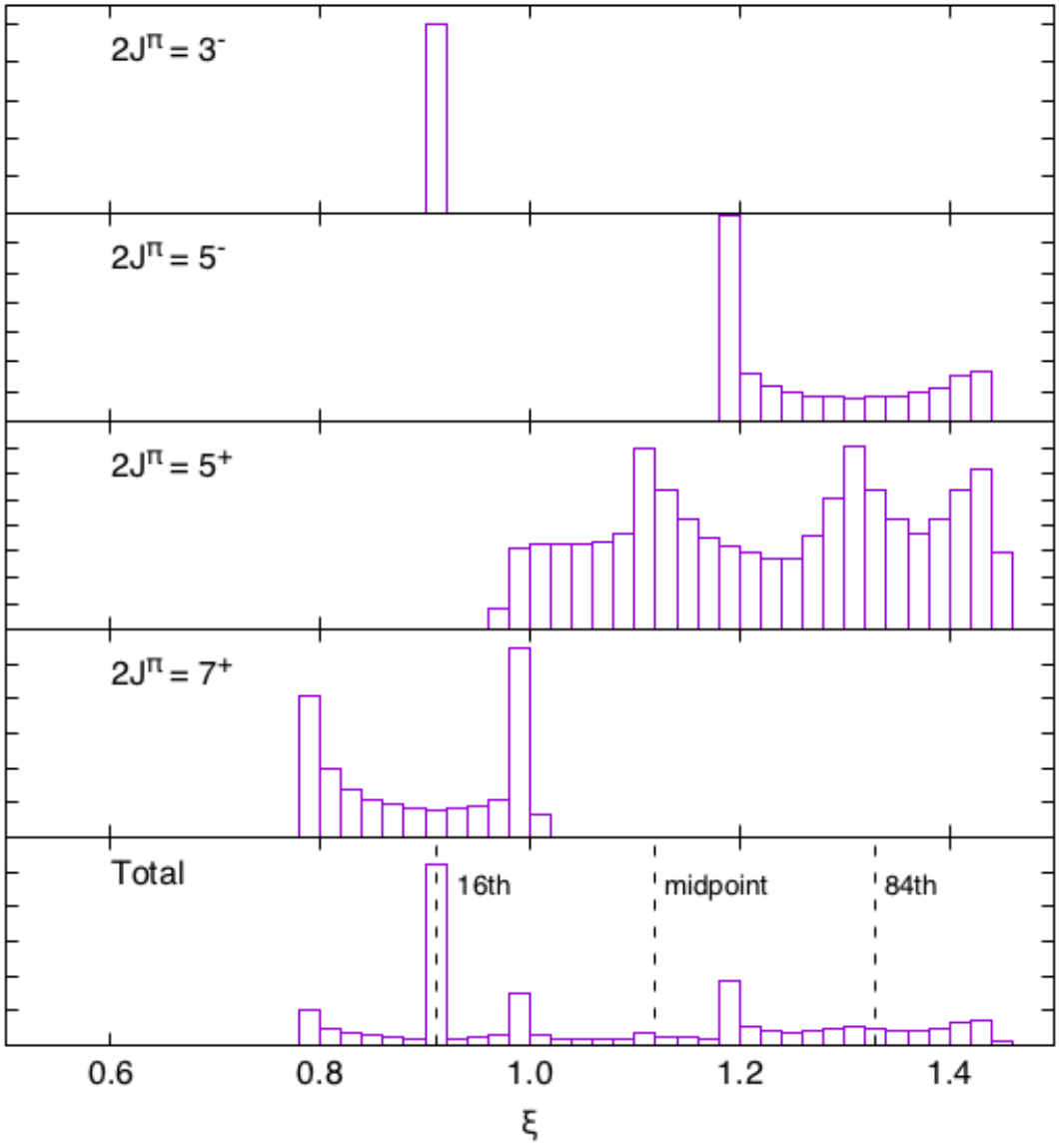

Figure 7.16: A distribution of angular correlation correction factors, ξ, is shown for each of the five plausible spin-parities for the 435-keV resonance. The bottom histogram, labeled "Total" shows the aggregate distribution. The lines indicate the 16th and 84th percentiles and their midpoint.

$\xi = 1.12 \pm 0.21$. The percent uncertainty (19%) illustrates the high-cost incurred when dealing with ambiguous spin-parity designations.

7.3.5: Resonance Strength

With the full analysis of the 435-keV and 620-keV resonances complete, we are now in a position to calculate the resonance strength, $\omega\gamma$, of the $E_r^{lab} = 435$ keV resonance. The determination of a resonance strength based on that of a known standard using the thick-target formalism, is given by Equation 4.128 in Iliadis [2015]:

$$\frac{\omega\gamma_{435}}{\omega\gamma_{620}} = \frac{\epsilon_{r,435}}{\epsilon_{r,620}} \frac{\lambda_{620}^2}{\lambda_{435}^2} \frac{Y_{max,435}}{Y_{max,620}} \quad , \tag{7.9}$$

where the $\epsilon_{r,i}$ are the effective stopping powers at the two resonance energies, λ_r^2 are the deBroglie wavelengths of the captured protons, and the $Y_{max,i}$ are the measured maximum yields. This differs from the expression used earlier in Section 7.2.4, since in this case only a single point on the yield curve (the maximum) was measured, and not the integrated yield. As a result, the ratio of effective stopping powers enters into the calculation.

The effective stopping power is determined by the stoichiometry of the target and also the individual stopping powers for protons in ^{30}Si and Ta (see Equation B.1). Since accurate stopping powers are available from `SRIM` [Ziegler *et al.*, 2010], a measurement of either $\epsilon_{r,435}$ or $\epsilon_{r,620}$ can be used to furnish the other. $\epsilon_{r,620}$ was calculated once already to determine the stoichiometry of the implanted ^{30}Si target using the yield curves in Section 6.2. It is performed again using the higher-statistics analysis of Section 7.1. The steps will not be outlined here, but the procedure is described in detail in Appendix B.2. The measured effective stopping power at $E_r^{lab} = 620$ keV is found to be:

$$\epsilon_{r,620} = 21.5 \pm 1.1 \quad \frac{\text{eV} \cdot \text{cm}^2}{10^{15} \text{ atoms}} \tag{7.10}$$

Using the individual stopping powers for ^{30}Si and Ta [Ziegler *et al.*, 2010], the effective stopping power at 435 keV is then given by:

$$\epsilon_{r,435} = 25.0 \pm 1.5 \quad \frac{\text{eV} \cdot \text{cm}^2}{10^{15} \text{ atoms}} \tag{7.11}$$

The maximum yield for the 620-keV resonance, based on the singles results of Table 7.3, is given by:

$$Y_{max,620} = \frac{N_{total}}{N_b} = \frac{14.93 \pm 0.10 \times 10^6}{3781 \ \ \mu\mathrm{C}/e} = 6.33 \pm 0.04 \times 10^{-10} \tag{7.12}$$

Using the total reaction intensity from Table 7.10 and the angular correlation correction factor, ξ, calculated in Section 7.3.4, the maximum yield for the 435-keV resonance is:

$$Y_{max,435} = \frac{\xi N_{total}}{N_b} = \frac{(1.12 \pm 0.21)(5.3 \pm 0.1 \times 10^5)}{1.997 \ \ \mathrm{C}/e} = 4.8 \pm 0.9 \times 10^{-14} \tag{7.13}$$

The proton deBroglie wavelengths are calculated at the measured resonance energies of 433.5 ± 0.3 keV and 620.2 ± 0.3 keV using Equation 2.x. For the standard resonance, the strength, $\omega\gamma = 1.95 \pm 0.10$ eV is used (See Section 7.1 for details). The resonance strength for the 435-keV resonance is then:

$$\omega\gamma_{435} = (8.8 \pm 1.9) \times 10^{-5} \quad \mathrm{eV} = 88 \pm 19 \quad \mu\mathrm{eV} \quad , \tag{7.14}$$

where all uncertainties have been added in quadrature. Although there are no previous measurements to contrast this figure to, it is worthwhile to see how it compares with the $\omega\gamma_{435}$ probability distribution used in the Iliadis *et al.* [2010b] rate evaluation, since this will provide an idea of how the new measurement affects the input to the ^{30}Si(p,γ)^{31}P reaction rate calculation. In that work, the resonance strength upper-limit, $\omega\gamma_{u.l.}$, was calculated based on the limited spectroscopic data of Vernotte *et al.* [1990], who observed evidence of the 7718-keV state as a feature on the larger, more prominent 7738-keV signal. Based on the intensity of the 7718-keV signal and the generous assumption that the state was populated via $\ell_p = 0$ (s-wave) protons, they placed an upper-limit of $\omega\gamma_{u.l.} < 0.23$ eV on the resonance strength and used this as input to the `RatesMC` program. This upper-limit serves to truncate the probability distribution over the plausible $\omega\gamma_{435}$ values, which itself is based on the observed distribution of measured proton partial widths, Γ_p, in unbound levels in ^{24}Mg, ^{28}Si, ^{30}P, ^{32}S, ^{36}Ar and ^{40}Ca [Longland *et al.*, 2010b]. For the Monte Carlo reaction rate calculation, this distribution is sampled at each iteration so that the resonance strength uncertainty may be properly incorporated into the stellar rate.

This probability distribution of the $\omega\gamma_{435}$ values is shown as a dotted-line in Figure 7.17. The upper-limit and mean $\omega\gamma$ are indicated. The measured resonance strength in this work is shown

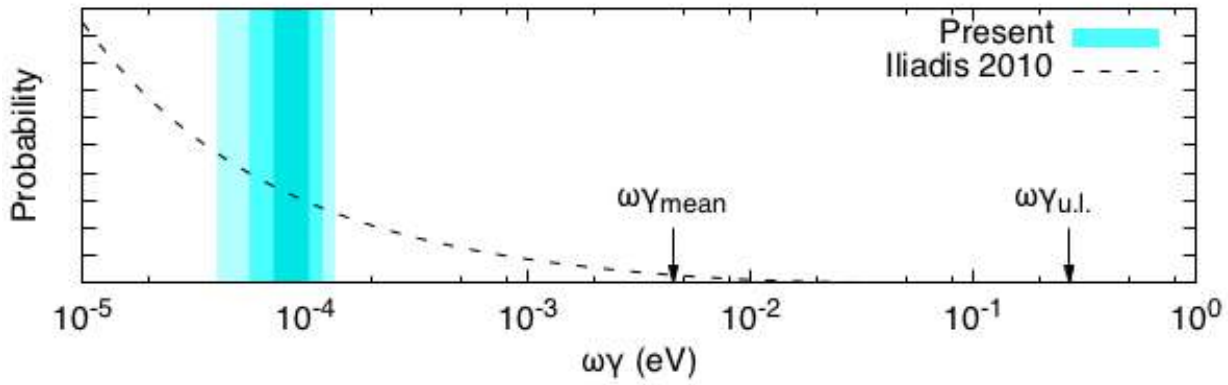

Figure 7.17: A comparison of the 435-keV $\omega\gamma$ probability distribution used in the Iliadis *et al.* [2010b] reaction rate evaluation for ^{30}Si(p,γ)^{31}P. The mean $\omega\gamma$ used in the rate calculation is shown, as is the calculated upper-limit based on the limited spectroscopic data of Vernotte *et al.* [1990]. The present measurement is found to be a factor of 50 below the mean.

as a vertical cyan band, where the gradation illustrates the probability density. It is found to be a factor of 50 less than the mean value used in the Iliadis *et al.* [2010b] reaction rate calculation. Because this resonance competes with several others at stellar temperatures of 100-300 MK range, the impact of this new measurement on the thermonuclear rate will not be to reduce it by the same factor. Rather, other stronger resonances will likely become more dominant in this temperature range. In the next chapter, the ^{30}Si(p,γ)^{31}P reaction rate is reevaluated using the new resonance measurements while also utilizing new features in the `RatesMC` program. The effect of these new measurements on the thermonuclear rate will be explored.

CHAPTER 8: REACTION RATE EVALUATION

The thermonuclear reaction rate for ^{30}Si(p,γ)^{31}P depends on both the resonant and non-resonant properties of the nuclear interaction. For the purposes of modeling stars and other astrophysical phenomena, an accurate description of both processes from temperatures of 10 MK to 10 GK is paramount. In this chapter, the body of work surrounding the ^{30}Si + p reaction is reviewed. Measurements of the resonance strengths, drawn from experiments spanning over half a century, are incorporated into a modern rate evaluation for ^{30}Si(p,γ)^{31}P, utilizing the statistical framework of the `RatesMC` program [Longland *et al.*, 2010b]. For resonances that have not been measured, their contribution to the rate is estimated based on the available data. Additionally, the contribution of non-resonant (direct) capture to the rate is estimated using theoretical cross section calculations. The end result will be a state-of-the-art reaction rate.

Section 8.1: Resonances

8.1.1: $E_r^{lab} > 600$ keV

We begin by considering the observed resonances in the range E_r^{lab} = 0.6 - 3.0 MeV. Several experiments have measured their resonances strengths relative to the E_r^{lab} = 620 keV standard resonance. The most comprehensive campaign was initiated by van Rinsvelt and Smith [1964]. In that work, the excitation function was measured for each resonance between 1.00 and 1.53 MeV. The resonance strengths were obtained by measuring the intensity of detected γ-ray pulses above a discriminator threshold of E_γ = 4.5 MeV and comparing that number directly to the same measurement taken at the 620-keV resonance. While this may seem crude in comparison to the analysis in Chapter 7, which took individual full-energy peaks, branching ratios, and detector efficiencies into account, the contribution of each of these individual resonances to the reaction rate is diminished significantly, owing to the width of the Gamow peak at these energies (see Section 3.4), and also the increasing nuclear level density with increasing excitation energy. At

stellar temperatures of T= 2 GK, for instance, the reaction rate is determined by a total of 28 resonances in the range E_r^{lab} = 600 - 1600 keV. Since this wide energy range encompasses so many resonances, each resonance does not require the same level of scrutiny incurred by the lower energy resonances, e.g., E_r^{lab} = 620 keV. Instead, the uncorrected γ-ray yield method practiced by these earlier studies is sufficient.

Their work was extended in van Rinsvelt and Endt [1966], where resonances in the range E_r^{lab} = 1.53 - 2.00 MeV were studied, and Bornman *et al.* [1967], who measured resonances from E_r^{lab} = 2 - 3 MeV. Both of these experiments used the same γ-ray discriminator threshold of E_γ = 4.5 MeV, providing a level of consistency between the data sets. Later, de Neijs *et al.* [1975] remeasured resonances in the range E_r^{lab} = 1.8 - 2.5 MeV.

Between E_r^{lab} = 620 and 1000 keV, the resonance strengths have been measured by Hoogenboom [1958] and Wolff *et al.* [1969]. Although the details of the Hoogenboom [1958] measurements are unpublished, the treatment of their results in Endt and Van der Leun [1967] and subsequent nuclear data evaluations suggests that the E_r^{lab} = 670.7 keV, 760.3 keV, and 777.4 keV resonance strengths were all measured relative to their resonant absorption value for the 620-keV resonance (see Section 7.1 for an overview of this measurement). In Wolff *et al.* [1969], a similar approach to that of the 499-keV analysis in Section 7.3 was followed, where the maximum yield at each resonance was compared with that of the standard. Using this method, they measured the resonance strengths of the E_r^{lab} = 835.3, 942.0, 959.3, 978.2, and 982.5 keV resonances.

Each of the aforementioned studies reported their results relative to the 620-keV resonance strength recommended at the time of the measurement. For the present evaluation, these have been rescaled to the adopted value, $\omega\gamma_{620} = 1.95 \pm 0.10$ eV (see Section 7.1). In Table 8.1, the resonance strengths included in the present rate evaluation between E_r^{lab} = 0.6 - 3.0 MeV are shown. There are a few instances where resonances were measured by multiple groups. The largest span of overlap is between E_r^{lab} = 1877.9 - 1994.6 keV, where each resonance was measured independently by van Rinsvelt and Endt [1966], de Neijs *et al.* [1975], and Bornman *et al.* [1967]. The agreement between the van Rinsvelt and Endt [1966] and de Neijs *et al.* [1975] measurements is exceptional, differing by no more than 6%. In this case, the average of the two results is used. The adopted uncertainty, 30%, is the value recommended by both groups independently. Since the Bornman *et al.* [1967] results have a larger uncertainty than the other groups (50%), they are only used in

cases where no other measurements exist, such as for E_r^{lab} = 2542 - 3027 keV energy range. For the resonances between E_r^{lab} = 2009.5 - 2505.4 keV, for which data from both de Neijs *et al.* [1975] and Bornman *et al.* [1967] are available, the de Neijs *et al.* [1975] values are adopted.

8.1.2: $E_r^{lab} < 600$ keV

At lower energies, with the exception of the 435-keV and 498-keV resonances measured in the present work, fewer data is available for the known resonances. Incorporation of their contribution to the thermonuclear rate frequently requires that parameters such as the partial widths, e.g., Γ_p, are estimated using the known nuclear physics properties of similar states. The `RatesMC` program [Longland *et al.*, 2010b] allows for a calculation of the reaction rate that takes these effects into account. Next, we look at the available experimental information for these low energy resonances to provide the most up-to-date input reaction rate calculation.

E_p^{lab} = 453 keV

In Vernotte *et al.* [1990], an unbound state in the ^{31}P nucleus at $E_x = 7736 \pm 4$ keV, corresponding to a laboratory frame proton energy of $E_p^{lab} = 453 \pm 4$ keV, was observed for the first time using the ^{30}Si(^{3}He, d)^{31}P stripping reaction. Based on the deuteron angular distribution, measured using an Enge split-pole magnetic spectrograph, they were able to determine that the excited state is populated by $\ell_p = 3$, or f-wave, protons. Using angular momentum and parity conservation, this limits the possible spin-parity values for this state to $J^\pi = \frac{5}{2}^-$ or $\frac{7}{2}^-$. By comparing the measured reaction cross-section with that of a single-particle optical model calculation, the proton spectroscopic factor, $C^2S = 0.02$, was also obtained for this state. This quantity is the product of the isospin Clebsch-Gordan coefficient, C, and the nuclear shell model spectroscopic factor, S. The spectroscopic factor can be used to calculate the proton partial width, Γ_p, using the relationship (Equation 2.197 in Iliadis [2015]):

$$\Gamma_p = C^2S\,\Gamma_{s.p.} = C^2S\frac{2\hbar^2}{\mu R^2}P_\ell\theta^2_{s.p.} \tag{8.1}$$

where the single-particle partial width, $\Gamma_{s.p.}$, is calculated from the penetration factor, P_ℓ, and the dimensionless single-particle reduced width, $\theta^2_{s.p.}$. The penetration factor was calculated by

E_p^{lab} (keV)	$\omega\gamma$	$\Delta\omega\gamma$ (eV)	E_p^{lab} (keV)	$\omega\gamma$	$\Delta\omega\gamma$ (eV)	E_p^{lab} (keV)	$\omega\gamma$	$\Delta\omega\gamma$ (eV)
620.4(12)	1.950	0.100 [a]	1769.9(11)	1.241	0.372 [e]	2393.2(10)	0.472	0.142 [f]
670.7(10)	0.078	0.006 [b]	1808.2(11)	1.950	0.585 [e]	2505.4(10)	2.768	0.830 [f]
760.3(9)	0.087	0.090 [b]	1815.0(11)	0.403	0.133 [e]	2542.0(20)	2.039	1.019 [g]
777.4(10)	0.440	0.032 [b]	1829.9(11)	2.133	0.452 [e]	2546.0(20)	5.318	2.659 [g]
835.3(13)	0.195	0.045 [c]	1877.9(6)	0.263	0.117 [e,f]	2551.0(20)	1.064	0.532 [g]
942.0(6)	0.881	0.200 [c]	1880.1(6)	0.625	0.638 [e,f]	2604.0(20)	0.355	0.177 [g]
959.3(6)	0.145	0.035 [c]	1893.5(6)	0.320	0.078 [e,f]	2607.0(20)	0.975	0.488 [g]
978.2(6)	0.692	0.150 [c]	1896.0(6)	0.754	0.186 [e,f]	2629.0(20)	0.310	0.155 [g]
982.5(6)	0.818	0.200 [c]	1920.1(6)	0.584	0.096 [e,f]	2632.0(20)	3.767	1.884 [g]
1094.6(6)	0.106	0.032 [d]	1922.2(6)	0.299	0.226 [e,f]	2641.0(20)	0.620	0.310 [g]
1175.4(7)	0.182	0.055 [d]	1942.6(6)	0.411	0.173 [e,f]	2655.0(20)	1.241	0.620 [g]
1203.4(7)	0.709	0.213 [d]	1973.7(6)	0.299	0.089 [e,f]	2657.0(20)	1.241	0.620 [g]
1213.1(7)	0.049	0.015 [d]	1994.6(6)	0.411	0.122 [e,f]	2698.0(20)	4.875	2.438 [g]
1288.8(8)	0.142	0.043 [d]	2009.5(7)	0.881	0.264 [f]	2717.0(20)	0.753	0.377 [g]
1297.7(8)	0.576	0.173 [d]	2022.1(7)	0.459	0.138 [f]	2733.0(20)	0.620	0.310 [g]
1301.0(8)	0.443	0.133 [d]	2025.2(7)	0.440	0.132 [f]	2738.0(20)	0.266	0.133 [g]
1321.9(8)	1.019	0.306 [d]	2061.3(7)	0.692	0.208 [f]	2756.0(20)	0.620	0.310 [g]
1330.7(8)	0.137	0.041 [d]	2091.0(8)	0.327	0.098 [f]	2793.0(20)	1.285	0.643 [g]
1348.1(8)	0.049	0.015 [d]	2130.9(8)	0.245	0.074 [f]	2814.0(20)	3.811	1.906 [g]
1389.7(8)	1.551	0.465 [d]	2133.7(8)	0.692	0.208 [f]	2842.0(20)	4.432	2.216 [g]
1398.2(8)	1.950	0.585 [d]	2173.9(8)	0.220	0.066 [f]	2872.0(20)	0.443	0.222 [g]
1480.5(8)	2.127	0.638 [d]	2187.0(8)	5.913	1.774 [f]	2886.0(20)	2.083	1.041 [g]
1482.0(8)	1.418	0.425 [d]	2216.3(9)	0.692	0.208 [f]	2889.0(20)	1.507	0.753 [g]
1489.7(8)	0.886	0.266 [d]	2224.7(9)	1.258	0.377 [f]	2896.0(20)	2.260	1.130 [g]
1506.5(8)	0.031	0.009 [d]	2253.7(9)	0.157	0.047 [f]	2914.0(20)	0.576	0.288 [g]
1509.7(8)	1.551	0.465 [d]	2303.0(9)	0.755	0.226 [f]	2943.0(20)	1.285	0.643 [g]
1515.9(9)	0.355	0.106 [d]	2315.2(10)	0.692	0.208 [f]	2952.0(20)	0.443	0.222 [g]
1595.1(9)	0.177	0.053 [e]	2350.4(10)	1.384	0.415 [f]	2993.0(20)	3.324	1.662 [g]
1660.2(10)	0.355	0.106 [e]	2357.9(10)	0.629	0.189 [f]	3027.0(20)	1.551	0.776 [g]
1667.2(10)	0.355	0.106 [e]	2365.4(10)	1.824	0.547 [f]			
1694.2(10)	1.064	0.319 [e]	2374.5(10)	0.692	0.208 [f]			
1754.0(10)	0.177	0.053 [e]	2379.3(10)	0.113	0.034 [f]			

[a] Paine and Sargood [1979]
[b] Hoogenboom [1958]
[c] Wolff *et al.* [1969]
[d] van Rinsvelt and Smith [1964]
[e] van Rinsvelt and Endt [1966]
[f] de Neijs *et al.* [1975]
[g] Bornman *et al.* [1967]

Table 8.1: The adopted resonances strengths and their uncertainties between E_r^{lab} = 0.6 and 3.0 MeV. All values have been rescaled relative to the E_r^{lab} = 620 keV resonance strength from Paine and Sargood [1979].

means of a code, `pene.f`, which uses the method of Bardin *et al.* [1972] to calculate the regular and irregular Coulomb wave functions at the channel radius. The single-particle reduced width, $\theta^2_{s.p.}$, was calculated based on the results of Iliadis [1997], which offers estimates of $\theta^2_{s.p.}$ for $\ell_p = 0, 1, 2$, and 3, for ranges of target mass and bombarding energy of the reaction in question. Using Equation 8.1, the proton partial width for the $E_p^{lab} = 453$ keV resonance is found to be $\Gamma_p = (9.6 \pm 3.8) \times 10^{-5}$ eV. A conservative uncertainty of 40% was adopted to incorporate the uncertainty of the stripping spectroscopic factor.

While this still leaves the γ-ray width, Γ_γ, unknown, we can make the assumption that $\Gamma_\gamma \gg \Gamma_p$. This is usually true of resonances below $E \approx 500$ keV [Iliadis, 2015]. In that case, the resonance strength can be calculated using:

$$\omega\gamma = \omega\frac{\Gamma_p\Gamma_\gamma}{\Gamma_p + \Gamma_\gamma} \approx \omega\frac{\Gamma_p\Gamma_\gamma}{\Gamma_\gamma} \approx \omega\Gamma_p \tag{8.2}$$

Finally, the spin of this resonance state is either $\frac{5}{2}$ or $\frac{7}{2}$, so there are two equally likely resonance strength values: $\omega\gamma = (2.9 \pm 1.2) \times 10^{-4}$ eV and $\omega\gamma = (3.8 \pm 1.5) \times 10^{-4}$ eV.

$E_p^{lab} = 403$ keV

Vernotte *et al.* [1990] observed a weak unbound state at $E_x = 7687 \pm 2$ keV, which corresponds to $E_r^{lab} = 403 \pm 2$ keV. No state had previously been reported here by any other transfer reaction study [Moss, 1969, Al-Jadir *et al.*, 1980]. Since they were not able to make a spin-parity or ℓ-transfer assignment, and given that they reported this measurement as being tentative, for the present rate evaluation we do not include the effects of this possible proton resonance.

$E_p^{lab} = 175$ keV

An unbound state at $E_x = 7466 \pm 2$ keV was discovered by De Voigt *et al.* [1971] using the ^{27}Al(α,γ)^{31}P reaction, corresponding to $E_r^{lab} = 175 \pm 2$ keV in ^{30}Si(p,γ)^{31}P. This state was later confirmed by Twin *et al.* [1974] using the ^{28}Si(α,pγ)^{31}P reaction. In that work, the primary transition deexcitation branching ratios were measured, which yielded spin-parity assignments of $J^\pi = \frac{7}{2}^-, \frac{9}{2}^\pm$ according to Endt and Van der Leun [1967]. Vernotte *et al.* [1990] did not observe a peak corresponding to this state. However, based on their reported spectrum (See Figure 1 in

Vernotte *et al.* [1990]), an upper-limit on the spectroscopic factor, C^2S, can be obtained.

The spin-parity assignments suggested by Endt and Van der Leun [1967] imply that the proton angular momentum transfer is either $\ell_p = 3$ (for $J^\pi = \frac{7}{2}^-$), $\ell_p = 4$ (for $J^\pi = \frac{9}{2}^+$), or $\ell_p = 5$ (for $J^\pi = \frac{9}{2}^-$). The lowest value, $\ell_p = 3$, will correspond to the highest (and most conservative) upper-limit for the resonance strength. Proceeding with the assumption that $\ell_p = 3$ for $E_x = 7466 \pm 2$ keV, a comparison to their $E_x = 7736 \pm 2$ keV peak (also $\ell_p = 3$) permits a rough estimate of the C^2S upper-limit. The spectrum of excited states, as measured by Vernotte *et al.* [1990], is shown in Figure 8.1. In addition to the $E_x = 7466$ keV state, three ^{31}P states that they definitively observed are indicated. There is a small excess of counts where the $E_x = 7466$ keV peak is expected. The maximum number of counts in this peak is 15% that of the $E_x = 7736$ keV peak. Based on the ratio of heights, an upper-limit of the spectroscopic factor for the $E_x = 7466$ keV state was calculated using $C^2S_{u.l.} = 0.15 \times C^2S_{(7736)} = 0.003$. Equations 8.1 and 8.2 were then used to determine an upper-limit on the resonance strength: $\omega\gamma_{u.l.} = 1.2 \times 10^{-10}$ eV.

$E_p^{lab} = 149$ keV

An excited state at $E_x = 7441 \pm 2$ keV in ^{31}P, corresponding to $E_r^{lab} = 149 \pm 2$ keV, was also discovered by De Voigt *et al.* [1971] and subsequently confirmed by Twin *et al.* [1974]. Based on the deexcitation branching ratios measured in the latter work, a spin-parity of $J^\pi = \frac{11}{2}^+$ was determined for this state. According to angular momentum and parity conservation, the only permissible proton orbital angular momentum transfer is $\ell_p = 6$. Unfortunately, this state has not yet been observed in any transfer reaction study, nor is an estimate of the $\theta^2_{s.p}$ readily available. Despite these deficiencies, an upper-limit for the resonance strength can still be calculated by assuming conservative values of $\theta^2_{s.p} = 1$ and $C^2S = 1$. In this case, we find $\omega\gamma_{u.l.} = 8.8 \times 10^{-16}$ eV.

$E_p^{lab} = 54$ keV

Moss [1969] and Al-Jadir *et al.* [1980] observed an unbound state at $E_x = 7356 \pm 9$ keV and $E_x = 7346 \pm 6$ keV, respectively, using the ^{29}Si(^{3}He,p)^{31}P reaction. In the latter work, a spin-parity assignment of $J^\pi = (\frac{3}{2}, \frac{5}{2})^-$ was made based on the success of the $\ell_d = 1 + 3$ fit to the measured

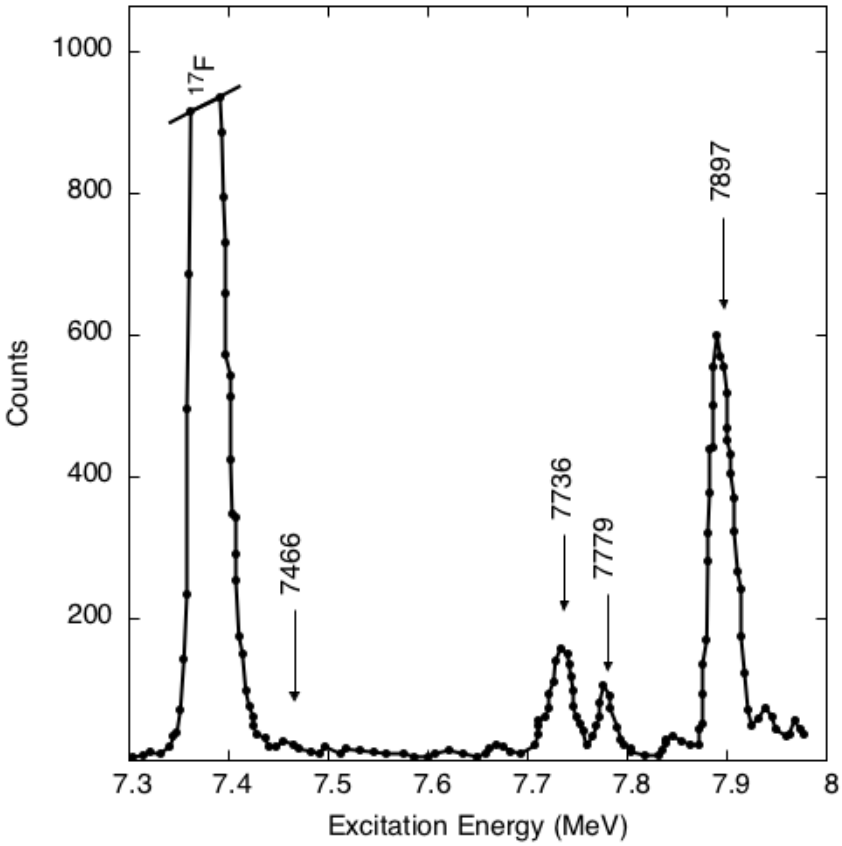

Figure 8.1: Spectrum of the ^{30}Si(^{3}He,d)^{31}P reaction measured by Vernotte *et al.* [1990]. Several excited states in ^{31}P are indicated, with their energies in units of keV. Note that these data were copied from the original publication using the online tool, `WebPlotDigitizer` [Rohatgi, 2015]. The black dots are shown to illustrate the resolution of the copied information.

proton angular distribution. The peak associated with this state was obscured in Vernotte *et al.* [1990], owing to the large ^{17}F contaminant peak (see Figure 8.1). Since Vernotte *et al.* [1990] was unable to furnish information regarding the spectroscopic factor, we adopt a conservative upper-limit based on the maximum C^2S and lowest possible orbital angular momentum value, $\ell_p = 1$. We obtain $\omega\gamma_{u.l.} = 1.3 \times 10^{-16}$ eV. For the resonance energy, we use the weighted mean, $E_x = 7349 \pm 5$ keV, corresponding to $E_r^{lab} = 54 \pm 5$ keV. This value is also found in Endt [1990].

$E_p^{lab} = 18$ keV

The excited state at $E_x = 7313.7 \pm 1.6$ keV ($E_r^{lab} = 17.9 \pm 2$ keV) was first observed by Moss [1969]. Later, using the ^{29}Si(^{3}He,p)^{31}P reaction, Al-Jadir *et al.* [1980] determined a spin-parity of $J^\pi = (\frac{1}{2}, \frac{3}{2})^+$ based on an $\ell_d = 0$ fit to the proton angular distribution. This result was superseded by the ^{30}Si(^{3}He,d)^{31}P analysis of Vernotte *et al.* [1990], who instead recommended $J^\pi = (\frac{5}{2}, \frac{7}{2})^-$ based on an $\ell_p = 3$ fit. Vernotte *et al.* [1990] also reported a spectroscopic factor, $C^2S = 0.002$. Using Equations 8.1 and 8.2, the two likely resonance strength values are $\omega\gamma = (1.2 \pm 0.5) \times 10^{-41}$ eV ($J^\pi = \frac{5}{2}^-$) and $\omega\gamma = (1.5 \pm 0.6) \times 10^{-41}$ eV ($J^\pi = \frac{7}{2}^-$). Both of these values will be incorporated into the reaction rate.

The calculated resonance strengths or their upper-limits are shown in Table 8.2. The strengths determined for the $E_r^{lab} = 435$ keV and $E_r^{lab} = 499$ keV resonances in the present work (Chapter 7) are also included. The adopted orbital angular momentum and spin-parity are indicated for all resonance strengths calculated using data from indirect measurements. In the case of the $E_x = 7314$ and 7736 keV excited states, the two $\omega\gamma$ values, as determined by the two plausible spin-parity designations for each state, are shown with their probabilities (column "Prob.") indicated. In Section 8.3, the methodology for incorporating both the multiple values for $\omega\gamma$ and the upper-limits into the reaction rate will be detailed.

Section 8.2: Direct Capture

For many reactions, the non-resonant radiative capture process provides an important contribution to the total cross section (see Section 3.2). It consists of a smooth background, usually on the order of $1 - 10$ micro-barns (1 barn $\equiv 10^{-24}$ cm^2), which varies slowly with incident particle energy. It is different from resonant capture in that it does not involve the creation of an intermediate compound state. For this reason, it is known as "direct capture". The magnitude of the direct-capture component and its effect on the astrophysical reaction rate can vary widely. One notable example is ^{17}O(p,γ)^{18}F, where direct capture is the predominant channel through which the reaction proceeds below stellar temperatures of 30 MK [Buckner *et al.*, 2015]. The recent history of ^{17}O + p cross section measurements, e.g., Buckner *et al.* [2015], Di Leva *et al.* [2014], and Fox *et al.* [2005], illustrates the importance of understanding this process.

For the ^{30}Si(p,γ)^{31}P reaction, there has not yet been an experimental investigation of its non-resonant cross section. Its effect on the thermonuclear reaction rate is so far unknown. For the present reaction rate evaluation, its contribution is estimated using the formalism described in Rolfs [1973]. The total direct capture cross section is given by an incoherent sum over orbital angular

E$_x$ (keV)[a]	E$_p^{cm}$ (keV)	E$_p^{lab}$ (keV)	ℓ_p	$2J^\pi$	$\omega\gamma$ (eV)	Prob.
7314(4)[b]	17(4)	18(4)	3	(5^-)	$1.2(5) \times 10^{-41}$	0.5
			3	(7^-)	$1.5(6) \times 10^{-41}$	0.5
7349(5)	52(2)	54(5)	1	(3^-)	$\leq 1.3 \times 10^{-16}$	
7441.2(7)	144.7(7)	149.5(7)	6	11^+	$\leq 8.8 \times 10^{-16}$	
7466(2)	169(2)	175(2)	3	(7^-)	$\leq 1.2 \times 10^{-10}$	
7716.0(3)[c]	**419.4(3)**	**433.5(3)**			$\mathbf{8.7(19) \times 10^{-5}}$	
7736(4)	439(4)	454(4)	3	(5^-)	$2.9(12) \times 10^{-4}$	0.5
			3	(7^-)	$3.8(15) \times 10^{-4}$	0.5
7779.8(2)[c]	**483.3(2)**	**499.5(2)**			$\mathbf{1.88(14) \times 10^{-1}}$	

[a] Excitation energies are adopted from Endt [1990], except where noted.
[b] From Vernotte *et al.* [1990].
[c] Present work, based on the analysis in Sections 7.2.3 and 7.3.2.

Table 8.2: Resonances below $E_r^{lab} = 620$ keV in ^{30}Si(p,γ)^{31}P. For resonances strengths and upper-limits calculated using assumed spectroscopic factors, orbital angular momenta and spin-parity values are listed. In instances where more than one $\omega\gamma$ is likely, the probability for each value is indicated. Values obtained in the present work are shown in bold.

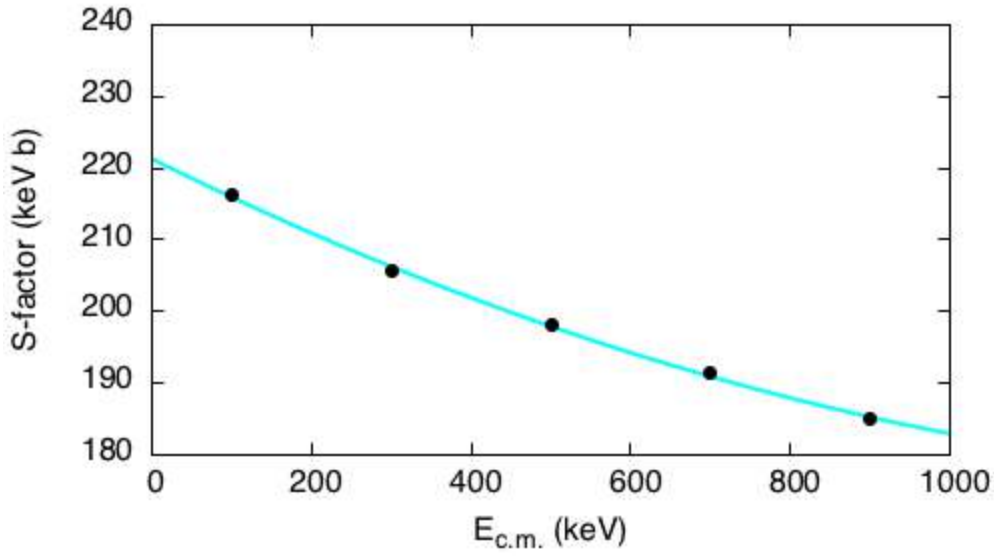

Figure 8.2: Present estimate of the non-resonant (direct capture) astrophysical S-factor for ^{30}Si(p,γ)^{31}P. The black data points represent the calculated S-factor based on the wave functions of the incoming and outgoing particles. The cyan curve is the 2nd-order polynomial best-fit line.

momenta ℓ_i and ℓ_f for all incoming and outgoing partial waves involved in the reaction:

$$\sigma^{\rm DC}_{\rm total} = \sum_{\ell_i,\ell_f} C^2S(\ell_f)\sigma^{\rm DC}_{\rm theory}(\ell_i,\ell_f)\ . \tag{8.3}$$

This sum was computed over all the bound states in the ^{31}P nucleus for bombarding energies in the range $E_p^{c.m.} = 0.1 - 1$ MeV using the program `DIRCAP`. The spectroscopic factors, C^2S, of the final bound states were adopted from Vernotte *et al.* [1990]. The theoretical cross section, $\sigma^{\rm DC}_{\rm theory}$, was determined for each final bound state via integration of the radial wave function, which was calculated using a Woods-Saxon potential. The potential parameters of the well-depth ($r_0 = 1.25$ fm, $a = 0.65$ fm) were the same as those used in Vernotte *et al.* [1990] for the calculation of the bound states. Nuclear masses were adopted, based on the atomic masses published in Wang *et al.* [2017]. The calculated masses are 29.9661 u, 30.9655 u, and 1.0073 u for ^{30}Si, ^{31}P, and ^{1}H, respectively. The Q-value based on the nuclear masses is then $Q = 7297.96$ keV, which is 1.4 keV greater than the atomic mass value.

The total non-resonant cross section was then converted to the astrophysical S-factor:

$$S(E) = \sigma^{\mathrm{DC}}_{\mathrm{total}}(E) E \exp(2\pi\eta) \ . \tag{8.4}$$

The S-factor is shown in Figure 8.2. Each black data point represents the calculated S-factor for a single bombarding energy using Equations 8.3 and 8.5. Recall from Section 3.2 that the S-factor is incorporated into the thermonuclear reaction rate through a polynomial of the form:

$$S(E) = S(0) + S'(0)E + \frac{1}{2}S''(0)E^2 \ . \tag{8.5}$$

The cyan curve represents the best-fit to the data assuming this function. The parameters used in the fit are shown in Table 8.3. For the reaction rate calculation, Equation 8.5 describes the non-resonant contribution below a cut-off energy of 1 MeV. Above this threshold, the effect of narrow resonances ensures that the non-resonant contribution is negligible because we observe the resonances, and not a smooth S-factor.

$S(0)$ (keV $\cdot$ b)	$S'(0)$ (b)	$S''(0)$ (keV^{-1} $\cdot$ b)
221.3	-5.52×10^{-2}	3.37×10^{-5}

Table 8.3: Parameters of the direct capture S-factor contribution to the ^{30}Si(p,γ)^{31}P reaction, based on the fit to the estimated S-factor shown in Figure 8.2.

Section 8.3: Monte Carlo Reaction Rate Calculation

In the preceeding sections, the available nuclear data relevant to the ^{30}Si(p,γ)^{31}P reaction was scrutinized. Resonances that have been measured, either directly or through transfer reactions, presented the easiest case. For three of the low-energy resonances, the available data preclude a firm estimate of the resonance strengths. Instead, upper limits were calculated based on a combination of spin-parity arguments and the observed intensities in published spectra. Finally, the direct capture cross section was estimated using theoretical calculations and experimentally obtained spectroscopic factors. In this section, these results are incorporated into a Monte Carlo reaction rate calculation for ^{30}Si(p,γ)^{31}P using the program `RatesMC`.

A full explanation of the RatesMC methodology is outside the scope of this dissertation. The reader is directed to Longland *et al.* [2010b], Iliadis *et al.* [2010a], and Iliadis *et al.* [2010b] for a thorough introduction. However, for an understanding of the present calculation, it is important to review how reaction rates are treated. Recall that the thermonuclear rate for a charged particle reaction, in a stellar plasma at thermal equilibrium, is given by (Equation 3.4):

$$N_A\langle\sigma v\rangle = N_A\left(\frac{8}{\pi\mu}\right)^{1/2}\frac{1}{(kT)^{3/2}}\int_0^\infty E\sigma(E)e^{-E/kT}$$

where E is the center-of-mass energy of the reaction, and $\sigma(E)$ is the total reaction cross section. At any stellar temperature, there is uncertainty in the thermonuclear rate, $N_A\langle\sigma v\rangle$, due to the uncertainties in the cross section. This may arise, for example, from measurement errors in the resonance strengths or the direct capture cross section. RatesMC takes into account this uncertainty by formulating the thermonuclear rate at each temperature in terms of a lognormal distribution:

$$f(x) = \frac{1}{\sigma\sqrt{2\pi}}\frac{1}{x}e^{-(\ln x-\mu)^2/(2\sigma^2)} \qquad \text{for } 0 < x < \infty\ , \tag{8.6}$$

where the two variables, μ and σ, parameterize the location and width. One advantage of describing the thermonuclear rate by a lognormal, rather than a Gaussian, is that the lognormal distribution is guaranteed to be non-zero only for $x > 0$. Since the thermonuclear rate is a manifestly positive quantity, this limiting behavior for $f(x)$ provides a level of consistency that is not afforded by the Gaussian, which can be non-zero at negative values and therefore give rise to unphysical negative reaction rates.

RatesMC calculates a probability density function of $N_A\langle\sigma v\rangle$ on a fixed temperature grid by sampling the relevant nuclear input, typically for a sample size of 5,000 or more. For the ^{30}Si(p,γ)^{31}P reaction, the total rate is calculated exclusively from narrow resonances and the non-resonant S-factor. Narrow resonances with a measured strength and uncertainty are associated with an expectation value and square root of the variance, respectively, of a lognormal distribution. The resonance strengths are sampled from their respective distributions during each step of the calculation. For the $E_r^{lab} = 18$ and 454 keV resonances, which each have two plausible pairs of strengths and uncertainties, the different alternatives are also sampled according to their probabilities listed

in Table 8.2.

In instances where only an upper-limit for a partial width can be calculated, the procedure is more complicated. Recall from Equation 8.1 that the proton partial width is the product of several factors. In this expression, the product of the spectroscopic factor and dimensionless single-particle reduced width, is defined as the dimensionless reduced width:

$$\theta^2 = C^2 S \theta^2_{s.p.} \quad . \tag{8.7}$$

For an unknown partial width, the dimensionless reduced width, θ^2, is sampled from a Porter-Thomas distribution. This is equivalent to the χ^2 distribution with one degree of freedom. It is given by:

$$f(\theta^2) = \frac{c}{\sqrt{\theta^2}} e^{-\theta^2/2\langle\theta^2\rangle} \ , \tag{8.8}$$

where c is a normalization constant and $\langle\theta^2\rangle$ is the mean value for the dimensionless reduced width. For the present rate evaluation, we adopt $\langle\theta^2\rangle = 0.0045$. This is based on the analysis of measured proton reduced widths of unbound states in ^{24}Mg, ^{28}Si, ^{31}P, ^{32}S, ^{36}Ar, and ^{40}Ca found in Longland *et al.* [2010b] and Pogrebnyak *et al.* [2013]. When an upper-limit on the resonance partial width, Γ_p, or resonance strength, $\omega\gamma$, is specified, the Porter-Thomas distribution for that state is truncated at the corresponding dimensionless reduced width value, as calculated using Equations 8.1 and 8.2.

Finally, the non-resonant S-factor is input as a 2nd-order polynomial function (See Equation 8.5). For each iteration, the magnitude of the S-factor is sampled according to a lognormal distribution with a user-set variance. The sampled value is then used in Equations 3.10 - 3.12 to compute the non-resonant contribution to the reaction rate at that temperature.

If the distribution of $N_A\langle\sigma v\rangle$ values is described well by a lognormal distribution, then the reaction rate median value and its respective uncertainty at that temperature are given by:

$$\text{median} \equiv x_{\text{med}} = e^{\mu}, \quad f.u. = e^{\sigma} \ , \tag{8.9}$$

where $f.u.$ denotes the factor uncertainty. The lower and upper bounds are then given by:

$$x_{\text{low}} = e^{\mu-\sigma} \ , \quad x_{\text{high}} = e^{\mu+\sigma} \ , \tag{8.10}$$

for a coverage probability of 68%. The goal for a Monte Carlo reaction rate calculation is to provide accurate σ and μ parameters for stellar temperatures important to nuclear astrophysics.

The `RatesMC` input file used for the present evaluation is given in Appendix A.3. The results from Tables 8.1, 8.2, and 8.3 were all included. For the interacting particles, the nuclear masses were adopted, as was the corresponding reaction Q-value (see Section 8.2). The thermonuclear rate probability density function was calculated using 20,000 samples at 60 temperatures in the range 10 MK - 10 GK. The lognormal parameters μ and σ are tabulated for each temperature in Table 8.4. Also shown are the x_{med}, x_{low}, and x_{high} reaction rate values. The last column, labeled "A-D", reports the Anderson-Darling test statistic, t_{AD}, which provides a measure of how well the reaction rate probability distribution conforms to the lognormal distribution [Iliadis *et al.*, 2010b]. A value greater than $t_{AD} \approx 1$ suggests that the reaction rate probability distribution is not lognormal. For values in excess of $t_{AD} \approx 30$, the departure from the lognormal is visually apparent. Based on these guidelines, the reaction rate distribution for temperatures below $T = 180$ MK are not described well by the lognormal density. A visualization of the disagreement is shown in Figure 8.3. Each plot represents the reaction rate probability distribution (shown in red) at the indicated temperature in GK. The black line represents the lognormal distribution employed to describe the reaction rate at that temperature. The Anderson-Darling statistic is shown in each plot for comparison. At $T = 180$ and 400 MK, the lognormal distribution appears to describe the probability density well, despite the 180 MK case having $t_{AD} > 1$. At $T = 100$ and 160 MK, where the test statistic $t_{AD} > 30$, the distributions have a sharp cut-off at $\approx 2 \times 10^{-12}$ and $\approx 2 \times 10^{-9}$ cm^3 mol^{-1} s^{-1}, respectively. This is an indication that a resonance strength upper-limit is truncating the distribution at these values, resulting in a probability density that appears to have characteristics of both the lognormal and (truncated) Porter-Thomas distributions. This effect was also observed in the previous Monte Carlo rate evaluation (See Section 4.5 in Iliadis *et al.* [2010b]) and will continue to be an issue until these resonances are studied. Despite the difficulties reconciling the ideal and observed distribution, the μ and σ values reported at these temperatures nevertheless offer a good estimate of the reaction rate and its uncertainty. At $T = 20$ and 50 MK, the reaction rate probability densities do not resemble lognormal distributions. Instead, they both have the likeness of a Porter-Thomas distribution. This indicates that the rate at these temperatures is entirely determined by the sampling of an unknown proton partial width, with little or no influence

T(GK)	Low Rate	Median Rate	High Rate	Lognormal μ	Lognormal σ	A-D
1.00×10^{-02}	8.63×10^{-39}	1.64×10^{-37}	4.15×10^{-36}	$-8.45 \times 10^{+01}$	$2.78 \times 10^{+00}$	$1.69 \times 10^{+02}$
1.10×10^{-02}	1.19×10^{-36}	3.39×10^{-35}	5.89×10^{-34}	$-7.95 \times 10^{+01}$	$2.85 \times 10^{+00}$	$5.71 \times 10^{+01}$
1.20×10^{-02}	1.28×10^{-34}	3.08×10^{-33}	3.74×10^{-32}	$-7.51 \times 10^{+01}$	$2.75 \times 10^{+00}$	$8.07 \times 10^{+01}$
1.30×10^{-02}	7.20×10^{-33}	1.40×10^{-31}	1.27×10^{-30}	$-7.14 \times 10^{+01}$	$2.60 \times 10^{+00}$	$1.34 \times 10^{+02}$
1.40×10^{-02}	2.29×10^{-31}	3.66×10^{-30}	2.67×10^{-29}	$-6.82 \times 10^{+01}$	$2.47 \times 10^{+00}$	$1.92 \times 10^{+02}$
1.50×10^{-02}	4.41×10^{-30}	6.09×10^{-29}	3.81×10^{-28}	$-6.54 \times 10^{+01}$	$2.37 \times 10^{+00}$	$2.51 \times 10^{+02}$
1.60×10^{-02}	5.66×10^{-29}	7.17×10^{-28}	3.89×10^{-27}	$-6.29 \times 10^{+01}$	$2.30 \times 10^{+00}$	$3.03 \times 10^{+02}$
1.80×10^{-02}	3.65×10^{-27}	4.18×10^{-26}	1.96×10^{-25}	$-5.89 \times 10^{+01}$	$2.21 \times 10^{+00}$	$3.78 \times 10^{+02}$
2.00×10^{-02}	9.39×10^{-26}	1.06×10^{-24}	4.79×10^{-24}	$-5.57 \times 10^{+01}$	$2.19 \times 10^{+00}$	$4.01 \times 10^{+02}$
2.50×10^{-02}	2.78×10^{-23}	3.25×10^{-22}	1.66×10^{-21}	$-4.99 \times 10^{+01}$	$2.25 \times 10^{+00}$	$3.34 \times 10^{+02}$
3.00×10^{-02}	1.05×10^{-21}	1.39×10^{-20}	8.59×10^{-20}	$-4.61 \times 10^{+01}$	$2.33 \times 10^{+00}$	$2.42 \times 10^{+02}$
4.00×10^{-02}	8.86×10^{-20}	1.40×10^{-18}	1.16×10^{-17}	$-4.14 \times 10^{+01}$	$2.39 \times 10^{+00}$	$1.10 \times 10^{+02}$
5.00×10^{-02}	1.54×10^{-18}	2.10×10^{-17}	2.09×10^{-16}	$-3.85 \times 10^{+01}$	$2.22 \times 10^{+00}$	$7.37 \times 10^{+01}$
6.00×10^{-02}	2.85×10^{-17}	1.40×10^{-16}	1.41×10^{-15}	$-3.62 \times 10^{+01}$	$1.81 \times 10^{+00}$	$2.84 \times 10^{+02}$
7.00×10^{-02}	5.45×10^{-16}	1.11×10^{-15}	5.81×10^{-15}	$-3.41 \times 10^{+01}$	$1.26 \times 10^{+00}$	$6.04 \times 10^{+02}$
8.00×10^{-02}	6.44×10^{-15}	1.32×10^{-14}	2.63×10^{-14}	$-3.19 \times 10^{+01}$	8.43×10^{-01}	$2.09 \times 10^{+02}$
9.00×10^{-02}	5.16×10^{-14}	1.13×10^{-13}	2.20×10^{-13}	$-2.98 \times 10^{+01}$	7.04×10^{-01}	$5.93 \times 10^{+01}$
1.00×10^{-01}	3.08×10^{-13}	7.02×10^{-13}	1.48×10^{-12}	$-2.80 \times 10^{+01}$	7.02×10^{-01}	$1.44 \times 10^{+02}$
1.10×10^{-01}	1.45×10^{-12}	3.38×10^{-12}	7.31×10^{-12}	$-2.65 \times 10^{+01}$	7.15×10^{-01}	$1.79 \times 10^{+02}$
1.20×10^{-01}	5.70×10^{-12}	1.31×10^{-11}	2.85×10^{-11}	$-2.51 \times 10^{+01}$	7.11×10^{-01}	$1.74 \times 10^{+02}$
1.30×10^{-01}	1.95×10^{-11}	4.29×10^{-11}	9.09×10^{-11}	$-2.39 \times 10^{+01}$	6.82×10^{-01}	$1.66 \times 10^{+02}$
1.40×10^{-01}	5.97×10^{-11}	1.23×10^{-10}	2.49×10^{-10}	$-2.28 \times 10^{+01}$	6.34×10^{-01}	$1.46 \times 10^{+02}$
1.50×10^{-01}	1.84×10^{-10}	3.34×10^{-10}	6.25×10^{-10}	$-2.18 \times 10^{+01}$	5.40×10^{-01}	$1.36 \times 10^{+02}$
1.60×10^{-01}	6.69×10^{-10}	9.96×10^{-10}	1.58×10^{-09}	$-2.07 \times 10^{+01}$	3.83×10^{-01}	$1.22 \times 10^{+02}$
1.80×10^{-01}	1.35×10^{-08}	1.52×10^{-08}	1.72×10^{-08}	$-1.80 \times 10^{+01}$	1.20×10^{-01}	$9.62 \times 10^{+00}$
2.00×10^{-01}	2.22×10^{-07}	2.41×10^{-07}	2.63×10^{-07}	$-1.52 \times 10^{+01}$	8.59×10^{-02}	5.40×10^{-01}
2.50×10^{-01}	4.24×10^{-05}	4.61×10^{-05}	5.01×10^{-05}	$-9.99 \times 10^{+00}$	8.49×10^{-02}	2.75×10^{-01}
3.00×10^{-01}	1.44×10^{-03}	1.56×10^{-03}	1.69×10^{-03}	$-6.46 \times 10^{+00}$	8.02×10^{-02}	2.03×10^{-01}
3.50×10^{-01}	1.81×10^{-02}	1.95×10^{-02}	2.10×10^{-02}	$-3.94 \times 10^{+00}$	7.40×10^{-02}	2.26×10^{-01}
4.00×10^{-01}	1.23×10^{-01}	1.31×10^{-01}	1.41×10^{-01}	$-2.03 \times 10^{+00}$	6.77×10^{-02}	3.29×10^{-01}
4.50×10^{-01}	5.51×10^{-01}	5.86×10^{-01}	6.23×10^{-01}	-5.34×10^{-01}	6.20×10^{-02}	4.44×10^{-01}
5.00×10^{-01}	$1.84 \times 10^{+00}$	$1.95 \times 10^{+00}$	$2.07 \times 10^{+00}$	6.69×10^{-01}	5.73×10^{-02}	4.88×10^{-01}
6.00×10^{-01}	$1.14 \times 10^{+01}$	$1.20 \times 10^{+01}$	$1.26 \times 10^{+01}$	$2.48 \times 10^{+00}$	5.09×10^{-02}	4.42×10^{-01}
7.00×10^{-01}	$4.17 \times 10^{+01}$	$4.37 \times 10^{+01}$	$4.59 \times 10^{+01}$	$3.78 \times 10^{+00}$	4.72×10^{-02}	3.93×10^{-01}
8.00×10^{-01}	$1.10 \times 10^{+02}$	$1.15 \times 10^{+02}$	$1.20 \times 10^{+02}$	$4.74 \times 10^{+00}$	4.50×10^{-02}	4.96×10^{-01}
9.00×10^{-01}	$2.32 \times 10^{+02}$	$2.42 \times 10^{+02}$	$2.53 \times 10^{+02}$	$5.49 \times 10^{+00}$	4.37×10^{-02}	5.81×10^{-01}
$1.00 \times 10^{+00}$	$4.19 \times 10^{+02}$	$4.37 \times 10^{+02}$	$4.56 \times 10^{+02}$	$6.08 \times 10^{+00}$	4.27×10^{-02}	6.70×10^{-01}
$1.25 \times 10^{+00}$	$1.19 \times 10^{+03}$	$1.24 \times 10^{+03}$	$1.29 \times 10^{+03}$	$7.12 \times 10^{+00}$	4.12×10^{-02}	$1.05 \times 10^{+00}$
$1.50 \times 10^{+00}$	$2.35 \times 10^{+03}$	$2.44 \times 10^{+03}$	$2.55 \times 10^{+03}$	$7.80 \times 10^{+00}$	4.01×10^{-02}	$1.42 \times 10^{+00}$
$1.75 \times 10^{+00}$	$3.79 \times 10^{+03}$	$3.94 \times 10^{+03}$	$4.10 \times 10^{+03}$	$8.28 \times 10^{+00}$	3.92×10^{-02}	$1.78 \times 10^{+00}$
$2.00 \times 10^{+00}$	$5.41 \times 10^{+03}$	$5.62 \times 10^{+03}$	$5.84 \times 10^{+03}$	$8.63 \times 10^{+00}$	3.86×10^{-02}	$2.10 \times 10^{+00}$
$2.50 \times 10^{+00}$	$8.95 \times 10^{+03}$	$9.28 \times 10^{+03}$	$9.63 \times 10^{+03}$	$9.14 \times 10^{+00}$	3.77×10^{-02}	$2.23 \times 10^{+00}$
$3.00 \times 10^{+00}$	$1.27 \times 10^{+04}$	$1.31 \times 10^{+04}$	$1.36 \times 10^{+04}$	$9.48 \times 10^{+00}$	3.74×10^{-02}	$1.82 \times 10^{+00}$
$3.50 \times 10^{+00}$	$1.65 \times 10^{+04}$	$1.71 \times 10^{+04}$	$1.77 \times 10^{+04}$	$9.75 \times 10^{+00}$	3.75×10^{-02}	$1.57 \times 10^{+00}$
$4.00 \times 10^{+00}$	$2.03 \times 10^{+04}$	$2.10 \times 10^{+04}$	$2.19 \times 10^{+04}$	$9.95 \times 10^{+00}$	3.77×10^{-02}	$1.57 \times 10^{+00}$
$5.00 \times 10^{+00}$	$2.77 \times 10^{+04}$	$2.87 \times 10^{+04}$	$2.99 \times 10^{+04}$	$1.03 \times 10^{+01}$	3.82×10^{-02}	$1.45 \times 10^{+00}$
$6.00 \times 10^{+00}$	$3.44 \times 10^{+04}$	$3.57 \times 10^{+04}$	$3.72 \times 10^{+04}$	$1.05 \times 10^{+01}$	3.89×10^{-02}	$1.44 \times 10^{+00}$
$7.00 \times 10^{+00}$	$4.02 \times 10^{+04}$	$4.18 \times 10^{+04}$	$4.35 \times 10^{+04}$	$1.06 \times 10^{+01}$	4.00×10^{-02}	$1.31 \times 10^{+00}$
$8.00 \times 10^{+00}$	$4.48 \times 10^{+04}$	$4.67 \times 10^{+04}$	$4.86 \times 10^{+04}$	$1.08 \times 10^{+01}$	4.12×10^{-02}	$1.18 \times 10^{+00}$
$9.00 \times 10^{+00}$	$4.84 \times 10^{+04}$	$5.05 \times 10^{+04}$	$5.27 \times 10^{+04}$	$1.08 \times 10^{+01}$	4.26×10^{-02}	$1.19 \times 10^{+00}$
$1.00 \times 10^{+01}$	$5.11 \times 10^{+04}$	$5.34 \times 10^{+04}$	$5.58 \times 10^{+04}$	$1.09 \times 10^{+01}$	4.39×10^{-02}	$1.26 \times 10^{+00}$

Table 8.4: The ^{30}Si(p,γ)^{31}P reaction rates from this study calculated using the reaction rate Monte Carlo code, `RatesMC` [Longland *et al.*, 2010b].

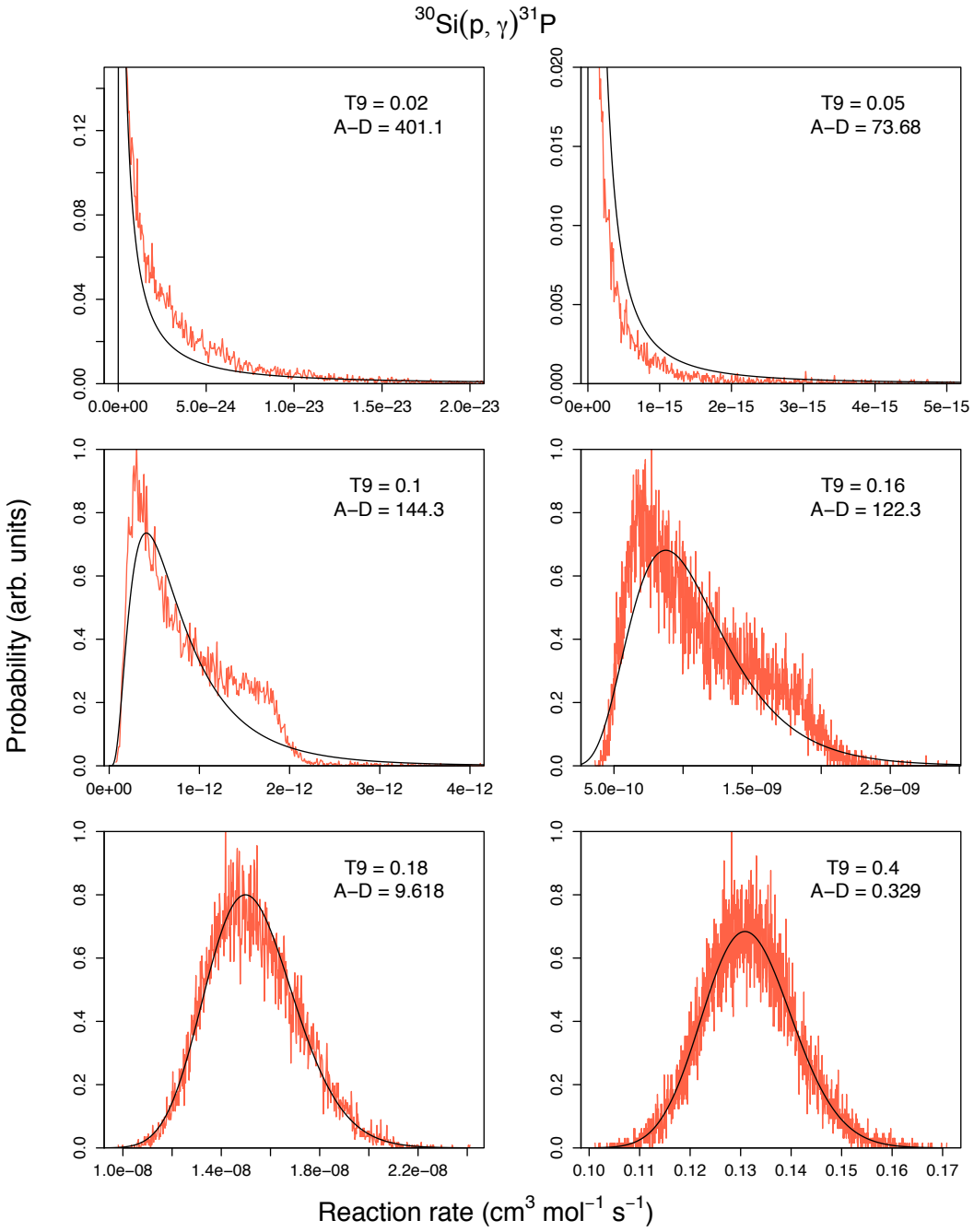

Figure 8.3: Reaction rate probability density functions calculated by the reaction rate Monte Carlo code, `RatesMC` [Longland *et al.*, 2010b], at $T = 0.02$ GK, 0.05 GK, 0.1 GK, 0.16 GK, 0.18 GK and 0.4 GK. The red histograms are the Monte Carlo rates and the solid black lines are lognormal probabilty density functions, calculated based on the mean and variance of the data. The Anderson-Darling test statistic is shown in each figure.

from experimentally determined values. Still, the description of these data using the lognormal distribution does appear to effectively communicate their width, which is their most important feature.

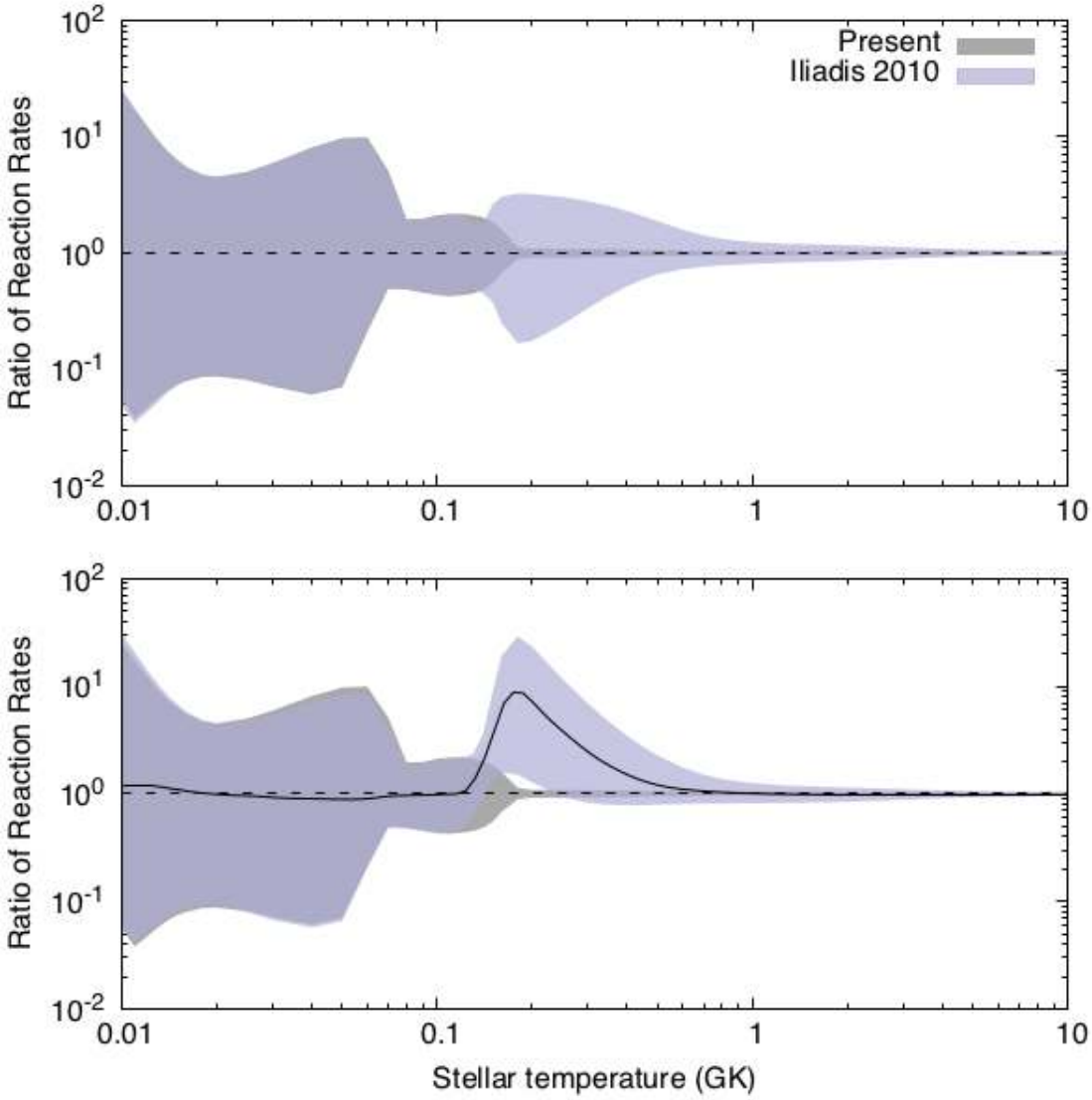

Figure 8.4: Reaction rate comparison of present results with the evaluation in [Iliadis *et al.*, 2010b]. The shaded areas correspond to the 68% coverage probability for the each rate. (Top) The two rates have been normalized to their respective median values. (Bottom) Both rates are normalized to the new recommended rate median value. The solid black line shows the ratio of previous and present recommended values.

A comparison of the new rate against the previous evaluation in Iliadis *et al.* [2010b] is shown in Figure 8.4. In the top panel, the present and previous recommended rates have been normalized to their median values. The shaded regions correspond to the 68% coverage interval of the Iliadis

et al. [2010b] rate (purple) and the new recommended rate (gray). The effect of the present work on the rate is clear: the rate uncertainty has been reduced significantly in the 160 MK to 1 GK range. This is because in the previous evaluation, Iliadis *et al.* [2010b], the contribution of the 435-keV resonance was estimated by sampling its resonance strength from a Porter-Thomas distribution. So, the broad uncertainty of their rate was due to the widely varying resonance strength. The new measurement of the 435-keV resonance strength improves upon this uncertainty dramatically. At a temperature of 200 MK, for instance, the factor uncertainty has been reduced from 3.52 to 1.09. The uncertainty below 100 MK has not been affected, since it is based entirely on the upper-limits of unobserved resonances. The upper-limits adopted in Iliadis *et al.* [2010b] were very similar to those in the present work, since many of the arguments in Section 8.1.2 applied to the previous evaluation as well.

In the bottom plot, the Iliadis *et al.* [2010b] rate has been normalized to the new recommended rate. The solid line shown is given by their ratio. This plot shows that the present work reduces the rate by nearly a factor of 10 at T= 180 MK. This is again a consequence of the 435-keV resonance strength, which is two orders of magnitude weaker than the Porter-Thomas mean value in Iliadis *et al.* [2010b]. This point was illustrated earlier in Figure 7.17.

A contour plot of the ^{30}Si(p,γ)^{31}P reaction rate is shown in Figure 8.5, where the rate samples have been normalized to their median value. The shading indicates the coverage probability in percent, as given by the legend on the right. The thick and thin black lines denote the high and low Monte Carlo rates for a coverage probability of 68% and 95%, respectively. The most striking feature of this plot is the width of the 95% coverage interval below 100 MK, which spans three orders of magnitude. As the coverage probability nears 100%, the distribution grows by another factor of 10.

The cause of this is elucidated in Figure 8.6, where the percent contribution of each resonance (or direct capture cross section) to the Monte Carlo reaction rate is indicated as a colored band. The width of each band represents the uncertainty in the contribution of the corresponding process. Note that the resonance energies are given in the center-of-mass frame. Between 70 and 180 MK, the $E_r^{c.m.} = 169$ keV resonance and the direct capture cross section are the two main contributers to the reaction rate. Their width indicates that the percent contribution for each is highly uncertain. This is a consequence of the unknown strength of the $E_r^{c.m.} = 169$ keV resonance. Below 80 MK,

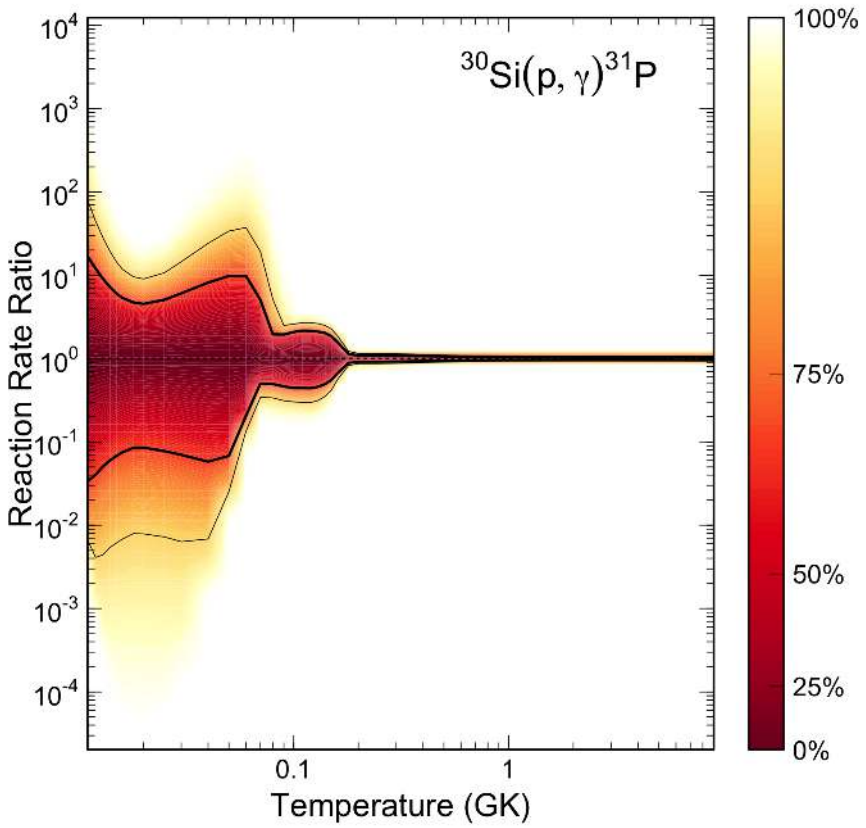

Figure 8.5: Contour plot of the reaction rate probability density as a function of temperature. The shading indicates the coverage probability in percent. The thick and thin solid black lines indicate the high and low Monte Carlo rates for a coverage probability of 68% and 95%, respectively.

the $E_r^{c.m.} = 52$ keV resonance appears to be the dominant process contributing to the rate. It should be emphasized that although the width of this band corresponds to the uncertainty in the contribution, the fact that this band is narrow does not indicate confidence in the magnitude of the rate at these temperatures. Rather, this implies that the $E_r^{c.m.} = 52$ keV resonance — whatever its true strength may be — is responsible for 100% of the reactions at these temperatures. This is a consequence of the incredibly weak resonance strength ($\omega\gamma \approx 10^{-41}$ eV) estimated for the $E_r^{c.m.} = 17$ keV resonance, which is practically negligible compared to the estimated contribution of the $E_r^{c.m.} = 52$ keV resonance, which has an upper limit of $\omega\gamma_{u.l.} \approx 10^{-16}$ eV. The contribution plot also shows that the 435-keV resonance, which was thought to be the dominant resonance at temperatures between 100-300 MK, is in fact inconsequential. The $E_r^{c.m.} = 483$ keV resonance, which was previously estimated to contribute less than 50% of the reactions in this range [Dermigny

and Iliadis, 2017], is instead the most dominant, accounting for nearly 100% of the reactions.

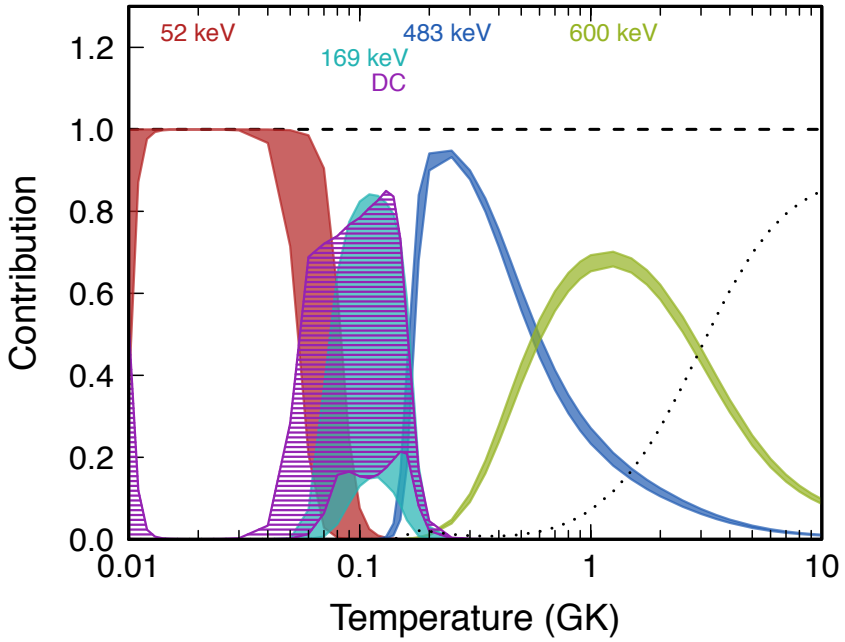

Figure 8.6: The fractional contributions made by ^{30}Si(p,γ)^{31}P resonances and direct capture (labeled "DC") towards the total reaction rate. The contribution ranges are shown as colored bands, which correspond to their label above. The thickness of each band represents the uncertainty of the contribution. Between 80 and 160 MK, the $E_r^{c.m.} = 169$ keV resonance and the direct capture process are the two main contributors. Below that, the $E_r^{c.m.} = 52$ keV resonance dominates. The dotted black line shows the contribution of resonances with energies larger than 620 keV.

Figure 8.6 also suggests new research directions for further improving the ^{30}Si(p,γ)^{31}P reaction rate. The current estimates for the $E_r^{c.m.} = 169$ keV ($E_r^{lab} = 179$ keV) resonance strength, which assumed $\ell_p = 3$, is conservative, and so its contribution is likely over estimated. An investigation of its resonance strength would therefore improve the reaction rate uncertainty between 80 and 180 MK. This resonance is within the energy range accessible to the Electron Cyclotron Resonance (ECR) source at LENA [Cesaratto *et al.*, 2010, Cooper *et al.*, 2018], however, a direct measurement might be difficult given the upper-limit of $\omega\gamma_{u.l.} = 1.2 \times 10^{-10}$ eV. Assuming even modest levels of background, the LENA system simply does not have the detection sensitivity required at present. For a point of comparison, inducing 100 (p,γ) reactions via the $E_r^{c.m.} = 169$ keV resonance, assuming $\omega\gamma = \omega\gamma_{u.l.}$, would require 2200 Coulombs of incident proton beam. If one considers the detection efficiencies and background signal, the necessary beam-time quickly becomes untenable. An indirect

reaction study using the ^{30}Si(^{3}He, d)^{31}P reaction would be much more appropriate, since it could be accomplished in far less time. For comparison, the data shown in Figure 8.1 was collected in less than one hour [Vernotte *et al.*, 1990]. A high statistics investigation of the $E_x = 7-8$ MeV range in the ^{31}P level structure, without interference from the ^{17}F contaminant peak observed in that work, could allow for a measurement of the spectroscopic factors for the 7349, 7441, and 7466-keV excited states. Such an experiment could also help to identify previously unobserved states important to the ^{30}Si(p,γ)^{31}P reaction.

CHAPTER 9: CONCLUSION

Globular clusters continue to be invaluable probes of stellar and galactic evolution. Among the most widely discussed problems today is the origin of their abundance anomalies. This dissertation represents a substantial effort towards understanding this complex issue. In particular, we focused on the Mg-K anticorrelation observed in the globular cluster NGC 2419. Two proton capture resonances were studied at the LENA accelerator facility in Durham, North Carolina. Analysis of their γ-ray deexcitation spectra allowed for an improved thermonuclear rate for the ^{30}Si(p,γ)^{31}P reaction, which had been identified in Dermigny and Iliadis [2017] as being critical to our understanding of this bizarre chemical signature.

This was the first direct measurement of the narrow resonance at $E_r^{lab} = 433.5 \pm 0.3$ keV. Little was known about this resonance, since it had been discovered only recently using indirect measurements in Vernotte *et al.* [1990]. A resonance strength of $\omega\gamma_{433} = 88 \pm 19$ μeV was obtained via a thick-target relative yield measurement. This is much weaker than had been estimated, and it was shown that this resonance must not contribute significantly to the ^{30}Si(p,γ)^{31}P reaction, as was previously thought. The resonance at $E_r^{lab} = 499.5 \pm 0.2$ keV was also studied using the same method. It had been measured before by Hoogenboom [1958] and Riihonen *et al.* [1979], though their results are in tension with one another, amounting to a factor of two discrepancy. The new resonance strength, $\omega\gamma_{499} = 188 \pm 14$ meV, is in excellent agreement with the Riihonen *et al.* [1979] value and improves upon the uncertainty. This resonance was thought to be a minor contribution to the reaction rate. However, in light of the new 435-keV resonance strength, it was instead found to be the dominant resonance in the temperature range 100 - 500 MK. Compared to the previous evaluation in Iliadis *et al.* [2010b], the effect of these new measurements is to lower the thermonuclear rate for the ^{30}Si(p,γ)^{31}P reaction by approximately a factor of 10 at temperatures between 160 MK and 300 MK. They also reduced the reaction rate factor uncertainty in this range dramatically.

As a result of this work, the ^{30}Si(p,γ)^{31}P reaction rate has been improved significantly at the

temperatures relevant to the pollution sequence in NGC 2419. This is only one piece of the puzzle though. To make further strides in this area, the ^{37}Ar(p,γ)^{38}K, ^{38}Ar(p,γ)^{39}K, and ^{39}K(p,γ)^{40}Ca reactions will need to measured, given their crucial roles in the Ar-K nucleosynthesis chain. These will be technically demanding experiments, requiring several new innovations in targetry. I am excited to see how the nuclear astrophysics community rises to meet these next challenges.

APPENDIX A: CODES, PROCEDURES, AND MISCELLANEA

In the following few sections the various codes used throughout this dissertation are described. The yield curve fitting program used in Section 6.2 is explained in Appendix A.1. In the interest of transparency, all of the programs used and the data are available on github for download or analysis at https://github.com/jdermigny.

APPENDIX A.1: Yield Curve Fitting

The yield curve fitting program is based on the `YCurve.R` code, which has been used for the analysis of yield curves in [Buckner, 2014, Cesaratto, 2011]. The main difference between the code used in this dissertation and previous analyses is that the newest version uses an affine invariant Markov Chain Monte Carlo (MCMC) ensemble sampler [Goodman and Weare, 2010] for Bayesian parameter estimation, whereas the previous version used an implementation of the Metropolis-Hastings algorithm. For highly-correlated parameters, the affine invariant sampler provided by the software package `emcee.py` [Foreman-Mackey *et al.*, 2013] affords a marked improvement in performance. For future analyses, this means that computationally expensive models will be more tractable.

The fitting model assumes that the observed data points are sampled from a Normal distribution with a mean given by $\epsilon \cdot Y(E,\hat{\theta})$, the adjusted yield excitation function at energy E given the parameters $\hat{\theta}$, and a variance determined by the counting statistics observed in the data. The adjustment factor, ϵ, represents the systematic offset of each data set, which might be a result of different detector geometry or error in charge integration, for example. The log-likelihood, assuming two data sets (labeled n and m) is given by:

$$\ln p(y|E,\hat{\theta},\epsilon_n,\epsilon_m) = -\frac{1}{2}\sum_n \left[\frac{(y_n-\epsilon_n Y(E,\hat{\theta}))^2}{\sigma_n^2}+\ln(2\pi\sigma_n^2)\right]-\frac{1}{2}\sum_m \left[\frac{(y_m-\epsilon_m Y(E,\hat{\theta}))^2}{\sigma_m^2}+\ln(2\pi\sigma_m^2)\right] \tag{A.1}$$

The vector $\hat{\theta}$ contains all of the parameters to determine the shape of the yield curve. This includes the resonance energy (E_r), the width of the target layer (ΔE), the beam-energy (Δ_b), the straggling constant (Δ_s), and the maximum yield (Y_{max}). For a discussion of how these are used to calculate

the yield curve, see Iliadis [2015]. For the analyses in this dissertation, E_r was set to the observed resonance energy and kept constant to facilitate efficient mixing. The priors for all the other parameters are uninformative, flat distributions, such that:

$$\ln p(\hat{\theta}) = 1 \tag{A.2}$$

For the two adjustment factors, ϵ_n and ϵ_m, the most likely value is unity, meaning that there is no systematic offset. This is encoded in the prior by assuming a Normal distribution for each:

$$\ln p(\epsilon_n, \epsilon_m) = -\frac{1}{2}\frac{(1-\epsilon_n)^2}{\alpha^2} - \frac{1}{2}\frac{(1-\epsilon_m)^2}{\alpha^2}, \tag{A.3}$$

where α, the standard deviation, is set to $\alpha = 3\%$. The posterior distribution, the probability of parameters θ, ϵ_n, and ϵ_m, given the data, is then:

$$p(\hat{\theta}, \epsilon_n, \epsilon_m|y) \propto \ln p(y|E, \hat{\theta}, \epsilon_n, \epsilon_m) + \ln p(\epsilon_n, \epsilon_m) + \ln p(\hat{\theta}). \tag{A.4}$$

For both of the yield curve analyses cited in Section 6.2, the posterior distribution was sampled for a total of 40,000 steps. Of these, the first 20,000 were discarded as "burn-in", since the sampler had not yet converged. The remaining samples were then histogrammed to form the marginalized posterior probability distributions. For the analysis of the "final" yield curve set, the trace, the sampled value at each of the accepted steps, is shown in Figure A.1 for each parameter. The random nature of the scatter indicates that the sampler has converged upon the solution. In Figure A.2, the values of all the parameters are plotted against each other, revealing covariances between the parameters. The elliptical distributions seen in the ϵ_1, ϵ_2, and Y_{max} scatter plots elucidate the coupling between these parameters. This relationship is intuitive, given that their products enter into the log-likelihood. At the top of each column, the marginalized posterior probability distribution for that parameter is shown. The Gaussian shape of the these suggests that the data is well described by the fitting model. Estimates for each parameter, based on the observed data, were then derived by calculating the highest probability interval from their respective distribution. A discussion of these results is found in Section 6.2.

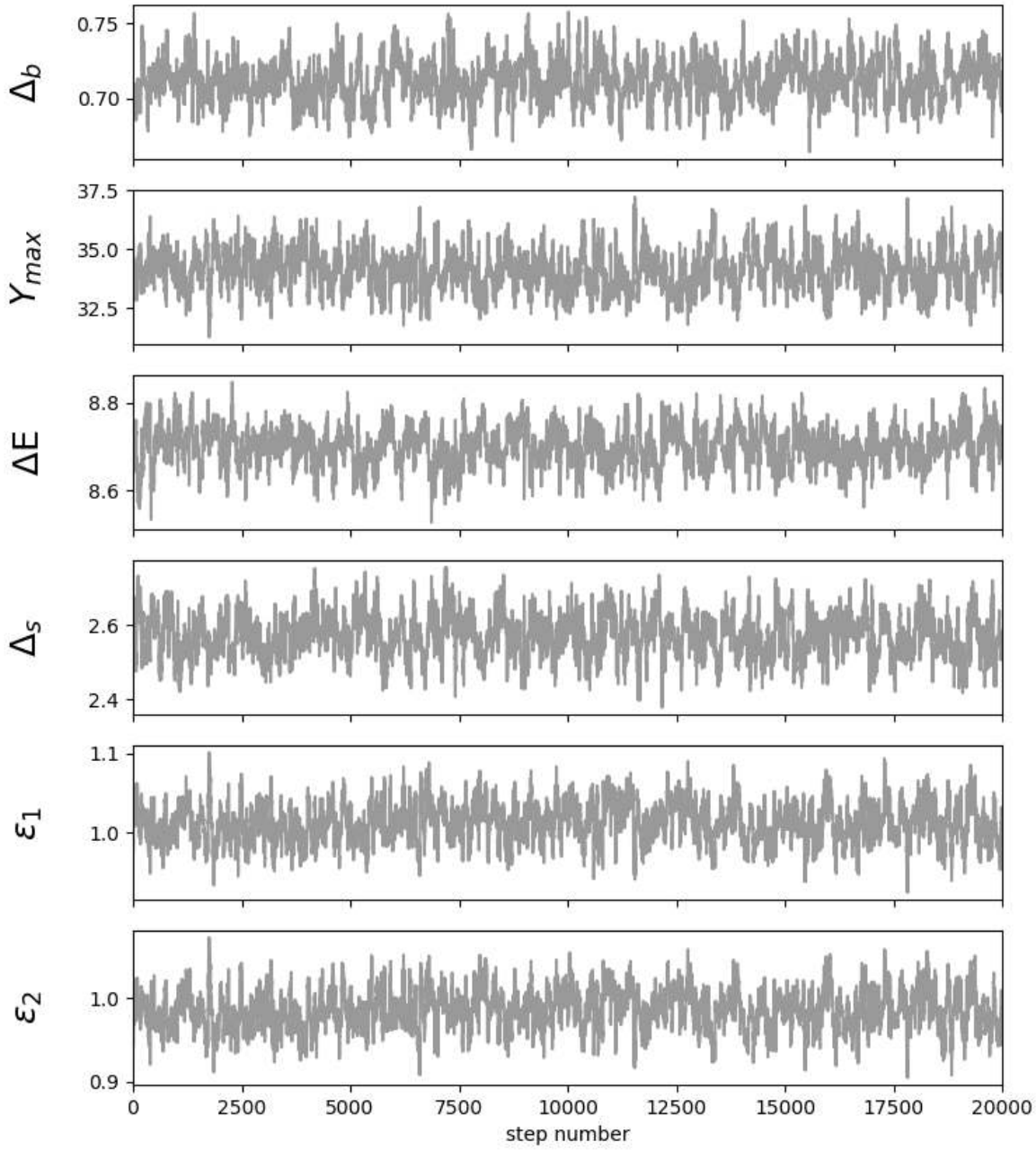

Figure A.1: The parameter values at each step during the posterior distribution sampling, or the "trace", is shown for the beam-width (Δ_b), the maximum yield (Y_{max}), the target thickness (ΔE), the straggling constant (Δ_s), and the two adjustment factors (ϵ_1 and ϵ_2).

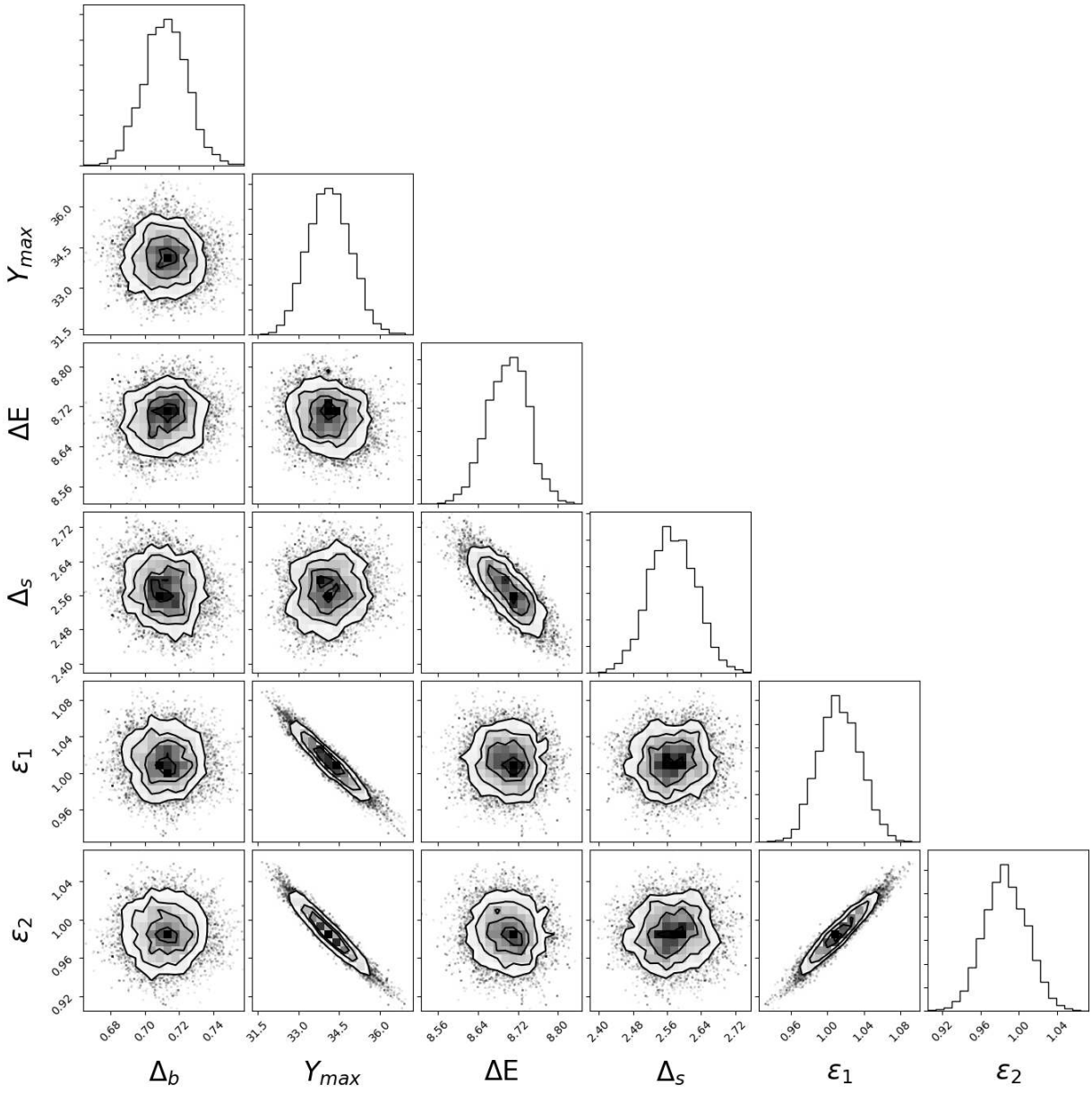

Figure A.2: A scatter-plot matrix of the yield curve parameter samples, built from the traces shown in Figure A.1. The relationships between distributions reveal covariances between the different parameters. Plots are shown for the beam-width (Δ_b), the maximum yield (Y_{max}), the target thickness (ΔE), the straggling constant (Δ_s), and the two adjustment factors (ϵ_1 and ϵ_2). This figure was generated using the `corner.py` package [Foreman-Mackey, 2016].

APPENDIX A.2: Sum Correction Code

In a close detector-source geometry, the analysis of a γ-ray pulse-height spectrum is often complicated by coincidence summing. This effect occurs when two or more γ-rays are emitted in coincidence from the decay of the same nucleus, and are recorded as one pulse within the resolving time of the detector. This can either add counts to a peak ("summing in") or subtract from the peak ("summing out"). The magnitude of this effect is dependent on the details of the decay scheme and the solid angle subtended by the detector. For the LENA $\gamma\gamma$-coincidence spectrometer, summing effects often need to be corrected for.

To that end, the program `semkow_uncertainty.py` was written to implement the sum coincidence correction method of Semkow *et al.* [1990]. Following their algorithm, the equation:

$$\frac{S_{ji}}{I_{ji}} - \frac{D_{ji}}{[N^{(0)}c]_{ji}} = \epsilon^{p}_{ji}, \tag{A.5}$$

is solved iteratively, where for the deexcitation from state j to i, S_{ji} is the measured photo-peak intensity in the presence of coincidence summing, I_{ji} is the emission rate, $[N^{(0)}c]_{ji}$ is the decay probability, and D_{ji} is a term that corrects for the effects of coincidence summing, and finally, ϵ^{p}_{ji} is the full-energy peak efficiency. In addition to the measured intensities, the program requires as input a table of all the relevant energy levels, their feeding fractions and their branching ratios with respective uncertainties. In Section 4.3, this program was used to calculate the peak efficiencies for γ-rays emanating from several different reactions. In Figure A.3, the input file used for the ^{14}N(p,γ)^{15}O data is shown. Alternatively, one could use this code to derive the total decay rate or simply to correct a single peak for coincidence summing.

```
N-Levels
7       0

Energy-Levels
0.0     0.0
5183.0  0.0
5240.9  0.0
6176.3  0.0
6793.1  0.0
6859.4  0.0
7275.9  0.0
7556.5  1.0

B-Values
1       0       100.0000        0.0000
2       0       100.0000        0.0000
3       0       100.0000        0.0000
4       0       100.0000        0.0000
5       0       100.0000        0.0000
6       0       4.0000          1.2000
6       2       100.0000        1.2000
7       0       1.500   0.0300
7       1       16.9000 0.4000
7       2       0.22000 0.0700
7       3       58.3000 0.3000
7       4       23.0000 0.3000
7       5       0.14000 0.0400

Measured
1       0       684.0000        39.0000
3       0       1945.0000       52.0000
4       0       745.0000        36.0000
7       0       230.0000        16.0000
7       1       1350.0000       44.5000
7       3       6762.9000       88.2000
7       4       3461.1000       77.0000
```

Figure A.3: An example input-file for `semkow_uncertainty.py`, written for the $E_p^{lab} = 278$ keV resonance in the ^{14}N(p,γ)^{15}O reaction. Branching ratios and their errors were adopted from Daigle *et al.* [2016]. Energy levels are those recommended in Ajzenberg-Selove [1991].

APPENDIX A.3: RatesMC input file for ^{30}Si(p,γ)^{31}P

The `RatesMC` input file used to calculate the new ^{30}Si(p,γ)^{31}P thermonuclear rate in Section 8.3 is presented. Due to the length of this file, it has been split into three pieces, shown consecutively in Figures A.4, A.5, and A.6. An explanation of the input file format can be found in Iliadis *et al.* [2010a]. The major differences over the input file used for the last reaction rate evaluation in Iliadis *et al.* [2010b] are the new resonance strength measurements for the $E_r^{lab} = 435$ and 498 keV resonances. The non-resonant (direct capture) S-factor parameterization has also been changed from a 1st order to 2nd order polynomial.

```
30Si(p,g)31P
*****************************************************************************************************************************************
1                 ! Zproj
14                ! Ztarget
0                 ! Zexitparticle (=0 when only 2 channels open)
1.0072764         ! Aproj [nuclear mass]
29.966082         ! Atarget [nuclear mass]
0                 ! Aexitparticle (=0 when only 2 channels open)
0.5               ! Jproj
0.0               ! Jtarget
0                 ! Jexitparticle (=0 when only 2 channels open)
7297.96           ! projectile separation energy (keV) [based on nuclear masses]
0                 ! exit particle separation energy (=0 when only 2 channels open)
1.25              ! Radius parameter R0 (fm)
2                 ! Gamma-ray channel number (=2 if ejectile is a g-ray; =3 otherwise)
*****************************************************************************************************************************************
1.0               ! Minimum energy for numerical integration (keV)
20000             ! Number of random samples (>5000 for better statistics)
0                 ! =0 for rate output at all temperatures; =NT for rate output at selected temperatures
*****************************************************************************************************************************************
Non-resonant contribution
S(keVb)           S'(b)         S''(b/keV)          fracErr      Cutoff Energy (keV)
221.3             -5.52e-2      3.37e-5             0.4          1000.0
0.0               0.0           0.0                 0.0          0.0
*****************************************************************************************************************************************
Resonant Contribution
Note: G1 = entrance channel, G2 = exit channel, G3 = spectator channel !! Ecm, Exf in (keV); wg, Gx in (eV) !!
Note: if Er<0, theta^2=C2S*theta_sp^2 must be entered instead of entrance channel partial width
Ecm         DEcm        wg          Dwg         Jr    G1    DG1   L1    G2    DG2   L2    G3    DG3   L3    Exf   Int   Prob
17.45       4.0         1.16E-41    4.64E-42    0     0     0     0     0     0     0     0     0     0     0     0
+                       1.55E-41    6.19E-42    0     0     0     0     0     0     0     0     0     0     0     0     0.5
419.4       0.3         8.70E-5     1.60E-54    0     0     0     0     0     0     0     0     0     0     0     0
439.45      4.0         2.87E-4     1.15E-4     0     0     0     0     0     0     0     0     0     0     0     0
+                       3.82E-4     1.53E-4     0     0     0     0     0     0     0     0     0     0     0     0     0.5
483.3       0.2         1.88E-01    0.17E-01    0     0     0     0     0     0     0     0     0     0     0     0
```

Figure A.4: (Part I) RatesMC input file for the ^{30}Si(p,γ)^{31}P reaction.

600.2	1.2	1.95E+00	1.00E–01	0	0	0	0	0	0	0	0	0	0	0	0
648.9	1.0	7.80E–02	6.00E–03	0	0	0	0	0	0	0	0	0	0	0	0
735.6	0.9	8.68E–02	9.00E–02	0	0	0	0	0	0	0	0	0	0	0	0
752.1	1.0	4.40E–01	3.20E–02	0	0	0	0	0	0	0	0	0	0	0	0
808.1	1.3	1.95E–01	4.50E–02	0	0	0	0	0	0	0	0	0	0	0	0
911.4	0.6	8.81E–01	2.00E–01	0	0	0	0	0	0	0	0	0	0	0	0
928.1	0.6	1.45E–01	3.50E–02	0	0	0	0	0	0	0	0	0	0	0	0
946.4	0.6	6.92E–01	1.50E–01	0	0	0	0	0	0	0	0	0	0	0	0
950.5	0.6	8.18E–01	2.00E–01	0	0	0	0	0	0	0	0	0	0	0	0
1059.0	0.6	1.06E–01	3.19E–02	0	0	0	0	0	0	0	0	0	0	0	0
1137.2	0.7	1.82E–01	5.45E–02	0	0	0	0	0	0	0	0	0	0	0	0
1164.3	0.7	7.09E–01	2.13E–01	0	0	0	0	0	0	0	0	0	0	0	0
1173.6	0.7	4.88E–02	1.46E–02	0	0	0	0	0	0	0	0	0	0	0	0
1246.9	0.8	1.42E–01	4.25E–02	0	0	0	0	0	0	0	0	0	0	0	0
1255.5	0.8	5.76E–01	1.73E–01	0	0	0	0	0	0	0	0	0	0	0	0
1258.7	0.8	4.43E–01	1.33E–01	0	0	0	0	0	0	0	0	0	0	0	0
1278.9	0.8	1.02E+00	3.06E–01	0	0	0	0	0	0	0	0	0	0	0	0
1287.4	0.8	0.14	0.04	0	0	0	0	0	0	0	0	0	0	0	0
1304.2	0.8	0.05	0.01	0	0	0	0	0	0	0	0	0	0	0	0
1344.5	0.8	1.55	0.47	0	0	0	0	0	0	0	0	0	0	0	0
1352.7	0.8	1.95	0.59	0	0	0	0	0	0	0	0	0	0	0	0
1432.3	0.8	2.13	0.64	0	0	0	0	0	0	0	0	0	0	0	0
1433.8	0.8	1.42	0.43	0	0	0	0	0	0	0	0	0	0	0	0
1441.2	0.8	0.89	0.27	0	0	0	0	0	0	0	0	0	0	0	0
1457.5	0.8	0.03	0.01	0	0	0	0	0	0	0	0	0	0	0	0
1460.6	0.8	1.55	0.47	0	0	0	0	0	0	0	0	0	0	0	0
1466.6	0.9	0.35	0.11	0	0	0	0	0	0	0	0	0	0	0	0
1543.2	0.9	0.18	0.05	0	0	0	0	0	0	0	0	0	0	0	0
1606.2	1.0	0.35	0.11	0	0	0	0	0	0	0	0	0	0	0	0
1613.0	1.0	0.35	0.11	0	0	0	0	0	0	0	0	0	0	0	0
1639.1	1.0	1.06	0.32	0	0	0	0	0	0	0	0	0	0	0	0
1696.9	1.0	0.18	0.05	0	0	0	0	0	0	0	0	0	0	0	0
1712.3	1.1	1.24	0.37	0	0	0	0	0	0	0	0	0	0	0	0
1749.4	1.1	1.95	0.59	0	0	0	0	0	0	0	0	0	0	0	0
1756.0	1.1	0.44	0.13	0	0	0	0	0	0	0	0	0	0	0	0
1770.4	1.1	1.51	0.45	0	0	0	0	0	0	0	0	0	0	0	0
1816.8	0.6	0.40	0.12	0	0	0	0	0	0	0	0	0	0	0	0
1818.9	0.6	2.13	0.64	0	0	0	0	0	0	0	0	0	0	0	0
1831.9	0.6	0.26	0.08	0	0	0	0	0	0	0	0	0	0	0	0
1834.3	0.6	0.62	0.19	0	0	0	0	0	0	0	0	0	0	0	0
1857.6	0.6	0.32	0.10	0	0	0	0	0	0	0	0	0	0	0	0
1859.7	0.6	0.75	0.23	0	0	0	0	0	0	0	0	0	0	0	0
1879.4	0.6	0.58	0.17	0	0	0	0	0	0	0	0	0	0	0	0
1909.5	0.6	0.30	0.09	0	0	0	0	0	0	0	0	0	0	0	0
1929.7	0.6	0.41	0.12	0	0	0	0	0	0	0	0	0	0	0	0
1944.1	0.7	0.88	0.26	0	0	0	0	0	0	0	0	0	0	0	0
1956.3	0.7	0.46	0.14	0	0	0	0	0	0	0	0	0	0	0	0
1959.3	0.7	0.44	0.13	0	0	0	0	0	0	0	0	0	0	0	0
1994.2	0.7	0.69	0.21	0	0	0	0	0	0	0	0	0	0	0	0
2023.0	0.8	0.33	0.10	0	0	0	0	0	0	0	0	0	0	0	0
2061.6	0.8	0.25	0.07	0	0	0	0	0	0	0	0	0	0	0	0
2064.3	0.8	0.69	0.21	0	0	0	0	0	0	0	0	0	0	0	0
2103.2	0.8	0.22	0.07	0	0	0	0	0	0	0	0	0	0	0	0
2115.9	0.8	5.91	1.77	0	0	0	0	0	0	0	0	0	0	0	0
2144.2	0.9	0.69	0.21	0	0	0	0	0	0	0	0	0	0	0	0

Figure A.5: (Part II) RatesMC input file for the ^{30}Si(p,γ)^{31}P reaction.

```
2152.3   0.9   1.26   0.38   0 0 0 0 0 0 0 0 0 0 0 0
2180.4   0.9   0.16   0.05   0 0 0 0 0 0 0 0 0 0 0 0
2228.1   0.9   0.75   0.23   0 0 0 0 0 0 0 0 0 0 0 0
2239.9   1.0   0.69   0.21   0 0 0 0 0 0 0 0 0 0 0 0
2273.9   1.0   1.38   0.42   0 0 0 0 0 0 0 0 0 0 0 0
2281.2   1.0   0.63   0.19   0 0 0 0 0 0 0 0 0 0 0 0
2288.5   1.0   1.82   0.55   0 0 0 0 0 0 0 0 0 0 0 0
2297.3   1.0   0.69   0.21   0 0 0 0 0 0 0 0 0 0 0 0
2301.9   1.0   0.11   0.03   0 0 0 0 0 0 0 0 0 0 0 0
2315.4   1.0   0.47   0.14   0 0 0 0 0 0 0 0 0 0 0 0
2423.9   1.0   2.77   0.83   0 0 0 0 0 0 0 0 0 0 0 0
2459.3   2.0   2.04   1.02   0 0 0 0 0 0 0 0 0 0 0 0
2463.2   2.0   5.32   2.66   0 0 0 0 0 0 0 0 0 0 0 0
2468.0   2.0   1.06   0.53   0 0 0 0 0 0 0 0 0 0 0 0
2519.3   2.0   0.35   0.18   0 0 0 0 0 0 0 0 0 0 0 0
2522.2   2.0   0.98   0.49   0 0 0 0 0 0 0 0 0 0 0 0
2543.5   2.0   0.31   0.16   0 0 0 0 0 0 0 0 0 0 0 0
2546.4   2.0   3.77   1.88   0 0 0 0 0 0 0 0 0 0 0 0
2555.1   2.0   0.62   0.31   0 0 0 0 0 0 0 0 0 0 0 0
2568.6   2.0   1.24   0.62   0 0 0 0 0 0 0 0 0 0 0 0
2570.6   2.0   1.24   0.62   0 0 0 0 0 0 0 0 0 0 0 0
2610.2   2.0   4.88   2.44   0 0 0 0 0 0 0 0 0 0 0 0
2628.6   2.0   0.75   0.38   0 0 0 0 0 0 0 0 0 0 0 0
2644.1   2.0   0.62   0.31   0 0 0 0 0 0 0 0 0 0 0 0
2648.9   2.0   0.27   0.13   0 0 0 0 0 0 0 0 0 0 0 0
2666.4   2.0   0.62   0.31   0 0 0 0 0 0 0 0 0 0 0 0
2702.1   2.0   1.29   0.64   0 0 0 0 0 0 0 0 0 0 0 0
2722.5   2.0   3.81   1.91   0 0 0 0 0 0 0 0 0 0 0 0
2749.6   2.0   4.43   2.22   0 0 0 0 0 0 0 0 0 0 0 0
2778.6   2.0   0.44   0.22   0 0 0 0 0 0 0 0 0 0 0 0
2792.1   2.0   2.08   1.04   0 0 0 0 0 0 0 0 0 0 0 0
2795.0   2.0   1.51   0.75   0 0 0 0 0 0 0 0 0 0 0 0
2801.8   2.0   2.26   1.13   0 0 0 0 0 0 0 0 0 0 0 0
2819.2   2.0   0.58   0.29   0 0 0 0 0 0 0 0 0 0 0 0
2847.3   2.0   1.29   0.64   0 0 0 0 0 0 0 0 0 0 0 0
2856.0   2.0   0.44   0.22   0 0 0 0 0 0 0 0 0 0 0 0
2895.6   2.0   3.32   1.66   0 0 0 0 0 0 0 0 0 0 0 0
2928.5   2.0   1.55   0.78   0 0 0 0 0 0 0 0 0 0 0 0
**********************************************************************************************************************************
Upper Limits of Resonances
Note: enter partial width upper limit by chosing non-zero value for PT, where PT=<theta^2> for particles and...
Note: ...PT=<B> for g-rays [enter: "upper_limit 0.0"]; for each resonance: # upper limits < # open channels!
Ecm   DEcm  Jr  G1        DG1       L1  PT      DPT     G2    DG2   L2  PT   DPT   G3    DG3    L3  PT   DPT   Exf   Int Prob
52.45 5.0   1.5 6.31e-17  2.5E-17   1   0.0045  0.0005  0.10  0.02  1   0.0  0.0   0     0      0   0    0     0.00  0
144.7 0.7   5.5 1.47e-16  5.8E-17   6   0.0045  0.0005  0.10  0.02  1   0.0  0.0   0     0      0   0    0     0.00  0
169.6 2.0   3.5 2.88e-11  1.2E-11   3   0.0045  0.0005  0.10  0.02  1   0.0  0.0   0     0      0   0    0     0.00  0
**********************************************************************************************************************************
Interference between Resonances [numerical integration only]
Note: + for positive, - for negative interference; +- if interference sign is unknown
Ecm     DEcm    Jr    G1     DG1   L1  PT   DPT    G2     DG2   L2  PT   DPT   G3    DG3   L3  PT   DPT   Exf
!+-
0.0     0.0     0.0   0.0    0.0   0   0    0      0.0    0.0   0   0    0     0.0   0.0   0   0    0     0.0
0.0     0.0     0.0   0.0    0.0   0   0    0      0.0    0.0   0   0    0     0.0   0.0   0   0    0     0.0
**********************************************************************************************************************************
Reaction Rate and PDF at NT selected temperatures only
Note: default values are used for reaction rate range if Min=Max=0.0
T9          Min   Max
0.01        0.0   0.0
0.1         0.0   0.0
**********************************************************************************************************************************
```

Figure A.6: (Part III) RatesMC input file for the ^{30}Si(p,γ)^{31}P reaction.

APPENDIX A.4: Fraction Fitting Posterior Distributions

Below, the posterior distributions obtained via the analysis in Section 7.1.1 are shown. These communicate the probability distribution of the template fractions values, which ultimately indicate what percentage of the data can be attributed to each template. Those shown are specifically for the "singles" mode analysis. Each is labeled according to the primary transition being modeled in that specific template. The Gaussian shape of each posterior argues strongly that the Markov Chain sampler had converged on the solution.

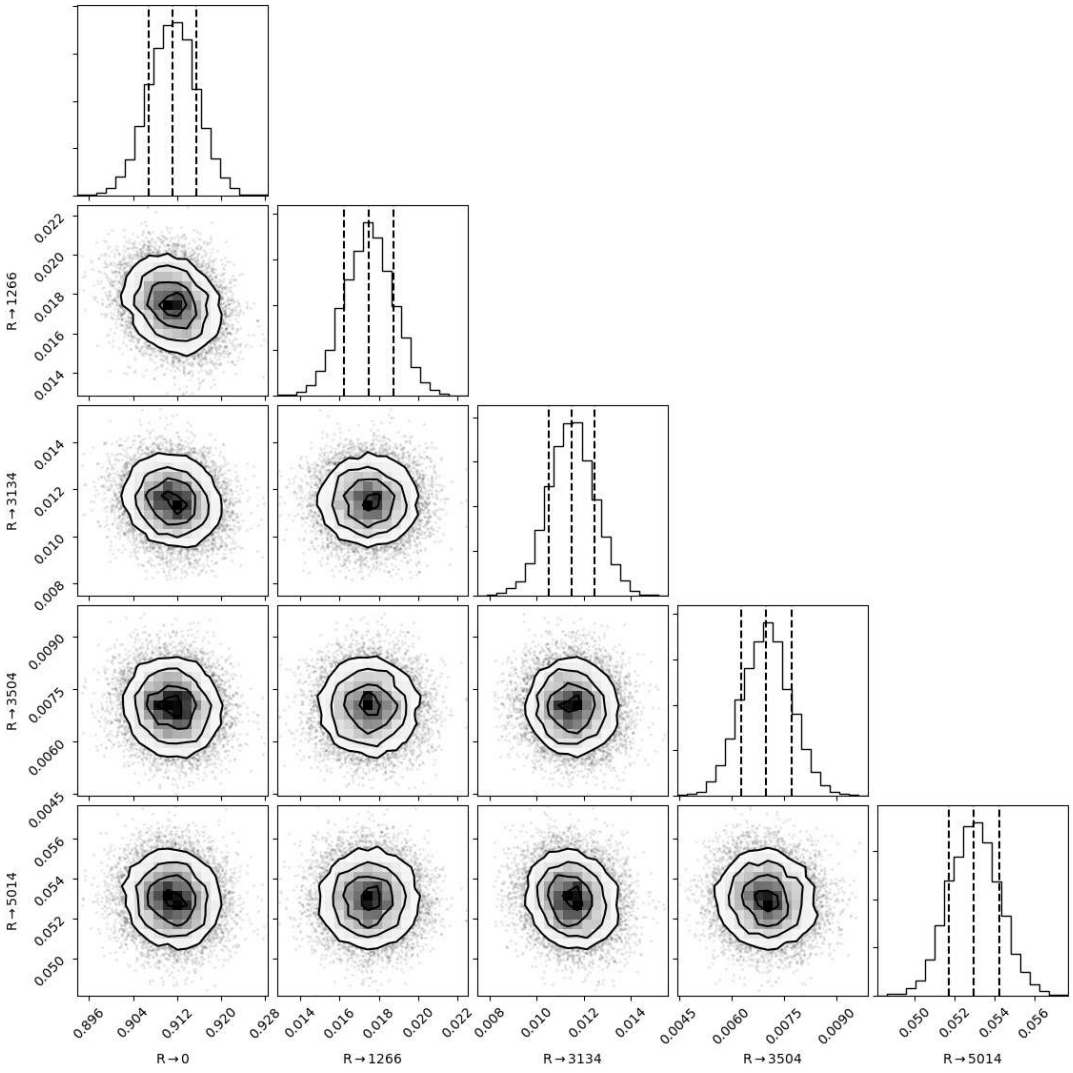

Figure A.7: A scatter-plot matrix of the fraction-fitting posterior distributions, obtained in Section 7.1.1. These refer to the template fractions of the singles mode analysis of the 620-keV resonance data. The vertical dotted lines denote the 16th, 50th, and 84th percentiles.

APPENDIX B: CALCULATIONS

APPENDIX B.1: Detector Response

In this section, the properties of the simulated $\gamma\gamma$-coincidence spectrometer are summarized. First, the dimensions of the simulated HPGe crystal are given. These depart from the values used in previous studies, e.g., Buckner *et al.* [2015] and Kelly *et al.* [2017], which adopted the mean values recommended by Carson *et al.* [2010] and Howard *et al.* [2013]. The decision to change these was motivated by the desire to better match the absolute efficiency calibration (see Section 4.3). The overall effect of the geometry assumed in this work is to lower the peak efficiency by $\approx 7\%$.

Detector Attribute	Adopted (Present work)	Previously Recommended[a]
Crystal length (mm)	89.6	91.6 ± 1.0
Crystal diameter (mm)	88.0	89.0 ± 0.5
Central hole diameter (mm)	9.5	8.5 ± 1.0
Central hole length (mm)	79.1	79.1
Contact layer thickness (mm)	1.5	1.2[b]

[a] Dimensions from Carson *et al.* [2010] unless stated otherwise.
[b] Recommended in Howard *et al.* [2013].

The peak efficiences are shown in Figure B.1 and the total efficiencies are given in Figure B.2. The peak attenuation coefficients, calculated up to order $n = 4$, are shown in Figure B.2. All of these simulations were performed between 400 and 8000 keV. For posterity, the simulated data is then given in Table B.1.

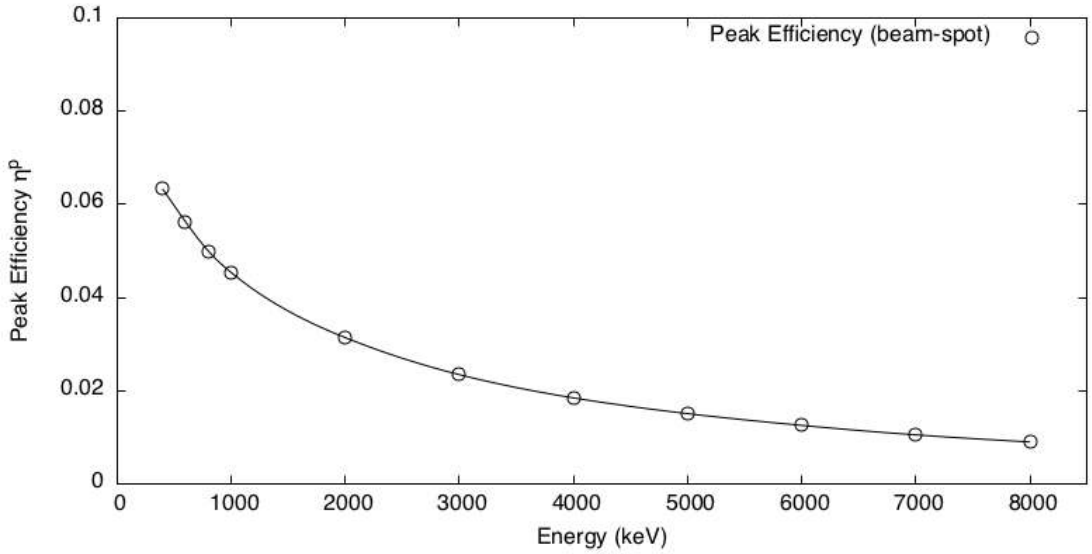

Figure B.1: The peak efficiencies, η^p , for γ-rays emitted from a "beam-spot" configuration over the energy range E_γ = 400-8000 keV. The open circles represent the simulated points, while the solid line is given by a cubic spline to these data.

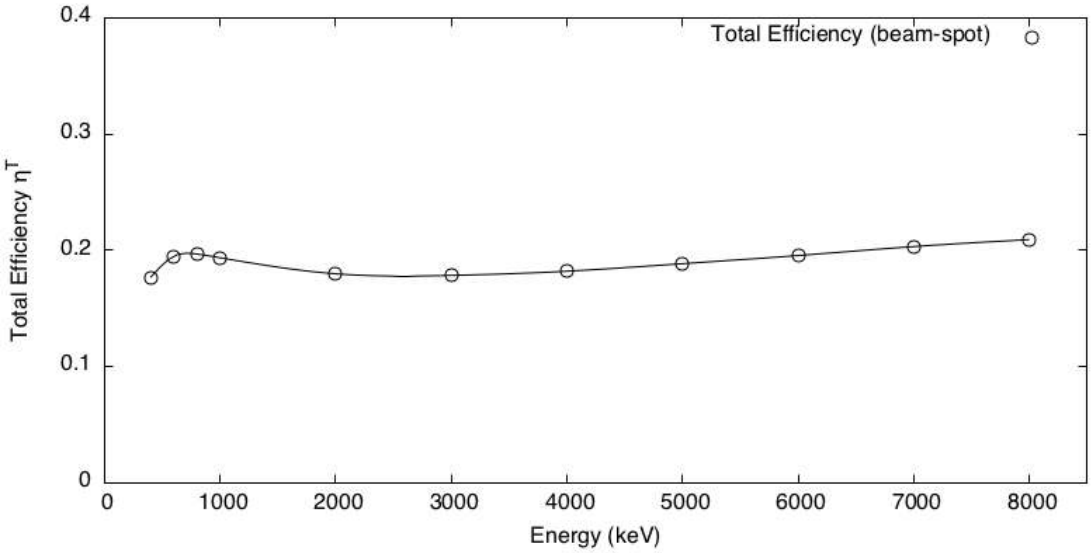

Figure B.2: The total efficiencies, η^T, for γ-rays emitted from a "beam-spot" configuration over the energy range E_γ = 400-8000 keV. The open circles represent the simulated points, while the solid line is given by a cubic spline to these data.

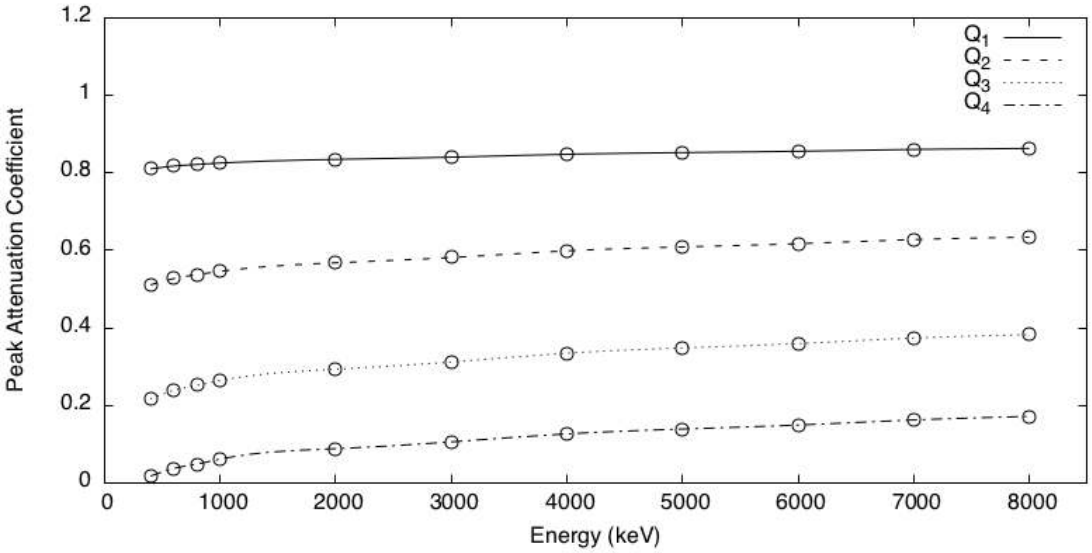

Figure B.3: The peak attenuation coefficients for γ-rays emitted from a "beam-spot" configuration over the energy range E_γ = 400-8000 keV. The data sets, labeled Q_n, demonstrate the attenuation coefficient for radiation emitted with an angular distribution given by an order n Legendre polynomial, as defined in Iliadis [2015]. The open circles represent the simulated points, while the solid line is given by a cubic spline to these data.

E_γ (MeV)	η^p	η^T	Q_1	Q_2	Q_3	Q_4
400	0.06331	0.1768	0.8104	0.5112	0.2174	0.01804
600	0.05629	0.1951	0.8174	0.5275	0.2391	0.0377
800	0.04997	0.1969	0.8217	0.5375	0.2520	0.04899
1000	0.04536	0.1937	0.8252	0.5459	0.2641	0.06154
2000	0.03139	0.1799	0.8347	0.568	0.2936	0.0886
3000	0.02345	0.1785	0.8405	0.5816	0.3122	0.1062
4000	0.01846	0.1821	0.8479	0.5988	0.3349	0.1267
5000	0.01508	0.1886	0.8523	0.6090	0.3485	0.1393
6000	0.01256	0.1956	0.8558	0.6173	0.3597	0.1496
7000	0.01052	0.2033	0.8603	0.6279	0.3739	0.1627
8000	0.0090	0.2093	0.8630	0.6343	0.383	0.1720

Table B.1: The data used to to generate Figures B.1, B.2 and B.3.

APPENDIX B.2: Target Properties

The ^{30}Si target used to measure resonance strengths for this dissertation was made via the implantation of ^{30}Si ions into a tantalum backing. Compared to other methods, such as evaporation or target anodization, where the stoichiometry it is often dictated by the chemical properties of the materials, implanted targets are much less predictable. The stoichiometry of the target is important for the analysis of resonance data, since it affects the effective stopping power, ϵ_{eff}, through the relation:

$$\epsilon_{\text{eff}} = \epsilon_{\text{Si}} + \frac{N_{\text{Ta}}}{N_{\text{Si}}}\epsilon_{\text{Ta}}, \tag{B.1}$$

where ϵ_{Si} and ϵ_{Ta} are the stopping powers of protons in silicon and tantalum, respectively, and N_{Ta} and N_{Si} are their number densities in the bulk of the target layer. Since the stopping powers are energy dependent, e_{eff} has to be calculated at each resonance energy in question.

A measurement of the target stoichiometry can be obtained using the reference resonance at $\text{E}_{\text{p}}^{lab} = 619.6 \pm 1.2$ keV [Kuperus *et al.*, 1959]. Rearranging Equation 4.125 from Iliadis [2015], the effective stopping power is given by:

$$\epsilon_{\text{eff}} = \frac{\lambda^2}{2}\,\omega\gamma\,\frac{N_p}{N_R}, \tag{B.2}$$

where $\lambda^2/2$ is the deBroglie wavelength of the incident proton, $\omega\gamma$ is the resonance strength, and N_R/N_p is the maximum yield, the number of reactions taking place per incident proton in an infinitely thick target. The deBroglie wavelength can be calculated using Equation 4.107 in Iliadis [2015]. The resonance strength, adopted from [Paine and Sargood, 1979], is $\omega\gamma = 1.95 \pm 0.10$ eV. The maximum yield was obtained using yield curve analysis in Section 6.2 and is given by $Y_{max} = 34.11^{+0.81}_{-0.78}$ counts $\cdot\ \mu\text{C}^{-1}$, however, this figure does not take into account the detector response, η^p, or the branching ratio, B, of the measured γ-ray. The corrected yield, appropriate for Equation B.2, is:

$$\frac{N_R}{N_p} = \frac{Y_{\text{max}} \cdot q}{B \cdot W(\theta) \cdot \eta^p},$$

where q is the elementary charge and $W(\theta)$, the angular correlation correction factor, is unity since

the decay is isotropic (see Section blah). The branching ratio of the observed γ-ray, the ground state transition from $E_x = 7896$ keV, is $95 \pm 1\%$, as measured by de Neijs *et al.* [1975]. For the detector response, the peak efficiency was obtained using the program `LENAGe` (see Section 4.3). The simulated peak efficiency for the ground-state transition γ-ray is $\eta^p_{7896} = 0.0090 \pm 0.0003$, where a conservative 4% systematic simulation error has been assumed. The corrected yield is therefore:

$$\frac{N_R}{N_p} = 6.39 \pm 0.30 \times 10^{-10} \qquad \frac{\text{reactions}}{\text{proton}}. \tag{B.3}$$

And so, using Equation B.2:

$$\epsilon_{\text{eff}} = 21.4 \pm 1.8 \qquad \frac{\text{eV} \cdot \text{cm}^2}{10^{15}\ \text{atoms}}. \tag{B.4}$$

With the effective stopping power calculated, the stoichiometry can then be deduced using Equation B.1. The stopping powers for the pure materials, ϵ_{Si} and ϵ_{Ta} are adopted from the program `SRIM` [Ziegler *et al.*, 2010]. Using this information, the ratio $N_{\text{Ta}}/N_{\text{Si}}$ is found to be 0.67 ± 0.11, or, in chemical notation, $\text{Ta}_5\text{Si}_{7.5\pm1.2}$ in the bulk of the target layer. A tabulation of the effective stopping power at the other resonance energies is shown in Table B.2. The stopping powers from `SRIM` are also shown.

E_r^{lab} (keV)	ϵ_{Ta}	ϵ_{Si}	ϵ_{eff} (eV $\cdot$ cm^2 $\cdot 10^{-15}$ atoms)
435.0	27.88	5.99	24.7 ± 3.1
499.0	26.48	5.57	23.3 ± 2.9
619.6	24.36	4.96	21.4 ± 1.8

Table B.2: The adopted stopping powers, ϵ_{Si} and ϵ_{Ta}, and the calculated effective stopping power, ϵ_{eff} for the resonances studied in this dissertation. The stopping powers are adopted from `SRIM` [Ziegler *et al.*, 2010]. The recommended error on the stopping powers are 4.0% and 2.0% for silicon and tantalum, respectively.

APPENDIX B.3: Bound State Branching Ratios

The following branching ratios were used to simulate the decay of bound states in ^{31}P using the `LENAGe` program. They are an important component of correctly simulating the response of the $\gamma\gamma$-spectrometer to the resonant reactions under consideration. The branching ratios were adopted from de Neijs *et al.* [1975]. Where an upper-limit is recommended, i.e., $< 2\%$, the mid point, i.e., 1%, was adopted. In these cases, the branching ratios were renormalized to unity for the simulations.

	Initial State, gamma decay to E_x in ^{31}P (%)								
E_x	0.0	1266.13	2233.6	3134.3	3295.0	3414.6	3506.1	4190.9	4260.4
0.0		100	100	97.3(3)	1.1(2)	< 0.8	57(2)	< 1.5	74.2(15)
1266.13			< 0.2	2.7(3)	78.2(10)	97.6(5)	43(2)	75(2)	25.8(15)
2233.6				< 0.2	20.7(10)	2.4(5)	< 5	25(2)	
3134.3									< 1
3295.0								< 0.5	< 0.5

	Initial State, gamma decay to E_x in ^{31}P (%)								
E_x	4431.2	4592.5	4634.2	4783.4	5014.9	5015.2	5116.0	6496.1	6594.3[a]
0.0	1.0(2)	26(2)	< 4	42.4(15)	72(3)	39(3)	< 5	76(5)	< 5
1266.13	1.9(5)	56(2)	3.0(10)	4.6(15)	23(3)	59(3)	50(3)	24(5)	50(5)
2233.6	53(3)	18(2)	26.3(10)	22(2)	< 1	< 1	25(2)		
3134.3	< 0.1		< 2	< 1		2.0(5)	< 4	< 5	
3295.0	40(2)	< 2	34.5(15)	31(2)	2.0(10)	< 3	11(2)	< 5	< 5
3414.6	4.1(5)	< 0.5	36.2(10)	< 2	< 0.5	< 2	14(2)		
3506.1		< 1	< 5		3.0(10)	< 1	< 4		< 3
4190.9									
4260.4									4(2)
4431.2									16(5)
4592.5									

[a] de Neijs *et al.* [1975] reports that 30% of the decay is unaccounted for.

Table B.3: The branching ratios adopted for the simulation of the ^{30}Si(p,γ)^{31}P reaction, as measured by de Neijs *et al.* [1975].

APPENDIX C: BAYESIAN ESTIMATION

The fundamental difference between Bayesian [Bayes, 1763] and classical (frequentist) statistics can best be understood by examining interval construction in both fields. For the frequentist, confidence intervals are characterized by the concept of *coverage*, which seeks to answer: 'If this experiment were to be repeated and reanalyzed N times, what fraction of the new confidence intervals contains the (fixed) parameter value?' This is a natural question for a frequentist, as they maintain that data are a repeatable random sample, with all parameters being fixed [James, 2006]. The Bayesian, on the other hand, has no such concept of coverage. Bayesian inference is fully conditioned on the observed data, while parameters values are unknown and described by probability distributions. Thus, the confidence interval associated with Bayesian inference, the *credible* interval, quantifies the belief that the parameter value lies within the interval, given the data [Gregory, 2005].

To analyze data using Bayesian inference, we assign distributions to describe model parameters, $\boldsymbol{\theta}$: both the joint unconditional probability distribution function (PDF), $P(\boldsymbol{\theta})$, and the joint conditional PDF, $P(\boldsymbol{\theta}|\boldsymbol{D})$, are taken to represent the *degree of belief* in different values of $\boldsymbol{\theta}$. For the joint conditional distribution, the degree of belief is conditional on the data set, $\boldsymbol{D}$. These are known as the prior and posterior PDF, respectively. The prior distribution summarizes the state of knowledge before performing a measurement. It can be either *informative*, in the sense that it has been influenced by past experiments or theory, or *non-informative*, i.e., any value of $\boldsymbol{\theta}$ is equally likely. To calculate the posterior distribution, practitioners "update" their prior beliefs using Bayes' theorem:

$$P(\boldsymbol{\theta}|\boldsymbol{D}) = \frac{P(\boldsymbol{D}|\boldsymbol{\theta})P(\boldsymbol{\theta})}{\int_\theta P(\boldsymbol{D}|\boldsymbol{\theta})P(\boldsymbol{\theta})} \quad , \tag{C.1}$$

where $P(\boldsymbol{D}|\boldsymbol{\theta})$ represents the likelihood of the collected data, $\boldsymbol{D}$, given the parameter values, $\boldsymbol{\theta}$. To obtain a posterior probability distribution for a single parameter, the parameter is marginalized out:

$$P(\theta_0|\boldsymbol{D}) = \int_{\theta_1,\theta_2,\ldots,\theta_k} P(\boldsymbol{\theta}|\boldsymbol{D})P(\boldsymbol{\theta}) \quad . \tag{C.2}$$

The marginalized posterior distribution, $P(\theta_0|\boldsymbol{D})$, summarizes all one's knowledge or belief concerning θ_0, given both the prior belief and the experimental data, $\boldsymbol{D}$. All the usual statistically

meaningful quantities can be obtained from this function, e.g., the location and spread of the distribution. A credible interval, $[\theta_L, \theta^U]$, with probability content β, can be defined by:

$$\int_{\theta_L}^{\theta^U} P(\theta_0|\boldsymbol{D})d\theta_0 = \beta \quad . \tag{C.3}$$

By this definition, the interval $[\theta_L, \theta^U]$ contains a fraction β of one's total belief about θ. In the present work, upper-limits are used to summarize posterior distributions of weak transitions. We can define an upper-limit by taking $\theta_L \to 0$. In this case, the interval suggests that the parameter value is less than the upper-limit value, θ^U, at the β credibility level.

REFERENCES

Agostinelli, S. *et al.* GEANT4: A Simulation toolkit. *Nucl. Instrum. Meth.*, A506:250–303, 2003.

Ajzenberg-Selove, F. Energy levels of light nuclei A = 11-12. *Nuclear Physics A*, 506(1):1 – 158, 1990. ISSN 0375-9474.

Ajzenberg-Selove, F. Energy levels of light nuclei A = 13-15. *Nuclear Physics A*, 523(1):1 – 196, 1991. ISSN 0375-9474.

Al-Jadir, M N I, Fortune, H T, and Pullen, D J. States of high Ex in ^{31}P. *Journal of Physics G: Nuclear Physics*, 6(6):731, 1980.

Angulo, C., Arnould, M., Rayet, M., Descouvemont, P., Baye, D., Leclercq-Willain, C., Coc, A., Barhoumi, S., Aguer, P., Rolfs, C., Kunz, R., Hammer, J.W., Mayer, A., Paradellis, T., Kossionides, S., Chronidou, C., Spyrou, K., Degl'Innocenti, S., Fiorentini, G., Ricci, B., Zavatarelli, S., Providencia, C., Wolters, H., Soares, J., Grama, C., Rahighi, J., Shotter, A., and Rachti, M. Lamehi. A compilation of charged-particle induced thermonuclear reaction rates. *Nuclear Physics A*, 656(1):3 – 183, 1999. ISSN 0375-9474.

Bardin, C., Dandeu, Y., Gauthier, L., Guillermin, J., Lena, T., Pernet, J.-M., Wolter, H.H., and Tamura, T. Coulomb functions in entire (η,ρ) plane. *Computer Physics Communications*, 3(2):73 – 87, 1972. ISSN 0010-4655.

Barlow, R. and Beeston, C. *Comp. Phys. Commun.*, 77(2):219 – 228, 1993.

Barlow, Roger. *Statistics: A Guide to the Use of Statistical Methods in the Physical Sciences*. John Wiley and Sons, New York, NY, 1989. ISBN 0471922951.

Barlow, Roger J. *Nucl. Instrum. Meth.*, A297:496–506, 1990.

Bastian, Nate, Cabrera-Ziri, Ivan, and Salaris, Maurizio. A general abundance problem for all self-enrichment scenarios for the origin of multiple populations in globular clusters. *Monthly Notices of the Royal Astronomical Society*, 449(3):3333–3346, 2015.

Bayes, T. *Phil. Trans. R. Soc.*, 53:370, 1763.

Bekki, Kenji. Secondary star formation within massive star clusters: origin of multiple stellar populations in globular clusters. *Monthly Notices of the Royal Astronomical Society*, 412(4):22412259, 2011. ISSN 0035-8711.

Betigeri, M., Bock, R., Duhm, H. H., Martin, S., and Stock, R. Die reaktionen ^{30}Si(d,p)^{31}Si und ^{30}Si(^{3}He,d)^{31}P. *Zeitschrift fur Naturforschung - Section A Journal of Physical Sciences*, 21(7):980–987, 1966. Cited By :34.

Bloecker, T. Stellar evolution of low and intermediate-mass stars. I. Mass loss on the AGB and its consequences for stellar evolution. *AAP*, 297:727, 1995.

Bornman, C.H., Meyer, M.A., and Reitmann, D. Resonances in the ^{30}Si(p,γ)^{31}P reaction between

2 and 3 MeV. *Nuclear Physics A*, 99(2):337 – 344, 1967. ISSN 0375-9474.

Bragaglia, A., Carretta, E., Gratton, R. G., Lucatello, S., Milone, A., Piotto, G., D'Orazi, V., Cassisi, S., Sneden, C., and Bedin, L. R. X-shooter observations of main-sequence stars in the globular cluster NGC 2808: First chemical tagging of a He-normal and a He-rich dwarf. *The Astrophysical Journal Letters*, 720(1):L41, 2010.

Broude, C, Green, L L, and Willmott, J C. The energy levels of ^{31}P I: γ-ray spectra and decay schemes. *Proceedings of the Physical Society*, 72(6):1097, 1958a.

Broude, C, Green, L L, and Willmott, J C. The energy levels of ^{31}P II: Angular distributions and correlations. *Proceedings of the Physical Society*, 72(6):1115, 1958b.

Buckner, M. Q., Iliadis, C., Cesaratto, J. M., Howard, C., Clegg, T. B., Champagne, A. E., and Daigle, S. Thermonuclear reaction rate of ^{18}O(p,γ)^{19}F. *Phys. Rev. C*, 86:065804, 2012.

Buckner, M. Q., Iliadis, C., Kelly, K. J., Downen, L. N., Champagne, A. E., Cesaratto, J. M., Howard, C., and Longland, R. High-intensity-beam study of ^{17}O$(p,\gamma)^{18}$F and thermonuclear reaction rates for $^{17}\mathrm{O} + p$. *Phys. Rev. C*, 91:015812, 2015.

Buckner, Matthew. *Hydrogen Burning of the Rate Oxygen Isotopes*. Ph.D. thesis, University of North Carolina at Chapel Hill, 2014.

Carretta, E., Bragaglia, A., Gratton, R. G., Recio-Blanco, A., Lucatello, S., DOrazi, V., and Cassisi, S. Properties of stellar generations in globular clusters and relations with global parameters. *Astronomy and Astrophysics*, 516:A55, 2010. ISSN 1432-0746.

Carson, Spencer, Iliadis, Christian, Cesaratto, John, Champagne, Art, Downen, Lori, Ivanovic, Marija, Kelley, John, Longland, Richard, Newton, Joseph R., Rusev, Gencho, and Tonchev, Anton P. Ratio of germanium detector peak efficiencies at photon energies of 4.4 and 11.7 MeV: Experiment versus simulation. *Nuclear Instruments and Methods in Physics Research Section A: Accelerators, Spectrometers, Detectors and Associated Equipment*, 618(1):190 – 198, 2010. ISSN 0168-9002.

Cesaratto, J. M., Champagne, A. E., Buckner, M. Q., Clegg, T. B., Daigle, S., Howard, C., Iliadis, C., Longland, R., Newton, J. R., and Oginni, B. M. Measurement of the $E_r^{\mathrm{c.m.}} = 138$ keV resonance in the ^{23}Na(p,γ)^{24}Mg reaction and the abundance of sodium in AGB stars. *Phys. Rev. C*, 88:065806, 2013.

Cesaratto, J.M., Champagne, A.E., Clegg, T.B., Buckner, M.Q., Runkle, R.C., and Stefan, A. Nuclear astrophysics studies at LENA: The accelerators. *Nuclear Instruments and Methods in Physics Research Section A: Accelerators, Spectrometers, Detectors and Associated Equipment*, 623(3):888 – 894, 2010. ISSN 0168-9002.

Cesaratto, John. *Resonant Proton Capture on ^{23}Na and Elemental Variations in Globular Cluster Stars*. Ph.D. thesis, University of North Carolina at Chapel Hill, 2011.

Cohen, Judith G. and Kirby, Evan N. The bizarre chemical inventory of NGC2419, an extreme outer halo globular cluster. *The Astrophysical Journal*, 760(1):86, 2012.

Cooper, Andrew L., Kelly, K. J., Machado, E., Pogrebnyak, I., Surbrook, J., Tysor, C., Thompson, P., Emamian, M., Walsh, B., Carlin, B., Dermigny, J. R., Champagne, A. E., and Clegg, T. B. Development of a variable-energy, high-intensity, pulsed-mode ion source for low-energy nuclear astrophysics studies. *Review of Scientific Instruments*, 89(8):083301, 2018.

Daigle, S., Kelly, K. J., Champagne, A. E., Buckner, M. Q., Iliadis, C., and Howard, C. Measurement of the $E_r^{\mathrm{c.m.}} = 259$ keV resonance in the $^{14}\mathrm{N}(p,\gamma)^{15}\mathrm{O}$ reaction. *Phys. Rev. C*, 94:025803, 2016.

De Angeli, Francesca, Piotto, Giampaolo, Cassisi, Santi, Busso, Giorgia, Recio-Blanco, Alejandra, Salaris, Maurizio, Aparicio, Antonio, and Rosenberg, Alfred. Galactic globular cluster relative ages. *The Astronomical Journal*, 130(1):116125, 2005. ISSN 1538-3881.

de Mink, S. E., Pols, O. R., Langer, N., and Izzard, R. G. Massive binaries as the source of abundance anomalies in globular clusters. *A&A*, 507(1):L1–L4, 2009.

de Neijs, E.O., Haasbroek, G.D., Meyer, M.A., Rossouw, R.S., and Reitmann, D. Levels of ^{31}P from proton capture in ^{30}Si. *Nuclear Physics A*, 254(1):4562, 1975. ISSN 0375-9474.

de Souza, R. S., Hilbe, J. M., Buelens, B., Riggs, J. D., Cameron, E., Ishida, E. E. O., Chies-Santos, A. L., and Killedar, M. The overlooked potential of generalized linear models in astronomy III. bayesian negative binomial regression and globular cluster populations. *Monthly Notices of the Royal Astronomical Society*, 453(2):19281940, 2015. ISSN 1365-2966.

De Voigt, M. J. A., Regenboog, D. A., Grootenhuis, J., and Van Der Leun, C. Levels of ^{31}P from α-particle capture in ^{27}Al. *Nucl. Phys.*, A176:97–109, 1971.

Decressin, T., Meynet, G., Charbonnel, C., Prantzos, N., and Ekström, S. Fast rotating massive stars and the origin of the abundance patterns in galactic globular clusters. *A&A*, 464(3):1029–1044, 2007.

Denissenkov, P. A. and Hartwick, F. D. A. Supermassive stars as a source of abundance anomalies of proton-capture elements in globular clusters. *Monthly Notices of the Royal Astronomical Society: Letters*, 437(1):L21–L25, 2014.

D'Ercole, Annibale, D'Antona, Francesca, Ventura, Paolo, Vesperini, Enrico, and McMillan, Stephen L. W. Abundance patterns of multiple populations in globular clusters: a chemical evolution model based on yields from AGB ejecta. *Monthly Notices of the Royal Astronomical Society*, 407(2):854869, 2010. ISSN 0035-8711.

Dermigny, J. R. and Iliadis, C. Sensitivity to thermonuclear reaction rates in modeling the abundance anomalies of NGC 2419. *The Astrophysical Journal*, 848(1):14, 2017.

Dermigny, J.R., Iliadis, C., Buckner, M.Q., and Kelly, K.J. γ-ray spectroscopy using a binned likelihood approach. *Nuclear Instruments and Methods in Physics Research Section A: Accelerators, Spectrometers, Detectors and Associated Equipment*, 830:427 – 437, 2016. ISSN 0168-9002.

Di Cecco, A., Becucci, R., Bono, G., Monelli, M., Stetson, P. B., DeglInnocenti, S., Prada Moroni, P. G., Nonino, M., Weiss, A., Buonanno, R., and et al. On the absolute age of the globular cluster M921. *Publications of the Astronomical Society of the Pacific*, 122(895):991999, 2010.

ISSN 1538-3873.

Di Criscienzo, M., D'Antona, F., Milone, A. P., Ventura, P., Caloi, V., Carini, R., D'Ercole, A., Vesperini, E., and Piotto, G. NGC 2419: a large and extreme second generation in a currently undisturbed cluster. *Monthly Notices of the Royal Astronomical Society*, 414(4):3381–3393, 2011.

Di Leva, A., Scott, D. A., Caciolli, A., Formicola, A., Strieder, F., Aliotta, M., Anders, M., Bemmerer, D., Broggini, C., Corvisiero, P., Elekes, Z., Fülöp, Zs., Gervino, G., Guglielmetti, A., Gustavino, C., Gyürky, Gy., Imbriani, G., José, J., Junker, M., Laubenstein, M., Menegazzo, R., Napolitani, E., Prati, P., Rigato, V., Roca, V., Somorjai, E., Salvo, C., Straniero, O., Szücs, T., Terrasi, F., and Trezzi, D. Underground study of the $^{17}O(p,\gamma)^{18}F$ reaction relevant for explosive hydrogen burning. *Phys. Rev. C*, 89:015803, 2014.

Endt, P. M. and Paris, C. H. Nuclear levels in ^{28}Si and ^{31}P. *Phys. Rev.*, 106:764–766, 1957.

Endt, P.M. Energy levels of A = 21-44 nuclei (VII). *Nuclear Physics A*, 521:1 – 400, 1990. ISSN 0375-9474.

Endt, P.M. and van der Leun, C. Energy levels of Z = 11-21 nuclei (IV). *Nuclear Physics A*, 105(1):1 – 488, 1967. ISSN 0375-9474.

Forbes, Duncan A., Bastian, Nate, Gieles, Mark, Crain, Robert A., Kruijssen, J. M. Diederik, Larsen, Søren S., Ploeckinger, Sylvia, Agertz, Oscar, Trenti, Michele, Ferguson, Annette M. N., Pfeffer, Joel, and Gnedin, Oleg Y. Globular cluster formation and evolution in the context of cosmological galaxy assembly: open questions. *Proceedings of the Royal Society A: Mathematical, Physical and Engineering Science*, 474(2210):20170616, 2018.

Forbes, Duncan A. and Bridges, Terry. Accreted versus in situ milky way globular clusters. *Monthly Notices of the Royal Astronomical Society*, 404(3):1203–1214, 2010.

Foreman-Mackey, D., Hogg, D. W., Lang, D., and Goodman, J. emcee: The MCMC Hammer. , 125:306, 2013.

Foreman-Mackey, Daniel. corner.py: Scatterplot matrices in python. *The Journal of Open Source Software*, 24, 2016.

Fox, C., Iliadis, C., Champagne, A. E., Fitzgerald, R. P., Longland, R., Newton, J., Pollanen, J., and Runkle, R. Thermonuclear reaction rate of ^{17}O$(p,\gamma)^{18}$F. *Phys. Rev. C*, 71:055801, 2005.

Fusi-Pecci, Flavio and Clementini, Gisella. Globular clusters. *The Encyclopedia of Astronomy and Astrophysics*, 2001.

Goodman, Jonathan and Weare, Jonathan. Ensemble samplers with affine invariance. *Communications in Applied Mathematics and Computational Science*, 5(1):6580, 2010. ISSN 1559-3940.

Goswami, A. and Prantzos, N. Abundance evolution of intermediate mass elements (C to Zn) in the Milky Way halo and disk. *AAP*, 359:191–212, 2000.

Gratton, R. G., Carretta, E., Bragaglia, A., Lucatello, S., and DOrazi, V. The second and third parameters of the horizontal branch in globular clusters. *Astronomy and Astrophysics*, 517:A81,

2010. ISSN 1432-0746.

Gregory, P. *Bayesian Logical Data Analysis for the Physical Sciences*. Cambridge University Press, 2005.

Hoogenboom, A. Ph.D. thesis, Utrecht University, 1958.

Hough, J.H., du Toit, Z.B., and Mouton, W.L. Level widths in ^{31}P. *Nuclear Physics A*, 109(2):393 – 400, 1968. ISSN 0375-9474.

Howard, C., Iliadis, C., and Champagne, A.E. Monte Carlo simulation of the LENA detector system. *Nuclear Instruments and Methods in Physics Research Section A: Accelerators, Spectrometers, Detectors and Associated Equipment*, 729:254 – 259, 2013. ISSN 0168-9002.

Iliadis, C. Proton single-particle reduced widths for unbound states. *Nuclear Physics A*, 618(1):166 – 175, 1997. ISSN 0375-9474.

Iliadis, C., Karakas, A. I., Prantzos, N., Lattanzio, J. C., and Doherty, C. L. On potassium and other abundance anomalies of red giants in NGC 2419. *The Astrophysical Journal*, 818(1):98, 2016.

Iliadis, C., Longland, R., Champagne, A.E., and Coc, A. Charged-particle thermonuclear reaction rates: III. nuclear physics input. *Nuclear Physics A*, 841(1):251 – 322, 2010a. ISSN 0375-9474. The 2010 Evaluation of Monte Carlo based Thermonuclear Reaction Rates.

Iliadis, C., Longland, R., Champagne, A.E., Coc, A., and Fitzgerald, R. Charged-particle thermonuclear reaction rates: II. tables and graphs of reaction rates and probability density functions. *Nuclear Physics A*, 841(1):31 – 250, 2010b. ISSN 0375-9474. The 2010 Evaluation of Monte Carlo based Thermonuclear Reaction Rates.

Iliadis, Christian. *Nuclear Physics of Stars*. Wiley-VCH Verlag GmbH Co. KGaA, 2015. ISBN 9783527336487.

Iliadis, Christian, Longland, Richard, Coc, Alain, Timmes, F X, and Champagne, Art E. Statistical methods for thermonuclear reaction rates and nucleosynthesis simulations. *Journal of Physics G: Nuclear and Particle Physics*, 42(3):034007, 2015.

James, F. and Roos, M. *Comput. Phys. Commun.*, 10:343, 1975.

James, Frederick. Statistical methods in experimental physics, 2006.

Jeffreys, H. *Proc. R. Soc. London A*, 196(12):453, 1946.

Kelly, K. J., Champagne, A. E., Downen, L. N., Dermigny, J. R., Hunt, S., Iliadis, C., and Cooper, A. L. New measurements of low-energy resonances in the $^{22}Ne(p,\gamma)^{23}Na$ reaction. *Phys. Rev. C*, 95:015806, 2017.

Kelly, Keegan. *Nuclear Reaction Rate Uncertainties and the $^{22}Ne(p,\gamma)^{23}Na$ Reaction: Classical Novae and Globular Clusters*. Ph.D. thesis, University of North Carolina at Chapel Hill, 2016.

Kim, I.J., Park, C.S., and Choi, H.D. Absolute calibration of ^{60}Co by using sum-peak method and

an HPGe detector. *Applied Radiation and Isotopes*, 58(2):227 – 233, 2003. ISSN 0969-8043.

Knoll, Glenn. *Radiation Detection and Measurement*. Wiley, New York, NY, 2010. ISBN 9780470131480.

Kruijssen, J M Diederik. Globular cluster formation in the context of galaxy formation and evolution. *Classical and Quantum Gravity*, 31(24):244006, 2014.

Kuperus, J., Smulders, P.J.M., and Endt, P.M. Energy measurements of proton resonances in light nuclei. *Physica*, 25(1):600 – 609, 1959. ISSN 0031-8914.

Longland, R., Daigle, S., Cesaratto, J.M., Iliadis, C., and Newton, J.R. Target backing contamination reduction. *TUNL Progress Report*, XLVIII:177 – 178, 2009.

Longland, R., Iliadis, C., Cesaratto, J. M., Champagne, A. E., Daigle, S., Newton, J. R., and Fitzgerald, R. Resonance strength in $^{22}Ne(p,\gamma)^{23}Na$ from depth profiling in aluminum. *Phys. Rev. C*, 81:055804, 2010a.

Longland, R., Iliadis, C., Champagne, A. E., Fox, C., and Newton, J. R. Nuclear astrophysics studies at the LENA facility: The γ-ray detection system. *Nuclear Instruments and Methods in Physics Research, Section A: Accelerators, Spectrometers, Detectors and Associated Equipment*, 566(2):452–464, 2006. ISSN 0168-9002.

Longland, R., Iliadis, C., Champagne, A.E., Newton, J.R., Ugalde, C., Coc, A., and Fitzgerald, R. Charged-particle thermonuclear reaction rates: I. Monte Carlo method and statistical distributions. *Nuclear Physics A*, 841(1):1 – 30, 2010b. ISSN 0375-9474. The 2010 Evaluation of Monte Carlo based Thermonuclear Reaction Rates.

Lyons, P.B., Toevs, J.W., and Sargood, D.G. Total yield measurements in ^{27}Al(p, γ)^{28}Si. *Nuclear Physics A*, 130(1):1 – 24, 1969. ISSN 0375-9474.

Maccarone, Thomas J. and Zurek, David R. Novae from isolated white dwarfs as a source of helium for second-generation stars in globular clusters. *Monthly Notices of the Royal Astronomical Society*, 423(1):2–6, 2012.

MacKay, D. J. C. *Neural Comp.*, 11(5):1035–1068, 1999.

MacMullin, Jacqueline. *Validation of the Background Model for the Majorana Demonstrator*. Ph.D. thesis, University of North Carolina at Chapel Hill, 2015.

Marino, A. F., Milone, A. P., and Lind, K. Horizontal branch morphology and multiple stellar populations in the anomalous globular cluster M 22. *The Astrophysical Journal*, 768(1):27, 2013. ISSN 1538-4357.

McCulloch, R.A., Clarke, N.M., Griffiths, R.J., Hanspal, J.S., Roman, S., and Barnwell, J.M. The interaction of 33 MeV polarised helions with ^{30}Si. *Nuclear Physics A*, 431(2):344 – 366, 1984. ISSN 0375-9474.

Meyer, M.A., Venter, I., and Reitmann, D. Energy levels of ^{28}Si. *Nuclear Physics A*, 250(2):235 – 256, 1975. ISSN 0375-9474.

Middleton, R. A versatile high intensity negative ion source. *Nuclear Instruments and Methods in Physics Research*, 220(1):105 – 106, 1984. ISSN 0167-5087.

Milone, A. P. Helium and multiple populations in the massive globular cluster NGC6266 (M62). *Monthly Notices of the Royal Astronomical Society*, 446(2):16721684, 2014. ISSN 0035-8711.

Moss, C.E. Excitation energies of levels in ^{31}P. *Nuclear Physics A*, 124(2):440 – 444, 1969. ISSN 0375-9474.

Mucciarelli, A., Bellazzini, M., Ibata, R., Merle, T., Chapman, S. C., Dalessandro, E., and Sollima, A. News from the galactic suburbia: the chemical composition of the remote globular cluster NGC 2419. *Monthly Notices of the Royal Astronomical Society*, 426(4):2889–2900, 2012.

Mucciarelli, Alessio, Bellazzini, Michele, Merle, Thibault, Plez, Bertrand, Dalessandro, Emanuele, and Ibata, Rodrigo. Potassium: A new actor on the globular cluster chemical evolution stage. the case of NGC2808. *The Astrophysical Journal*, 801(1):68, 2015.

Newton, J. R., Iliadis, C., Champagne, A. E., Coc, A., Parpottas, Y., and Ugalde, C. Gamow peak in thermonuclear reactions at high temperatures. *Phys. Rev. C*, 75:045801, 2007.

Ouellet, Christian and Singh, Balraj. Nuclear data sheets for A=31. *Nuclear Data Sheets*, 114(2):209 – 396, 2013. ISSN 0090-3752.

Paine, B.M. and Sargood, D.G. (p, γ) resonance strengths in the s-d shell. *Nuclear Physics A*, 331(2):389 – 400, 1979. ISSN 0375-9474.

Parada, Javiera, Richer, Harvey, Heyl, Jeremy, Kalirai, Jason, and Goldsbury, Ryan. Formation and evolution of blue stragglers in 47 tucanae. *The Astrophysical Journal*, 830(2):139, 2016.

Patil, Anand, Huard, David, and Fonnesbeck, Christopher. PyMC 2: Bayesian stochastic modelling in python. *Journal of Statistical Software*, 35(4), 2010.

Piotto, G., Bedin, L. R., Anderson, J., King, I. R., Cassisi, S., Milone, A. P., Villanova, S., Pietrinferni, A., and Renzini, A. A triple main sequence in the globular cluster NGC 2808. *The Astrophysical Journal Letters*, 661(1):L53, 2007.

Pogrebnyak, I., Howard, C., Iliadis, C., Longland, R., and Mitchell, G. E. Mean proton and α-particle reduced widths of the porter-thomas distribution and astrophysical applications. *Phys. Rev. C*, 88:015808, 2013.

Prantzos, N., Charbonnel, C., and Iliadis, C. Light nuclei in galactic globular clusters: constraints on the self-enrichment scenario from nucleosynthesis. *Astronomy Astrophysics*, 470(1):179190, 2007a. ISSN 1432-0746.

Prantzos, N., Charbonnel, C., and Iliadis, C. Light nuclei in galactic globular clusters: constraints on the self-enrichment scenario from nucleosynthesis. *A&A*, 470(1):179–190, 2007b.

Riihonen, M., Keinonen, J., and Anttila, A. Hydrogen burning of ^{29,30}Si in explosive carbon burning. *Nuclear Physics A*, 313(1):251 – 268, 1979. ISSN 0375-9474.

Rinsvelt, H.A. Van and Endt, P.M. Decay scheme, spin and parity of the 3.13, 3.29, 3.41 and 3.51 MeV levels in ^{31}P. *Physica*, 32(3):529 – 547, 1966. ISSN 0031-8914.

Rohatgi, Ankit. Webplotdigitizer, 2015.

Rolfs, C. Spectroscopic factors from radiative capture reactions. *Nuclear Physics A*, 217(1):29 – 70, 1973. ISSN 0375-9474.

Rosenberg, A., Saviane, I., Piotto, G., and Aparicio, A. Galactic globular cluster relative ages. *The Astronomical Journal*, 118(5):23062320, 1999. ISSN 0004-6256.

Sallaska, A. L., Iliadis, C., Champange, A. E., Goriely, S., Starrfield, S., and Timmes, F. X. STARLIB: A next-generation reaction-rate library for nuclear astrophysics. *The Astrophysical Journal Supplement Series*, 207(1):18, 2013.

Semkow, Thomas M., Mehmood, Ghazala, Parekh, Pravin P., and Virgil, Mark. Coincidence summing in gamma-ray spectroscopy. *Nuclear Instruments and Methods in Physics Research Section A: Accelerators, Spectrometers, Detectors and Associated Equipment*, 290(2):437 – 444, 1990. ISSN 0168-9002.

Sills, Alison and Glebbeek, Evert. Multiple populations in globular clusters: the possible contributions of stellar collisions. *Monthly Notices of the Royal Astronomical Society*, 407(1):277–284, 2010.

Smith, P. B. and Endt, P. M. Resonant absorption of gamma radiation from the $^{30}Si(p,\gamma)^{31}$P reaction. *Phys. Rev.*, 110:1442–1445, 1958.

Swartz, K. B., Visser, Dale, and M. Baris, John. A java-based data acquisition system for nuclear physics. 463:354–360, 2001.

Tilley, D.R., Cheves, C.M., Kelley, J.H., Raman, S., and Weller, H.R. Energy levels of light nuclei, A = 20. *Nuclear Physics A*, 636(3):249 – 364, 1998. ISSN 0375-9474.

Twin, P J, Jayasinghe, E M, Jones, G D, Lornie, P R G, Nagel, A, Price, H G, and Thomas, M F. Gamma-ray spectroscopy in ^{31}P: levels below 7.5 MeV (populated in ^{28}Si(α,pγ) reaction). *Journal of Physics A: Mathematical, Nuclear and General*, 7(12):1410, 1974.

van Rinsvelt, H.A. and Endt, P.M. The ^{30}Si(p,γ)^{31}P reaction for bombarding energies between 1.53 and 2.00 MeV. *Physica*, 32(3):513 – 528, 1966. ISSN 0031-8914.

van Rinsvelt, H.A. and Smith, P.B. The ^{30}Si(p,γ)^{31}P reaction for bombarding energies between 1.00 and 1.53 MeV. *Physica*, 30(1):59 – 83, 1964. ISSN 0031-8914.

Ventura, Paolo, D'Antona, Francesca, Criscienzo, Marcella Di, Carini, Roberta, D'Ercole, Annibale, and vesperini, Enrico. Super-AGB-AGB evolution and the chemical inventory in NGC2419. *The Astrophysical Journal Letters*, 761(2):L30, 2012.

Vermilyea, D.A. The kinetics of formation and structure of anodic oxide films on tantalum. *Acta Metallurgica*, 1(3):282 – 294, 1953. ISSN 0001-6160.

Vernotte, J., Khendriche, A., Berrier-Ronsin, G., Grafeuille, S., Kalifa, J., Rotbard, G., Tamisier, R., and Wildenthal, B. H. ^{30}Si(^{3}He,d)^{31}P reaction at 25 MeV. *Phys. Rev. C*, 41:1956–1974, 1990.

Wang, Meng, Audi, G., Kondev, F.G., Huang, W.J., Naimi, S., and Xu, Xing. The AME2016 atomic mass evaluation (II). tables, graphs and references. *Chinese Physics C*, 41(3):030003, 2017.

Willmes, Henry and Harris, Gale I. Investigation of excited states of ^{31}P with the ^{30}Si(p,γ)^{31}P reaction. *Phys. Rev.*, 162:1027–1035, 1967.

Wolff, A.C., Boelhouwer, W.C.R., and Endt, P.M. Spin determinations of ^{31}P levels from the ^{30}Si(p,γ) reaction. *Nuclear Physics A*, 124(2):273 – 286, 1969. ISSN 0375-9474.

Wolff, A.C., Meyer, M.A., and Endt, P.M. A study of the excited states of ^{31}P with the ^{30}Si(p,γ)^{31}P reaction. *Nuclear Physics A*, 107(2):332 – 346, 1968. ISSN 0375-9474.

Yedave, S., Tang, Y., Byl, O., and Sweeney, J. Silicon tetrafluoride dopant gas for silicon ion implantation. In *2014 20th International Conference on Ion Implantation Technology (IIT)*, pages 1–4, 2014.

Ziegler, James F., Ziegler, M.D., and Biersack, J.P. SRIM the stopping and range of ions in matter. *Nuclear Instruments and Methods in Physics Research Section B: Beam Interactions with Materials and Atoms*, 268(11):1818 – 1823, 2010. ISSN 0168-583X. 19th International Conference on Ion Beam Analysis.